Magnetometer array-based indoor navigation using Kalman filter

Makia Zmitri

Communauté UNIVERSITÉ Grenoble Alpes

THÈSE

Pour obtenir le grade de

DOCTEUR DE LA COMMUNAUTÉ UNIVERSITÉ GRENOBLE ALPES

Spécialité : **Automatique - Productique**

Arrêté ministériel : 25 mai 2016

Présentée par

Makia ZMITRI

Thèse dirigée par **Christophe PRIEUR**
et codirigée par **Hassen FOURATI**

préparée au sein du **Laboratoire Grenoble Images Parole Signal Automatique (GIPSA-Lab)**
dans **l'École Doctorale Électronique Électrotechnique Automatique et Traitement du Signal (EEATS)**

Magnetometer Array-Based Indoor Navigation Using Kalman Filter

Thèse soutenue publiquement le **29 septembre 2021**, devant le jury composé de:

Monsieur Mazen ALAMIR
Directeur de Recherche, CNRS, GIPSA-Lab, Président

Monsieur Fredrik GUSTAFSSON
Professeur, Linköping University, Rapporteur

Madame Valérie RENAUDIN
Directrice de Recherche, Université Gustave Eiffel, Rapporteure

Monsieur Axel BARRAU
Ingénieur de Recherche, SAFRAN, Examinateur

Monsieur Hendrik MEIER
Ingénieur de Recherche, SYSNAV, Examinateur

Monsieur Noureddine MANAMANNI
Professeur, Université de Reims Champagne-Ardenne, CReSTIC, Examinateur

Monsieur Christophe PRIEUR
Directeur de Recherche, CNRS, GIPSA-Lab, Directeur de thèse

Monsieur Hassen FOURATI
Maître de Conférences, UGA, GIPSA-Lab, Co-Encadrant de thèse, Invité

"À mon père, Lotfi Zmitri, que ton âme repose en paix..."

Acknowledgments

Accomplishing this thesis would not have been possible without the tremendous support of many people that I have met during these three years.

First of all, I would like to thank my thesis director, Christophe Prieur, for his continuous trust and encouragement, and for his genuine dedication, not only on the scientific level, but also on the personal one. The professionalism of Christophe made this experience pleasant and fruitful.
I also thank my supervisor, Hassen Fourati, for first, offering me the opportunity to join GIPSA-Lab as an intern during my last engineering year, and second, for believing in me to pursue a PhD afterwards. Hassen has always given me useful insights to better value my work and grow my skills, for which I am very grateful.

I express my gratitude to the entire SYSNAV team, Mathieu Hillion, Hendrik Meier, and Thomas Bonis, for the valuable discussions that we shared, and for providing me with the sensor module, used in the experimental benchmark of this work.
More particularly, I thank Charles-Ivan Chesneau, for his assistance during the beginning of my PhD, which enabled me to better detect and understand the difficulties of my thesis subject.

I am also very thankful to the team of the Biomeca room at GIPSA-Lab, Jonathan Dumon, Clementine Darj and Sebastien Dycke, for their true commitment to the success of my experiments with the motion capture system. Despite the many encountered constraints, they gladly helped me, from the conception of the markers frame, to the recorded data acquisition.

I would also like to send a special shout-out to some of the special people that I was lucky to know throughout my years in GIPSA-Lab: Mazen Alamir, for his compassion and support during the tough times that I have went through, and for his honest opinions and advice accordingly. Virginie Faure, for always uplifting me after each conversation we had, and my colleagues, for putting up with my incessant wining for the entire three years! In short, thank you to anyone who contributed in making my stay in GIPSA-lab enjoyable.

Last but not least, I thank all my friends: Kaouther, Rania, Amgad, Omar, Malek, Sly,..., and many others! Without your presence, and your unconditional support, I would not have been able to reach this day. No words can express how grateful I am to having each one of you around me, food will however do the trick ;)

Finally, a thought to my entire family, for being the source of my strength, my father, Lotfi Zmitri, my hero, my role model and my inspiration. Every sacrifice you have done, has finally paid off. I hope that you are watching over me, and that you are proud, from up above.

Contents

Nomenclature

$[\omega^b\times]$	Skew-symmetric matrix of the angular velocity ω^b
α	Multiplication factor of the measurement covariance adapter
$\alpha_{1,\cdots,5}$	The elements of ∇B^n
$\beta_{1,\cdots,5}$	The elements of ∇B^b
Δr	Difference between the MIT and the Qualisys sample rates
δ_d	Detection threshold of a zero-velocity detector
ε	Threshold of the measurement covariance adapter
η	Process noise of a dynamic model, assumed to be zero-mean, white and Gaussian
η^b_ω	Angular velocity noise contained in ω^b_{IMU}
η^b_a	Acceleration noise contained in a^b_{IMU}
$\eta^b_{\nabla B}$	Noise contained in ∇B^b
η^b_B	Magnetic field noise contained in magnetometer measurements
γ^b	Linear acceleration vector, expressed in the body frame $\Re^b$
$\gamma_{1,\cdots,7}$	The elements of T^b
$\lambda_{1,\cdots,3}$	Eigenvalues of ∇B^b
$\mathscr{O}$	Observability matrix of a dynamic model
$\mathfrak{B}^{\mathfrak{b}}$	Orthonormal basis associated with $\Re^b$ and coincides with the sensor board inner sensors axes
$\mathfrak{B}^{\mathfrak{n}}$	Orthonormal basis associated with $\Re^n$
∇B^b	Gradient of the magnetic field B^b
∇B^n	Gradient of the magnetic field B^n
ν	Measurement noise of a dynamic model, assumed to be zero-mean, white and Gaussian
Ω^b	Quaternion representation of the angular velocity ω^b
ω^b	Angular velocity of $\Re^b$ with respect to $\Re^n$
ω^b_{IMU}	Angular velocity vector measured by an IMU
ϕ	Roll angle, representing the rotation around the $X-axis$ of $\Re^b$
ψ	Yaw angle (or heading), representing the rotation around the $Z-axis$ of $\Re^b$

$\mathfrak{R}^b$	Body frame of reference, attached to the moving rigid body under study
$\mathfrak{R}^n$	Inertial frame of reference, fixed with respect to the Earth, in which the trajectory is estimated.
σ_ω^2	Variance of ω^b
σ_a^2	Variance of a^b
$\tau_{\nabla B}^b$	Time constant corresponding to a first-order model of ∇B^b
θ	Pitch angle, representing the rotation around the $Y-axis$ of $\mathfrak{R}^b$
$\widehat{X}$	State vector estimate of a dynamic model
a^b	Acceleration vector, expressed in the body frame $\mathfrak{R}^b$
a_{IMU}^b	Acceleration vector measured by an IMU
a^n	Acceleration vector, expressed in the inertial frame $\mathfrak{R}^n$
a_l^n	Linear acceleration vector, expressed in the inertial frame $\mathfrak{R}^n$
B^b	Earth's magnetic field vector, expressed in the body frame $\mathfrak{R}^b$
b_ω^b	Angular velocity bias contained in ω_{IMU}^b
b_a^b	Acceleration bias contained in a_{IMU}^b
B^n	Earth's magnetic field vector, expressed in the inertial frame $\mathfrak{R}^n$
B_{pli}^n	Magnetic field vector in $\mathfrak{R}^n$, corresponding to power-line interference
d	Zero-velocity detector, can have either 0 or 1 value
D_B	Declination of B^n
d_e	Distance error between a position estimate and ground truth
dT	Sample time
F	State matrix of a particular model
$f(.)$	State transition function of a particular model, and $f_d(.)$ its discrete form
F_B	Total intensity of B^n
g^n	Gravity vector, expressed in the inertial frame $\mathfrak{R}^n$
H	Measurement matrix of a particular model
$h(.)$	Measurement function of a particular model, and $h_d(.)$ its discrete form
H_B	Horizontal intensity of B^n
I_B	Inclination of B^n
M	A fixed point of the rigid body under study
M^b	Position vector, expressed in the body frame $\mathfrak{R}^b$
M^n	Position vector, expressed in the inertial frame $\mathfrak{R}^n$

N	Measurement noise covariance matrix of a Kalman filter
O^b	The point representing the fixed origin of $\mathfrak{B}^{\mathfrak{b}}$, and is the center of gravity of the sensor board strapped to the rigid body
O^n	The point representing the fixed origin of $\mathfrak{B}^{\mathfrak{b}}$
p_i	Position of a magnetometer i in the sensor array
Q	Process noise covariance matrix of a Kalman filter
q	Unit quaternion, a four elements vector that represents the attitude of a rigid body
R_n^b	Attitude matrix, representing the orientation of the rigid body from from $\mathfrak{R}^n$ to $\mathfrak{R}^b$
R_b^n	Attitude matrix, representing the orientation of the rigid body from from $\mathfrak{R}^b$ to $\mathfrak{R}^n$
S_ω	Gyroscope's scale factor
$SO(3)$	Special orthogonal group of order 3 (or the group of rotations in $3D$ Euclidean space)
T^b	Hessian of the magnetic field B^b
T^n	Hessian of the magnetic field B^n
T_s	Test statistics of the zero-velocity detector
u	Input vector of a dynamic model
v^b	Velocity vector, expressed in the body frame $\mathfrak{R}^b$
v^b_{BiLSTM}	Velocity vector, predicted by the BiLSTM
v^n	Velocity vector, expressed in the inertial frame $\mathfrak{R}^n$
W_s	Window size of a zero-velocity detector
X	State vector of a dynamic model
y	Measurement vector of a dynamic model
y^b_B	Measured magnetic field in $\mathfrak{R}^b$
fs_{MIT}	Sample frequency of the MIT
$fs_{Qualisys}$	Sample frequency of the Qualisys cameras

List of Abbreviations

AI Artificial Intelligence

ANN Artificial Neural Network

ARE Angular Rate Energy Detector

BiLSTM Bidirectional Long Short-Term Memory Network

CDF Cumulative Distribution Function

CNN Convolutional Neural Network

CPU Central Processing Unit

DAE Denoising Autoencoder

DL Deep Learning

DNN Deep Neural Network

EKF Extended Kalman Filter

GLRT General Likelihood Ratio Test

GPS Global Positioning System

GPU Graphics Processing Unit

IEKF Invariant Extended Kalman Filter

IMU Inertial Measurement Unit

INS Inertial Navigation System

LSTM Long Short-Term Memory Network

MAE Mean Absolute Error

MAG Acceleration Magnitude Detector

MEMS Micro Electro Mechanical Systems

MINAV Magneto-Inertial Navigation

MIT Magneto-Inertial Tachymeter

ML Machine Learning

MSE Mean Squared Error

MV Acceleration Moving Variance Detector

NED North East Down

NN Neural Network

PDR Pedestrian Dead Reckoning

PSD Power Spectral Density

QSF Quasi-Static magnetic Field

QTM Qualysis Track Manager

QUEST QUaternion ESTimator

ResNet Residual Neural Network

RFID Radio Frequency Identification

RMSE Root Mean Squared Error

RNN Recurrent Neural Network

SD Secure Digital

SHOE Stance Hypothesis Optimal Detector

SLAM Simultaneous Localization And Mapping

SNR Signal to Noise Ratio

WLAN Wireless Local Area Network

WMM World Magnetic Model

ZUPT Zero-Velocity Update Technique

General Introduction

The recent growth of interest in smart systems technology, autonomous robotics and location-aware services generates a strong motivation to develop robust and efficient techniques for tracking the position of a moving body, in both outdoor and indoor environments. The most current positioning technologies that emerged in this sense, use radio frequency-based signals, from which Global Positioning System (GPS) is the most common Ref. [Parakkal2017]. While GPS is known to be most of the times efficient in determining position, its performance can be easily corrupted with outer disturbances (e.g. skyscrapers, extreme atmospheric conditions, etc.) Ref. [Afraimovich2002]. Most importantly, when considering indoor applications, such as malls, subways, parking lots, etc., the latter is usually useless Ref. [Fallah2013].

This limited indoor coverage of GPS encouraged nowadays, the rise of different solutions to deal with the indoor navigation problem. Most of these solutions use a variety of sensors that usually require pre-installed infrastructures, from those based on Wireless Local Area Network (WLAN) structures, such as Bluetooth beacons Ref. [Kaewpinjai2020], to those relying on Radio Frequency Identification (RFID) Ref. [Motroni2021], or vision-based techniques Ref. [Martín-Gorostiza2019]. These approaches can be inaccessible in certain applications that have hostile environment conditions (e.g. smoke in building), cost, and time constraints. For this reason, alternative navigation solutions that are independent from pre-equipped buildings must be explored.

The most common solution to the case where the conditions of intervention, and the availability of pre-installed equipment are unknown, is the use of low-cost Inertial Measurement Units (IMUs), composed of $3-axis$ accelerometers and $3-axis$ gyroscopes. Different approaches have been proposed to effectively explore these sensors, as they introduce biases and errors, and a simple integration of their outputs can not provide any accurate position or orientation (attitude) estimations Ref. [Jang2020]. One of the best approaches that are used to compensate these IMU drifts relies on including additional sensors to conduct the estimation process, from which magnetometers are the most explored.

The knowledge on the magnetic field plays a crucial role, especially in attitude estimation, as discussed in Ref. [Wahba1965]. In that work, it is stated that in order to identify a rotation matrix between a fixed and a body frame, at least two known vectors in these frames are required. By using the acceleration and the magnetic field as observation vectors, in addition to the integration of angular rate measurements, the attitude estimation problem can be solved under a *data fusion* framework.

Many of the first developed solutions treating Wahba's problem Ref. [Markley2000] assume negligible magnetic perturbations surrounding the moving body under study. Nevertheless, in an indoor environment, magnetic perturbations can be very large Ref. [Bachmann2004], due to all metals used in buildings (door frames, aluminum windows, etc.) and potentially, to the strong electric currents propagating close-by. Consequently, when the magnetic field is used as a compass, i.e. to determine the direction of the moving body in a certain trajectory, also known as the heading Ref. [Afzal2011b], it can suffer from up to 30 $degrees$ (deg) of error because of magnetic

disturbances. Such large deviation represents a sufficient argument to question the reliability of magnetometers in providing heading information.

One way to face such problem is through compensation-based approaches that are developed to reject magnetic disturbances. This is done by identifying the Earth's magnetic field from the overall perturbed one through the design of adequate detectors. While many techniques have been suggested and evaluated in related state-of-the-art Ref. [Michel2017], such task remains difficult especially when dealing with an indoor environment that introduces multiple sources of magnetic perturbations.

Conversely, instead of defining magnetic disturbances as an anomaly to be excluded, one may wonder if there are any valuable information in them that can be explored. It turns out that magnetic disturbances are not in fact a random noise. On the contrary, they are well structured by physics equations and can be used to extract trajectory information. This makes of the magnetic field inhomogeneity, a huge asset to the indoor navigation community Ref. [Storms2010].

Most of the research that has emerged in this context is focused on map-based approaches that compare $3-axis$ magnetometer measurements with a pre-existing map of the magnetic field, allowing therefore the estimation of absolute position Ref. [Raquet2013]. While such techniques are evolving towards being entirely independent from any prior-mapping, most of them has to be combined with complementary methods in order for them to work Ref. [Robertson2013].

Another solution in this case, that takes advantage of magnetic information, even when perturbed, and that does not rely on any map-matching procedure, was introduced in Ref. [Afzal2011c]. The approach relies on detecting Quasi-Static magnetic Field (QSF) periods, where the field remains constant. It uses then its temporal gradient to aid with the error estimation of the angular rate. Such use of the magnetometer is attractive since information is provided other than the heading. Nevertheless, the approach requires a careful tuning of the test statistics parameters to generate an optimal performance. The importance of such step intervenes mainly when dealing with different sensor placements Ref. [Bancroft2012] or applications.

In such circumstances, an alternative methodology that studies not only the temporal variation of the magnetic field but also the spatial one, without requiring any tuning procedure was first suggested in Ref. [Vissière2007a] and further investigated in Refs. [Dorveaux2011b, Praly2013, Batista2013,Caruso2016,Chesneau2016]. The proposed technique, referred to as Magneto-Inertial Navigation (MINAV), explores the physical relationship that links the magnetic field to the velocity, and enables its estimation, as long as information about the spatial gradient of the magnetic field is available. This is achieved under a sensor fusion framework, using solely a $3-axis$ accelerometer, a $3-axis$ gyroscope, and a $3-axis$ magnetometer array, which is a setup that has been explored by only few other works in related state-of-the-art Ref. [Skog2018a].

Scope

This thesis targets essentially improving the velocity estimation of a moving body, in a GPS-denied indoor environment. The direction taken during this work is to provide a global solution that works independently from any major requirements. Initially, an Extended Kalman Filter (EKF) Ref. [Daum2015] is designed from a derived navigation model, to conduct an accurate estimation process.
This goal is rather ambitious, as such setup introduces different limitations that must be handled. This leads to exploring other state-of-the-art methods in order to enhance the performance of the estimation process. In this sense, two famous schemes are discussed: the Zero-Velocity Update

Technique (ZUPT) Ref. [Wahlström2020], usually applied under a pedestrian foot-mounted sensor framework, and Deep Neural Networks (DNNs), one of the basic tools in Artificial Intelligence (AI).
While both these schemes can be of benefit, they introduce however, certain constraints, such as the need for a specific sensor attachment, hyperparameters tuning, the availability and diversity of data, the low computational cost, etc. These limitations encourage developing a rather flexible solution, that does not demand large resources to be implemented, and that can be easily accessible to different use cases.

Main contributions

The main contributions of this thesis are the following:

1. A better modeling of the navigation problem and more particularly, that of the magnetic field gradient, is conducted. As initially suggested in Ref. [Chesneau2018], higher order spatial derivatives of the magnetic field are explored using an adequate architecture of the magnetometer array. This enables to efficiently model the dynamics of the magnetic field gradient, and consequently improve the velocity estimation results. Both the theoretical and experimental benefits of doing so are demonstrated on simulated and real datasets.

2. Two possible implementations of the proposed navigation model are introduced and compared, both representing a magnetic field gradient-based EKF structure. This provides the user of more flexibility when it comes to the EKF architecture and the handling of its different parameters.

3. The performance of the derived single magnetic field gradient-based EKF approach is evaluated under a pedestrian foot-mounted sensor framework, and then improved using the ZUPT. Such solution provides promising results, especially when considering the trajectory reconstruction.

4. To have a global solution that can be applied not only on the foot-mounted sensor case but also on any other sensor attachment, an innovative approach is proposed that combines the magnetic field gradient-based EKF with an AI-based technique, known as the Bidirectional Long Short-Term Memory Network (BiLSTM), to improve the velocity estimation accuracy, without any heavy computation or complex tuning.

5. The different discussed approaches are evaluated and compared on a real case study with a complete experimental benchmark using a Magneto-Inertial Tachymeter (MIT) provided by SYSNAV company Ref. [Sysnav2020] and a motion capture system from Qualisys brand Ref. [Qualisys2021]. The benefit of using the MIT mostly resides on the generation of magnetometer array measurements, which are unavailable in all used open-source datasets chosen in this thesis. This experimental benchmark is the most adequate validation that can be conducted to evaluate the performance of the different studied approaches.

Organization of the manuscript

This thesis is divided into two parts. Part I is dedicated to the introduction of magneto-inertial navigation with a focus on the magnetic field gradient modeling. In this part, Chapter 1 discusses the theory behind the navigation problem and introduces the "traditional" MINAV model. Then, it highlights its different limitations, especially those related to the magnetic field gradient determination. Chapter 2 proposes an improved navigation model after exploring spatial derivatives of the magnetic field. A special setting of two magnetic field gradient-based EKFs is

derived, which performance is evaluated under a simulation scheme, and promising results are obtained. Chapter 3 treats the special case of trajectory reconstruction under a pedestrian foot-mounted sensor framework. A new single EKF architecture is proposed and then enhanced with the ZUPT. Different comparisons are conducted under an open-source simulated foot-mounted dataset. Part II discusses the inclusion of AI-based techniques in the magneto-inertial navigation scheme. In this part, Chapter 4 highlights the limitations that the proposed EKF may introduce, that cannot be handled by the ZUPT when considering a non foot-mounted context. An innovative solution that combines the EKF with a BiLSTM is then proposed and evaluated on a public dataset with real measurements. Finally, Chapter 5 presents a real case study where the MIT and motion capture system are used to conduct several experiments with different trajectory scenarios and sensor attachments. The estimation accuracy of the different discussed methods in this thesis is then evaluated. Final results prove the pertinence of the EKF-BiLSTM approach compared to the existing state-of-the-art works.

Publications

This thesis led to the publication of two peer-reviewed international journal papers and two articles in the proceedings of international peer-reviewed conferences. These publications are the objects of the different chapters in this thesis (except Chapter 1).

Journal papers

1. M. Zmitri, H. Fourati and C. Prieur. BiLSTM Network-Based Extended Kalman Filter for Magnetic Field Gradient Aided Indoor Navigation (to appear). *IEEE Sensors Journal*, 2021 **(Chapter 5)**.

2. M. Zmitri, H. Fourati and C. Prieur. Magnetic Field Gradient-Based EKF for Velocity Estimation in Indoor Navigation. *Sensors*, vol. 20, no. 20, pages 5726, 2020. doi: 10.3390/s20205726 **(Chapter 3)**.

Conference papers

1. M. Zmitri, H. Fourati and C. Prieur. Inertial Velocity Estimation for Indoor Navigation Through Magnetic Gradient-based EKF and LSTM Learning Model. *IEEE/RSJ International Conference on Intelligent Robots and Systems (IROS)*, pages 4545-4550, 2020. doi: 10.1109/IROS45743.2020.9340772 **(Chapter 4)**.

2. M. Zmitri, H. Fourati and C. Prieur, Improving Inertial Velocity Estimation Through Magnetic Field Gradient-based Extended Kalman Filter. *International Conference on Indoor Positioning and Indoor Navigation (IPIN)*, pages 1-7, 2019. doi: 10.1109/IPIN.2019.8911813 **(Chapter 2)**.

Part I

Magneto-Inertial Navigation (MINAV)

1

Velocity Estimation With a Magnetometer Array

This chapter starts by introducing in Section 1.1, preliminary notions about the navigation problem along with the notation used throughout this thesis. Then, inertial navigation with low-cost sensors is discussed, where it is demonstrated why they are insufficient to obtain an estimate of attitude, velocity and position. The use of magnetometers to complement inertial sensors is proposed in Section 1.2. Thanks to the magnetic field disturbances present in an indoor environment, a technique called Magneto-Inertial Navigation (MINAV) is presented, that enables the reconstruction of the velocity, under some conditions. These conditions revolve essentially around the magnetic field gradient that needs to be precisely determined. In Section 1.3, limitations of the usually applied approximations using a magnetometer array are highlighted. This encourages the development of more sophisticated models to represent the magnetic field gradient. In this sense, some state-of-the-art attempts are presented and conclusions are made.

Contents

1.1 Introduction

The indoor magneto-inertial navigation problem consists in tracking a rigid body motion, over time, with respect to an inertial frame, located in an indoor environment. This is achieved using a low-cost strapdown (i.e. attached to the rigid body) Micro Electro Mechanical Systems (MEMS) sensor board containing: *an Inertial Measurement Unit (IMU)*, composed of a $3-axis$ accelerometer and a $3-axis$ gyroscope and completed with *an array of at least three non-aligned* $3-axis$ *magnetometers.* Motion tracking can be summarized with the determination of three entities: attitude, velocity, and position. In this chapter, the kinematic differential equations connecting these entities to the sensor board measurements are presented. Relying on these equations introduces several limitations that are discussed in detail in the following sections.

1.1.1 Preliminaries and notation

Frames of reference

To mathematically present the navigation problem, two frames are introduced. Let $\mathfrak{R}^n = (O^n, \mathfrak{B}^{\mathfrak{n}})$ be a *local inertial frame*, fixed to the Earth, where $\mathfrak{B}^{\mathfrak{n}}$ is its associated orthonormal basis such as $\mathfrak{B}^{\mathfrak{n}} = (e_1^n, e_2^n, e_3^n)$, and $\langle e_i^n, e_j^n \rangle = \delta_{ij}$ for all $i, j = 1, ..., 3$, where δ_{ij} is the Kronecker delta symbol, i.e., $\delta_{ij} = 1$ if $i = j$ and is zero otherwise. The point O^n represents a fixed origin. This local frame is oriented according to the North East Down (NED) convention, such as the unit vectors of (e_1^n, e_2^n, e_3^n) point respectively to the directions north, east and gravity. For each application considered in this thesis, the Earth's curvature and its angular velocity are neglected.

Remark 1 *Most of low-cost MEMS gyroscopes are not sensitive enough to measure angular velocities with a magnitude close to the Earth's one* ($\approx 7.3 * 10^{-5} rads^{-1}$). *This is why the Earth's rotation is neglected in this entire thesis.*

Consider then a *body frame* attached to the rigid body under study $\mathfrak{R}^b = (O^b, \mathfrak{B}^{\mathfrak{b}})$, where O^b is the center of gravity of the sensor board strapped to the rigid body, and $\mathfrak{B}^{\mathfrak{b}}$ is another direct orthonormal basis, that coincides with the sensor board inner sensors axes. In the entire thesis, the index n (resp. b) denotes the coordinates of vectors in the inertial frame $\mathfrak{R}^n$ (resp. in the body frame $\mathfrak{R}^b$).

Attitude

The attitude is defined as the transfer matrix from $\mathfrak{R}^n$ to $\mathfrak{R}^b$ such as $A = R_n^b = (R_b^n)^\top$. The attitude matrix $R_n^b \in \mathbb{R}^{3\times 3}$ belongs to $SO(3)$, the group of rotations in $3D$ Euclidean space. This means that $(R_n^b)^{-1} = (R_n^b)^\top$.
The rotation matrix R_n^b is formed with a succession of three elementary rotations $R1$, $R2$ and $R3$ around the three axes of the inertial frame. These rotations are represented with three angles, called *Euler angles*, where ϕ is the roll angle, representing the rotation around the $X-axis$ of $\mathfrak{R}^b$, θ is the pitch angle, defining the rotation around the $Y-axis$ and ψ is the yaw angle (or heading angle), describing the rotation around the $Z-axis$. Several combinations of these rotations are possible Ref. [Shuster1993] (here a ZYX combination). Accordingly, the rotation matrix R_n^b is

given by

$$
\begin{aligned}
R_n^b = R3(\phi)\, R2(\theta)\, R1(\psi) &= \begin{bmatrix} 1 & 0 & 0 \\ 0 & c_\phi & s_\phi \\ 0 & -s_\phi & c_\phi \end{bmatrix} \begin{bmatrix} c_\theta & 0 & -s_\theta \\ 0 & 1 & 0 \\ s_\theta & 0 & c_\theta \end{bmatrix} \begin{bmatrix} c_\psi & s_\psi & 0 \\ -s_\psi & c_\psi & 0 \\ 0 & 0 & 1 \end{bmatrix} \\
&= \begin{bmatrix} c_\theta c_\psi & c_\theta s_\psi & -s_\theta \\ s_\phi s_\theta c_\psi - c_\phi s_\psi & s_\phi s_\theta s_\psi + c_\phi c_\psi & s_\phi c_\theta \\ c_\phi c_\psi s_\theta + s_\phi s_\psi & s_\theta s_\psi c_\phi - s_\phi c_\psi & c_\phi c_\theta \end{bmatrix}
\end{aligned} \tag{1.1}
$$

where $s_\psi = sin\ \psi$ and $c_\theta = cos\ \theta$, for example.

Remark 2 *Attitude can be represented entirely with Euler angles. However, the problem with such representation is the existence of singularities: in some cases, a same attitude in space can be obtained by an infinite number of rotations. For instance, if* $\theta = \frac{\pi}{2}$*, the rotation axes of* $R1$ *and* $R3$ *are identical. This phenomena is called the gimbal lock Ref. [Diebel2006].*

To avoid the singularity problem encountered by Euler angles, another form of attitude representation is used: *quaternions* Ref. [Kuipers1999]. A quaternion describes the orientation of $\Re^b$ with respect to $\Re^n$ by a three dimensional vector $\vec{u}$ and a rotation α_r around this vector. It is then defined such that

$$
q = \begin{bmatrix} cos\ \dfrac{\alpha_r}{2} \\ sin\ \dfrac{\alpha_r}{2}\ \vec{u} \end{bmatrix} \tag{1.2}
$$

with $\|\vec{u}\| = 1$.
The unit quaternion represents then a quadruplet $q = [q_0\ \ q_v^\top]^\top \in \mathbb{R}^{4\times 1}$, where q_0 is the scalar part, and $q_v = [q_1\ \ q_2\ \ q_3]^\top$ the vector part, such that $q_0^2 + q_v^\top q_v = 1$.
In this entire thesis, the attitude matrix R_n^b is numerically represented by an associated unit quaternion as follows

$$
R_n^b = R_n^b(q) = \begin{bmatrix} 2(q_0^2+q_1^2)-1 & 2(q_1q_2+q_0q_3) & 2(q_1q_3-q_0q_2) \\ 2(q_1q_2-q_0q_3) & 2(q_0^2+q_2^2)-1 & 2(q_2q_3+q_0q_1) \\ 2(q_1q_3+q_0q_2) & 2(q_2q_3-q_0q_1) & 2(q_0^2+q_3^2)-1 \end{bmatrix} \tag{1.3}
$$

Reciprocally, given the attitude matrix R_n^b, the quaternion that represents the same rotation can be computed. First, the trace of R_n^b is calculated (i.e. the sum of the elements on the main diagonal of the matrix)

$$
\begin{aligned}
Tr(R_n^b) =& R_{11} + R_{22} + R_{33} \\
=& 2(3q_0^2 + q_1^2 + q_2^2 + q_3^2) - 3 \\
=& 2(3q_0^2 + (1 - q_0^2)) - 3 \\
=& 4q_0^2 - 1
\end{aligned} \tag{1.4}
$$

where $Tr(R_n^b)$ is the trace of R_n^b, and R_{11}, R_{22} and R_{33} are the diagonal elements of R_n^b, going from the up left till the right down.
Solving Eq. (1.4) gives

$$
|q_0| = \sqrt{\frac{Tr(R_n^b)+1}{4}} \tag{1.5}
$$

with $|\,.\,|$, referring to the absolute value.
Once the scalar part q_0 is obtained, q_1 can be determined from R_{11} such that

$$\begin{aligned} R_{11} =& 2(q_0^2+q_1^2)-1 = 2\left(\frac{Tr(R_n^b)+1}{4}+q_1^2\right)-1 \\ |q_1| =& \sqrt{\frac{R_{11}}{2}+\frac{1-Tr(R_n^b)}{4}} \end{aligned} \tag{1.6}$$

Similarly, q_2 and q_3 are computed from R_{22} and R_{33}, respectively

$$|q_2| = \sqrt{\frac{R_{22}}{2}+\frac{1-Tr(R_n^b)}{4}} \tag{1.7}$$

$$|q_3| = \sqrt{\frac{R_{33}}{2}+\frac{1-Tr(R_n^b)}{4}} \tag{1.8}$$

Angular velocity

Denote $\omega^b = [\omega_x^b \;\; \omega_y^b \;\; \omega_z^b]^\top \in \mathbb{R}^{3\times 1}$, the angular velocity of $\mathfrak{R}^b$ with respect to $\mathfrak{R}^n$. Implicitly, it can be defined such that

$$\left.\frac{dR_n^b}{dt}\right|_{\mathfrak{R}^n} = -[\omega^b\times]R_n^b \tag{1.9}$$

where $[\omega^b\times] \in \mathbb{R}^{3\times 3}$ is the skew-symmetric matrix having this following form

$$[\omega^b\times] = \begin{bmatrix} 0 & -\omega_z^b & \omega_y^b \\ \omega_z^b & 0 & -\omega_x^b \\ -\omega_y^b & \omega_x^b & 0 \end{bmatrix} = -[\omega^b\times]^\top \tag{1.10}$$

Remark 3 *In this entire thesis, time derivations are performed with respect to the inertial frame* $\mathfrak{R}^n$. *For simplicity reasons, the notation* $\left.\frac{d}{dt}\right|_{\mathfrak{R}^n}$ *is omitted and* $\frac{d}{dt}$ *is rather used.*

The relationship between attitude and ω^b can also be expressed in terms of quaternion with

$$\frac{dq}{dt} = \frac{1}{2}\Omega^b q \tag{1.11}$$

where $\Omega^b = \Omega^b(\omega^b) \in \mathbb{R}^{4\times 4}$, such that

$$\Omega^b = \begin{bmatrix} 0 & -(\omega^b)^\top \\ \omega^b & -[\omega^b\times] \end{bmatrix} \tag{1.12}$$

Acceleration

Denote $a^b = [a_x^b \;\; a_y^b \;\; a_z^b]^\top \in \mathbb{R}^{3\times 1}$, the rigid body's acceleration in $\mathfrak{R}^b$. It can be defined with the following form

$$a^b = R_n^b a^n = R_n^b(a_l^n + g^n) = a_l^b + R_n^b g^n \tag{1.13}$$

with $a^n = [a_x^n \;\; a_y^n \;\; a_z^n]^\top \in \mathbb{R}^{3\times 1}$, the acceleration vector in $\mathfrak{R}^n$, $a_l^n = [a_{lx}^n \;\; a_{ly}^n \;\; a_{lz}^n]^\top \in \mathbb{R}^{3\times 1}$, the linear acceleration in $\mathfrak{R}^n$, $\gamma^b = [a_{lx}^b \;\; a_{ly}^b \;\; a_{lz}^b]^\top \in \mathbb{R}^{3\times 1}$, its corresponding form in $\mathfrak{R}_b$, and $g^n = [0 \;\; 0 \;\; g_z^n]^\top \in \mathbb{R}^{3\times 1}$, is the gravity vector. In this work, Coriolis acceleration (the acceleration induced by the Earth's rotation) is neglected, and $g_z^n \in \mathbb{R}$ is considered a known positive constant, as the chosen convention for the local inertial frame is NED.

Remark 4 *In reality, assuming that the gravity is a known constant vector is not entirely valid. The latter actually depends on the attitude of the rigid body, which itself, is unknown. In a purely inertial navigation framework, this hypothesis may degrade the accuracy of the velocity and position estimations. Thus, several techniques in the literature are developed to precisely estimate the gravity vector Ref. [Manos2018, De Celis2018].*

Position

Consider M a fixed point of the rigid body. Let $M^n = [M_x^n \;\; M_y^n \;\; M_z^n]^\top \in \mathbb{R}^{3\times 1}$ be its representation with cartesian coordinates in $\Re^n$, and $M^b = [M_x^b \;\; M_y^b \;\; M_z^b]^\top \in \mathbb{R}^{3\times 1}$, its corresponding form in $\Re^b$. It is considered that M^b is superposed with the origin of the body frame $\Re^b$, so $M^b = O^b$. The trajectory of the rigid body is then defined as the evolution of $(R_n^b, M^n) \in SE(3)$ with respect to time, where $SE(3)$ is the special Euclidean group of rigid body displacements in $3D$. The vector M^n represents then, the position of the rigid body under consideration.

Velocity

The corresponding velocity in $\Re^n$ to the position M^n is denoted by $v^n = [v_x^n \;\; v_y^n \;\; v_z^n]^\top \in \mathbb{R}^{3\times 1}$ and is obtained with

$$v^n = \frac{dM^n}{dt} \tag{1.14}$$

Inertial velocity dynamics can also be represented in terms of attitude and body acceleration such that

$$\frac{dv^n}{dt} = a_l^n = R_b^n a^b - g^n \tag{1.15}$$

In $\Re^b$, the velocity $v^b = R_n^b v^n = [v_x^b \;\; v_y^b \;\; v_z^b]^\top \in \mathbb{R}^{3\times 1}$ can then be derived as follows

$$\begin{aligned} \frac{dv^b}{dt} =& \frac{dR_n^b v^n}{dt} = \frac{dR_n^b}{dt} v^n + R_n^b \frac{dv^n}{dt} \\ =& -[\omega^b \times] R_n^b v^n + R_n^b (R_b^n a^b - g^n) \end{aligned} \tag{1.16}$$

By simplifying Eq. (1.16), the basic differential equation describing the temporal variation of v^b is deduced

$$\frac{dv^b}{dt} = -\omega^b \times v^b + a^b - R_n^b g^n \tag{1.17}$$

where $\times$ is the cross product of two vectors in $\mathbb{R}^3$.

Remark 5 *It is brought to the attention of the reader that* $\frac{dR_n^b v^n}{dt} \neq R_n^b \frac{dv^n}{dt}$*, which may represent a confusion during derivations. This is because the change of frame through* R_n^b *applies to Eq.* (1.9)*. This also means that* $a_l^b \neq \frac{dv^b}{dt}$ *and* $v^b \neq \frac{dM^b}{dt}$.

1.1.2 Limitations of IMU measurements

Implications on attitude estimation

Regrouping the different kinematics equations stated above leads to the following system

$$\frac{dq}{dt} = \frac{1}{2}\Omega^b q \tag{1.18}$$

$$\frac{dv^b}{dt} = -\omega^b \times v^b + a^b - R_n^b g^n \tag{1.19}$$

$$\frac{dM^n}{dt} = R_b^n v^b \tag{1.20}$$

The true angular velocity ω^b and acceleration a^b are the inputs for Eqs. (1.18)-(1.20). These true measurements are contained in the outputs of the IMU's $3-axis$ gyroscope and $3-axis$ accelerometer, respectively, alongside with biases and noises as follows

$$\omega^b_{IMU} = \omega^b + b^b_\omega + \eta^b_\omega \tag{1.21}$$

$$a^b_{IMU} = a^b + b^b_a + \eta^b_a \tag{1.22}$$

where $b^b_\omega = [b^b_{\omega x} \;\; b^b_{\omega y} \;\; b^b_{\omega z}]^\top \in \mathbb{R}^{3\times 1}$ and $b^b_a = [b^b_{ax} \;\; b^b_{ay} \;\; b^b_{az}]^\top \in \mathbb{R}^{3\times 1}$ are the biases of the gyroscope and accelerometer, and $\eta^b_\omega = [\eta^b_{\omega x} \;\; \eta^b_{\omega y} \;\; \eta^b_{\omega z}]^\top \in \mathbb{R}^{3\times 1}$ and $\eta^b_a = [\eta^b_{ax} \;\; \eta^b_{ay} \;\; \eta^b_{az}]^\top \in \mathbb{R}^{3\times 1}$ are their corresponding noises, respectively. This means that deriving Eqs. (1.18)-(1.20) implicates the use of ω^b_{IMU} and a^b_{IMU} as there is no full knowledge on biases and noises, and thus they cannot be directly subtracted from Eqs. (1.21)-(1.22). In fact, the problem with the presence of biases intervenes during integration. For instance, a bias of order ε^b on the accelerometer measurements has an impact of order $\frac{1}{2}\varepsilon^b t^2$ on the determined position after t *seconds* (s), leading to a huge cumulative drift. The same happens when computing quaternion from angular velocity measurements. For example, consider a 1 *minute* (min) trajectory, where a subject is moving in an office environment with a low-cost IMU attached to his ankle. A gyroscope with a bias of approximately 0.003 $rads^{-1}$ and a noise standard deviation of 0.005 $rads^{-1}$ is used to compute Eq. (1.18). As illustrated with Fig. 1.1, by comparing the ground truth quaternion q_1 (red line) and the integrated one $\widehat{q_1}$ (blue line), the drift occur starting from less than 3 s and becomes larger over time, making attitude estimation diverge. The other elements of $\widehat{q}$ have also the same behavior as $\widehat{q_1}$.

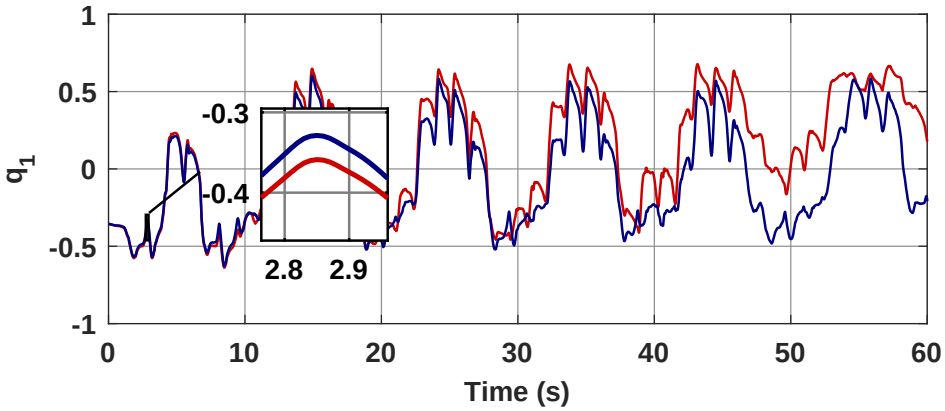

Figure 1.1: Example of quaternion drift caused by integrating biased gyroscope measurements. In red is the ground truth q_1 and in blue is the integrated one $\widehat{q_1}$

To better highlight the impact of using noisy and biased angular velocity measurements on the attitude, the integrated quaternion $\widehat{q}$ is converted to Euler angles representation through both Eq. (1.1) and Eq. (1.3). Then, the difference between the ground truth Euler angles and the integrated ones is evaluated. In Fig. 1.2, the error of the pitch angle is displayed. In only 3 s, an error of around 4 *degrees* (deg) is obtained, that accumulates through time till it reaches approximately 140 deg in 1 *min*, causing this trajectory drift. This calls for the need to develop efficient solutions that can treat such crucial problem.

IMU biases determination

From the observations above, it is clear that measurements' errors cannot be neglected when studying an inertial navigation problem. Typically, a two-stage calibration step can be conducted before using the IMU, where both the deterministic and stochastic parts of these errors are identified Ref. [Amirsadri2012]. Considering biases as fixed errors, the simplest method to determine them

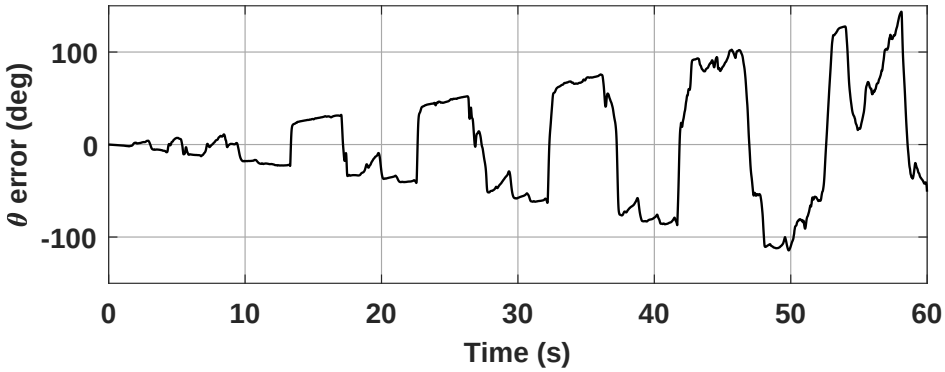

Figure 1.2: Example of pitch error caused by integrating biased gyroscope measurements

is by measuring the output while the IMU is stationary. For the gyroscope, the true angular rate in Eq. (1.21) is set to zero when the IMU is static. By taking the mean of its measurements over few minutes and provided that η_{ω}^{b} is zero-mean, white and Gaussian, the bias is obtained such that

$$b_{\omega}^{b} = S_{\omega}\overline{\omega}_{IMU}^{b} \tag{1.23}$$

where $\overline{\omega}_{IMU}^{b}$ is the measured angular rate's mean, and S_{ω} is the gyroscope's scale factor, which can be estimated using information from the IMU's data sheet Ref. [Amirsadri2012]. To cover most cases of interest, the gyroscope's scale factor can be substituted with a diagonal matrix of scale factors for each axis, that is multiplied with a skew-symmetric matrix representing sensor's misalignment terms. Both these matrices are alternatively gathered in one general matrix, to be determined through the calibration process, as studied in detail in Ref. [Dorveaux2011a]. It is reminded that the Earth's rotation has a magnitude of $\approx 7.3 * 10^{-5}$ $rads^{-1}$, which is considered negligible for the above procedure. Following the same principle used for the gyroscope, i.e. static calibration, the bias of the accelerometer is computed by considering that at rest, the latter measures the gravity vector. By neglecting Coriolis acceleration and supposing that gravity on the vertical axis g_{z}^{n} is a known constant, the accelerometer's bias can be determined.
While such procedure succeeds to provide an initial estimation of biases, it can become unsatisfactory in the presence of some external factors that may affect the IMU's nature. For instance, low-cost sensors tend to have strong thermal dependencies Ref. [Reginya2018], which means that, changes in ambient temperature induce changes in the IMU's behavior. In other words, IMU's biases may not remain constant during long period experiments causing the sensor's components to heat. This implies that biases vary, and thus, it is rather appropriate to consider them as part of the state vector. Different methods in the literature are proposed in this sense, such as in Refs. [Tie2018, Liu2019, Javed2020, Nazemipour2020]. However, the accuracy of these approaches usually depends on the availability of reference data, the validity of model assumptions and observability conditions. Estimation errors in such case are inevitable, which makes depending only on bias determination to obtain accurate velocity and position estimates through the integration of Eqs. (1.18)-(1.20) unreliable.
That being said, one should stress that the effectiveness of classical approaches such as the one initially presented in this section (static calibration) is preserved during short period experiments, where no significant change in sensor's temperature is detected. A benchmark with the used sensor board in this thesis, have demonstrated that gyroscope and accelerometer biases remain almost constant for an entire 20 *minutes* (min) of recordings. For trajectories that last not more than 4 *min* (refer to Chapter 5), it is safe to follow such assumption and consider biases as constant parameters. This is why, for the continuity of this thesis, biases are determined during a pre-processing phase by relying on the static calibration method, and then subtracted from the IMU's measurements, before they are fed to the navigation filter. For simulation scenarios, they are chosen null

directly, as the same method can be applied during the measurements preparation step.
Nevertheless, under challenging conditions, such as longer period trajectories, developing more sophisticated methods for biases estimation, that take into consideration their potential variation, remains necessary. A preliminary work is elaborated in this sense and is presented at the end of this thesis as a future perspective. The inability of eliminating imperfections from IMU's measurements entirely encourages the design of approaches that can limit their detrimental effect, and thus reduce the navigation errors. While attitude can be partially restored with sensor fusion-based algorithms Refs. [Wu2019a, Renaudin2014, Makni2019, Crassidis2007], velocity and position estimations are more complicated, especially when maintaining the low-cost strapdown sensors framework.

1.2 The MINAV technique

Beside to accelerometers and gyroscopes, modern low-cost IMUs are designed nowadays with integrated magnetometers as they provide an additional solution to the navigation problem. This preserves the main advantage of purely inertial technology: no pre-installed infrastructure or additional information source are required.

1.2.1 The magnetic field in indoor environments

Heading estimation

The use of magnetometers to solve the navigation problem has been largely treated in the literature. For instance, the magnetic field is widely used in attitude estimation algorithms, where it is fused with other IMUs, to compensate the errors contained in their measurements.
In this sense, a wide range of solutions have been proposed since the introduction of Wahba's problem Ref. [Wahba1965], to combine inertial and magnetic sensor measurements in a relevant manner. TRIAD-based algorithms Refs. [Black1964, Tanygin2007] are one of the earliest methods that were explored, followed by QUaternion ESTimators (QUESTs) Refs. [Shuster1981, Cheng2005], as well as a variety of filters, such as, Particle Refs. [Oshman2006, Zhang2016, Zhou2021], Kalman Refs. [Choukroun2006, Sabatini2006, Makni2014] and complementary filters Refs. [Mahony2008, Madgwick2011, Wu2019a]. In these algorithms, magnetometers usually play a role of a compass to determine which direction the moving body is facing, also known as heading estimation Refs. [Afzal2011b, Wu2018]. For outdoor applications, such technique is very effective, assuming the Earth's declination angle is known. However, for indoor applications, the use of magnetometers as a compass is not as straight forward, see Refs. [Bachmann2004, De Vries2009]. One obvious solution in this case, for accurate attitude estimation in the presence of magnetic perturbations, resides on developing compensation techniques that can efficiently reject them, such as those proposed in Refs. [Roetenberg2005, Renaudin2012a, Yadav2014, Madgwick2020], for example. A detailed comparative between many of these techniques is conducted in Ref. [Michel2017]. For these approaches to work, one must develop magnetic field detectors that are able to correctly identify the Earth's magnetic field from the existing perturbations. Such task however, can become very challenging in an indoor environment that contains various external sources of magnetic disturbances.

Indoor magnetic disturbances

The magnetic field measured by a magnetometer in an indoor environment may vary widely from the Earth's one that is observed outdoor away from any perturbations[1]. According to the most recent World Magnetic Model (WMM) calculator Ref. [NOAA2021], the magnitude of the Earth's magnetic field in Grenoble, where all experiments of this thesis are conducted, is around ≈ 0.466 *Gauss* (G). In an indoor environment, magnetic disturbances can occur due to electrical currents and devices, building infrastructure, or any type of activity relying on ferrous materials such as steel, for example. The measured magnitude of these disturbances depends on the distance between the moving body holding/wearing the magnetometer and their source. In Fig. 1.3, the magnitude (determined by applying the norm) of a $3-axis$ magnetometer's output is recorded over approximately 5 *min* of trajectory performed by a subject inside a research laboratory. The varia-

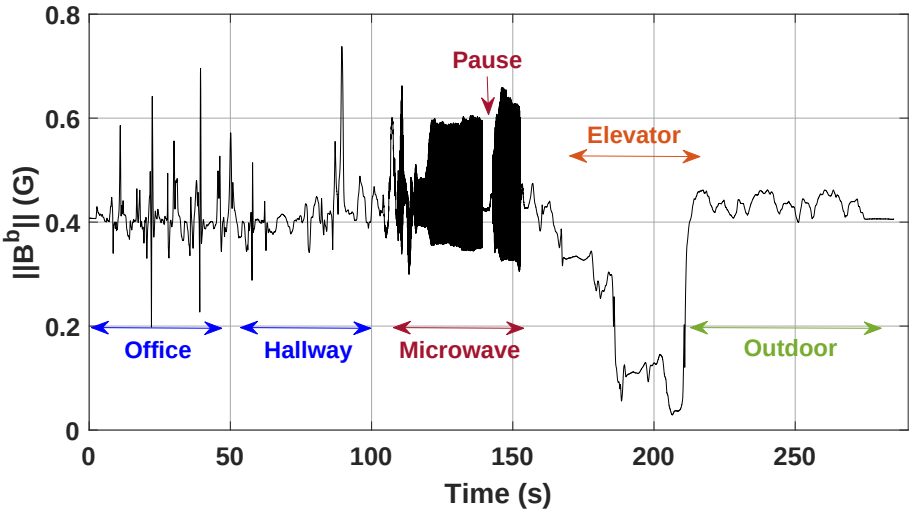

Figure 1.3: Magnitude of the magnetic field B^b measured by a $3-axis$ magnetometer during an indoor trajectory

tion in the displayed magnitude confirms the assumptions previously stated about the presence of magnetic disturbances. For instance, walking around the office and the hallway generates multiple fluctuations in the measured magnetic field, which are explained by the presence of heaters, screens, metallic tables, etc. This is followed by enormous perturbations caused by standing next to a running microwave in the kitchen. When the microwave is paused (for about 4 *s*), almost no magnetic perturbations are observed. Afterwords, the subject goes inside an elevator, where the measured magnitude of the magnetic field significantly decreases, since the elevator in question is constructed with a similar structure to a Faraday's cage [Krauss1992], and its doors and walls are equipped with glass-wool insulation. Finally, by going outside the building, a magnitude very close to the Earth's one is recorded, which is expected with the absence of magnetic disturbances in an outdoor environment.

As many works in the literature discuss the high magnetic field disturbances measured close to elevators, and due to the special structure of the previously tested one, a second experiment is undertaken where a subject walks through a different hallway, having less magnetic field perturbations, towards a standard elevator. As demonstrated in Fig. 1.4, by standing near the elevator, the norm of the magnetic field increases drastically to reach more than 1.5 *G*, which proves the presence of high magnetic field disturbances around the elevator's door. It follows that this norm decreases by going inside the elevator, again, explained by the Faraday's cage phenomena. Both

[1] In the entire thesis, the word *perturbation* is equivalent to *disturbance*.

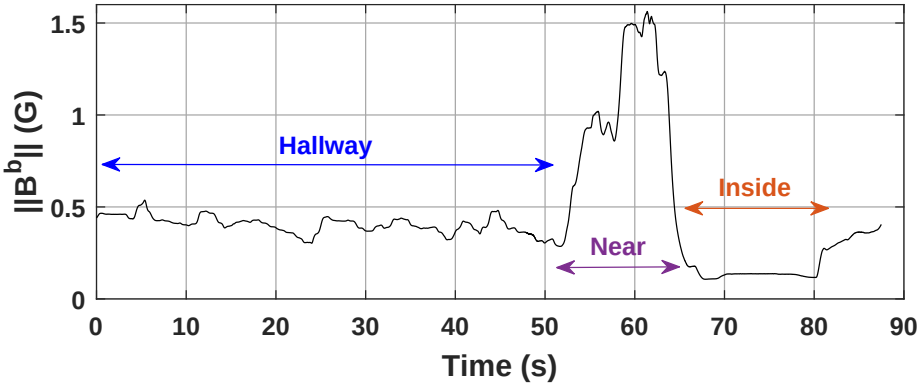

Figure 1.4: Magnitude of the magnetic field B^b measured by a $3-$axis magnetometer close to and inside an elevator

these experiments demonstrate efficiently the presence of magnetic field perturbations in an indoor environment and rise the question of how to take advantage of such conditions to accurately reconstruct the velocity, position, and attitude of a moving body.

Magnetic field-based mapping

While magnetic disturbances represent a problem for heading estimation, which encourages the development of solutions to reject them as in Refs. [Ye2020, Árvai2020], the idea of using the magnetic field inhomogeneity for positioning instead has emerged in the recent years like in Refs. [Ashraf2021, Galván-Tejada2020]. Some techniques that take the lead in this context are *fingerprinting* such as in Refs. [Kuang2018, Chen2020b] and *Simultaneous Localization And Mapping* (SLAM), see for example Refs. [Kok2018, Liu2021]. In these approaches, the magnetic field is used to reconstruct a trajectory that is matched with a pre-existing map. Even though such techniques may work without requiring any pre-installed or additional equipment, they do need prior information on the building infrastructure, which doesn't meet the expectations of this thesis: purely inertial and magnetic navigation, without additional information sources.

Angular rate update using quasi-static magnetic field periods

An approach that employs magnetometer measurements in a perturbed environment, while maintaining a map-free framework, was introduced in Refs. [Afzal2011a, Afzal2011c] and further developed in Ref. [Renaudin2014]. The technique resides mainly on detecting Quasi-Static magnetic Field (QSF) periods in the body frame, and using them as measurements under a non-linear filter scheme. This is done in the purpose of better estimating attitude and gyroscope errors.
In these works, it was shown that the magnetic field can have a constant magnitude and direction for some locations or short periods (e.g. when the body is not moving). During these instances, the rate of change of the magnetic field, which is referred to as its temporal gradient, can be equal or very close to zero. Such information enables developing a measurement error model that is used for updating the state vector of the navigation filter, to improve the estimation process.
To ensure an accurate detection of QSF periods, the tuning of the test statistics parameters: the detection threshold, the noise variance and the window size, must be carefully handled. These parameters can vary largely with the studied sensor placement Ref. [Bancroft2012] or the application, for instance, from pedestrians, to vehicles navigation. Such desired diversity cannot guarantee the ability to detect QSF periods continuously, unless an adaptive tuning process is considered.

MINAV and related state-of-the-art

In order to make use of the Earth's magnetic field in indoor environments, two of its properties are exploited: First, it is assumed to be *stationary*, i.e. time-invariant in the inertial frame $\mathfrak{R}^n$ for few seconds to hours. Second, it varies with respect to the position in space, which is the strategy of fingerprinting-based approaches. Then, considering that information about the spatial variation of the magnetic field is available, one can link the magnetic field temporal variation in the body frame $\mathfrak{R}^b$, to the velocity v^b of the sensor board (containing the magnetometers) that is strapped to the moving subject under study. It becomes then possible to combine an array of spatially distributed magnetometers with an IMU to obtain velocity estimates, position, and attitude, without building any map. Unlike the QSF approach, such methodology does not rely on any tuned parameters or the detection of specific trajectory characteristics, which gives it a fairly general aspect. This idea, referred to as Magneto-Inertial Navigation (MINAV), was firstly proposed in Ref. [Vissière2007a], where it was shown how to use low-cost magnetometers' measurements as a velocity information source in a sensor fusion framework. This represents an alternative and promising way of using the magnetic field for indoor navigation purposes. Few works were then developed in a similar manner, mostly by the same authors Refs. [Vissière2007b, Dorveaux2011a, Dorveaux2011b, Dorveaux2011c, Praly2013, Batista2013, Chesneau2016, Chesneau2017, Chesneau2018, Caruso2016, Caruso2017a, Caruso2017b, Caruso2017c, Caruso2018, Caruso2019], where different theoretical and experimental results are presented.
In the same direction, another research team has elaborated solutions that also take advantage of the magnetic field perturbations recorded by a magnetometer array Refs. [Skog2014, Skog2016, Skog2018a, Skog2018b, Skog2018c]. In these works, authors consider a model parameter estimation problem where the velocity is viewed as a free parameter and is fitted to the observed data. This is different from the approach in Ref. [Vissière2007a], where velocity is directly estimated by solving a differential equation that links the rate of change of the magnetic field to its spatial gradient as well as the gyroscope measurements. In Ref. [Skog2018b], authors represent the magnetic field variations using a second order polynomial model and then derive a maximum likelihood estimator Ref. [Myung2003] that determines the displacement of the magnetometer array. To have an idea on the needed architecture of the array and the possible performance of the method, identifiability and Cramér-Rao analyses of the estimation problem are conducted Ref. [Skog2016]. However, while the derived identifiability conditions show that attitude can also be determined using the discussed approach, the performance of the latter is only evaluated for the case where the rotation is known, which lays some concerns on how well such solution can estimate attitude, especially under challenging conditions (e.g. low magnetic perturbations, trajectory's static periods, etc.). Contrarily to purely IMU arrays that are widely spread in the literature, see survey in Ref. [Nilsson2016], studying the capabilities of magnetometer arrays is not as extensive, which motivates reviewing the challenges that the MINAV technique may introduce to the indoor navigation problem.

1.2.2 The MINAV model

The magnetic field in the inertial frame

Following the notation previously introduced, the vector field $B^n = [B^n_x \;\; B^n_y \;\; B^n_z]^\top \in \mathbb{R}^{3\times 1}$ is introduced, representing the Earth's magnetic field in $\mathfrak{R}^n$. The component B^n_x is directed towards the geographic north, B^n_y represents the east, while the vertical and positive component directed downwards into the Earth is B^n_z. Four parameters can be employed to describe B^n: the *horizontal intensity* $H_B = \|(B^n_x)^2 + (B^n_y)^2\|$, the *total intensity* $F_B = \|(B^n_x)^2 + (B^n_y)^2 + (B^n_z)^2\|$, the *inclination* $I_B = arctan\ \dfrac{B^n_z}{H_B}$ and the *declination* $D_B = arctan\ \dfrac{B^n_y}{B^n_x}$. These quantities can be directly deduced from Ref. [NOAA2021], by indicating the desired location and time of the measurements. The

Earth's magnetic field B^n is then expressed with

$$B^n = [H_B cos\, D_B \;\; H_B sin\, D_B \;\; F_B sin\, I_B]^\top \tag{1.24}$$

Originally, the magnetic field B^n can be represented as a function of two variables: time t, and space/position M^n. In this sense, its temporal variation can be expressed with a multivariable chain rule differentiation as follows

$$\frac{dB^n(t,M^n)}{dt} = \frac{\partial B^n}{\partial M^n}\frac{dM^n}{dt} + \frac{\partial B^n}{\partial t} \tag{1.25}$$

Assuming B^n is stationary in $\Re^n$ implicates that $\dfrac{\partial B^n}{\partial t} = 0$, making the field only dependent on the space variable M^n. Therefore, Eq. (1.25) is reduced to

$$\frac{dB^n(M^n)}{dt} = \frac{\partial B^n}{\partial M^n}\frac{dM^n}{dt} = \frac{\partial B^n}{\partial M^n}v^n \tag{1.26}$$

This leads to the definition of the Jacobian matrix ∇B^n, representing the magnetic field spatial gradient $\in \mathbb{R}^{3\times 3}$, such that

$$\nabla B^n = \frac{\partial B^n}{\partial M^n} \tag{1.27}$$

Remark 6 *Using Eq. (1.27), and according to the rule of vector derivative versus vector, the magnetic field gradient ∇B^n should be defined as a 9×1 vector. However, it can also be mapped by a unique bijection to a matrix in $\mathbb{R}^{3\times 3}$, which justifies the previous dimension definition.*

The magnetic field in the body frame

In navigation applications, the Earth's magnetic field can be measured using a $3-axis$ magnetometer that is contained in the sensor board attached to the moving body. It comes without saying that the latter needs to be represented in the body frame $\Re^b$ such that $B^b = [B^b_x \;\; B^b_y \;\; B^b_z]^\top \in \mathbb{R}^{3\times 1}$. The rotation between $\Re^n$ and $\Re^b$ is conducted using simply

$$B^b = R^b_n B^n \tag{1.28}$$

In the same manner as the velocity in Eq. (1.17), the dynamics in Eq. (1.26) can also be transformed to the body frame $\Re^b$ using both Eq. (1.28) and Eq. (1.9). This leads to the following derivation

$$\begin{aligned}\frac{dB^b}{dt} =& \frac{dR^b_n B^n}{dt} = \frac{dR^b_n}{dt}B^n + R^b_n\frac{dB^n}{dt}\\ =& -[\omega^b\times]R^b_n B^n + R^b_n \nabla B^n v^n\end{aligned} \tag{1.29}$$

The rotation of the magnetic field gradient ∇B^n is achieved according to the $2nd$ rank tensors (i.e. matrices) transformation formula as follows

$$\nabla B^n = R^n_b \nabla B^b R^b_n \tag{1.30}$$

where $\nabla B^b \in \mathbb{R}^{3\times 3}$ is the magnetic field gradient in $\Re^b$ and is expressed with

$$\nabla B^b = \frac{\partial B^b}{\partial M^b} \tag{1.31}$$

Remark 7 *Similarly to ∇B^n definition, the magnetic field gradient ∇B^b can be either represented as a matrix in $\mathbb{R}^{3\times3}$ or a vector in $\mathbb{R}^{9\times1}$ through a bijection.*

Going back to Eq. (1.29), and replacing ∇B^n with Eq. (1.30) gives

$$\frac{dB^b}{dt} = -\omega^b \times B^b + R_n^b R_b^n \nabla B^b R_n^b v^n \tag{1.32}$$

A simplification of the terms $R_n^b R_b^n$ and $R_n^b v^n$ leads to

$$\frac{dB^b}{dt} = -\omega^b \times B^b + \nabla B^b v^b \tag{1.33}$$

The equation above represents the base of the MINAV technique, that enables the estimation of the velocity v^b, by relying on IMU and magnetometers measurements. An analysis on the benefit of this equation is conducted in the following section.

Remark 8 *It is highlighted that any non-uniform vector field may be used to estimate the velocity v^b in a similar manner to Eq.* (1.33)*. For instance, the magnetic field can be replaced by the electric one which information on its variation is acquired using a set of electrometers Ref. [Lee2008].*

Stationarity of the magnetic field

The model presented in Eq. (1.33) relies on the assumption that the magnetic field in the inertial frame B^n is stationary. Nevertheless, this hypothesis can become untrue in indoor environments due to the presence of additional perturbations related to the electric field. Different solutions can be suggested in this case, depending on the nature of the perturbation, that is, periodic or non-periodic. The most usual one that may occur in an indoor environment is due to *power-line interference*. Under such circumstances, a periodic component at the 50 Hz frequency (in Europe) is contained in the magnetic field vector. This component can go up to 1 μT in amplitude in some cases (e.g. office close to train station), causing a significant drift during the estimation process, as discussed in Ref. [Chesneau2018]. Therefore, it is considered necessary to take power-line interference into account during the magnetic field's modeling.
In Ref. [Chesneau2018], the magnetic field is presented as the sum of a stationary field, and a disturbance field in $\Re^n$, denoted B_{pli}^n, such that, the measured total field y_B^b by the sensor board, is defined with

$$y_B^b = B^b + R_n^b B_{pli}^n \tag{1.34}$$

By denoting ω_{pli} the pulsation of power-line interference, the dynamics of B_{pli}^n are then determined such that

$$\frac{d^2 B_{pli}^n}{dt^2} = -\omega_{pli}^2 B_{pli}^n \tag{1.35}$$

The equation above is considered in the state-space model, in addition to Eq. (1.33), to represent the overall dynamics of the magnetic field.
Similarly to Ref. [Chesneau2018], and to account for power-line interference, in Ref. [Dorveaux2011a], the magnetic field is modeled with

$$y_B^b = B^b cos(\omega_{pli} t + \Phi) \tag{1.36}$$

where Φ is an unknown phase. Considering the latter null, as a simplifying assumption, one has

$$\frac{dy_B^b}{dt} = -\omega^b \times B^b cos(\omega_{pli} t) + \nabla B^b v^b cos(\omega_{pli} t) - B^b \omega_{pli} sin(\omega_{pli} t) \tag{1.37}$$

It is suggested in Ref. [Dorveaux2011a] that, an asymptotic observer relying on magnetic measurements and Eq. (1.37) can enable the reconstruction of velocity. This indicates the effectiveness

of the MINAV approach, even under the magnetic field's non-stationary condition.
When no assumption on the time-varying component of the magnetic field can be made, it is possible to compensate its unsteadiness using an extra measurement, as the electric field, for example. By relying on Maxwell's equations describing the relationship between the *curls* of the magnetic and electric fields Ref. [Jackson1998], an extra term is added to Eq. (1.33) such that

$$\frac{dB^b}{dt} = -\omega^b \times B^b + \nabla B^b v^b - \nabla \times E^b \tag{1.38}$$

where $E^b \in \mathbb{R}^{3\times 1}$ is the output of an electric field sensor (e.g. electrometer) and $\nabla \times E^b$ is its curl. Alternatively, by completely dropping the stationarity hypothesis of the magnetic field, and replacing it by an assumption on its spectrum, a more general model is given in Ref. [Chesneau2018], where in addition to Eq. (1.34) and Eq. (1.35), the magnetic field is defined with

$$\frac{dB^b}{dt} = -\omega^b \times B^b + \nabla B^b v^b + R_n^b B_p^n \tag{1.39}$$

where $B_p^n \in \mathbb{R}^{3\times 1}$, is a non-stationary component of the magnetic field, different from power-line interference, and is modeled with

$$\frac{dB_p^n}{dt} = -\frac{B_p^n}{\tau_{B_p}} \tag{1.40}$$

where τ_{B_p} is a time constant, representing the settling time of a magnetic instationarity.
The proposed models in both discussed references Refs. [Dorveaux2011a, Chesneau2018] demonstrate that the applicability of MINAV approach is not restricted to the presence of a stationary magnetic field and can be generalized to the unsteady case. This is done by either using dedicated models for compensating electric interference at known frequency (power-line), or by adding an additional information, as for the non-periodic case (e.g. output of an electrometer).
Assuming a time-periodic perturbed magnetic field, and more particularly, a power-line interference at 50 Hz, a substitute methodology can be performed, that does not require any further modeling of the magnetic field, other than Eq. (1.33). In fact, instead of taking into account the non-stationary component in the measured magnetic field vector y_B^b, it can be initially rejected through the use of a *notch filter* Ref. [Hirano1974], during a pre-processing phase. Preliminary experiments have demonstrated that, in a regular office environment, the magnitude of power-line interference is most of the time negligible, compared to the stationary component of y_B^b. Such observation is realized through a frequency domain analysis of the measured magnetic field vector from a real sensor board. Following the fact that B_{pli}^n is insignificant, it was later verified that for most of the conducted experiments in this thesis, using the magnetic field measurements in the proposed state-space model, even without any pre-processing, does not have any major impact on the state's estimation accuracy. It follows that, the magnetic field models for the non-stationary case suggested in Refs. [Dorveaux2011a, Chesneau2018] are not adopted in this thesis, to avoid augmenting the state vector and adding more complexity to the proposed solution. The notch filter is however maintained during the measurements' pre-processing phase, to ensure the elimination of the 50 Hz periodic component whenever it exists.

1.2.3 Velocity observability

MINAV main state-space model

Writing back the set of Eqs. (1.18)-(1.20) and adding Eq. (1.33) results in the following system that constructs MINAV main state-space model.

$$\frac{dq}{dt} = \frac{1}{2}\Omega^b q \tag{1.41}$$
$$\frac{dv^b}{dt} = -\omega^b \times v^b + a^b - R_n^b g^n \tag{1.42}$$
$$\frac{dB^b}{dt} = -\omega^b \times B^b + \nabla B^b v^b \tag{1.43}$$
$$\frac{dM^n}{dt} = R_b^n v^b \tag{1.44}$$

The choice of this model is inspired from Ref. [Chesneau2016], and is mainly used here to demonstrate the velocity observability conditions. This model is improved in the next chapter and constitutes the first contribution of this thesis.
The state vector here is then $X(t) = [q \;\; v^b \;\; B^b \;\; M^n]^\top \in \mathbb{R}^{13\times 1}$ and the output vector is $y(t) = B^b \in \mathbb{R}^{3\times 1}$. Direct measurements of ω^b, a^b, and ∇B^b are available using the IMU and the magnetometers, like in Ref. [Chesneau2018]. Thus, the input u is expressed with $u(t) = [\omega^b \;\; a^b \;\; \nabla B^b]^\top \in \mathbb{R}^{11\times 1}$. It is brought to the attention of the reader that in this model, ∇B^b is represented as a function of 5 elements (instead of 9). The reason for this simplification is explained in details in Section 1.3, where all properties of the magnetic field gradient are attentively discussed.
The model above, governed by Eqs. (1.41)-(1.44), can be written in the form of a non-linear state-space model as follows

$$\dot{X}(t) = f(X(t), u(t), \eta(t)) \tag{1.45}$$
$$y(t) = h(X(t), \nu(t)) \tag{1.46}$$

where $X(t)$ is the state vector at time t, $y(t)$ is the known output vector (measurement vector), $u(t)$ is the input, $f(.)$ is a non-linear function that represents the state transition model, $h(.)$ is a non-linear function that represents the measurement (observation) model, and $\eta(t)$ and $\nu(t)$ are the process and measurement noises, respectively, assumed to be zero-mean, white, Gaussian and uncorrelated.
To solve Eqs. (1.45)-(1.46), many observers, specifically designed for non-linear systems, are proposed in the literature, such as those in Ref. [Besançon2007]. In Chapter 2, the observer used in this thesis is presented, and the reasons behind that choice are detailed.

Linearization

In order to compute the system's observability matrix, a linearization of the model is undertaken, by computing the Jacobians of $f(.)$ and $h(.)$ as follows

$$F = \frac{\partial f}{\partial X}|_{\widehat{X}(t),u(t)} \tag{1.47}$$
$$H = \frac{\partial h}{\partial X}|_{\widehat{X}(t)} \tag{1.48}$$

where F is the state matrix, and H is the measurement one. The current estimate of $X(t)$ is denoted by $\widehat{X}(t)$.
In the case of the model formed by Eqs. (1.41)-(1.44), the derived state matrix $F \in \mathbb{R}^{13\times 13}$ has the

following form

$$F = \begin{bmatrix} \frac{1}{2}\Omega^b & 0_{4\times3} & 0_{4\times3} & 0_{4\times3} \\ A_1 & -[\omega^b\times] & 0_{3\times3} & 0_{3\times3} \\ 0_{3\times4} & \nabla B^b & -[\omega^b\times] & 0_{3\times3} \\ A_2 & A_3 & 0_{3\times3} & 0_{3\times3} \end{bmatrix} \tag{1.49}$$

with $A_1 = \dfrac{\partial(-R_n^b g)}{\partial q} \in \mathbb{R}^{3\times4}$, $A_2 = \dfrac{\partial(R_b^n v^b)}{\partial q} \in \mathbb{R}^{3\times4}$ and $A_3 = \dfrac{\partial(R_b^n v^b)}{\partial v^b} \in \mathbb{R}^{3\times3}$. A zero matrix and its dimensions is represented with $0_{i\times j}$, where i corresponds to the number of rows and j to columns.
As the output model is formed with only the magnetic field B^b, the measurement matrix $H \in \mathbb{R}^{3\times13}$, is expressed with

$$H = \begin{bmatrix} 0_{3\times7} & I_3 & 0_{3\times3} \end{bmatrix} \tag{1.50}$$

with I_3 representing the identity matrix $\in \mathbb{R}^{3\times3}$.

Observability matrix

The observability matrix of a system Ref. [Kalman1960b] is defined with $\mathscr{O} = [H \quad HF \quad HF^2 \cdots HF^{n_s-1}]^\top \in \mathbb{R}^{n_s m_s \times n_s}$ where n_s is the number of state variables and m_s is the outputs one. The studied system corresponding to Eq. (1.49) is with $n_s = 13$ state variables, and $m_s = 3$ outputs, its corresponding observability matrix is then $\mathscr{O} = [H \;\; HF \;\; HF^2 \cdots HF^{12}]^\top \in \mathbb{R}^{39\times13}$. It yields that

$$\mathscr{O} = \begin{bmatrix} 0_{3\times4} & 0_{3\times3} & I_3 & 0_{3\times3} \\ 0_{3\times4} & \nabla B^b & -[\omega^b\times] & 0_{3\times3} \\ \nabla B^b A_1 & -W_1 & [\omega^b\times]^2 & 0_{3\times3} \\ \frac{1}{2}\nabla B^b A_1 \Omega^b - W_1 A_1 & W_1[\omega^b\times] + [\omega^b\times]^2 \nabla B^b & -[\omega^b\times]^3 & 0_{3\times3} \\ \vdots & \vdots & \vdots & \vdots \end{bmatrix} \tag{1.51}$$

with $W_1 = (\nabla B^b[\omega^b\times] + [\omega^b\times]\nabla B^b) \in \mathbb{R}^{3\times3}$.
On the basis of the *Kalman observability criterion* for linear dynamic systems Ref. [Kalman1960b], a system is called observable if and only if

$$rank(\mathscr{O}) = n_s \tag{1.52}$$

However, it is clear through this derivation that $rank(\mathscr{O}) < n_s$. By looking at the last column of $\mathscr{O}$, it comes without saying that the observability matrix is 3 states deficient (last column is all zeros). These 3 states correspond to the 3 elements of the position vector M^n. The position is then unobservable, which makes considering it as a state in the model formed by Eqs. (1.41)-(1.44) a questionable choice by [Chesneau2018]. For instance, the position estimate $\widehat{M^n}$ can be directly deduced through a simple integration of the velocity estimate $\widehat{v^b}$, without being included in the estimation approach. However, maintaining it in the state vector has a numerical effect on estimation accuracy in the context of Kalman filtering Ref. [Kalman1960a, Grewal2020].

Observability of the velocity

As discussed in Ref. [Dorveaux2011a], in order for velocity to be observable, the magnetic field gradient ∇B^b needs to be *non-singular* (as it occurs in the second column of $\mathscr{O}$). A square matrix

A is non-singular if and only if its determinant is nonzero. More precisely, the observability matrix of Eq. (1.51) can be of $rank(\mathscr{O}) = 10$, only if ∇B^b is full-rank. For the quaternion, its observability also depends on A_1, if the latter is full-rank, three of the quaternion elements are observed thanks to the term $\nabla B^b A_1$ in the first column (and third block line) of $\mathscr{O}$, while the fourth element may be recovered from the next block lines of $\mathscr{O}$. In practice, the non-singularity condition of ∇B^b is very linked to the presence of magnetic field disturbances. In fact, if there are very low perturbations in the surrounding environment of the moving body, one or more of the magnetic field gradient's directions may have nearly-null values, which implies that ∇B^b is no more a full-rank matrix. Nevertheless, it is reminded that the presence of sufficient magnetic field disturbances is a condition that is usually satisfied in indoor environments as previously demonstrated in Section 1.2.1. In the worst case scenario where $\nabla B^b = 0_{3\times 3}$ (in outdoor environments, for example), $rank(\mathscr{O}) = 3$ and only the magnetic field is observable (thanks to the identity matrix in the third column). This highlights the dependency of the MINAV technique on the presence of magnetic perturbations and more specifically on the availability of ∇B^b.
In the next section, the magnetic field gradient is presented in detail, where its different properties and models are discussed and commented.

1.3 Limitations of the magnetic field gradient determination

As elaborated in the previous section, the magnetic field gradient plays a key role in the MINAV scheme as it ensures velocity observability and enables its reconstruction alongside with attitude and position. Analyzing this entity is then crucial to understand not only its capabilities but also its challenges.

1.3.1 The magnetic field gradient properties

What makes of the magnetic field an interesting asset to the navigation problem is its properties that act explicitly on the magnetic field gradient, and enable the simplification of the model formed by Eqs. (1.41)-(1.44). These properties are governed by Maxwell's equations Ref. [Jackson1998] for a source-free region, and are detailed subsequently.

Divergence

In the absence of electric sources, the divergence of the magnetic field is equal to zero, i.e.

$$\nabla \cdot B^b = 0 \tag{1.53}$$

This implies that the trace of its Jacobian, representing the magnetic field gradient ∇B^b in its 3×3 matrix form, is zero i.e.

$$\partial_x B^b_x + \partial_y B^b_y + \partial_z B^b_z = 0 \tag{1.54}$$

with ∂_x, ∂_y and ∂_z, referring to the partial derivative of an element with respect to M^b_x, M^b_y and M^b_z, respectively.
It follows that the number of independent terms in ∇B^b is reduced to 8 instead of 9.

Curl

In the case of stationary fields and in absence of electric and magnetic sources, the curl of the magnetic field is equal to zero, i.e.

$$\nabla \times B^b = 0 \tag{1.55}$$

This implies that its Jacobian matrix is symmetric i.e.,

$$\forall i,j \in \{x,y,z\}, \partial_i B_j^b = \partial_j B_i^b \tag{1.56}$$

This means that the number of independent terms in ∇B^b is now down to 5 instead of 8.

1.3.2 The magnetometer array: extracting the magnetic field gradient

A planar arrangement of 3 magnetometers

Thanks to the previously presented properties, the magnetic field gradient ∇B^b can be expressed with the following form

$$\nabla B^b = \begin{bmatrix} \frac{\partial B_x^b}{\partial M_x^b} & \frac{\partial B_y^b}{\partial M_x^b} & \frac{\partial B_z^b}{\partial M_x^b} \\ \frac{\partial B_x^b}{\partial M_y^b} & \frac{\partial B_y^b}{\partial M_y^b} & \frac{\partial B_z^b}{\partial M_y^b} \\ \frac{\partial B_x^b}{\partial M_z^b} & \frac{\partial B_y^b}{\partial M_z^b} & \frac{\partial B_z^b}{\partial M_z^b} \end{bmatrix} = \begin{bmatrix} \beta_1 & \beta_2 & \beta_3 \\ \beta_2 & \beta_4 & \beta_5 \\ \beta_3 & \beta_5 & -\beta_1-\beta_4 \end{bmatrix}_{\beta_{1,\cdots,5}\in\mathbb{R}} \tag{1.57}$$

By a finite differences scheme, it is evident that, in order to reconstruct ∇B^b, an array of at least 3 non-aligned $3-axis$ magnetometers is required. As the magnetic field gradient is symmetric and traceless, as shown in Eq. (1.57), the third column of ∇B^b can be recovered from the first two columns. This suggests that a $2D$ arrangement of the 3 magnetometers is sufficient to obtain the full magnetic field gradient. Conception wise, this is advantageous as it enables having a user-friendly embedded system, that can be easily strapped to the moving body under study.

Remark 9 *While this assumption is theoretically justifiable, it may be interesting to explore a non-planar disposition of the magnetometer array. In fact, in Ref. [Hanley2018], it was demonstrated that, in indoor environments, the magnetic field can vary significantly as a function of height. Despite that this evaluation was performed on a higher scale than the one concerning a sensor array (usually, the distance between the magnetometers doesn't exceed the centimeter level), it provides a useful insight on the matter.*

Determination of the magnetic field gradient

Since the sensor board does not directly provide the magnetic field gradient, it needs to be deduced from the measurements of the magnetometer array. To do so, several approximation-based solutions can be exploited, such as finite differences Ref. [Grossmann2007], polynomial interpolation Ref. [Atkinson1988], or any regression-based technique Ref. [Manski1991].
To have a clearer idea on the targeted problem in this case, consider a vector $p_i = [p_{ix} \;\; p_{iy} \;\; p_{iz}]^\top \in \mathbb{R}^{3\times 1}$, representing the position of a magnetometer i in the sensor array. In Fig. 1.5, a simplified diagram of the magnetometer array is displayed.
Suppose that the magnetometer 0, measuring B_0^b, is centered at the origin of the array, denoted with $p_0 = [0 \;\; 0 \;\; 0]$. The two magnetometers 1 and 2 are symmetric, i.e. $p_{1x} = -p_{2x}$ and $p_{1y} = p_{2y}$. Also, $|p_{1x}| = |p_{1y}|$.
It is assumed that the magnetic field and its gradient are known at p_0 such that

$$B^b(p_0) = B_0^b \tag{1.58}$$

$$\nabla B^b(p_0) = \nabla B_0^b \tag{1.59}$$

with B_0^b and ∇B_0^b expressed in the same forms as their standard definitions.

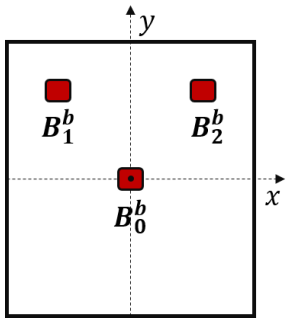

Figure 1.5: Diagram of a magnetometer array

Remark 10 *In reality, the assumption that the magnetic field is known at p_0 is not totally accurate, as the 3 axes of magneteometer 0 do not coincide precisely with the considered origin. The assumption is done only for estimation.*

According to Taylor's formula Ref. [Li2016] for functions of several variables, the following approximation is introduced

Corollary 1 *Let $f : \mathbb{R}^2 \to \mathbb{R}$ be two times differentiable in $(a,b) \in \mathbb{R}^2$, then:*

$$\begin{aligned} f(a+h,b+k) = f(a,b) &+ \frac{\partial f(a,b)}{\partial x}h + \frac{\partial f(a,b)}{\partial y}k + \frac{1}{2}\frac{\partial^2 f(a,b)}{\partial x^2}h^2 \\ &+ \frac{1}{2}\frac{\partial^2 f(a,b)}{\partial y^2}k^2 + \frac{\partial^2 f(a,b)}{\partial x \partial y}hk \\ &+ o(h^2+k^2) \end{aligned} \tag{1.60}$$

Using this corollary, the magnetic field B_i^b measured by a magnetometer i can be expressed at any point p_i, with the following first-order approximation

$$B_i^b(p_i) = B_0^b + \nabla B_0^b p_i \tag{1.61}$$

In matrix form, Eq. (1.61) is rewritten as follows

$$B_i^b = \begin{bmatrix} B_x^b \\ B_y^b \\ B_z^b \end{bmatrix} + \begin{bmatrix} \beta_1 & \beta_2 & \beta_3 \\ \beta_2 & \beta_4 & \beta_5 \\ \beta_3 & \beta_5 & -\beta_1 - \beta_4 \end{bmatrix} \begin{bmatrix} p_{ix} \\ p_{iy} \\ p_{iz} \end{bmatrix} \tag{1.62}$$

The measured magnetic field B_i^b is then the result of a multiplication between a non-square matrix and an unknown vector as shown below

$$B_i^b = \begin{bmatrix} 1 & 0 & 0 & p_{ix} & p_{iy} & p_{iz} & 0 & 0 \\ 0 & 1 & 0 & 0 & p_{ix} & 0 & p_{iy} & p_{iz} \\ 0 & 0 & 1 & -p_{iz} & 0 & p_{ix} & -p_{iz} & p_{iy} \end{bmatrix} \begin{bmatrix} B_x^b \\ B_y^b \\ B_z^b \\ \beta_1 \\ \beta_2 \\ \beta_3 \\ \beta_4 \\ \beta_5 \end{bmatrix} = P_i X_B \tag{1.63}$$

where $P_i \in \mathbb{R}^{3\times 8}$ is a known matrix containing the different position coordinates of magnetometer i with respect to the origin p_0, and $X_B \in \mathbb{R}^{8\times 1}$ is the vector to be estimated, containing both the magnetic field and its gradient at the origin p_0 of the magnetometer array. The magnetometer array of Fig. 1.5 generates measurements of three magnetometers such that $B_{Total} = [B_0^b \;\; B_1^b \;\; B_2^b]^\top \in \mathbb{R}^{9\times 1}$, and its corresponding $P_{Total} = [P_0 \;\; P_1 \;\; P_2]^\top \in \mathbb{R}^{9\times 8}$. It yields that Eq. (1.63) is re-written such that

$$B_{Total} = P_{Total} X_B \tag{1.64}$$

The matrix P_{Total} is called *skinny*, i.e. a rectangular $m \times n$ matrix with $m > n$. This implicates that Eq. (1.64) represents an overdetermined system of linear equations, i.e. there exist more equations than unknowns.
One approach that has proven to be efficient for solving this kind of equation, resides on the following points:

- define a residual or error e such as $e = P_{Total} X_B - B_{Total}$;
- find $X_B = X_{ls}$ that minimizes $\|e\|$.

The matrix X_{ls} is called the *least-squares* solution Ref. [Boyd2018] of Eq.(1.64).
Assume P_{Total} is full rank and skinny. To find X_{ls}, the following norm of the error, squared, is minimized

$$\|e\|^2 = X_B^\top P_{Total}^\top P_{total} X_B - 2B_{Total}^\top P_{Total} X_B + B_{Total}^\top B_{total} \tag{1.65}$$

The gradient with respect to X_B is then set to zero at minimum

$$\nabla_{X_B} \|e\|^2 = 2P_{Total}^\top P_{Total} X_B - 2P_{Total}^\top B_{Total} = 0 \tag{1.66}$$

This yields the normal equation

$$P_{Total}^\top P_{Total} X_B = P_{Total}^\top B_{Total} \tag{1.67}$$

Assumptions imply that $P_{Total}^\top P_{Total}$ is invertible, thus

$$X_{ls} = (P_{Total}^\top P_{Total})^{-1} P_{Total}^\top B_{Total} \tag{1.68}$$

The expression noted with $(P_{Total}^\top P_{Total})^{-1} P_{Total}^\top$ is called the pseudo-inverse matrix of P_{Total} and is noted $P_{Total}^\dagger$. The latter is a left inverse of P_{Total}, which means

$$P_{Total}^\dagger P_{Total} = (P_{Total}^\top P_{Total})^{-1} P_{Total}^\top P_{Total} = I \tag{1.69}$$

with $I \in \mathbb{R}^{9\times 8}$, the identity matrix.
The vector containing the magnetic field and its gradient X_B is then estimated with

$$X_B = X_{ls} = P_{Total}^\dagger B_{Total} \tag{1.70}$$

Recall that $P_{Total}^\dagger$ contains the coordinates of the positions of the different magnetometers in the sensor board, and therefore it is known. While the vector B_{Total} represents the recorded measurements of the magnetometer array and is also known.

What about finite differences?

Usually, the most straightforward method to determine the Jacobian matrix of a vector field is based on a finite differences scheme. Recall that the properties of the magnetic field gradient introduced in Section 1.3.1 allow to distribute the magnetometers array only in a plane. This enables the determination of only two lines of ∇B^b and not taking into account the $z-axis$ of the magnetometer array. More precisely, for a $2D$ system having the three magnetometers located

according to the schematic on Fig. 1.5, where magnetometer 0 is assumed centered at the origin p_0, the main goal is to determine $\frac{\partial B_0^b}{\partial M_x^b}$ and $\frac{\partial B_0^b}{\partial M_y^b}$, while the magnetic field partial derivative with respect to z, denoted $\frac{\partial B_0^b}{\partial M_z^b}$, is concluded.

A first step to solve this problem is to use Taylor's approximation Eq. (1.60). Applying this formula on B_1^b leads to the following first-order approximation

$$B^b(0-p_{2x},0+p_{2y}) = B^b(0,0) - \frac{\partial B^b(0,0)}{\partial M_x^b}p_{2x} + \frac{\partial B^b(0,0)}{\partial M_y^b}p_{2y} \tag{1.71}$$

The same approximation is applied on B_2^b

$$B^b(0+p_{2x},0+p_{2y}) = B^b(0,0) + \frac{\partial B^b(0,0)}{\partial M_x^b}p_{2x} + \frac{\partial B^b(0,0)}{\partial M_y^b}p_{2y} \tag{1.72}$$

The summation of Eq. (1.71) and Eq. (1.72) gives

$$B_1^b + B_2^b = 2B_0^b + 2\frac{\partial B_0^b}{\partial M_y^b}p_{2y} \tag{1.73}$$

This implies that

$$\frac{\partial B_0^b}{\partial M_y^b} = \begin{bmatrix}\beta_2\\ \beta_4\\ \beta_5\end{bmatrix} = \frac{B_1^b + B_2^b - 2B_0^b}{2p_{2y}} \tag{1.74}$$

Similarly, subtracting Eq. (1.71) from Eq. (1.72) gives

$$B_2^b - B_1^b = 2\frac{\partial B_0^b}{\partial M_x^b}p_{2x} \tag{1.75}$$

It is deduced then that

$$\frac{\partial B_0^b}{\partial M_x^b} = \begin{bmatrix}\beta_1\\ \beta_2\\ \beta_3\end{bmatrix} = \frac{B_2^b - B_1^b}{2p_{2x}} \tag{1.76}$$

As the least-squares method, the estimated magnetic field gradient ∇B^b through a finite differences scheme is dependent not only on the measurements of the magnetometers but also on their positions in the array.

Challenges and discussion

What makes of the finite differences method a less interesting choice to determine the magnetic field gradient is its high sensitivity to the synchronization between the different magnetometers. As discussed in Ref. [Dorveaux2011a], data from the magnetometers can be acquired at slightly different times, depending on their specifications, which induces a certain time delay between the measurements. For instance, consider a sensor board sampled at 50 Hz, moving at the speed of 1 ms^{-1}. If the measurements of two magnetometers, distanced by 0.1 m, are acquired with a one step delay $dT = \frac{1}{50} = 0.02\,s$, then the induced displacement is of $0.02 * 1 = 0.02\,m$. This represents 20% of error in the magnetic field gradient estimate. In addition to errors generated by delays (i.e. time delays between the various sensors: IMU and the magnetometers, acquisition delays,

internal computations delays, etc.), the finite differences scheme is rather unhandy dealing with singularities induced by boundary conditions, which is also discussed in Ref. [Dorveaux2011a]. Most of all, the simplicity of such derivation comes from the assumption on the planar arrangement of the magnetometers, making of this method, a $2D$ estimation problem. However, in practice, it is nearly impossible to have a perfectly planar sensor board as magnetometers are designed with a certain width between their outer box and their axes. It follows that their positions with respect to the $z-axis$, p_{iz}, are better to be taken into account.
These difficulties encourage the use of a more flexible approximation method such as the least-squares. However, having a high accuracy determination of the magnetic field gradient through such an approximation method is also challenging for few reasons:

- while magnetometers' positions with respect to all axes are taken into account, it is natural to consider that knowing their values precisely is not evident as there's always a millimeter-wise gap between the axes and the magnetometers' covers. A technique using a straight rail is used in Ref. [Dorveaux2011a] to determine these parameters, a system that may be unavailable in general cases;

- the magnetic field gradient is computed using the set of magnetometers. These sensors have to be accurate, which is not always the case. This may lead to a vanishing magnetic field gradient, and consequently to velocity observability issues. The resolution and the distance between the different magnetometers represent then a constraint on the precision of the magnetic field gradient determination.

In addition, the magnetic field measurements from the magnetometer array are noisy. Since they are used to compute the magnetic field gradient, no matter what the approximation method, it yields that the latter suffers also from noise, affecting thereafter the velocity estimation. The noise contained in the magnetic field measurements is not in fact a white noise, and identifying it from the other *"beneficial"* magnetic field perturbations induced by the indoor environment is not a straightforward task. This makes relying on standard filtering methods an unsuitable option.
To illustrate the last point, the sensor board represented in Fig. 1.5 is placed on the floor, motionless, in an outdoor environment where there is no source for magnetic disturbances. Being static, the magnetometer array is measuring the Earth's magnetic field (assumed constant during the time of the experiment), noise, and bias, as the case for any MEMS sensor. Assuming that this noise is white, the Power Spectral Density (PSD) Ref. [Miller2004] of $\eta^b_{B_0} = B^b_0 - \overline{B^b_0}$ is expected to be flat (i.e. constant all along the frequency range), with $\eta^b_{B_0}$ representing the noise of the magnetic field B^b_0, and $\overline{B^b_0}$ its corresponding mean. In Fig. 1.6, the PSD of $\eta^b_{B_0}$, (in $decibels$ (dB)), is plotted. By looking at the form of this PSD, it is clear that the studied signal is not flat and thus it does not correspond to a white noise. Because of all the above limitations, the determined magnetic field gradient may lack precision. As the latter plays a key role in the MINAV technique and guarantees velocity observability, a more precise solution should be found for a better determination of this state.

Calibration of a magnetometer array

The major reason for the inaccuracy of magnetometers' measurements, that also represents a big challenge for the magnetic field gradient determination, is the efficiency of the calibration step. Calibration algorithms are usually intended to compensate the magnetometers' instrumentation errors, such as scale factors, misalignments, non-orthogonality, and biases. They are also meant to reduce the impact of two fundamental phenomena known as *hard and soft iron* effects. Hard iron errors are caused by any magnetic source, natural or electric, generating its own magnetic field that is added to the Earth's one. On the contrary, soft iron errors are induced by ferromagnetic materials that influence the Earth's magnetic field, by changing its direction depending on

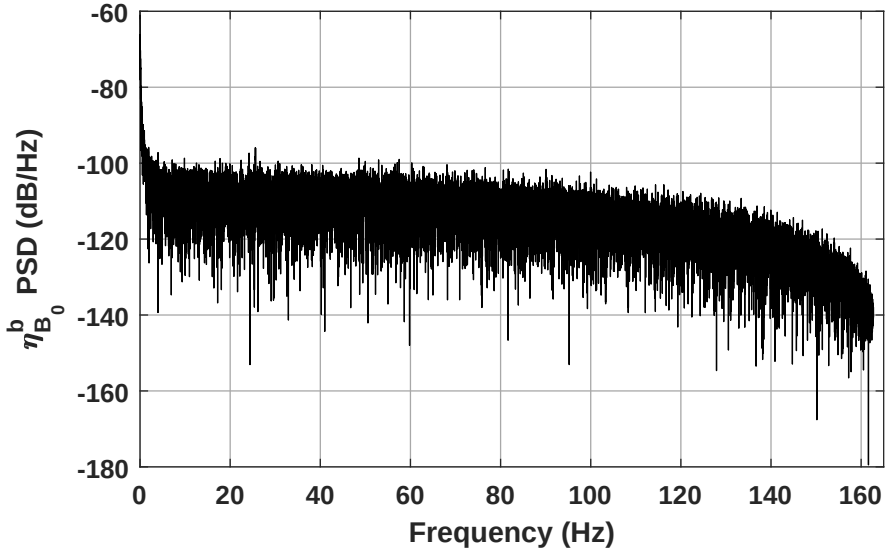

Figure 1.6: Power spectral density of $\eta^b_{B_0}$ in an outdoor environment

their orientation. Several approaches have been proposed in related state-of-the-art to perform an adequate calibration of the magnetometers. From these methods, many are based on the Ellipsoid fitting principle Refs. [Foster2008, Dorveaux2009, Vasconcelos2011, Mohamadabadi2014], as it has no specific requirements on sensor orientation during the calibration process, and does not need any additional hardware. Nevertheless, the performances of these approaches usually depend on several assumptions, that may not always reflect reality, such as the nature of hard and soft iron errors (linear and without hysteresis) Refs. [Foster2008, Dorveaux2009], or the magnetic field dynamics (homogeneous field with invariant norm) Ref. [Mohamadabadi2014]. In Ref. [Renaudin2010], an adaptive least squares estimator, suited for non-linear equations, is derived to find the parameters of the ellipsoid in a statistically consistent way. Unlike many works in the literature, it does not rely on any simplification on the sensor error modeling and can fully estimate the magnetometer's calibration parameters. Conversely, in Ref. [Chesneau2018], it is stated that ellipsoid fitting calibration techniques cannot ensure a predefined calibration reference frame and do not give any information on magnetometers' effective positions. If the magnetic field gradient is to be computed from multiple magnetometer measurements, especially under an inhomogeneous field, such limitation can drastically degrade the accuracy of its determination. Thus, in Ref. [Chesneau2018], the author proposes two replacement calibration methods that are rather suitable for applications relying on magnetometer arrays. The first approach relies on the use of an arrangement of $3-axis$ Helmholtz coils Ref. [Frix1994], to generate an unknown and inhomogeneous magnetic field. The magnetometer array is then placed inside the coils in multiple unknown positions, while independent and known currents are provided to each coil. Using the measurements of the array, in addition to the currents, one can compute the performed trajectory of the magnetometer array inside the coils-based setting. The main advantage of this approach over ellipsoid fitting is enabling the determination of magnetometers effective positions, allowing therefore the calibration of the entire array. Unlike the coils-based calibration procedure, the second proposed approach Ref. [Chesneau2019] does not require any dedicated calibration setup. It relies however on exploring the relationship between raw magnetic field measurements and available position and attitude information. This is achieved by undertaking arbitrary trajectories inside a motion capture setup and then using the collected data to solve the optimization problem. Indeed, when the magnetic field is stationary and not specifically homogeneous, and that positioning information is available, the identifiability conditions show that the array's calibration parameters can be derived. The determined parameters include the effective positions of the different magnetometers within

the sensor board, which are essential for the determination of the magnetic field gradient.
The methods proposed in Ref. [Chesneau2018] have been used to calibrate the sensor board employed in this thesis (see Chapter 5). No further work has been conducted in this direction and any possible improvements could be considered for future perspectives.

1.3.3 State-of-the-art models and discussion

In the previously presented model formed by Eqs. (1.41)-(1.44), the magnetic field gradient ∇B^b is considered known as in Refs. [Dorveaux2011a, Chesneau2018]. It is then used as an input in Eq. (1.43) without accounting for its uncertainties caused by approximations and noise.
If a representative dynamic model of ∇B^b, one can add it as a state for the considered model and rather estimate it through a non-linear observer framework.
In [Vissière2007a], direct measurements of the magnetic field gradient are not considered available. In fact, using a single $3-axis$ magnetometer is not sufficient to determine ∇B^b. For this reason, it is estimated instead by an observer. Then, a differential equation representing the dynamics of ∇B^b should be considered. In [Vissière2007a], authors assume that the magnetic field gradient satisfies some first order dynamics driven by white noise such as

$$\frac{d\nabla B^b}{dt} = \frac{-\nabla B^b}{\tau^b_{\nabla B}} + \eta^b_{\nabla B} \tag{1.77}$$

where $\tau^b_{\nabla B} \in \mathbb{R}_{>0}$ is a time constant and $\eta^b_{\nabla B}$ is a white noise. In reality, this model is not the most convenient option to capture full information on the dynamics of ∇B^b. In fact, from the same experiment shown in Fig. 1.3, a magnetic field gradient is determined through the least-squares approximation. The evolution of its first element β_1 is shown for the first 20 s of the test in Fig. 1.7.

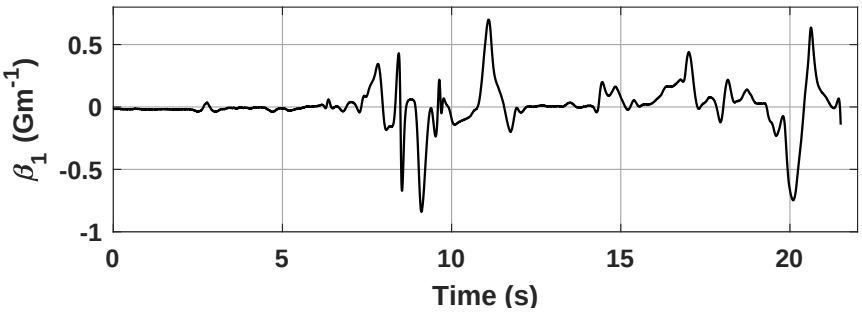

Figure 1.7: Variation of β_1 during an indoor trajectory

The displayed variations and the nature of the depicted slopes of β_1 suggest that the second derivatives of the magnetic field are not negligible. Thus, modeling its gradient using Eq. (1.77) does not fit well with the actual dynamics of ∇B^b.
In [Vissière2007b], authors extend their work to using three $3-axis$ magnetometers and determining the magnetic field gradient through a finite differences scheme. However, contrarily to Refs. [Dorveaux2011a, Chesneau2018], ∇B^b is not considered as a known input, even after being computed from the magnetometer array. Instead, it is included in the state vector and also serves in the measurement one, such as, using our notation from Eq. (1.61)

$$y^b_{B_i} = B^b_i(p_i) \tag{1.78}$$

where $y^b_{B_i} \in \mathbb{R}^{9\times 1}$ is the measurements vector corresponding to an orthogonal trihedron of magnetometers. For simplicity reasons, the model used in this case to describe the magnetic field gradient is

$$\frac{d\nabla B^b}{dt} = \eta^b_{\nabla B} \tag{1.79}$$

Again, representing the dynamics of the magnetic field gradient with a white noise is not very informative, especially that such characterization does not take into account the attitude, the velocity, etc. One way to solve this problem is to investigate higher-order spatial derivatives of the magnetic field given a proper setting of the magnetometer array.

1.4 Conclusion

Purely inertial navigation Low-cost MEMS inertial sensors do not provide an accurate estimation of attitude, velocity and position over more than a few seconds up to one minute in the best case scenario. This is due to the presence of sensor biases whose effect is amplified with every integration.

Magnetometers for heading estimation Complementing inertial sensors with magnetometers is a very common solution to solve the inertial navigation problem, especially for attitude estimation. In fact, magnetometers are largely used to determine heading, as long as they are not perturbed by the outer environment. In case they are, compensation methods are developed to reject or reduce these perturbations.

Magnetic disturbances in indoor environments In an indoor environment, the presence of magnetic perturbations can be very large, due to all metals used in buildings and potentially to the strong electric currents propagating close-by. One may think that these disturbances can only represent a constraint for navigation, as in heading applications. However, these perturbations are not in fact a random noise. On the contrary, they are well structured by physics equations. Therefore, it is considered that rich information lies in these disturbances.

Mapping or extra equipment Most of the techniques that take advantage of the magnetic field disturbances present indoor require either a prior information on the building infrastructure (map) or extra equipment, which opposes with the objectives of this thesis: indoor navigation using solely low-cost sensors and no prior knowledge. Besides, the main goal of most of these works is usually trajectory/position reconstruction and not velocity estimation.

MINAV technique An approach was firstly introduced in 2007 that demonstrates the relationship between the magnetic field and the velocity. The method ensures the observability of the velocity and an accurate reconstruction of the latter as long as the magnetic field gradient is non-singular. The estimation is conducted through a non-linear observer framework, where the magnetic field gradient is considered as a known input.

Modeling the magnetic field gradient The magnetic field gradient is usually determined through approximation schemes applied on a magnetometer array. The magnetic field gradient is then subject to many uncertainties as well as noise, and thus considering it as a known input in the observer may lead to large estimation errors. A dynamic model needs to be derived in order to add this magnetic field gradient to the state vector and estimate it instead. Few attempts are proposed in the literature to do so, but they are rather too simplistic and do not fully capture the richness of the magnetic field gradient dynamics. A more sophisticated model is then derived in Chapter 2 by exploiting higher-order spatial derivatives of the magnetic field through a more complete magnetometer array setting.

2

Two Magnetic Field Gradient-Based Extended Kalman Filters

The main goal of this chapter is to derive a new model describing the dynamics of the magnetic field gradient. Unlike previous works in the state-of-the-art, the proposed model highlights the richness of the magnetic field gradient variations, and their relationship with velocity and attitude. To do so, higher-order spatial derivatives of the magnetic field are explored in Section 2.1. Then, a specific configuration of two Extended Kalman Filters (EKFs) is proposed in Section 2.2 to estimate not only the velocity, position and attitude of the moving body, but also the magnetic field and its gradient. Different comparisons are undertaken between including the magnetic field gradient in the state vector to be estimated (with different models) or directly using it as an input, under some approximations. This is achieved under a simulation framework in Section 2.3, where the accuracy of the velocity estimation is shown to be higher when the magnetic field gradient is modeled as a state.

Contents

2.1 Higher-order spatial derivatives of the magnetic field

As shown in the previous chapter, the magnetic field gradient plays a crucial role not only for the estimation of the velocity but also the attitude and position. Therefore, its estimation has to be well-founded, in order to avoid the much more errors caused by approximation models and better remove the noise coming from the magnetometer array measurements. In the literature Refs. [Vissière2007a, Chesneau2018], it is recommended to explore higher-order spatial derivatives of the magnetic field in order to better model the magnetic field gradient and relate its dynamics to the attitude and velocity.

2.1.1 Problem statement

The targeted problem in this chapter is how to improve velocity estimation, as well as position and attitude, by adding the dynamics of the magnetic field gradient to the main model, presented in Chapter 1. Instead of considering the magnetic field gradient as a known input in the state-space model, it is rather moved to the state vector to be estimated. This is done while maintaining the low-cost sensor board framework and only through employing inertial and magnetic measurements in a non-linear observer scheme.

2.1.2 Chapter contribution

The main contribution in this chapter is the introduction of a new specific equation, to describe the dynamics of the magnetic field gradient. This equation is derived through exploring higher-order spatial derivatives of the magnetic field, as encouraged in [Vissière2007a, Chesneau2018]. These derivatives are computed thanks to a determined arrangement of a magnetometer array. The proposed dynamic model also preserves a direct link between the magnetic field gradient and the velocity, as well as the attitude (angular velocity), which efficiently exhibits the richness of the magnetic field spatial variations, especially in an indoor environment. The advantage of the proposed state-space model is evaluated through an Extended Kalman Filter (EKF) approach. Different comparisons are undertaken under a simulation scheme, where the importance of considering the magnetic field gradient as a state is highlighted. The proposed dynamic model is then shown to outperform state-of-the-art ones, by inducing the best estimation accuracy results.

2.1.3 Second order spatial derivative

In order to represent the dynamics of ∇B^b, an equation describing its temporal variation needs to be derived. To preserve full information on these dynamics and to follow the same vector field calculus used in Chapter 1, the derivative of the magnetic field gradient with respect to time is written in function of its spatial derivative and velocity such that

$$\frac{d\nabla B^b(M^b)}{dt} = f\left(\frac{\partial \nabla B^b}{\partial M^b}, v^b\right) \tag{2.1}$$

Remark that the equation above is very similar to Eq. (1.33), where B^b and ∇B^b are replaced with their respective spatial derivatives.

Before figuring out the equation describing $\frac{d\nabla B^b}{dt}$, the temporal derivative of the magnetic field gradient in $\Re^n$ is determined. By applying the chain rule differentiation for a non-stationary field as demonstrated previously in Eq. (1.25), the following equation is obtained

$$\frac{d\nabla B^n(t,M^n)}{dt} = \frac{\partial \nabla B^n}{\partial M^n}\frac{dM^n}{dt} + \frac{\partial \nabla B^n}{\partial t} \tag{2.2}$$

It is reminded that B^n is assumed stationary in R^n, which implicates that $\frac{\partial \nabla B^n}{\partial t} = 0$. Thus, it is safe to write

$$\frac{d\nabla B^n(M^n)}{dt} = \frac{\partial \nabla B^n}{\partial M^n}\frac{dM^n}{dt} = \frac{\partial \nabla B^n}{\partial M^n} v^n \tag{2.3}$$

A new entity is then introduced, the magnetic field hessian, representing the second order spatial derivative of the magnetic field in $\mathfrak{R}^n$. It is denoted $T^n \in \mathbb{R}^{3\times3\times3}$ and defined as follows

$$T^n = \frac{\partial \nabla B^n}{\partial M^n} \tag{2.4}$$

To ease the reading, this tensor is alternatively represented as a matrix in $\mathbb{R}^{9\times3}$ through a unique bijection, and can be written in the following form

$$T^n = \begin{bmatrix} \nabla\alpha_1 & \nabla\alpha_2 & \nabla\alpha_3 \\ \nabla\alpha_2 & \nabla\alpha_4 & \nabla\alpha_5 \\ \nabla\alpha_3 & \nabla\alpha_5 & -\nabla\alpha_1 - \nabla\alpha_4 \end{bmatrix}_{\alpha_{1,\cdots,5}\in\mathbb{R}} \tag{2.5}$$

where $\nabla\alpha_i = [\frac{\partial \alpha_i}{\partial M_x^n} \ \frac{\partial \alpha_i}{\partial M_y^n} \ \frac{\partial \alpha_i}{\partial M_z^n}]^\top$, with $\alpha_{i\in\{1,\cdots,5\}}$ representing the elements of the magnetic field gradient in $\mathfrak{R}^n$.
As measurements from the magnetometer array are acquired in $\mathfrak{R}^b$, one must write Eq. (2.3) in $\mathfrak{R}^b$ rather than $\mathfrak{R}^n$. The following derivation is then conducted

$$\frac{d\nabla B^b}{dt} = \frac{d(R_n^b \nabla B^n R_b^n)}{dt} = \frac{dR_n^b}{dt}\nabla B^n R_b^n + R_n^b \frac{d\nabla B^n}{dt} R_b^n + R_n^b \nabla B^n \frac{dR_b^n}{dt} \tag{2.6}$$

Recalling the temporal derivative of R_n^b in Eq. (1.9) and the one of ∇B^n in Eq. (2.3) yields

$$\frac{d\nabla B^b}{dt} = -[\omega^b\times]R_n^b \nabla B^n R_b^n + R_n^b T^n v^n R_b^n + R_n^b \nabla B^n R_b^n [\omega^b\times] \tag{2.7}$$

It follows by taking into account the frame transformation induced by the multiplication with R_n^b and its transpose to have

$$\frac{d\nabla B^b}{dt} = T^b v^b + \nabla B^b [\omega^b\times] - [\omega^b\times]\nabla B^b \tag{2.8}$$

where $T^b \in \mathbb{R}^{3\times3\times3}$ is the magnetic field hessian expressed in $\mathfrak{R}^b$ and defined with

$$T^b = \frac{\partial \nabla B^b}{\partial M^b} \tag{2.9}$$

This tensor can also be represented with a matrix in $\mathbb{R}^{9\times3}$, as a function of $\beta_{i\in\{1,\cdots,5\}}$ such that

$$T^b = \begin{bmatrix} \nabla\beta_1 & \nabla\beta_2 & \nabla\beta_3 \\ \nabla\beta_2 & \nabla\beta_4 & \nabla\beta_5 \\ \nabla\beta_3 & \nabla\beta_5 & -\nabla\beta_1 - \nabla\beta_4 \end{bmatrix}_{\beta_{1,\cdots,5}\in\mathbb{R}} \tag{2.10}$$

where $\nabla\beta_i = [\frac{\partial \beta_i}{\partial M_x^b} \ \frac{\partial \beta_i}{\partial M_y^b} \ \frac{\partial \beta_i}{\partial M_z^b}]^\top$.
The temporal derivative of ∇B^b is then described as a function of the magnetic field gradient itself, the hessian T^b, the velocity v^b, and the angular rate ω^b[1]. Through the proposed Eq. (2.8), the richness of the dynamics of the magnetic field gradient is preserved, unlike state-of-the-art models that limit its variations to those of a first order system or simply a white noise.

[1] In the entire thesis, the expression "angular rate" is equivalent to "angular velocity".

2.1.4 Properties of the magnetic field hessian

Before further investigating the added value of Eq. (2.8), it is almost evident to check the properties that define the new introduced magnetic filed hessian T^b, in order to take advantage of any simplifications that can be applied.
One may wonder if the planar arrangement possibility of the magnetometer array can be maintained when working with a second order spatial derivative. First, recall that ∇B^b is expressed with only 5 elements ($\beta_{1,\cdots,5}$), thanks to its properties from Eq. (1.54) and Eq. (1.56). It follows from Eq. (2.10), that T^b determination is reduced from 27 to only $5\times 3 = 15$ elements that constitute $\nabla\beta_{1,\cdots,5}$. Then, to further reduce the computations, Schwarz's theorem [Hairer1996] is recalled.

Theorem 2.1.1 *Let U be an open set of $\mathbb{R}^n$. Consider $p\in\mathbb{R}^n$ a point such that some neighborhood of p is contained in U. If f is a function of U in $\mathbb{R}^p$ and of class C^2 on U (i.e. two times differentiable and its second derivative is continuous). Then, $\forall\, i,j\in 1,\cdots,n$, the following equality holds*

$$\frac{\partial^2}{\partial x_i\partial x_j}f(p)=\frac{\partial^2}{\partial x_j\partial x_i}f(p) \tag{2.11}$$

This theorem implies that for a sufficiently regular function, the order of derivation with respect to its variables does not matter. As long as the partial derivatives exist in the neighborhood of a point p and are continuous in p, then it is possible to invert the order of derivation.
Assuming that components of B^b are regular enough, then Schwarz's theorem applies, and the symmetry of the hessian is established. A proof by recurrence taking into account the first order derivation in Eq. (1.56) is performed in Ref. [Chesneau2018]. Using the same notation as Eq. (1.56) gives

$$\forall\, i,j,k\in\{x,y,z\}, \partial_i\partial_j B^b_k=\partial_j\partial_i B^b_k \tag{2.12}$$

It follows that from Eq. (2.12), one can determine only 7 elements of T^b instead of 15, while the rest of the values can be deduced. To better demonstrate this affirmation, two more detailed examples are undertaken. Recall that a priori $\nabla\beta_{1,\cdots,5}$ are to be computed. Using Eq. (2.12), the following equalities can be written

$$\begin{aligned}\nabla\beta_1(3)=&\frac{\partial^2 B^b_x}{\partial M^b_z\partial M^b_x}=\frac{\partial^2 B^b_x}{\partial M^b_x\partial M^b_z}=\frac{\partial}{\partial M^b_x}\left(\frac{\partial B^b_x}{\partial M^b_z}\right)=\frac{\partial}{\partial M^b_x}\left(\frac{\partial B^b_z}{\partial M^b_x}\right)=\frac{\partial^2 B^b_z}{\partial (M^b_x)^2}\\ =&\nabla\beta_3(1)\end{aligned} \tag{2.13}$$

$$\begin{aligned}\nabla\beta_3(3)=&\frac{\partial^2 B^b_z}{\partial M^b_z\partial M^b_x}=\frac{\partial^2 B^b_z}{\partial M^b_x\partial M^b_z}=\frac{\partial}{\partial M^b_x}\left(\frac{\partial B^b_z}{\partial M^b_z}\right)=\frac{\partial}{\partial M^b_x}\left(-\frac{\partial B^b_x}{\partial M^b_x}-\frac{\partial B^b_y}{\partial M^b_y}\right)\\ =&-\frac{\partial^2 B^b_x}{\partial (M^b_x)^2}-\frac{\partial^2 B^b_y}{\partial M^b_x\partial M^b_y}=-\nabla\beta_1(1)-\nabla\beta_2(2)\end{aligned} \tag{2.14}$$

In the same way as Eqs. (2.13)-(2.14), the rest of T^b elements are determined:

$$\nabla\beta_2(1)=\nabla\beta_1(2) \tag{2.15}$$
$$\nabla\beta_2(3)=\nabla\beta_3(2) \tag{2.16}$$
$$\nabla\beta_4(1)=\nabla\beta_2(2) \tag{2.17}$$
$$\nabla\beta_4(3)=\nabla\beta_5(2) \tag{2.18}$$
$$\nabla\beta_5(1)=\nabla\beta_3(2) \tag{2.19}$$
$$\nabla\beta_5(3)=-\nabla\beta_1(2)-\nabla\beta_4(2) \tag{2.20}$$

From Eqs. (2.13)-(2.20), it is demonstrated that only $\nabla\beta_1(1)$, $\nabla\beta_1(2)$, $\nabla\beta_2(2)$, $\nabla\beta_3(1)$, $\nabla\beta_3(2)$, $\nabla\beta_4(2)$ and $\nabla\beta_5(2)$ should be determined in order to conclude all the 27 elements of T^b, which highly simplifies the computation later on.

2.1.5 Determination of the magnetic field hessian

Since the sensor board does not directly provide the magnetic field hessian, the latter should be deduced from the measurements of the magnetometer array. In fact, T^b is going to be included in the state-space model of Eqs. (1.45)-(1.46) as an input. Thus, it is approximated in the same way as for the magnetic field gradient.
In Chapter 1, an array of three magnetometers is employed to perform the necessary approximations to determine the magnetic field gradient. Nevertheless, in order to access the second order spatial derivative of the magnetic field, at least five magnetometers are mandatory to compute the entire 7 elements of T^b. This condition on the number of the magnetometers can be determined under a finite differences scheme. By relying on Eq. (1.60) and approximations for partial derivatives that are either mixed or not, the hessian can be reconstructed. The finite differences scheme is not detailed nor employed in this section because of its several drawbacks, previously discussed in Section 1.3.2. Instead, the least-squares method is used to determine T^b, similarly to the derivation previously done in Section 1.3.2. In Fig. 2.1, a simplified diagram of the proposed magnetometer array is displayed, where two magnetometers measuring B_3^b and B_4^b are added to the array of Fig. 1.5.

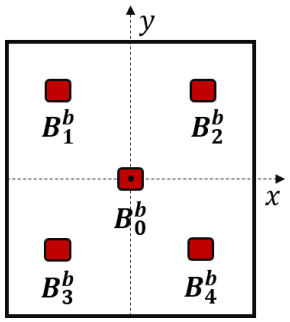

Figure 2.1: Diagram of the proposed magnetometer array for hessian determination

Similarly to magnetometers 1 and 2, the added magnetometers (3 and 4) are symmetric with respect to p_0, i.e. $p_{3x} = -p_{4x}$ and $p_{3y} = p_{4y}$. Also, $|p_{3x}| = |p_{3y}|$.
According to the second-order Taylor series expansion previously presented in Eq. (1.60), the magnetic field B_i^b measured by a magnetometer i can be expressed at any point p_i, with the following approximation

$$B_i^b(p_i) = B_0^b + \nabla B_0^b p_i + (T_0^b)^\top (p_i \odot p_i^\top) \tag{2.21}$$

where $\odot$ is the Hadamard product (also known as the element-wise product), which leads to

$$p_i \odot p_i^\top = \begin{bmatrix} p_{ix}^2 & p_{ix}p_{iy} & p_{ix}p_{iz} \\ p_{iy}p_{ix} & p_{iy}^2 & p_{iy}p_{iz} \\ p_{iz}p_{ix} & p_{iz}p_{iy} & p_{iz}^2 \end{bmatrix} \tag{2.22}$$

For computation reasons, this matrix is written in vector form as follows

$$p_i \odot p_i^\top = [p_{ix}^2 \;\; p_{ix}p_{iy} \;\; p_{ix}p_{iz} \;\; p_{iy}p_{ix} \;\; p_{iy}^2 \;\; p_{iy}p_{iz} \;\; p_{iz}p_{ix} \;\; p_{iz}p_{iy} \;\; p_{iz}^2]^\top \tag{2.23}$$

To ease the reading, T^b is represented in terms of the parameters $\gamma_{1,\dots,7}$ such that

$$T^b = \begin{bmatrix} \gamma_1 & \gamma_2 & \gamma_5 & \gamma_2 & \gamma_4 & \gamma_7 & \gamma_5 & \gamma_7 & -\gamma_1-\gamma_4 \\ \gamma_2 & \gamma_4 & \gamma_7 & \gamma_4 & \gamma_3 & \gamma_6 & \gamma_7 & \gamma_6 & -\gamma_2-\gamma_3 \\ \gamma_5 & \gamma_7 & -\gamma_1-\gamma_4 & \gamma_7 & \gamma_6 & -\gamma_2-\gamma_3 & -\gamma_1-\gamma_4 & -\gamma_2-\gamma_3 & -\gamma_5-\gamma_6 \end{bmatrix} \tag{2.24}$$

In the same manner as Eq. (1.62), the matrix form of Eq. (2.21) is

$$B_i^b = \begin{bmatrix} B_x^b \\ B_y^b \\ B_z^b \end{bmatrix} + \begin{bmatrix} \beta_1 & \beta_2 & \beta_3 \\ \beta_2 & \beta_4 & \beta_5 \\ \beta_3 & \beta_5 & -\beta_1 - \beta_4 \end{bmatrix} \begin{bmatrix} p_{ix} \\ p_{iy} \\ p_{iz} \end{bmatrix} + \frac{1}{2} T^b p_i \odot p_i^\top \tag{2.25}$$

By recalling Eq. (1.63), the magnetic field B_i^b measured by a magnetometer i can then be expressed with

$$B_i^b = [P_i \;\; P_{i,h}] X_{B,h} \tag{2.26}$$

where $X_{B,h} \in \mathbb{R}^{15\times 1}$ is the vector to be estimated, containing the magnetic field, its gradient and the hessian at the origin p_0 of the magnetometer array. The matrix $P_i \in \mathbb{R}^{3\times 8}$ is previously defined in Eq. (1.63). The matrix $P_{i,h} \in \mathbb{R}^{3\times 7}$ defines the magnetometer's i position coordinates related to T^b and is expressed as follows

$$P_{i,h} = [P1_{i,h} \;\; P2_{i,h}] \tag{2.27}$$

with

$$P1_{i,h} = \begin{bmatrix} {p_{ix}}^2 - {p_{iz}}^2 & p_{ix}p_{iy} + p_{iy}p_{ix} & 0 \\ 0 & p_{ix}^2 - p_{iz}^2 & p_{iy}^2 - p_{iz}^2 \\ -p_{ix}p_{iz} - p_{iz}p_{ix} & -p_{iy}p_{iz} - p_{iz}p_{iy} & -p_{iy}p_{iz} - p_{iz}p_{iy} \end{bmatrix} \tag{2.28}$$

and

$$P2_{i,h} = \begin{bmatrix} {p_{iy}}^2 - {p_{iz}}^2 & p_{ix}p_{iz} + p_{iz}p_{ix} & 0 & p_{iy}p_{iz} + p_{iz}p_{iy} \\ p_{ix}p_{iy} + p_{iy}p_{ix} & 0 & p_{iy}p_{iz} + p_{iz}p_{iy} & p_{ix}p_{iz} + p_{iz}p_{ix} \\ -p_{ix}p_{iz} - p_{iz}p_{ix} & p_{ix}^2 - p_{iz}^2 & p_{iy}^2 - p_{iz}^2 & p_{ix}p_{iy} + p_{iy}p_{ix} \end{bmatrix} \tag{2.29}$$

The magnetometer array of Fig. 2.1 generates measurements of five magnetometers such that $B_{Total,h} = [B_{Total} \;\; B_3^b \;\; B_4^b]^\top \in \mathbb{R}^{15\times 1}$, and its corresponding $P_{Total,h} = [P_{Total} \;\; P_3 \;\; P_4]^\top \in \mathbb{R}^{15\times 15}$. Recall that, the matrices $B_{Total} \in \mathbb{R}^{9\times 1}$ and $P_{Total} \in \mathbb{R}^{9\times 8}$ are previously defined in Eq. (1.64). It yields that Eq. (1.64) is re-written such that

$$B_{Total,h} = P_{Total,h} X_{B,h} \tag{2.30}$$

Note that the matrix $P_{Total,h}$ is square, which represents a special case for the least-squares problem. If $P_{Total,h}$ is non-singular, one can solve Eq. (2.30) with the standard linear algebra solution such that

$$X_{B,h} = P_{Total,h}^{-1} B_{Total,h} \tag{2.31}$$

Nevertheless, to keep a more general condition on the magnetometer array architecture, and the correlation between the different magnetometers' positions, the derivation elaborated in Eqs. (1.65)-(1.70) is applied. The vector $X_{B,h}$ containing the magnetic field hessian T^b is then determined as follows

$$X_{B,h} = X_{ls,h} = P_{Total,h}^{\dagger} B_{Total,h} \tag{2.32}$$

Recall that $P_{Total,h}^{\dagger}$ contains the coordinates of the positions of the different magnetometers in the sensor board, and therefore it is known. While the vector $B_{Total,h}$ represents the recorded measurements of the five magnetometers and is also known, enabling therefore the determination of $X_{B,h}$.

By approximating T^b through the magnetometer array, all inputs in Eq. (2.8) are now known. Thus, ∇B^b can be considered as a state and be added to the continuous-time model of Eqs. (1.41)-(1.44).

2.2 Proposed magnetic field gradient-based EKFs

In this section, an augmented MINAV model is proposed to better estimate the velocity of a moving body in an indoor environment, alongside with attitude and position. The novelty of the model resides on the adding of a specific equation Eq. (2.8) that is derived to describe efficiently the dynamics of the magnetic field gradient. Within this framework, a specific set configuration of two Extended Kalman Filters (EKFs) is proposed to not only focus on the estimation of velocity, attitude and position but also on the magnetic field and its gradient. Some simulations for a specific scenario are proposed to show the improvements that are brought to the velocity estimation when introducing the new magnetic field gradient equation. Comparisons with state-of-the-art models are also conducted to highlight the benefit of deriving an equation that takes into consideration higher-order spatial derivatives of the magnetic field.

2.2.1 Proposed continuous-time model

The proposed continuous-time model is obtained by augmenting the main model governed by Eqs. (1.41)-(1.44) with the equation describing the magnetic field dynamics Eq. (2.8). This gives

$$\frac{dq}{dt} = \frac{1}{2}\Omega^b q \tag{2.33}$$

$$\frac{dv^b}{dt} = -\omega^b \times v^b + a^b - Rg^n \tag{2.34}$$

$$\frac{dB^b}{dt} = -\omega^b \times B^b + \nabla B^b v^b \tag{2.35}$$

$$\frac{d\nabla B^b}{dt} = T^b v^b + \nabla B^b [\omega^b \times] - [\omega^b \times] \nabla B^b \tag{2.36}$$

$$\frac{dM^n}{dt} = R_b^n v^b \tag{2.37}$$

The new state vector is then $X(t) = [q \;\; v^b \;\; B^b \;\; \nabla B^b \;\; M^n]^\top \in \mathbb{R}^{18\times 1}$ and the measurement vector is $y(t) = [B^b \;\; \nabla B^b] \in \mathbb{R}^{8\times 1}$. The determination of T^b from the magnetometer array, using the least-squares method, enables considering it in the input vector such that $u(t) = [\omega^b \;\; a^b \;\; T^b]^\top \in \mathbb{R}^{13\times 1}$. It is recalled that in this model, T^b is represented as a function of 7 elements (instead of 27), which was explained earlier in Section 2.1.4.

2.2.2 Observability of the proposed model

Similarly to the steps undertaken from Eq. (1.47) to Eq. (1.51) in Chapter 1, a linearization is applied to both the state transition and the measurement functions of the proposed model, by computing their Jacobians with respect to the current estimate $\widehat{X}(t)$. The derived state matrix $F \in \mathbb{R}^{18\times 18}$ is then expressed such that

$$F = \begin{bmatrix} \frac{1}{2}\Omega^b & 0_{4\times 3} & 0_{4\times 3} & 0_{4\times 5} & 0_{4\times 3} \\ A_1 & -[\omega^b \times] & 0_{3\times 3} & 0_{3\times 5} & 0_{3\times 3} \\ 0_{3\times 4} & \nabla B^b & -[\omega^b \times] & A_4 & 0_{3\times 3} \\ 0_{5\times 4} & A_5 & 0_{5\times 3} & A_6 & 0_{5\times 3} \\ A_2 & A_3 & 0_{3\times 3} & 0_{3\times 5} & 0_{3\times 3} \end{bmatrix} \tag{2.38}$$

with $A_4 = \dfrac{\partial(\nabla B^b v^b)}{\partial \nabla B^b} \in \mathbb{R}^{3\times 5}$, $A_5 = \dfrac{\partial(T^b v^b)}{\partial v^b} \in \mathbb{R}^{5\times 3}$ and $A_6 = \dfrac{\partial(\nabla B^b [\omega^b \times] - [\omega^b \times] \nabla B^b)}{\partial \nabla B^b} \in \mathbb{R}^{5\times 5}$. The rest of the elements are already defined in Eq. (1.49).

In the same manner, the measurement matrix $H \in \mathbb{R}^{8\times 18}$ is defined with

$$H = \begin{bmatrix} 0_{8\times 7} & I_8 & 0_{8\times 3} \end{bmatrix} \tag{2.39}$$

where I_8 is the identity matrix in $\mathbb{R}^{8\times 8}$.
The observability matrix of the proposed model $\mathscr{O}' \in \mathbb{R}^{144\times 18}$ is then expressed as follows

$$\mathscr{O}' = \begin{bmatrix} 0_{3\times 4} & 0_{3\times 3} & I_3 & 0_{3\times 5} & 0_{3\times 3} \\ 0_{5\times 4} & 0_{5\times 3} & 0_{5\times 3} & I_5 & 0_{5\times 3} \\ 0_{3\times 4} & \nabla B^b & -[\omega^b\times] & A_4 & 0_{3\times 3} \\ 0_{5\times 4} & A_5 & 0_{5\times 3} & A_6 & 0_{5\times 3} \\ \nabla B^b A_1 & W_2 & [\omega^b\times]^2 & W_3 & 0_{3\times 3} \\ A_5 A_1 & W_4 & 0_{5\times 3} & A_6^2 & 0_{5\times 3} \\ \frac{1}{2}\nabla B^b A_1 \Omega^b + W_2 A_1 & W_5 & -[\omega^b\times]^3 & [\omega^b\times]^2 A_4 + W_3 A_6 & 0_{3\times 3} \\ \frac{1}{2} A_5 A_1 \Omega^b + W_4 A_1 & -W_4[\omega^b\times] + A_6^2 A_5 & 0_{5\times 3} & A_6^3 & 0_{5\times 3} \\ \vdots & \vdots & \vdots & \vdots & \vdots \end{bmatrix} \tag{2.40}$$

with $W_2 = -W_1 + A_4 A_5 \in \mathbb{R}^{3\times 3}$, $W_3 = -[\omega^b\times]A_4 + A_4 A_6 \in \mathbb{R}^{3\times 3}$, $W_4 = -A_5[\omega^b\times] + A_6 A_5 \in \mathbb{R}^{5\times 3}$ and $W_5 = -W_2[\omega^b\times] + [\omega^b\times]^2 \nabla B^b + W_3 A_5 \in \mathbb{R}^{3\times 3}$.
Same as the observability matrix derived in Chapter 1, it turns out that $\mathscr{O}'$ is 3 states deficient (last column is all zeros), which corresponds to M^n. This is expected as the added magnetic field gradient model Eq. (2.36) does not have a direct relationship with M^n. Thus, its observability does not undergo any changes.
By looking at the first and second columns of $\mathscr{O}'$, corresponding to the quaternion and velocity states, respectively, new terms linked to the proposed magnetic field gradient model appear (i.e. A_4, A_5 and A_6). More particularly, the presence of the term A_5 involving T^b in the second column of $\mathscr{O}'$, implies an evident effect on the velocity observability. In fact, if $rank(A_5) = 3$, velocity can be reconstructed, and three elements of the quaternion vector are observable (supposing A_1 is full-rank and relying on the term $A_5 A_1$ in the first column of $\mathscr{O}'$). The fourth quaternion element may be recovered from the next block lines. In this case, all states (except the position) are observable and $rank(\mathscr{O}') = 15$. The presence of A_5 provides an additional degree of freedom to the observability condition of the proposed model. So to guarantee $rank(\mathscr{O}') = 15$, it is sufficient to have one of these conditions satisfied

- ∇B^b is non-singular;
- $rank(A_5) = 3$.

It is believed that further investigations may reveal special cases where these two conditions can be rather complementary. For example, one can use ∇B^b to observe only 2 dimensions of the velocity while the third one is reconstructed using A_5.

2.2.3 Extended Kalman Filter

Choice of the observer

Putting under test any navigation model requires first choosing an adequate estimation algorithm to use with an efficient architecture. First, the implemented algorithm must be able to converge to the true values of observable states, even with the presence of measurement errors. Second, it

needs to have an appropriate method that quantifies the estimation uncertainty, in order to better comprehend the sources of errors generated during the process. Finally, as this algorithm will be used on a real embedded system (see Chapter 5), it needs to respect certain computational constraints, related to the microcontroller computing power, memory allocation, time-consumption, and so on. This implicates the importance of using an observer that meets these criteria, or at least some of them.
The first obvious intuition in this work, is the need for an estimator that can be applied on a non-linear system, as this is the kind of model that is dealt with in this thesis.
One of the first state estimators that appeared in the field of navigation and proved their efficiency in providing an accurate state estimate for a dynamical system with digital measurements is the Kalman filter Ref. [Kalman1960a, Grewal2020]. This filter is optimal for state estimation of linear systems. Nevertheless, systems are rarely linear in practice, especially in the field of navigation, where kinematics laws and measurements bring a lot of complexity.
An extension of the Kalman filter, the Extended Kalman Filter (EKF) Ref. [Daum2015], was then introduced to generalize the applicability of the Kalman filter for systems with non-linear transition and observation functions. It turns out that the EKF works well in many cases, which encouraged its use in the related literature Refs. [Vissière2007b, Chesneau2016, Barrau2015, Ligorio2013, Wagstaff2018]. In Ref. [Chesneau2018], it was shown that the EKF is an approximately appropriate choice that meets the different criteria mentioned above. For this reason, it was chosen as the main approach to achieve state estimation.

Extended Kalman Filter

Recall from Chapter 1, the continuous-time state-space model presented with Eqs. (1.45)-(1.46). In discrete-time, this system can be re-written as

$$X_k = f_d(X_{k-1}, u_k, \eta_k) \tag{2.41}$$
$$y_k = h_d(X_k, \nu_k) \tag{2.42}$$

where $f_d(.)$ and $h_d(.)$ are two non-linear functions that represent the state transition and the measurement (observation) models, respectively. At time step k, the state vector is X_k, the measurement vector is y_k, and u_k is the input. The process and measurement noises η_k and ν_k, are assumed to be zero-mean, white, Gaussian and uncorrelated. The EKF, applied to this non-linear model, defines an estimate $\widehat{X}_k$ at each step k through the following steps of initialization, prediction and update:

$$\textit{Initialization} \quad \begin{aligned} \widehat{X}_{0|0} &= E[X_0] \\ P_{0|0} &= E[(X_0 - \widehat{X}_0)(X_0 - \widehat{X}_0)^\top] \end{aligned} \tag{2.43}$$

where $\widehat{X}_{0|0}$, is the initial state estimate, $E[.]$ represents the expected value of a random variable X, and X_0 is the state vector at $k = 0$. The initial estimate of the covariance matrix (a measure of the estimated accuracy of the state estimate) is $P_{0|0} \in \mathbb{R}^{n\times n}$, with $n \in \mathbb{N}_{>0}$, representing the length of X.

$$\textit{Prediction} \quad \begin{aligned} \widehat{X}_{k|k-1} &= f_d(\widehat{X}_{k-1|k-1}, u_k) \\ P_{k|k-1} &= F_k P_{k-1|k-1} F_k^\top + Q_k \end{aligned} \tag{2.44}$$

such that $Q_k \in \mathbb{R}^{n\times n}$ is the process noise covariance matrix corresponding to η_k and $P_{k|k-1} \in \mathbb{R}^{n\times n}$ is the predicted covariance estimate.
Because of the non-linearity of the studied system, the covariance prediction equation of the linear version of Kalman cannot use the state transition function $f_d(.)$ directly. Instead, its Jacobian $F_k \in \mathbb{R}^{n\times n}$, in discrete-time, needs to be computed around the current estimate $\widehat{X}_{k-1|k-1}$ as follows,

$$F_k = \frac{\partial f_d}{\partial X}\Big|_{\widehat{X}_{k-1|k-1}, u_k} \tag{2.45}$$

Similarly to the state transition function, the discrete-time Jacobian of the measurement function, denoted $H_k \in \mathbb{R}^{m\times n}$ is determined through

$$H_k = \frac{\partial h_d}{\partial X}|_{\widehat{X}_{k|k-1}} \tag{2.46}$$

with $m \in \mathbb{N}_{>0}$, representing the length of y.
Then, the Kalman gain $K_k \in \mathbb{R}^{n\times m}$ is computed in order to conduct the correction step through updating both the state and the covariance estimates as follows

$$Update \begin{cases} S_k = H_k P_{k|k-1} H_k^\top + N_k \\ K_k = P_{k|k-1} H_k^\top S_k^{-1} \\ \widehat{X}_{k|k} = \widehat{X}_{k|k-1} + K_k(y_k - h_d(\widehat{X}_{k|k-1})) \\ P_{k|k} = (I_n - K_k H_k) P_{k|k-1} \end{cases} \tag{2.47}$$

where $N_k \in \mathbb{R}^{m\times m}$ is the measurement noise covariance matrix corresponding to v_k and I_n is the identity matrix in $\mathbb{R}^{n\times n}$.

Model discretization

The implementation of the EKF governed by Eqs.(2.43)-(2.47) requires transforming the proposed model of Eqs.(2.33)-(2.37) into the form of a discrete-time system as Eqs. (2.41)-(2.42).
There are many existing methods in the literature for the numerical treatment of differential equations Ref. [Grossmann2007], from which Euler's method is the most known. The method is very straightforward which makes it practical for theoretical demonstrations. However, it is numerically unstable and its accuracy is very dependent on the sample time. Furthermore, as it is based on a first-order approximation, the method may fail for complex problems and/or boundary conditions. The rich dynamics introduced in the proposed model especially when dealing with the magnetic field and its spatial derivatives suggest considering a higher-order discretization method for a better stability and higher accuracy. In this sense, the Runge-Kutta $4th$ order method (RK4) Ref. [Grossmann2007] is employed, as it represents a good balance between stability, the level of accuracy and the computational cost.
Applying the RK4 method on the proposed model implicates defining the state transition function $f_d(.)$ as follows

$$\begin{aligned} f_d &= RK4(f) \\ &= X_{k-1} + \frac{dT}{6}(k_1 + 2k_2 + 2k_3 + k_4) \end{aligned} \tag{2.48}$$

where

$$k_1 = f(t_{k-1}, X_{k-1}) \tag{2.49}$$

$$k_2 = f(t_{k-1} + \frac{dT}{2}, X_{k-1} + \frac{dT}{2}k_1) \tag{2.50}$$

$$k_3 = f(t_{k-1} + \frac{dT}{2}, X_{k-1} + \frac{dT}{2}k_2) \tag{2.51}$$

$$k_4 = f(t_{k-1} + dT, X_{k-1} + dTk_3) \tag{2.52}$$

with dT, the sample time, and t_{k-1} representing the time vector at step $k-1$.
As most of the commercialized IMUs and magnetometers provide nowadays discrete-time measurements, the continuous-time output model $y(t)$ is considered equivalent to the one in discrete-time $y(k)$. This means that no discretization step of the measurement function $h(.)$ is then necessary, which implicates $h_d(.) = h(.)$.

Remark 11 *The discretization of the state transition function $f(.)$ implies that its Jacobian undergoes the same transformation. This means that a discrete-time version of the state matrix F, defined in Eq. (2.38), is determined. This is done by simply computing the Jacobian of $f_d(.)$ with Eq. (2.45), and is not further detailed, for its representation complexity. The measurement matrix H is maintained, as no discretization is applied on the observation model.*

2.2.4 Architecture of the magnetic field gradient-based EKFs

The proposed model in Eqs. (2.33)-(2.37) introduces strong correlations between the different states, which makes detecting the sources of errors, induced by the estimation process, much more difficult. Also, by considering ∇B^b as a state, the proposed model endures more non-linearities (the term $\nabla B^b v^b$, for example). In this case, the computed Jacobian F_k of the state transition function $f_d(.)$ becomes more sensitive to errors, and can therefore affect the estimation accuracy. Besides to the linearization problem, the EKF can suffer from a divergence of its state estimates in the case where the noise covariance matrices Q and N are not properly specified. In fact, there is no general solution to accurately tune these covariance matrices and commonly, empirical methods based on a trial and error scheme are used. However, with a complex model as the proposed one, such manual procedure is long and difficult to conduct as it requires studying the interaction of the different noise parameters induced by the filter, which are highly non-linear and stochastic.

Remark 12 *The estimation of Kalman noise covariance matrices represents itself a common problem that generated a lot of research on the matter. A brief discussion about the existing state-of-the-art methods is conducted in Chapter 4. In this chapter of the thesis, the covariance matrices are chosen through a heuristic hand-tuning.*

In other words, each time a change is brought to the model representing the dynamics of ∇B^b, all of the parameters of the process noise covariance matrix Q need to be tuned all over again. This is due to the correlation of ∇B^b with the other states. As different model comparisons are conducted in the next section, an EKF architecture that uses the proposed model entirely, is not practical.
For all the reasons above, and in order to avoid augmenting the complexity of the proposed model while maintaining the contribution of Eq. (2.36), a specific EKF architecture is designed as illustrated in Fig. 2.2.

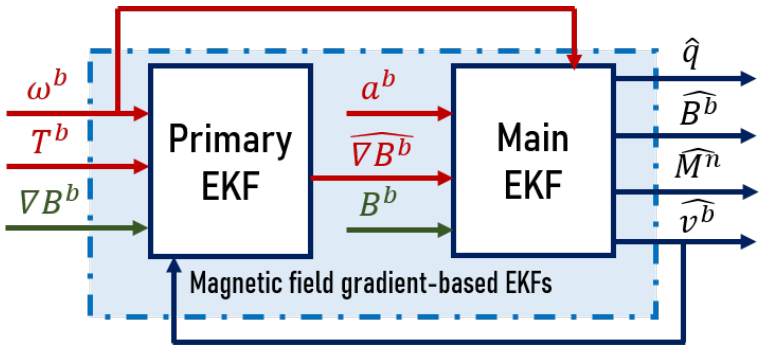

Figure 2.2: Proposed magnetic field gradient-based EKFs, in red are the inputs, in green are the measurements and in blue are the estimates

The proposed setting is based on two EKFs, in cascade. The primary EKF uses Eq. (2.36) describing the magnetic field gradient dynamics, while the main EKF acts on the rest of the model. At each time step, the estimated magnetic field gradient $\widehat{\nabla B^b}$ is determined in the primary EKF using the inputs ω^b, T^b and the determined ∇B^b from the magnetometer array measurements, through the least-squares scheme. Then, it is fed to the main EKF alongside with ω^b and a^b, as well as the measurements of B^b, to estimate the rest of the states. Note that the estimated velocity $\widehat{v^b}$ is itself injected in the primary EKF and considered as one of its inputs.

Remark 13 *It is brought to the attention of the reader, that measurements from only one* $3-axis$ *magnetometer are used to represent* B^b. *The choice of which magnetometer to use, is done taking into account the position of the latter, that needs to represent the center of inertia of the sensor board. In Fig. 2.1, it is considered that the origin with the position vector* p_0, *represents this center of inertia. The magnetic field at this origin, is measured by magnetometer* 0. *For this reason, the values of* B_0^b *are used in the measurement vector of the proposed model. It is underlined here, that the accelerometer and the gyroscope are also placed very close to this origin.*

2.3 Simulation results and comparisons

This section aims to illustrate the performance and accuracy of the designed EKFs-based observer. Some numerical simulations are carried out under MATLAB to estimate a rigid body's velocity, attitude, position, magnetic field and its gradient, based on theoretical inertial and magnetic measurements. The obtained estimates with the proposed approach are compared to the theoretical ground truth data, as well as the main EKF, that does not include the estimation of the magnetic field gradient. Furthermore, the proposed model describing the dynamics of ∇B^b, and defined with Eq. (2.36), is compared to the state-of-the-art ones, discussed in Section 1.3.3, and represented with Eq. (1.77) and Eq. (1.79).

2.3.1 Simulation scenario and details for implementation

First, the following angular rate scenario is simulated

$$\omega_x^b = -1.8\ sin(1.5t) \tag{2.53}$$

$$\omega_y^b = 0.5\ cos(0.9t) \tag{2.54}$$

$$\omega_z^b = 1.5\ sin(1.2t) \tag{2.55}$$

where t is the time vector varying until 200 s, under a time sample of 0.02 s. Then, the equation describing the dynamics of the quaternion Eq. (1.11) is solved to obtain the continuous-time motion in quaternion, which represents the attitude variation example. The obtained quaternion is used as a reference to compare it with the estimated one from the proposed EKFs-based observer. The rotation matrix in Eq. (1.3) is also computed using the reference quaternion. This is followed by the generation of a reference trajectory M^n of the moving body using both the rotation matrix and a random translation vector. This enables thereafter to compute the acceleration a^n in $\mathfrak{R}^n$ through a two-times derivation of M^n. Note that in order to express the accelerometer measurements in $\mathfrak{R}^b$, Eq. (1.13) is applied. After that, the measurements of magnetometer 0 of Fig. 2.1 are simulated by applying Eq. (1.28), where B_0^n values are chosen according to Eq. (1.24), and the magnetic field calculator in Ref. [NOAA2021] at the time of the algorithm's implementation such that

$$B_0^n = [0.22cos(2)\ \ 0\ \ 0.47sin(61)]^\top \tag{2.56}$$

To generate the rest of the magnetometer array measurements, small random variations are added to B_0^b, in a way that the corresponding magnetic field gradient values are coherent with what is measured in a magnetically disturbed environment (eigenvalues of ∇B^b are no less than 0.05 Gm^{-1}). The simulation scheme does not include constraints like the ones that may be encountered during real experiments, such as measurements synchronization problems, imprecise knowledge on the magnetometers' positions, etc. For this reason, a simple finite differences scheme is used to compute ∇B^b and T^b. That being said, a close to reality simulation needs to consider sensor imperfections. To do so, an additive random zero-mean white Gaussian noise is considered for

all measurements with a large standard deviation (see Table 2.1). It is underlined here, that the chosen values for the standard deviations are actually over-evaluated. This choice is conducted in order to better highlight the advantage of the proposed approach, that succeeds to converge to the true states values, despite the presence of high noises in the inputs and measurements. It is also reminded that, sensor biases are considered null, as bias modeling is not studied in this thesis. In practice, the different sensor biases can be pre-identified and subtracted from the measurements, before applying the proposed approach.

Table 2.1: Noise characteristics of sensor measurements

Sensor	Parameter	Standard deviation	Unit
$3-axis$ accelerometer	η_a^b	0.1	ms^{-2}
$3-axis$ gyroscope	η_ω^b	0.05	rads^{-1}
$3-axis$ magnetometers	η_B^b	0.1	G

During the EKFs implementation, the noise covariances, Q and N, are set according to the considered sensor noise levels. They are assumed constant, and do not vary during the simulation. Also, to optimize the computation time and memory allocation, the Jacobian matrices F_k and H_k are computed periodically (every 1000 samples), instead of each step. The accuracy on the two EKFs estimation is not impacted, while having a lighter algorithm. The choice of this periodic value is done taking into account the trajectory dynamics that are repetitive almost every 1000 samples. This simplification does not work necessarily in a real life experiment where the moving body's dynamics can change drastically every few seconds.
In the proposed simulation, the theoretical model and the two EKFs-based observer are initialized with different values. Notice that this choice allows to illustrate the convergence of these EKFs even though they are initialized with values that are far from the actual states of the model.

2.3.2 EKFs estimation results

Implementing the proposed EKFs using the model composed of Eqs. (2.33)-(2.37) enables the estimation of 5 states, that form the vector $\widehat{X}$: quaternion, velocity, position, magnetic field and its gradient. In the following, comparisons between $\widehat{X}$ and the theoretical ground truth states in the vector X are performed.

Quaternion estimation

Recall that the angular velocity data is corrupted with noise. It follows that the quaternion determined through the integration of Eq. (2.33) contains some errors. The latter is expected to be corrected with the main EKF, that converges in the end towards the ground truth quaternion. In Fig. 2.3, the estimation results for the four quaternion components are plotted. It is shown through the green line how simply integrating Eq. (2.33) induces errors that accumulate through time. The implementation of the main EKF however, succeeds to compensate this drift and provide an accurate quaternion estimation.
Despite initializing the main EKF with values that are far from the theoretical ones, the estimated quaternion $\widehat{q}$ components converge in less than 2 s, which illustrates the efficiency of the proposed two EKFs-based observer. However, even when initializing the integration of Eq. (2.33) with the same values as the theoretical quaternion, an inevitable accumulation of error (norm of the difference between theoretical and estimated quaternion elements) is generated, as represented in Fig. 2.4. The zoomed area illustrates that the initial error considered for the integration process

is zero, contrarily to the proposed EKFs approach that rather starts with a large error, and yet converges to a very small one (≈ 0.02).

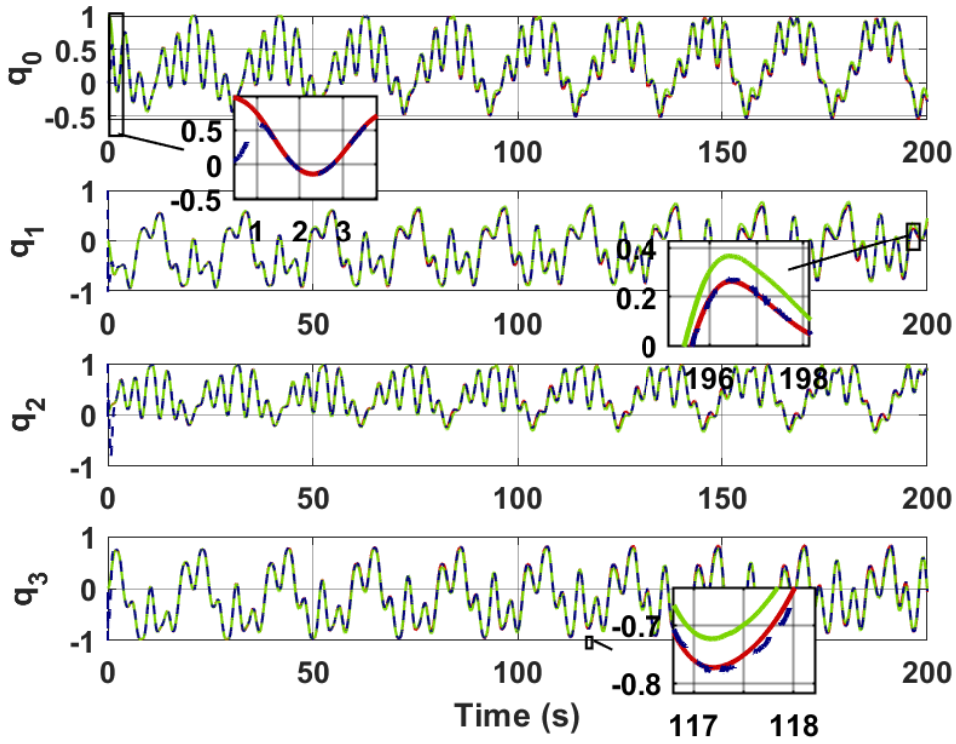

Figure 2.3: Estimation results of the quaternion. In red is the theoretical quaternion representing the ground truth, in green is the determined one through integrating Eq. (2.33), and in blue is the EKFs estimated one $\widehat{q}$

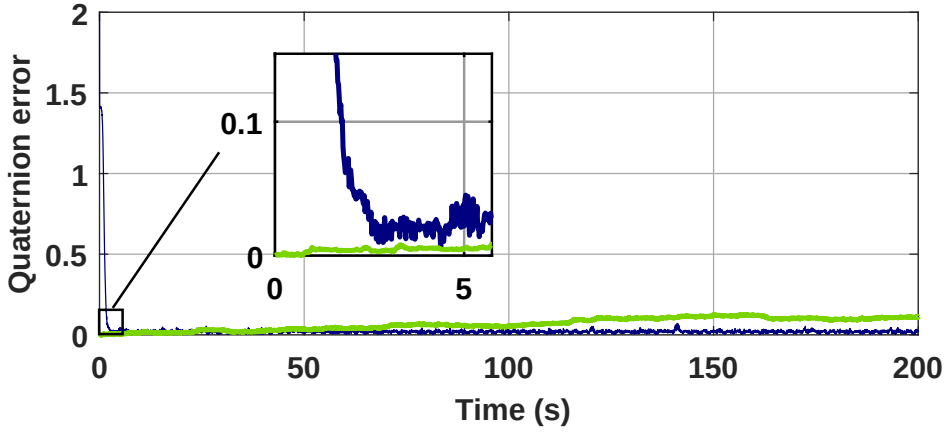

Figure 2.4: Quaternion error results. In blue from the proposed EKFs estimation, and in green from the integration of Eq. (2.33)

Velocity estimation

The main contribution of the proposed MINAV solution resides mainly in its velocity estimation capabilities. This means that in order to assess the performance of the proposed magnetic field gradient-based EKFs, the velocity estimate $\widehat{v^b}$ is investigated. In Fig. 2.5, the velocity estimation

results are compared to the ground truth ones for the considered the simulation time.
Similarly to the quaternion, it is observed that the convergence of the velocity estimation is reached after few seconds of the simulation time, despite the contained noise in the inputs and the different initialization of the ground truth and estimated states. This would not have been possible without using the magnetic field measurements alongside with the main equation Eq. (2.35) that links the velocity observability to the magnetic field gradient. Notice the presence of some small remaining errors along the trajectory. These errors are the consequence of the different uncertainties considered in the simulation scenario, i.e., the approximations taken into account to extract the spatial derivatives (∇B^b and T^b), the linearization process of the two EKFs, the hand-tuning of the noise covariance matrices, etc.

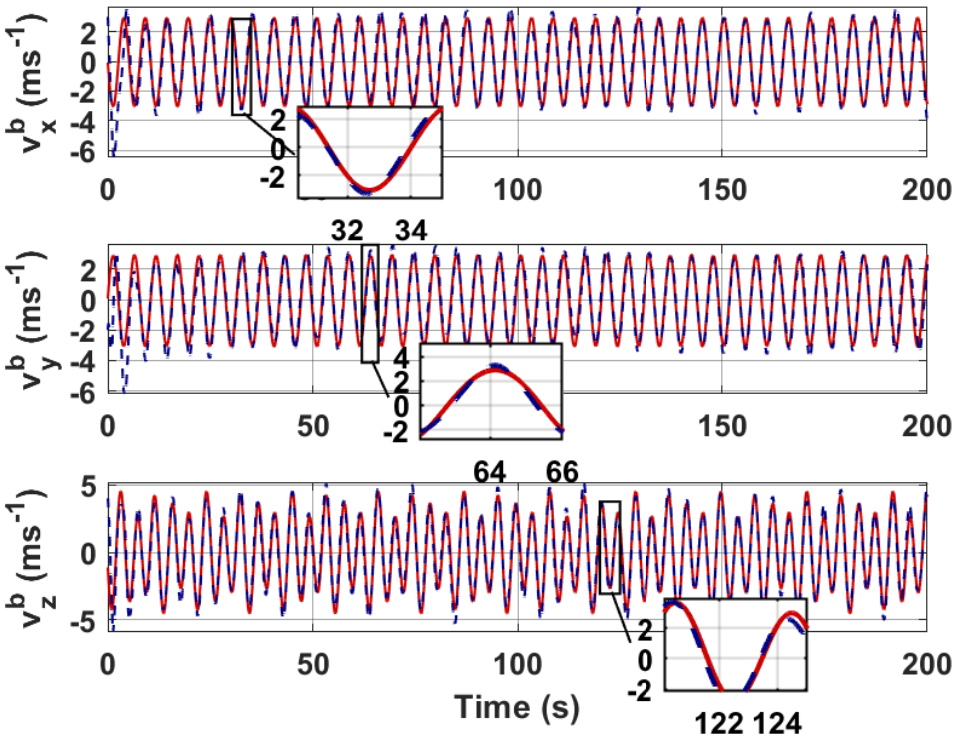

Figure 2.5: Estimation results of the velocity. In red is the theoretical velocity representing the ground truth, and in blue is the EKFs estimated one $\widehat{v^b}$

Magnetic field estimation

To evaluate the advantage of the proposed two EKFs on the magnetic field estimation, a noise with a large standard deviation is considered in the measurements of magnetometer 0. Note that the chosen value of 0.1 G is overestimated compared to the noise contained in commercial magnetometers, but yet taken into account in the purpose of demonstrating the contribution. In Fig. 2.6, it is shown that the estimated magnetic field $\widehat{B^b}$ converges to the theoretical one given the noisy measurements. The same behavior is expected for its corresponding gradient.

Magnetic field gradient estimation

Recall that noise is added to the five magnetometers of Fig. 2.1. The same noise standard deviation is considered for these magnetometers but noise amplitude vary differently from one magnetometer to another. This reflects a realistic behavior of sensors, that, even when having the same brand

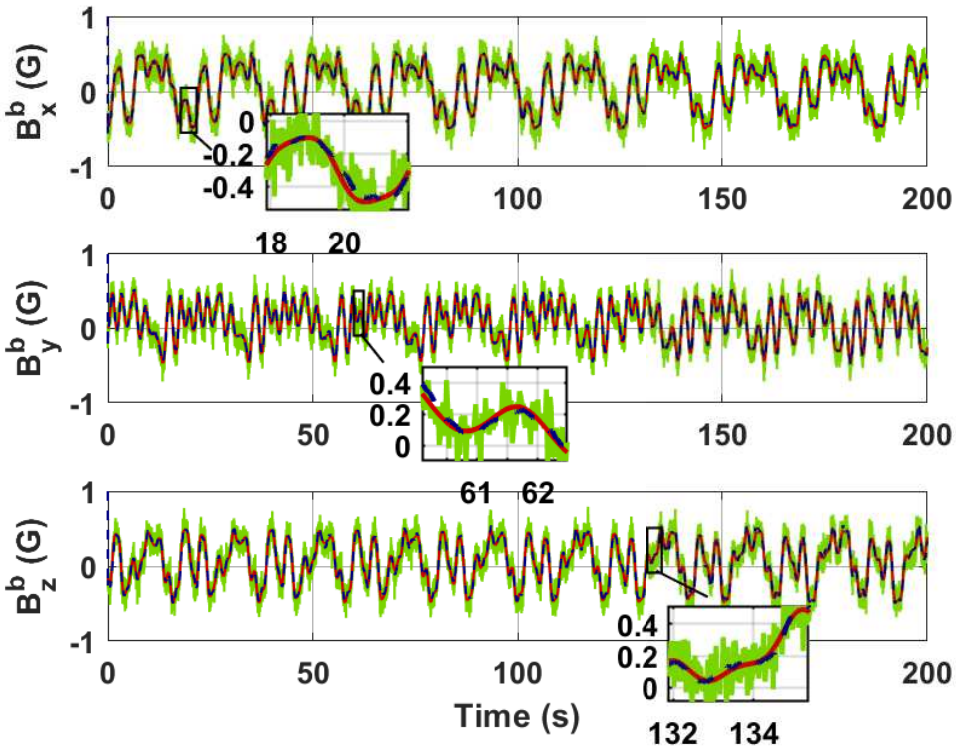

Figure 2.6: Estimation results of the magnetic field. In red is the theoretical magnetic field representing the ground truth, in green is the real one used in the measurement vector of the main EKF and in blue is the estimated one $\widehat{B^b}$

and model, are never completely identical, due to the manufacturing process.
The noise contained in the magnetometers impacts the corresponding gradient, which will most likely generate errors during the velocity estimation as mentioned in Chapter 1. This is where the proposed magnetic field gradient model described by Eq. (2.37) and implemented through the primary EKF comes in handy. Fig. (2.7) displays the estimation results for ∇B^b.
The primary EKF succeeds to reconstruct ∇B^b using the proposed dynamic model and the noisy measurements. The magnetic field gradient $\widehat{\nabla B^b}$ is very close to the theoretical one. This is very beneficial as employing $\widehat{\nabla B^b}$ enables a more accurate velocity estimation than the one relying on a noisy ∇B^b.

Position estimation

The proposed two EKFs scheme fails at some time steps to accurately estimate the velocity due to the different sources of errors previously mentioned. These velocity estimation errors, as small as they may be, lead to a noticeable position drift after integration. It is recalled that the position M^n is not observable. It follows that the main EKF cannot achieve a good estimation of the position M^n. In Fig. (2.8), it is shown how the position reconstruction suffers from a remarkable drift, compared to the theoretical trajectory.
In order to obtain an accurate position reconstruction, it is mandatory then to improve further the velocity estimation, as these two states are linked by a simple integration. However, in this chapter, the main objective is to illustrate the improvement that is brought to the velocity estimation in the case where ∇B^b is estimated rather than being used as an input. Further enhancements on the velocity estimation are proposed in the next chapters.

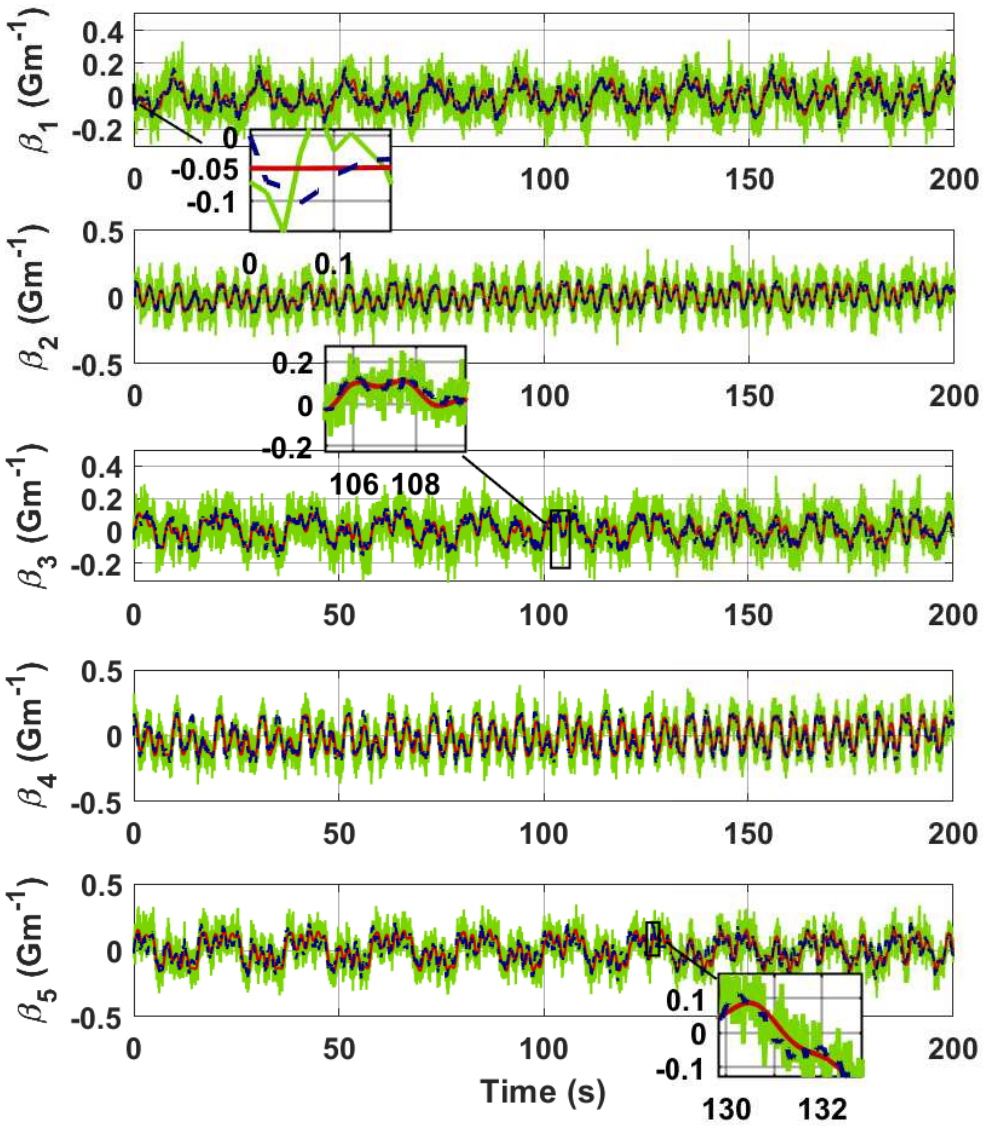

Figure 2.7: Estimation results of the magnetic field gradient. In red is the theoretical magnetic field gradient representing the ground truth, in green is the real one used in the measurement vector of the primary EKF and in blue is the estimated one $\widehat{\nabla B^b}$

2.3.3 Estimation with and without the primary EKF

The contribution of the proposed magnetic field gradient-based EKFs resides mainly on the implementation of the primary EKF that uses the equation describing the magnetic field gradient ∇B^b dynamics. If this primary EKF is not considered, then the magnetic field gradient is fed to the main EKF as an input, usually with noise, and the main model of Eqs.(1.41)-(1.44) is applied as illustrated in Fig. 2.9.

To evaluate the importance of the primary EKF, the velocity estimation accuracy is assessed with and without it. To do so, the Monte-Carlo simulation technique Ref. [Kroese2014] is applied to run the algorithm for 100 times. This is achieved to obtain more meaningful results as the different noises generation under MATLAB follows a random scheme so the estimation error values can change from one code execution to another. Using the Monte-Carlo technique, the mean of the velocity error with respect to the chosen number of simulations is computed.

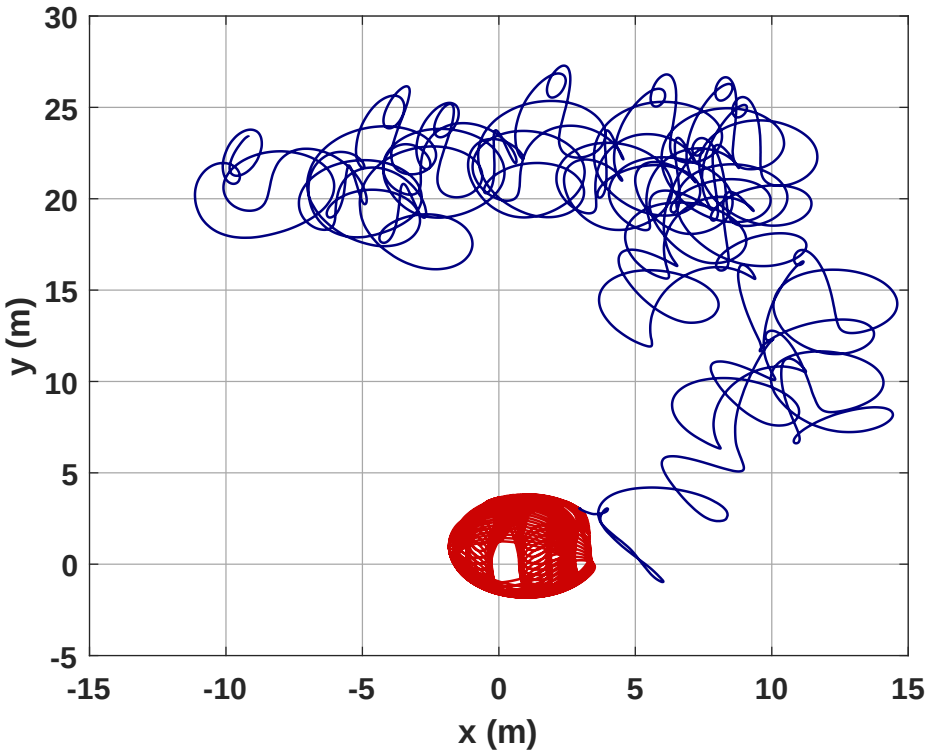

Figure 2.8: Estimation results of the position. In red is the theoretical trajectory representing the ground truth M^n and in blue is the estimated one $\widehat{M^n}$

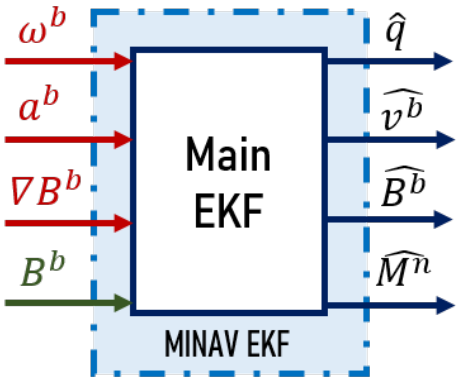

Figure 2.9: Main EKF architecure, without the primary EKF, in red are the inputs, in green are the measurements and in blue are the outputs

Table 2.2 displays the Mean Squared Error (MSE) and the Mean Absolute Error (MAE) Ref. [Li2001] between the velocity estimate $\widehat{v^b}$ and the theoretical one v^b for the two studied cases: with the implementation of the primary EKF alongside with the main EKF to estimate ∇B^b, and without it (the magnetic field gradient is used in the main EKF as a noisy input). It is observed that both the MSE and the MAE of the velocity significantly decrease with the addition of the primary EKF and the estimation of ∇B^b instead of using it directly as an input in the main EKF. This proves the contribution of deriving an equation that describes the dynamics of ∇B^b and considering it as a state in the proposed model.
The same conclusion is outlined in Fig. 2.10 by computing the Cumulative Distribution Function (CDF) Ref. [Forbes2011] in both cases.

Table 2.2: Velocity error mean results

Primary EKF	***Without***	***With***
MSE (ms^{-1})	0.48	0.29
MAE (ms^{-1})	0.57	0.43

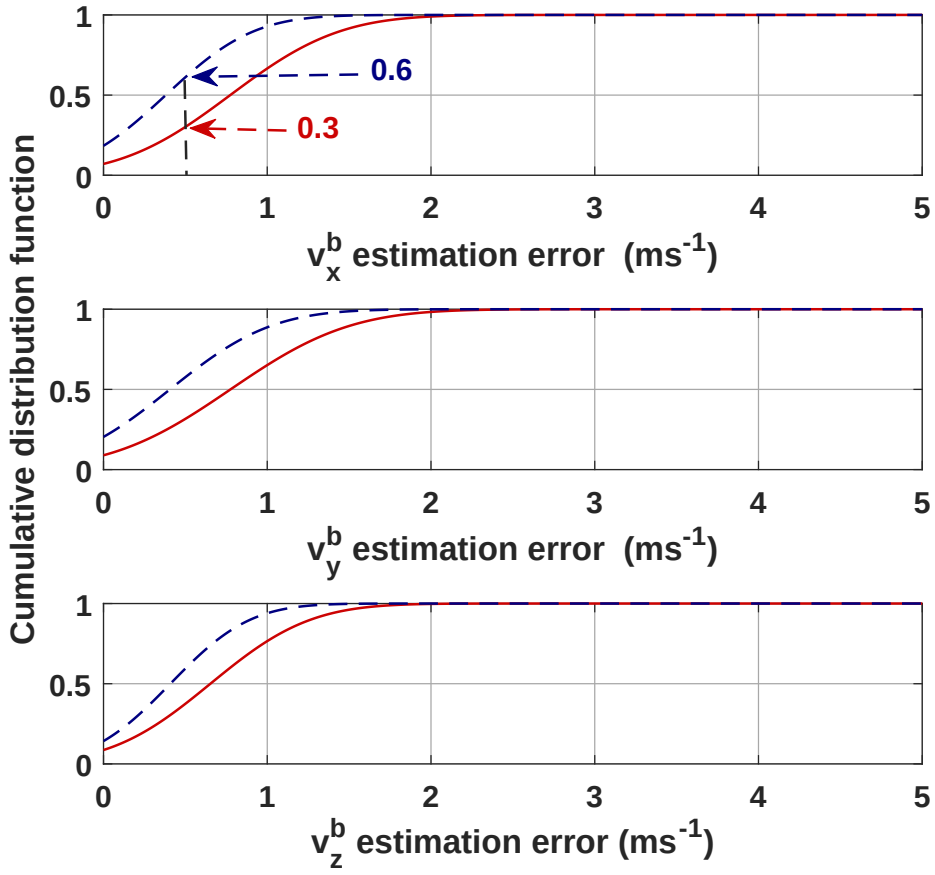

Figure 2.10: Cumulative distribution function of the velocity estimation error. In red without the primary filter, and in blue with it

Fig. 2.10 shows how the proposed approach provides better results, in terms of error between the theoretical velocity and the estimated one. For instance, without using the primary EKF, only 30% of v_x^b estimation error is inferior to 0.5 ms^{-1}, contrarily to 60% when applying the primary EKF. In the next section, the proposed magnetic field gradient model is compared to two other ones of the state-of-the-art and it provides the best accuracy.

2.3.4 Comparison with other magnetic field gradient models

Considering the magnetic field gradient as a state to be estimated by an observer has already been discussed in previous works Ref. [Vissière2007a, Vissière2007b] and was detailed in Section 1.3.3. Two models (1 and 2) are studied in this sense and are described by Eq. (1.77) and Eq. (1.79), re-

spectively. For comparison, the primary EKF is fed with the three models (the proposed one and the two of the state-of-the-art), one at a time. In order to avoid the influence of the velocity estimation error on the performance of the proposed model, the latter is considered known and the theoretical velocity representing the ground truth is used in Eq. (2.36). This means that for this comparison, the main EKF is omitted.
In order to implement models 1 (given by Eq. (1.77)) and 2 (given by Eq. (1.79)), two parameters ($\eta^b_{\nabla B}$ and $\tau^b_{\nabla B}$) need to be determined. This can be problematic as introducing more unknowns to the studied model demands a careful tuning process and implies the loss of generality of the solution. In other words, the chosen standard deviation of $\eta^b_{\nabla B}$ is highly dependent on the used magnetometer array characteristics and can even vary during the trajectory due to external factors (temperature, for example). Furthermore, choosing the time constant $\tau^b_{\nabla B}$ in the first order model Eq. (1.77) implies making an assumption on the behavior of the model's exponential decay, which may not properly describe the actual dynamics of ∇B^b, especially in a highly magnetically perturbed environment. For these two reasons, it is almost impossible to determine the optimal model for ∇B^b when considering such solutions.
However, to achieve this comparison, the value of the standard deviation of $\eta^b_{\nabla B}$ is chosen the same as the one for η^b_B. The time constant $\tau^b_{\nabla B}$ is fixed to 0.2 s after some hand-tuning.
In Fig. 2.11, the Power Spectral Density (PSD) of ∇B^b estimation error (the difference between $\widehat{\nabla B^b}$ and the theoretical one) is shown, when the primary EKF is used for the three studied models. This metric as it describes how the power of a signal is distributed over frequency, represents an

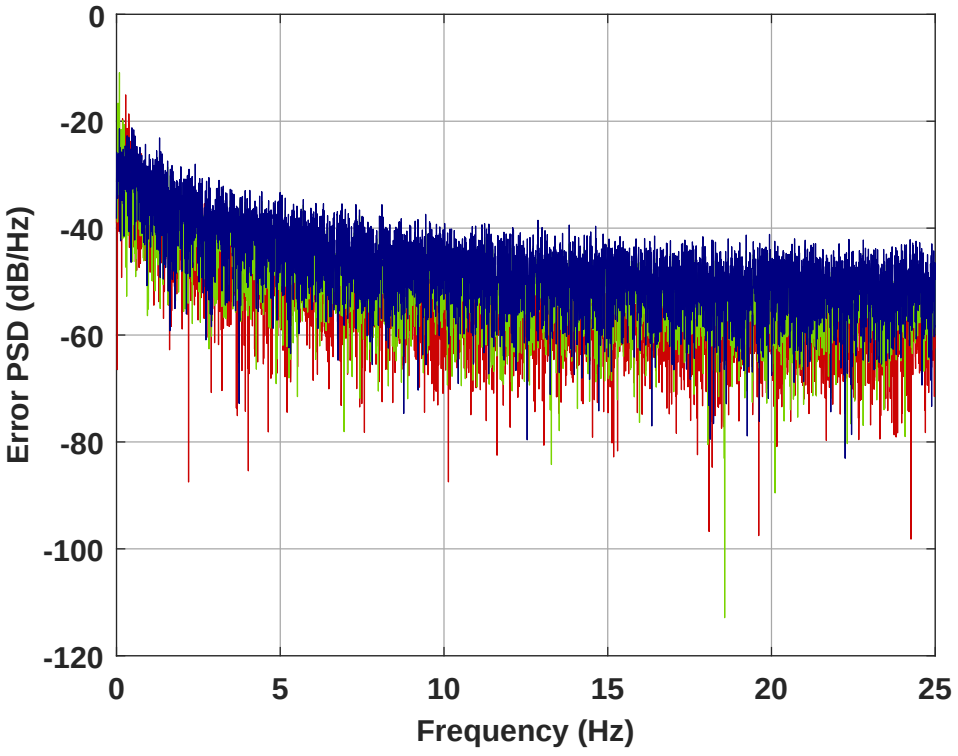

Figure 2.11: Power spectral density of the magnetic field gradient error. In red for the proposed model, in green for model 1 *and in blue for model* 2

interesting criterion to evaluate the noise compensation performed by the three compared models. Fig. 2.11 shows that in case ∇B^b is estimated using the proposed model, the noise power of its elements, is lower than the ones obtained using the other two models. The first-order model (model 1) is slightly better than the only noise-based one (model 2), which is expected as the latter assumes a more dynamic behavior of the magnetic field gradient. It is reminded though, that these

results are highly influenced by the models' parameters tuning as well as the simulation scheme, that does not reflect precisely the actual magnetic field dynamics encountered in a magnetically disturbed environment. In other words, no simulation scenario can replicate the perturbations that are generated by office equipment, building structure, electrical currents, etc. So, the used magnetic field measurements lack such physical complexity. For this reason, model 1 and 2, despite their simplicity, provide acceptable results. Nevertheless, in a real life experiment, these models are not able to recover the richness of ∇B^b, which makes the proposed model the best solution in this case. Evaluations with experimental data and real sensors are conducted in the next chapters. The same results can be presented in terms of the magnetic field gradient error's CDF, as illustrated in Fig. 2.12. By looking at the CDF of the estimation error of ∇B^b for the three models, it is evident that the best performance belongs to the proposed model (i.e. the proposed model has bigger percentages of low errors compared to the other models). This is expected as the latter preserves maximum information on the magnetic field dynamics by introducing higher-order spatial derivatives and conserving their relationship with the velocity and angular rate.

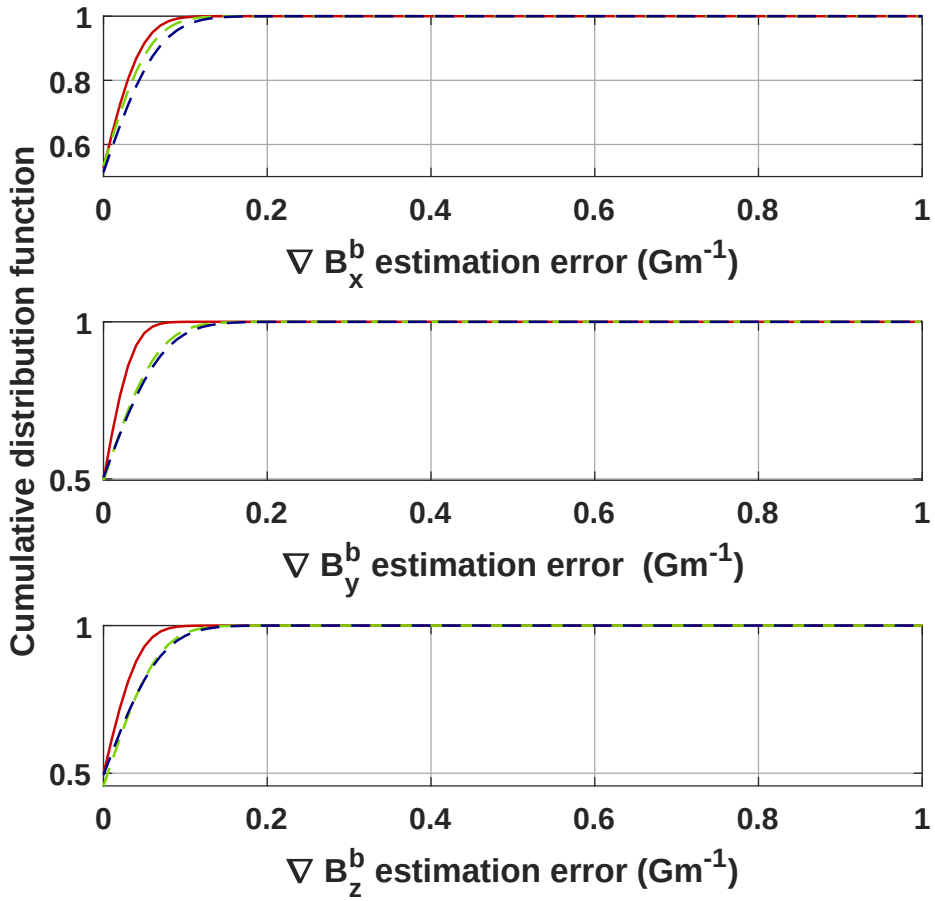

Figure 2.12: Cumulative distribution function of the magnetic field gradient estimation error. In red for the proposed model, in green for model 1 *and in blue for model* 2

2.4 Conclusion

Magnetic field gradient proposed model As elaborated in Chapter 1, there is a clear advantage in modeling the magnetic field gradient and including it in the state vector of the main model. Higher-order spatial derivatives of the magnetic field are explored, then a new equation is proposed that efficiently describes the magnetic field gradient dynamics and guarantees its relationship to the magnetic field hessian, the velocity and the angular rate.
The magnetic field hessian The magnetic field hessian is a tensor that represents an input to the proposed model, and needs to be determined using the magnetometer array. At least 5 magnetometers are required to recover 7 tensor elements, either with a finite differences scheme or the least-squares method. These 7 elements enable the computation of the entire magnetic field hessian thanks to its properties.
Special architecture of EKFs To avoid complexity and to facilitate the implementation of the proposed model, a special architecture of two EKFs, in cascade, is proposed. In fact, the EKF introduces few limitations related to its noise covariances tuning, its linearization process, etc. By handling the proposed magnetic field gradient model separately, in a primary EKF, it is possible to examine its behavior under different conditions, without having to worry about the different noise parameters of the rest of the model, used by the main EKF.
Limitations of state-of-the-art models Two models of related literature are compared to the proposed magnetic field gradient model. A first observation states that these two models do not reflect the actual dynamics of the magnetic field, especially in a highly disturbed environment. It is also highlighted that these models introduce two more unknown parameters that require a proper tuning in order for them to provide a reasonable performance. A condition that is not easily satisfied, especially when dealing with a real experimental setup under various uncertainties.
The simulation results are encouraging The proposed magnetic field gradient-based EKFs are evaluated under a simulation framework. It it shown that the proposed model outperforms the case where the magnetic field gradient is used as an input, under some noises. The proposed model appears also to outperform the related literature ones, in the case of the chosen parameters' values. In the next chapter, a closer to reality setup is adopted (closer to a real experimental scenario, with complex dynamics and many uncertainties), to further explore the capabilities of the proposed approach as well as its possible weaknesses.

3

Single Magnetic Field Gradient-Based Extended Kalman Filter

This chapter treats the special case of trajectory reconstruction under a foot-mounted sensor framework, that represents one of the most common setups used in pedestrian inertial navigation. An introduction of such scheme is presented in Section 3.1, where a method usually employed under this particular sensor placement, called the Zero-Velocity Update Technique (ZUPT), is introduced. This technique is used to complement the previously proposed magnetic field gradient-based EKFs in a new proposed EKF setting presented in Section 3.2. To assess the performance of the proposed approach, a simulated trajectory that is based on a real human walk pattern is used in Section 3.3. The obtained results demonstrate the interest in using the proposed solution when dealing with a foot-mounted application, and especially when targeting position estimation.

Contents

3.1 Introduction

One of the advantages of the magnetic field gradient-based EKFs approach proposed in the previous chapter is its generality and adaptability to any kind of application. Whether it is a pedestrian, a moving vehicle or a robot, the proposed solution can be applied with no imposed restrictions, as long as it is used under a magnetically disturbed environment. In the case of a specific application, the proposed approach can be enhanced, taken into account the characteristics of the studied conditions. In other words, knowing the nature of the targeted application opens doors for complementary methods that can be added to the proposed magnetic field gradient-based EKFs, in order to improve the estimation accuracy.

3.1.1 Pedestrian Dead Reckoning

The first application that comes in mind when dealing with indoor navigation, is the one related to the pedestrian trajectory reconstruction. In the last decades, there has been a growing interest in what is referred to as Pedestrian Dead Reckoning (PDR) Refs. [Hou2020,Wu2019b,Jiménez2009]. Such process resides on the determination of the subject's current position by using the previously known one, and advancing that position over time through either a step detection, a step length estimation and a knowledge on the walking direction Refs. [Wang2019a, Yao2020, Susi2013] or through a generation of velocity estimates Refs. [Lo2011, Tong2019, Ju2018], which is more in the scope of this thesis. The PDR approach is typically (but not necessarily, see for example Ref. [Renaudin2012b]) applied when the sensor board is worn on the foot of the subject under study, and it relies basically on analyzing the foot movement and its corresponding characteristics. In fact, the walking activity of a human (at any speed) can be defined as a cyclic pattern of body movements that propagates a subject's position. Therefore, all walking cycles can be considered nearly similar. Thus, investigating the walking process can be summarized with the study of one walking cycle known as the *gait cycle* or the *stride*. Fig. 3.1 is a simplistic illustration of a pedestrian gait cycle. The gait cycle is composed of two separate phases: the first is the *stance*

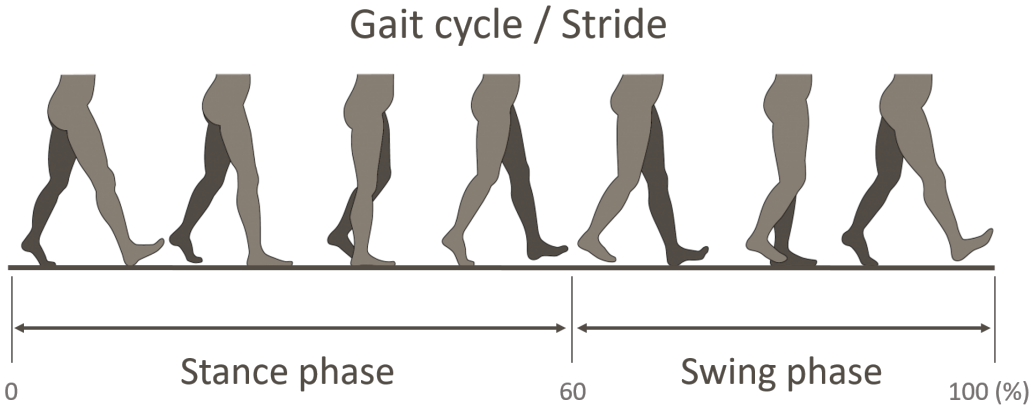

Figure 3.1: Illustration of a gait cycle of a pedestrian walk for the right leg (clear grey color)

phase, representing the period of time during which the foot is in contact with the ground (the right leg in a clear grey color), usually forming around 60% of the stride's duration time. The second is the *swing phase*, representing the entire period during which the foot is in the air for limb advancement, and it takes about 40% of the gait cycle time. Detecting these two phases plays a crucial role in PDR as they provide information not only on step length but also on velocity. While step length detection represents a wide research area with promising perspectives, this thesis is rather focused on velocity estimation. In fact, as the proposed magnetic field gradient-based EKFs already provide a velocity estimate, it can be of benefit to introduce a complementary method that

can enhance the velocity estimation accuracy in the context of foot-mounted inertial navigation.

3.1.2 About the Zero-velocity Update Technique

During a gait cycle, there are specific times when the velocity and acceleration of the sensor board mounted on a subject's foot are equal to (or near) zero. These periods occur each time the foot contacts the ground during the stance phase. This information can represent a sort of external velocity measurement whenever such a situation is detected. For the times when the foot is off the ground (swing phase), various Inertial Navigation System (INS) algorithms can be applied Ref. [Hasan2009], which leaves a very limited time for the trajectory to start drifting, before it is again corrected with the zero velocity observation. This methodology is referred to as the Zero-velocity Update Technique (ZUPT) Refs. [Wahlström2020, Fourati2015, Nilsson2010], which has enabled the growth of a lot of research in the inertial navigation field for several decades now. There exist many ways of employing the ZUPT in a foot-mounted INS framework, from which conventional PDR methods are the most obvious. For instance, the relative position of a walking subject can be determined through a simple integration of the velocity. The latter itself is deduced from the sensor board measurements, attached to the foot (by integrating the accelerometer and gyroscope data) and is periodically set to zero on each detected stance phase during the subject's trajectory. Yet, as repeatedly discussed in this thesis, relying solely on the integration of sensor measurements is not efficient, even after including the ZUPT, as the latter cannot correct attitude errors generated by integrating the angular rate (see Section 3.3.4). For this reason, the use of an estimation filter remains necessary and in such case, the ZUPT is used as some sort of a velocity measurement update to the filter, as largely investigated in the related literature Refs. [Zhao2021, Nilsson2014a, Benzerrouk2014, Jiménez2010].
This suggests that in the context of this thesis, the proposed magnetic field gradient-based EKFs can be aided by the ZUPT solution in the case of foot-mounted inertial navigation in the purpose of improving not only the velocity, but also the position estimation results.

3.1.3 Zero-velocity detector

Before performing a zero-velocity update, one needs to accurately identify the time epochs when the sensor board strapped to the subject's foot is stationary. This task is handled by a measurements-based statistical algorithm called a zero-velocity detector. The objective of a zero-velocity detector is to decide whether, during a time epoch that consists of $W_s \in \mathbb{N}$ observations or number of sensor readings (i.e. window size) between the samples m and $m+W_s-1$, the sensor board strapped to the subject's foot is moving or stationary, given the measurements a^b and ω^b. At each sample, this detector, denoted d, can have one of the two values: $d=1$, which corresponds to the stance phase or $d=0$, which represents the swing phase. The most common ZUPT detectors are based on statistical features, from which signals energy (e.g. angular velocity and acceleration) and their variances are employed, to distinguish the zero velocity instants. The zero-velocity detection also requires the tuning of a certain threshold with which the test statistics are compared. Mathematically, this detection process can be seen as a binary hypothesis testing problem, where the detector indicates that the sensor board is stationary (i.e. $d=1$) if

$$T_s(a^b, \omega^b) \leq \delta_d \tag{3.1}$$

where $T_s(a^b, \omega^b)$ stands for the test statistics of the detector and δ_d is the the detection threshold. The test statistics can have multiple forms depending on the chosen detector type. In related works, different detectors have been evaluated Ref. [Skog2010b] from the ones depending only on accelerometer data (such as Acceleration Moving Variance Detector (MV) and Acceleration Magnitude Detector (MAG)), to those that are angular rate-based (Angular Rate Energy Detector (ARE)), or even those that rely on pressure measurements Ref. [Ma2018]. In this thesis, the

Stance Hypothesis Optimal Detector (SHOE) Ref. [Skog2010a] is chosen, an efficient detector that is derived within a General Likelihood Ratio Test (GLRT) framework. It represents a combination between acceleration and angular rate-based detectors, and has proven to outperform other detectors in the literature for its robustness to changes in gait speed as well as its high positional accuracy. Concretely, SHOE computes $T_s(a^b, \omega^b)$ in the following way

$$T_s(a^b, \omega^b) = \frac{1}{W_s} \sum_{k=m}^{m+W_s-1} \left(\frac{1}{\sigma_a^2} ||a_k^b - g^n \frac{\bar{a}_m^b}{||\bar{a}_m^b||}||^2 + \frac{1}{\sigma_\omega^2} ||\omega_k^b||^2 \right) \tag{3.2}$$

where σ_a^2 and σ_ω^2 are the variances of the acceleration and angular rate measurements, respectively. The mean over W_s samples is denoted $\bar{a}_m^b$ such that

$$\bar{a}_m^b = \frac{1}{W_s} \sum_{k=m}^{m+W_s-1} a_k^b \tag{3.3}$$

In order for ZUPT to work efficiently, the detection threshold δ_d must be carefully tuned to account for the different human walking paces that may occur during one trajectory. Indeed, even if the use of ZUPT has been successful in PDR related research over the years, its implementation remains nontrivial due to the necessity to adapt to the large variations of human dynamics. Such concern encouraged the rising of several adaptive threshold-based ZUPT approaches to meet this particular challenge Refs. [Cho2019, Wang2019c], from which a large quantity are based on Artificial Intelligence (AI) techniques. This is discussed further in Part II of this thesis. For the time being, as the used dataset in the next sections is synthetic and most of its characteristics are already known, choosing the value of the ZUPT detection threshold is not of a high complexity. Therefore, no sophisticated method is employed, and a heuristic hand-tuning of δ_d is rather achieved.

3.2 Proposed single EKF setting

In this section, a new estimation solution that is used to solve the foot-mounted inertial navigation problem is proposed. First, the magnetic field gradient-based EKFs introduced earlier in Chapter 2 are modified to a more compact architecture which advantages are discussed. Then, this condensed version of the magnetic field gradient-based EKFs is enhanced, by incorporating the ZUPT in its estimation process, in the purpose of not only bounding the errors of the velocity estimate, but also reducing the propagation of the position's drift.

3.2.1 Proposed magnetic field gradient-based EKF

In the previous chapter, it was elaborated that an EKF architecture which uses the entire model governed by Eqs. (2.33)-(2.37) is complex to conceive, especially when performing different model comparisons. For this reason, a specific configuration of two EKFs (primary and main), in cascade, was proposed and illustrated with Fig. 2.2. While the former architecture is of high benefit especially when dealing with noise covariance matrices tuning (as explained in Section 2.2.4), a compact design may also have its advantages. One should take into consideration the realistic aspect of any proposed solution. For instance, if a certain model contains coupled and correlated states, such connection should not be interrupted even if it's computationally more convenient to do so. Therefore, it is rather rigorous to design a single EKF that uses all equations of the proposed model to conduct the estimation process.
After gaining more proficiency and a better understanding on how to efficiently hand-tune the noise covariance matrices of the EKF, it is proposed to simplify the estimation architecture in

Fig. 2.2. This is done by designing a single EKF that uses the model of Eqs. (2.33)-(2.37) altogether. The proposed magnetic field gradient-based EKF is presented in Fig. 3.2.

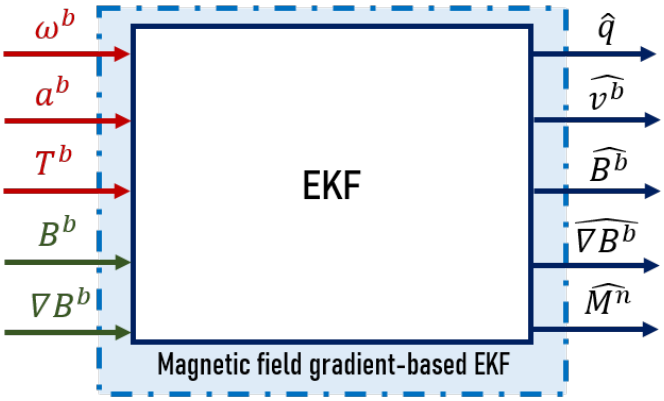

Figure 3.2: Proposed magnetic field gradient-based EKF, in red are the inputs, in green are the measurements, and in blue are the estimates

One important criteria that must be verified when proceeding with such modification of the previously proposed solution is the computation time. As earlier discussed in Section 2.2.3, one of the constraints that need to be kept in mind for any proposed algorithm in this thesis, is its capability to be integrated in an embedded system, and eventually adapted to a real-time application. Consequently, conceiving an algorithm that is less energy consuming is highly preferred.
Within this framework, it is highlighted that there's one main difference between the two studied architectures, that has the biggest effect on the time consumption. This dissimilarity resides on the computational process of the Jacobians corresponding to the state transition and measurement functions. More particularly, in the two EKFs setting, two state matrices are computed: one that is related to the primary EKF and one that corresponds to the main EKF. While for the single EKF configuration, only one state matrix is derived, yet with larger dimensions. This makes the assessment of the time consumption of both settings rather difficult theoretically which calls for a simulation-based validation.
To obtain an estimation of the computation time of the new proposed magnetic field gradient-based EKF, compared to the previous architecture (of Fig. 2.2), the Monte-Carlo simulation conducted in Section 2.3.3 is reproduced, where the two proposed configurations are tested. The algorithms are run under the same conditions, on a Central Processing Unit (CPU) Intel Core *i*7@1.9 Gigahertz (GHz). Under Matlab, the *tic toc* commands are placed right before the algorithm starts and after it ends, respectively. Simulations are run for 100 times, where the computation time is saved for each execution of the entire algorithm (estimation of a trajectory of 200 *s*). In Fig. 3.3, a histogram of the *toc* command output for both the examined architectures (single EKF and two EKFs) is displayed. It is observed in Fig. 3.3 that the average computation time of the proposed single EKF architecture (represented with the red bins), is slightly lower than the one of the two EKFs (illustrated with the blue bins). For example, the histogram bin corresponding to the computation time in between 8.1 *s* and 8.2 *s* has a percentage of 39% for the single EKF architecture versus only 2% for the two EKFs setting. The latter's maximum percentage of runs takes around 8.4 *s* and 8.5 *s* of computation time, which represents about 0.3 *s* of difference compared to the proposed single EKF configuration. What needs to be highlighted in this case, is that even though the proposed new configuration is more complex in terms of Jacobians computation, it is rather faster than the divided version of the EKF (two EKFs), which is advantageous when dealing with an embedded system. As long as the noise covariance matrices parameters are properly tuned, having a single EKF solution is then much more efficient.

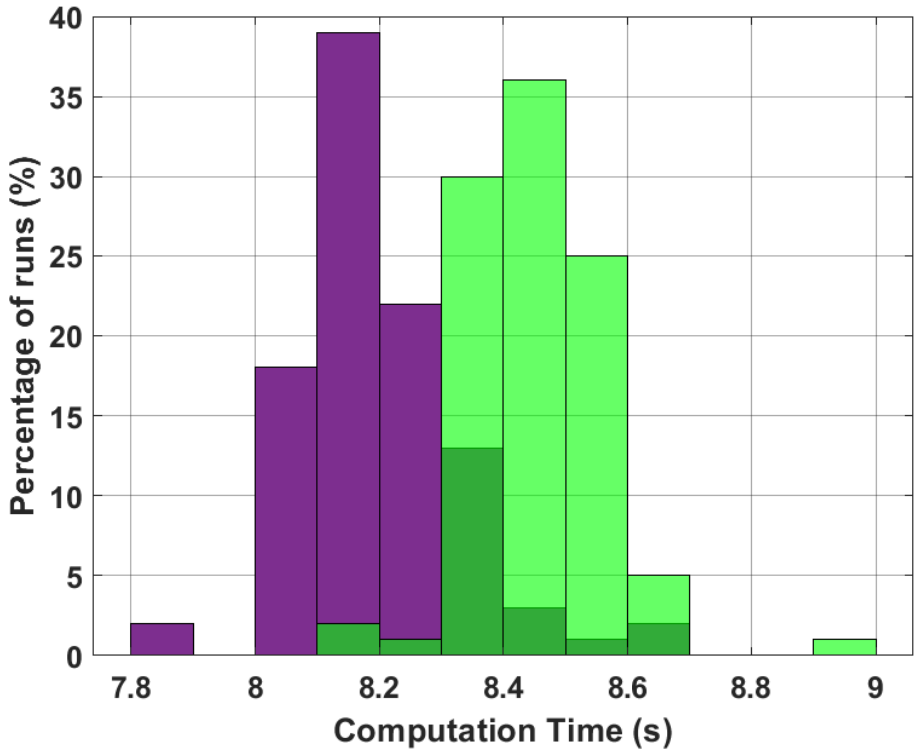

Figure 3.3: Toc outputs for 100 *runs. In light green for the two EKFs-based architecture, and in purple for the proposed single EKF. The dark green color is the superposition of both results*

3.2.2 ZUPT-aided magnetic field gradient-based EKF

In the context of foot-mounted inertial navigation, the ZUPT technique enables not only the correction of velocity estimation errors, but also those of position. As a matter of fact, the unobservability of the position in the proposed magnetic field gradient-based EKF, makes its reconstruction an unstraightforward task. As noticed in Section 2.3, the proposed scheme fails at some time steps to accurately estimate the velocity, which is totally expected in light of the different uncertainties taken into account during the simulation scenario. These velocity estimation errors, as small as they may be, lead to a noticeable position drift after integration of Eq. (2.37). The proposed EKF is unable to recover the true trajectory as no source of correction is available for the position estimate $\widehat{M^n}$. Such limitation encourages combining the EKF with a convenient solution to compensate the accumulating drift. Accordingly, a new algorithm is proposed that fuses the ZUPT with the proposed magnetic field gradient-based EKF. The general scheme of estimation is presented in Fig. 3.4. The ZUPT-aided magnetic field gradient-based EKF works in three steps: first, the EKF uses the sensor board measurements, and the dynamic model of Eqs. (2.33)-(2.37), to provide an estimate of its state vector $\widehat{X}$. Second, the zero-velocity detector d (represented with the red block) declares whether the sensor board under study is stationary at that time step (i.e. $d = 1$) or not (i.e. $d = 0$). This is by computing the test statistics T_s using the angular velocity ω^b and the acceleration a^b measurements. If the detector d has declared the stationary case, the EKF velocity estimate $\widehat{v^b}$ is expected to give a zero-velocity value. However, due to the various potential sources of errors, it most likely will not. In this case, the ZUPT (illustrated with the green block) "manually" resets the velocity estimate $\widehat{v^b}$ to zero (i.e. $\widehat{v^b} = 0_{3\times1}$). Consequently, by continuously updating the velocity estimate in the EKF loop using the ZUPT, the accumulated estimation errors are efficiently bounded. A better position estimation is then obtained compared to the case of using only the magnetic field gradient-based EKF.

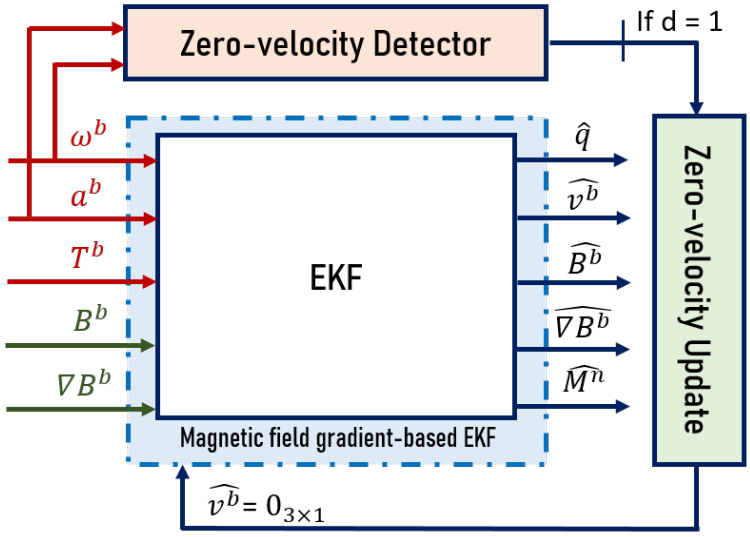

Figure 3.4: ZUPT-aided magnetic field gradient-based EKF, in red are the inputs, in green are the measurements and in blue are the estimates

3.3 Estimation results in a foot-mounted scenario

In this section, the performance of the proposed ZUPT-aided magnetic field gradient-based EKF is assessed under a realistic simulation of a pedestrian trajectory with the sensor board attached to their foot. Before that, a number of comparisons is conducted between the different discussed solutions, where it is shown that the proposed approach provides the best results in terms of the states' estimation accuracy.

3.3.1 About the foot-mounted IMU dataset

One of the main limitations of the simulations undertaken in Chapter. 2 is the fact that they do not represent a reality-like trajectory scenario (recall the generation of random sinusoidal signals for the angular rate measurements in Section 2.3.1). While such methodology may represent a good starting point for evaluations, it is mandatory to have a rather realistic setup to validate the proposed approach. The importance comes from the fact that in the case of foot-mounted inertial navigation, the walking dynamics must be properly introduced in order for them to be accurately identified by the zero-velocity detector.
In Ref. [Zampella2011], authors generate a $3D$ trajectory (position and attitude) that is based on a simplified human walk pattern. This is implemented using the step patterns that are observed with a motion capture system, and through the solving of an optimization-based problem. From this ground truth, a synthetic noiseless IMU data is derived (i.e. measurements from a $3-axis$ accelerometer, a $3-axis$ gyroscope and a $3-axis$ magnetometer), by exploiting the equations linking these measurements to the trajectory, as defined in Section. 1.1.1.
On the basis of Ref. [Zampella2011], in Ref. [LOPSI2021], a closed $3-$loop trajectory with a rectangular path of 12×7 m is provided. The dataset contains not only the simulated IMU measurements, but also ground truth position, velocity, and orientation (Euler angles and rotation matrix). All data is sampled at a frequency of 100 Hz, and the walking steps are normalized at 1 s duration.
To maintain the same sensor configuration as the one introduced in Fig. 2.1, a set of measurements from the spatially distributed magnetometer array is also considered. Magnetometer 0 measurements are provided by Ref. [Zampella2011], while the remaining others (magnetometer 1 to 4) are simulated. This is done in a similar manner to the simulations in Section 2.3.1 of Chapter 2, where

small random variations are added to B^{b0} in a way that preserves the non-singularity condition of the magnetic field gradient ∇B^b.
To reproduce the characteristics of a real sensor board, additive random zero-mean white Gaussian noises are considered for all the simulated measurements. The standard deviations of these noises are chosen by following the specific datasheet of a real IMU, the Xsens MTi module Ref. [MTi2021], and are indicated in Table 3.1. Note that, similarly to the simulations conducted

Table 3.1: Noise characteristics of sensor measurements

Sensor	Parameter	Standard deviation	Unit
$3-axis$ accelerometer	η_a^b	0.012	ms^{-2}
$3-axis$ gyroscope	η_ω^b	0.0087	rads^{-1}
$3-axis$ magnetometers	η_B^b	0.03	G

in Section. 2.3.2, the same noise standard deviation is considered for all five magnetometers' measurements. However, noise amplitude vary differently from one magnetometer to another, which represents a realistic behavior of any commercialized sensors.

Remark 14 *It is underlined that, the chosen value of the standard deviation of the magnetometers' noises is actually over-evaluated. In fact, in commercialized magnetometers, it is found that the standard deviation of output noise can go up to* 0.01 *G in some cases, but the most common range is around* 0.005 *G. However, as the used data in this section is from Ref. [Zampella2011], it is interesting to choose close parameters to theirs. In Ref. [Diaz2015], the same authors indicate that the magnetometer has an added* 0.1 *G standard deviation zero-mean Gaussian noise. This is considered very high compared to reality. For this reason, it is preferred to select a value that is between the previously found* 0.01 *G and* 0.1 *G, hence the choice of* 0.03 *G in Table 3.1.*

It is reminded that sensor biases are not taken into account, as no bias modeling is conducted in the proposed approach.
During the entire simulations, the process and the measurement noise covariances, Q and N, of any tested EKF architecture, are chosen based on the noise characteristics of the IMU and magnetic measurements. They are kept fixed during the EKF computation. The EKF linearization is conducted during each time step, around the current state estimate. During all experiments, the theoretical model and the EKF-based observer are initialized with different values. Notice that this choice allows to illustrate the convergence of the EKF even though it is initialized with values that are far from the actual states of the model.

3.3.2 Proposed single EKF compared to two EKFs

Before demonstrating the benefit of combining the magnetic field gradient-based EKF with the ZUPT, one should first assess the estimation accuracy of the proposed single EKF in Fig. 3.2, compared to the earlier introduced two EKFs setting (primary and main in Fig. 2.2). To do so, the two architectures are applied using the foot-mounted dataset presented above, in the purpose of estimating the velocity, attitude and position, as well as the magnetic field and its gradient.
As the considered measurements noise patterns are generated randomly, the estimation results may slightly vary on each execution of the proposed algorithm. For this reason, the Monte-Carlo technique is used to run the EKFs under study for 100 times. Then, the mean of the different error results is computed with respect to these 100 runs. Table 3.2 presents the Root Mean Squared Error (RMSE) and the MAE between the velocity estimate $\widehat{v^b}$ and the ground truth one (provided in the dataset), for the two studied cases (single EKF and two EKFs). The reason behind this

Table 3.2: Velocity estimation results of the proposed single EKF and the two EKFs architectures

Metrics	***Two EKFs***	***Single EKF***
RMSE (ms^{-1})	0.18	0.16
MAE (ms^{-1})	0.14	0.11

evaluation is to illustrate that, even though the proposed single EKF architecture is rather complex when it comes to the linearization process as well as the tuning of the noise covariance matrices, better estimation accuracy results can be achieved, as long as the noise parameters of Q and N are properly chosen. Indeed, it is shown through Table 3.2 that the RMSE and the MAE of the velocity estimation using the proposed single version of the EKF (in Fig. 3.2) are lightly better than the ones of the previous proposed architecture in Fig. 2.2. To be more precise, the proposed approach is actually more accurate for 86 times out of 100 using the RMSE metric and 97 times out of 100 through the MAE evaluation. This represents enough statistical proof to validate the efficiency of the proposed single EKF.
To better visualize the distribution of the velocity estimation errors, the obtained RMSE and the MAE values are plotted for the conducted 100 Monte-Carlo runs as represented by Figs. 3.5-3.6.

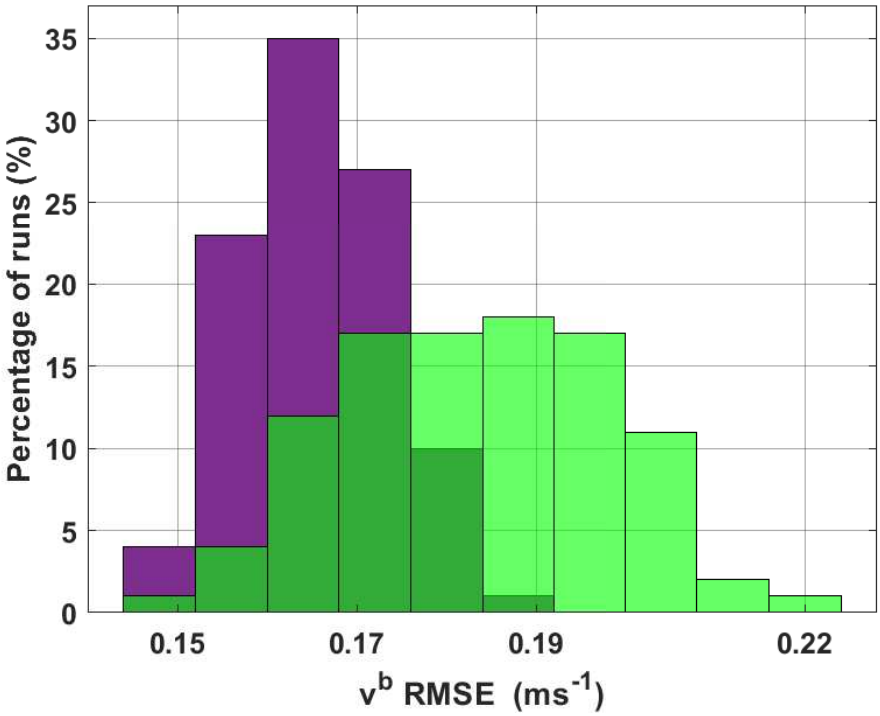

Figure 3.5: Distribution of velocity RMSE during 100 *runs. In light green for the two EKFs-based architecture, and in purple for the single EKF*

Through this assessment, it is clear that the proposed single EKF outperforms the case of using the two EKFs setting, no matter the chosen random noise pattern of the employed measurements. In fact, by looking at these histograms, one can see for example in Fig. 3.6, that 41% of runs generate a velocity MAE in between 0.11 ms^{-1} and 0.12 ms^{-1} when using the proposed single EKF, versus only 1% through the two EKFs configuration.
As discussed in Section. 3.2.1, this improvement on the velocity estimation accuracy can be ex-

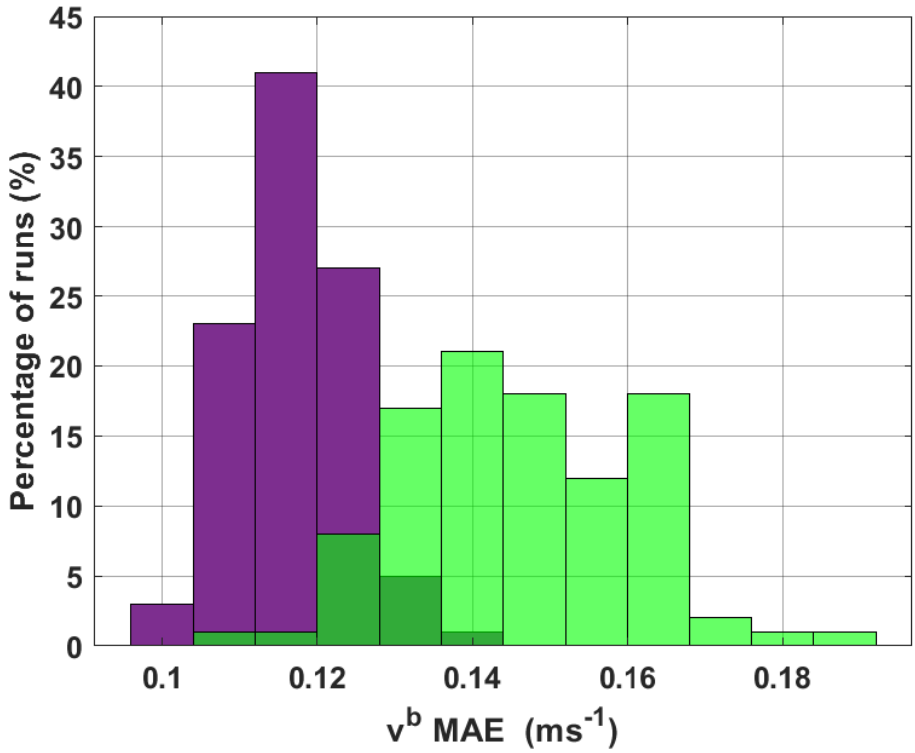

Figure 3.6: Distribution of velocity MAE during 100 *runs. In light green for the two EKFs-based architecture, and in purple for the single EKF*

plained based on two main reasons: first, due to the better handling of the tuning process of the EKF noise covariance matrices, and second, thanks to preserving the complex relationship between the different states that hold valuable information behind their non-linear connections.
The same positive outcome can be seen when considering the position estimation. For instance in Table 3.3, the traveled distance error percentage with respect to the ground truth one is presented for both the studied EKF architectures. It is shown that, using the single EKF configuration provides a better accuracy, confirming in this case, the pertinence of the proposed approach.

Table 3.3: Position estimation results of the proposed single EKF and the two EKFs architecture

Metric	***Two EKFs***	***Single EKF***
Traveled distance error $(\%)$	23.48	21.86

For all these performance improvements, in the rest of the thesis, the EKF is always used in its compact form (single EKF architecture).

3.3.3 Proposed EKF compared to the main EKF

In this section, the proposed EKF (single EKF in Fig. 3.2), using the model of Eqs. (2.33)-(2.37), is compared to the main EKF of Fig. 2.9, corresponding to the model of Eqs. (1.41)-(1.44). As demonstrated earlier in Chapter 2, there is a clear advantage in estimating the magnetic field gradient ∇B^b, instead of using it directly as a noisy input in the EKF. The benefit from doing so was assessed using a simulation scheme in Section 2.3. However, the comparison was done

with the two EKFs architecture of Fig. 2.2 and not with the new proposed single EKF. Also, the simulation groundwork was not reflecting a real walking scenario of a pedestrian equipped with a foot-mounted sensor, which is the targeted application in this chapter. In this sense, new comparisons are conducted in this particular framework and the different estimation results are presented accordingly.

Estimating the magnetic field gradient

The main contribution of the proposed EKF resides in its corresponding model, and more particularly, Eq. (2.36), that enables the filtering of ∇B^b, in the purpose of better estimating the different states, especially the velocity. The main EKF lacks however this equation, and considers instead ∇B^b as a known input, and not a state.
In Fig. 3.7, the estimation result of the first element β_1 of ∇B^b by the proposed EKF is presented. The other elements ($\beta_{2\cdots5}$) have the same behavior and are not plotted for simplicity reasons. The

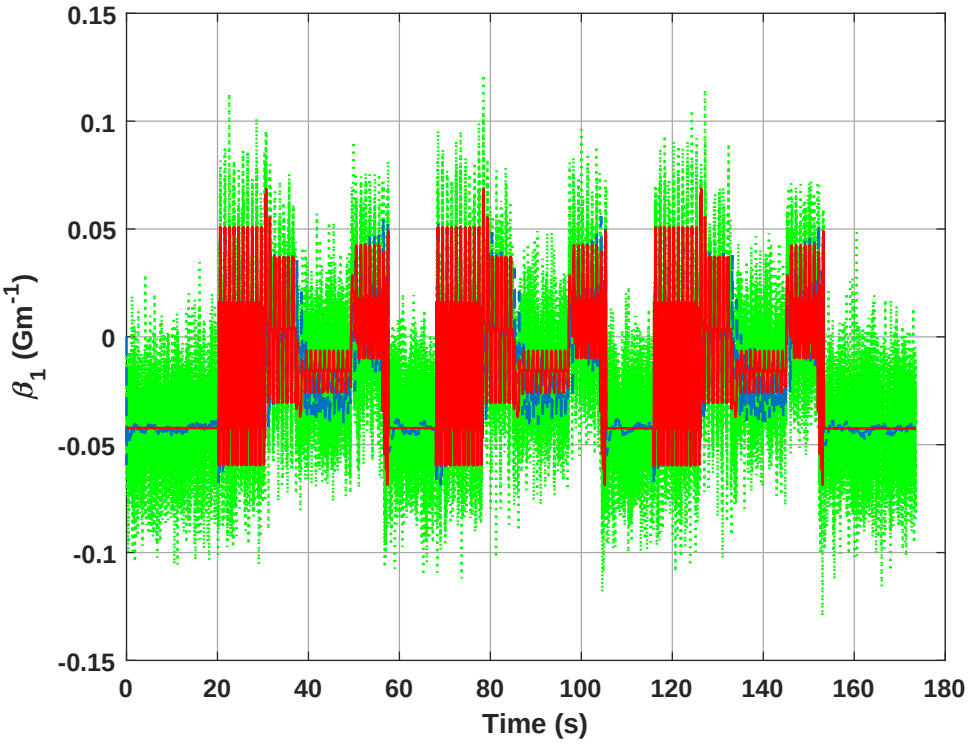

Figure 3.7: Estimation results of β_1. In red is the ground truth, in green is the measured one, and in blue is the proposed EKF estimate $\widehat{\beta}_1$

estimated element of the magnetic field gradient element $\widehat{\beta}_1$ (in blue dashed line) is close to the ground truth one (in red solid line), even though the initialization values of the EKF are different from the actual ones. Note that the measured β_1 (in green dotted line), that is used as an input in the main EKF, is very noisy. This will remarkably affect later the accuracy of the velocity estimation.
Let $\eta^b_{\beta_1}$ represent the noise of the first element β_1 of ∇B^b. In Fig. 3.8, the PSD of this noise is presented, before and after estimating ∇B^b with the proposed EKF. Recall that a zero-mean white Gaussian noise is added to all magnetic measurements in the beginning of these simulations. This noise is illustrated with the red "flat" line in the PSD representation. Then, the advantage of applying the proposed EKF that estimates ∇B^b using Eq. (2.36) can be seen through the blue line behavior. In fact, the PSD of $\eta^b_{\widehat{\beta}_1}$ significantly decreases from around $-55\ dB/Hz$ to about

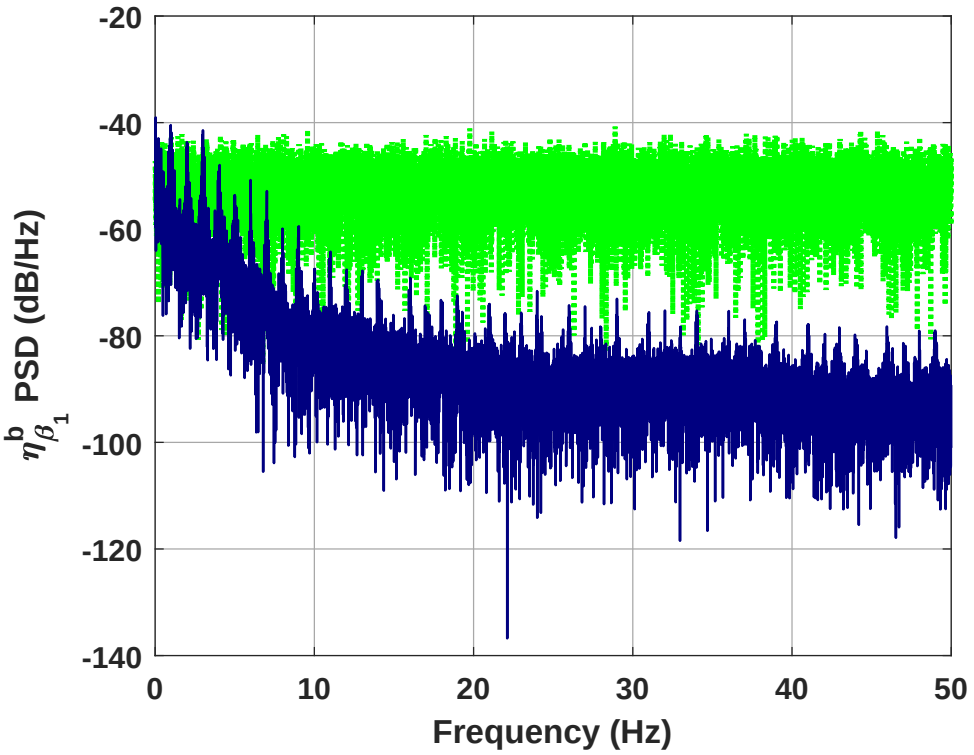

Figure 3.8: PSD of $\eta^b_{\beta_1}$. In green is the measured one, and in blue is $\eta^b_{\widehat{\beta}_1}$ from the proposed EKF

$-95\ dB/Hz$ along the frequency range, which justifies the effectiveness of the proposed approach in reducing the noise contained in ∇B^b. Note here that $\eta^b_{\widehat{\beta}_1}$ does not represent only a white noise (i.e. is not flat), as it contains also the estimation errors contained in $\widehat{\beta}_1$, that are generated by the proposed EKF.
Another way that is used to quantify noise in a signal is by computing the Signal to Noise Ratio (SNR) Ref. [Oppenheim2015], which is the ratio of the power of the ground truth signal β_1 to the power of its noise $\eta^b_{\beta_1}$. The SNR of β_1 increases from $SNR_{\beta_1} = -9.4\ dB$ when ∇B^b is not estimated, to $SNR_{\widehat{\beta}_1} = -0.42\ dB$ when it is done. This proves again that ∇B^b noise is greatly reduced with the proposed model and EKF.

Quaternion estimation results

The major advantage of estimating the magnetic field gradient ∇B^b with the proposed EKF, rather than using it as a noisy input in the main one of Fig. 2.9, is mostly seen on the velocity estimation accuracy results. However, this contribution of modeling ∇B^b has an implicit relationship with attitude estimation, which can be mainly detected when analyzing the model's observability matrix in Section 2.2.2. For this reason, the quaternion q is estimated using the two studied models. Then, Eq. (1.1) and Eq. (1.3) are applied, to transform the quaternion estimate $\widehat{q}$ into Euler angles representation as shown in Fig. 3.9. Such attitude representation is preferred during the results evaluation, as it provides a more "physical" information on the rotations than the quaternion, which is rather "abstract". Note that the chosen quaternion value during the initialization of both the compared EKFs is different from the ground truth one. Yet, the proposed EKF as well as the main one converge to the actual state in less than 20 s of the walking scenario. The proposed EKF performs slightly better, as its corresponding Euler angles estimates are closer to the ground truth, than the main EKF, which can be easily detected in the zoomed areas of Fig. 3.9. This confirms

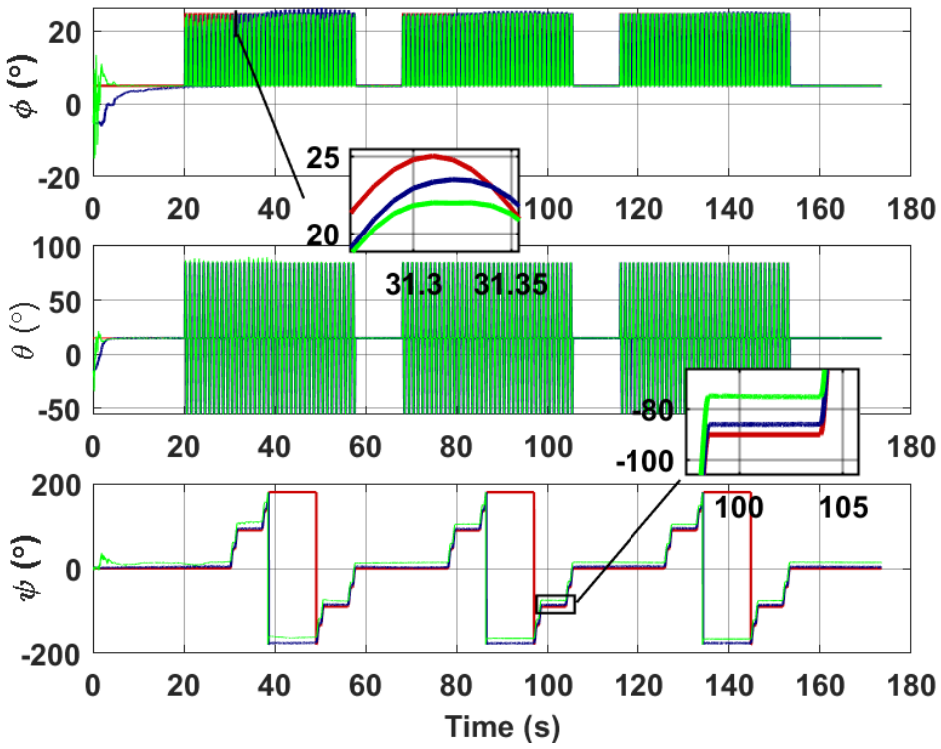

Figure 3.9: Euler angles estimation results. In red is the ground truth, in green is the main EKF estimation, and in blue is the proposed EKF one

again, that estimating ∇B^b using Eq. (2.36), has a positive impact on the estimation process.

Remark 15 *Some jumps are seen on the yaw angle estimate $\widehat{\psi}$ when the estimated pitch angle $\widehat{\theta}$ reaches 90°. This is a great example of the common problem of singularity in Euler angle's representation, previously discussed in Section 1.1.1. Also, recall that it is assumed that the direction of gravity defines the vertical $z-$axis of the considered sensor board. As the yaw angle represents the rotation around this axis, any error in $\widehat{\psi}$ will then generate errors in position reconstruction along the $z-$axis.*

Velocity estimation results

The pertinence of the proposed EKF compared to the main one is mainly observed during the velocity estimation, that has a direct link with the magnetic field gradient (i.e. the term $\nabla B^b v^b$ in Eq. (2.35)). In Fig. 3.10, the $x-axis$ of the ground truth velocity, the estimate from the proposed approach as well as the one from the main EKF are plotted. The other two velocity axes have nearly the same behavior and are omitted from the plot for clarity purposes. It is clear from Fig. 3.10, that the velocity estimation using the proposed EKF (in blue line) provides a better accuracy than the one from the main EKF (in green line). This can be easily detected especially during static phases (i.e. velocity is equal to zero), where $\widehat{v_x^b}$ from the proposed EKF is closer to the ground truth (in red line) than the green line estimate. This is actually a very important advantage of the proposed EKF, that is expected after studying the observability of its corresponding model. When the magnetic field gradient is very low/or equal to zero (which is the case at some time frames of β_1 in Fig. 3.7), the main EKF fails at providing an accurate velocity estimation due to the potential unobservability of the latter. Nevertheless, the use of the proposed model adds more flexibility to the observability conditions as discussed in Section 2.2.2, in a way that can better recover the

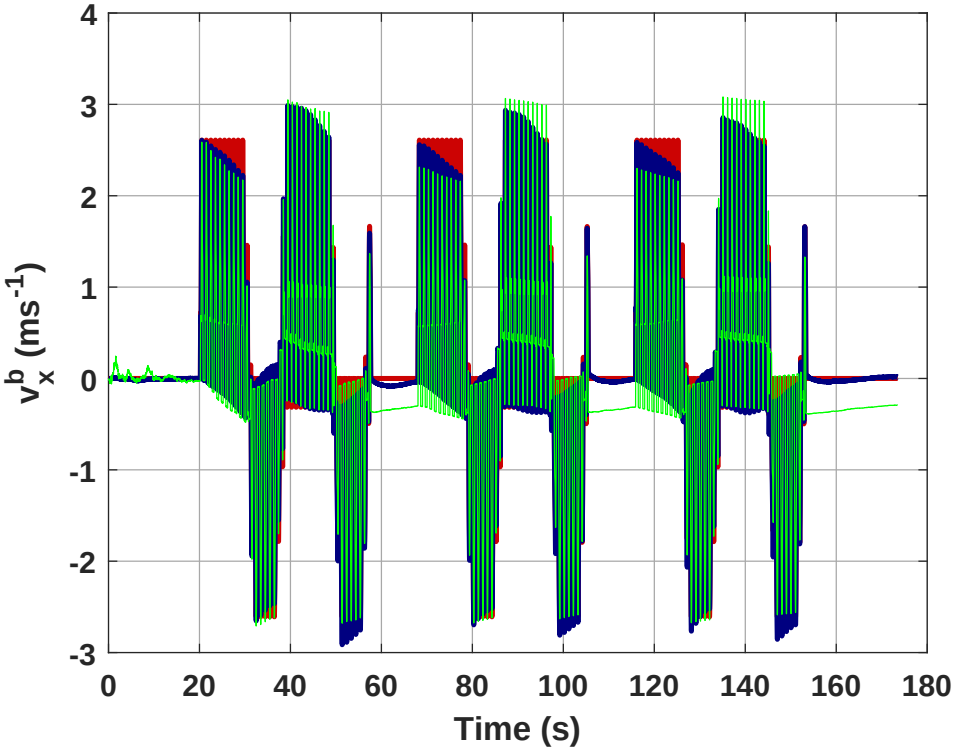

Figure 3.10: v_x^b estimation results. In red is the ground truth, in green is the main EKF estimation, and in blue is the proposed EKF one

velocity even in critical magnetic field-related situations. This limitation of the magnetic field gradient-based EKF is discussed further in detail in the next chapter.

Remark 16 *Independently from the magnetic field gradient state, attitude and velocity estimations may suffer from inevitable drifts during static phases (constant attitude and zero velocity). In Ref. [Chesneau2018], it was stated that for a trajectory to be observable, it is necessary, but not sufficient, that the targeted object is continually moving, which is considered an impractical constraint in a realistic use case. In the same reference, it was discussed that the reason behind these drifts is due heavily to the presence of sensor biases. It is believed that further investigations may reveal all the exact conditions where the proposed model's observability matrix is state deficient. In the meantime, a complementary solution is used, to compensate for these limitations of the proposed EKF and provide an all-time working approach (as long as it's a foot-mounted application).*

For comparison reasons, the Monte-Carlo simulation used in the previous section is reproduced here for the main EKF, in order to compute the velocity RMSE and MAE of the latter as indicated in Table 3.4. Again, it is observed through the velocity estimation error results, that the

Table 3.4: Estimation results of v^b with the proposed EKF and the main EKF

Metrics	***Main EKF***	***Proposed EKF***
RMSE (ms^{-1})	0.21	0.16
MAE (ms^{-1})	0.15	0.11

proposed EKF outperforms the main EKF that does not consider ∇B^b as a state and uses it in its noisy input. While the difference in accuracy is not enormous, for instance the RMSE is reduced from 0.21 ms^{-1} to 0.16 ms^{-1}, a such improvement is important when dealing with the position estimation, due to the integration relationship that links it with the velocity.

Position estimation results

The biggest evidence that highlights the importance of the decrease of the velocity estimation error, is the position reconstruction through the integration of Eq. (2.37). The impact can be seen by plotting the 2D representation of the estimated trajectory in Fig. 3.11. A noticeable drift

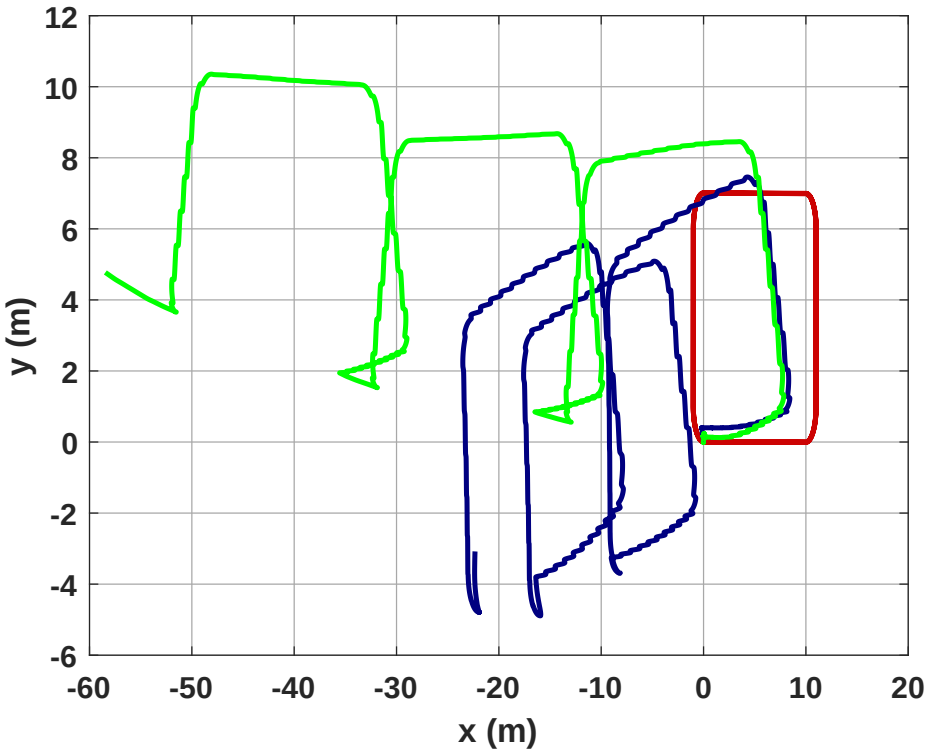

Figure 3.11: M^n estimation results. In red is the ground truth trajectory, in green is the main EKF estimation, and in blue is the proposed EKF one

compensation is observed when the proposed EKF is applied. Indeed, the slightest improvement in velocity estimation can increase the accuracy of the trajectory reconstruction, as less errors are generated. Therefore, there is less of their accumulation during the integration process. It is observed that there is a jump after each loop for both the green and the blue plots in Fig. 3.11. This is explained by the less accurate estimation of velocity during static phases (as shown in Fig. 3.10), where the latter tends to drift but quickly recovers after. It is underlined here that the jumps in the blue plot are narrower, which proves the advantage of the proposed approach.
In the same context, by looking at Table 3.5, it is seen that the traveled distance error percentage of the studied trajectory is reduced from 36.05% to 21.86%, when using the proposed approach. This improvement of 14.19% is very beneficial for position reconstruction, especially when dealing with applications of longer trajectories.

3.3.4 Estimation results of the proposed EKF-ZUPT

Despite the contribution of the proposed EKF in velocity estimation, the obtained error results are still not satisfactory if position reconstruction needs to be conducted, which is observed in

Table 3.5: Estimation results of M^n with the proposed EKF and the main EKF

Metric	*Main EKF*	*Proposed EKF*
Traveled distance error (%)	36.05	21.86

Table 3.5. In fact, whether its computed with or without the proposed model, $\widehat{v^b}$ still suffers from some drifts. One reason for these errors is the earlier discussed observability loss issue, during static trajectories or when the magnetic field gradient does not satisfy the non-singularity condition (for instance, if one of its columns is almost/or equal to zero). Other errors are due to the different uncertainties considered in the simulation scenario, i.e. the generation of the four additional magnetic fields, the approximation of the spatial derivatives ∇B^b and T^b, the linearization process of the EKF, etc. These errors lead to drifts when the position is reconstructed, as seen in Fig. 3.11.
For the different reasons stated above, the proposed magnetic field gradient-based EKF is combined with the ZUPT, as presented in Fig. 3.4, and the same comparisons as the previous section are conducted.

Velocity correction using the ZUPT

The magnetic field gradient-based EKF fails at providing an accurate velocity estimate $\widehat{v^b}$ during instants where the latter is equal to zero. As explained in Section 3.2.2, the advantage of the ZUPT comes from being able to efficiently detect these instants, and consequently, to manually assign $0_{3\times1}$ to $\widehat{v^b}$, inside the EKF loop. Such correction enables to continuously reset the errors contained in $\widehat{v^b}$ to zero, and thus, avoid any drifting through time.
In Fig. 3.12, the velocity estimation results of the proposed ZUPT-aided magnetic field gradient-based EKF (EKF-ZUPT), as well as the main EKF, also combined with the ZUPT (Main EKF-ZUPT) are plotted.
By correcting the velocity estimate $\widehat{v_x^b}$ of the magnetic field gradient-based EKF with ZUPT, the latter is now almost perfectly superposed with the ground truth velocity v_x^b, and there are no more visible estimation errors, especially during the instants where the velocity is equal to zero.
What is is also interesting to see, is that even after adding the ZUPT to the main EKF, which indirectly discards the benefit of estimating ∇B^b, the proposed EKF-ZUPT solution is still slightly better in terms of velocity estimation accuracy, which can be detected in the zoomed area of Fig. 3.12. In fact, in a foot-mounted framework where the ZUPT can be used, the advantage of eliminating noise from ∇B^b by considering it as a state instead of an input, is very less remarkable. Yet, it is important to keep in mind that the ZUPT is only added to the EKF, in the context of foot-mounted navigation, and does not represent a global solution that can be always adopted.
In the same manner as the previous section, the Monte-Carlo simulation is conducted in order to compute the mean RMSE and MAE of the velocity estimate with the two studied approaches. First, from Table 3.6, it is shown how the proposed ZUPT-aided magnetic field gradient-based EKF succeeds to accurately estimate $\widehat{v^b}$ with a remarkable decrease in the RMSE and MAE results, compared to the case of not using the ZUPT (e.g. RMSE that decreases from 0.16 ms^{-1} in Table 3.4 to 0.02 ms^{-1}).
Second, while the difference in velocity errors between the two approaches of Table 3.6 is considered irrelevant, it is believed that for position estimation, this improvement can be beneficial, especially when dealing with long trajectories.

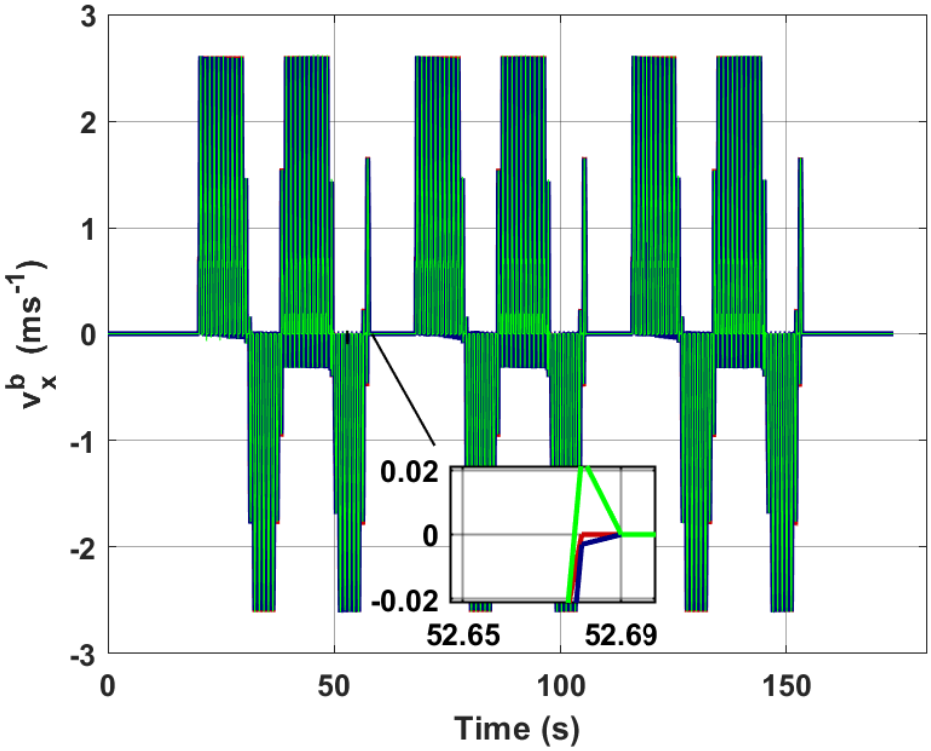

Figure 3.12: v_x^b estimation results. In red is the ground truth, in green is the main EKF-ZUPT estimation, and in blue is the proposed EKF-ZUPT one

Table 3.6: Estimation results of v^b with the proposed EKF-ZUPT and the main EKF-ZUPT

Metrics	***Main EKF-ZUPT***	***Proposed EKF-ZUPT***
RMSE (ms^{-1})	0.025	0.020
MAE (ms^{-1})	0.016	0.009

Position reconstruction using EKF-ZUPT

The accurate estimation of $\widehat{v^b}$ using the proposed EKF-ZUPT approach plays a major role during the position reconstruction. Unlike the performance of the magnetic field gradient-based EKF in Fig. 3.11, using the proposed EKF-ZUPT approach provides an accurate trajectory estimation as demonstrated in the $2D$ and $3D$ plots of Figs. 3.13-3.14.
The previous drifts contained in $\widehat{M^n}$ are almost entirely removed, providing this way nearly the exact same ground truth trajectory. In both figures, it is shown that even when adding ZUPT, the proposed approach (EKF-ZUPT), still slightly outperforms the case of when ∇B^b is not estimated (Main EKF-ZUPT), especially around the $z-axis$. This can be explained by the difference in the yaw angle estimation accuracy, earlier illustrated in Fig. 3.9. In fact, it is observed that the arrival point of the proposed approach (in blue) is closer to the ground truth one (in red) than the green point (Main EKF-Zupt). Note that all trajectories begin at the same coordinates and the starting and arrival points for the ground truth trajectory are the same.

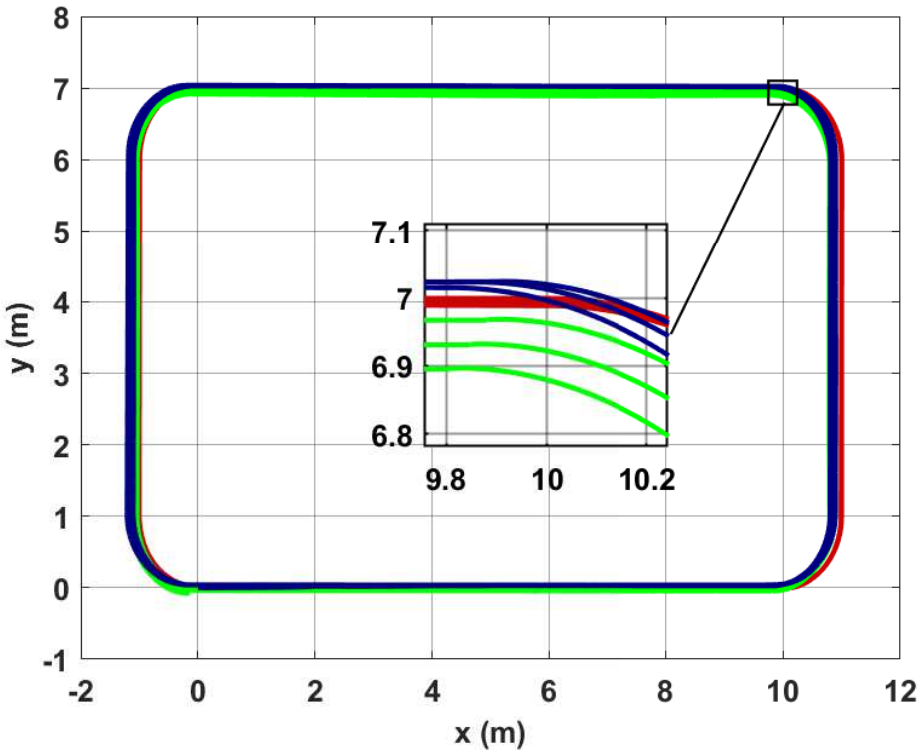

Figure 3.13: 2D trajectory reconstruction aided by ZUPT. In red is the ground truth trajectory, in green is the main EKF-ZUPT estimation, and in blue is the proposed EKF-ZUPT one

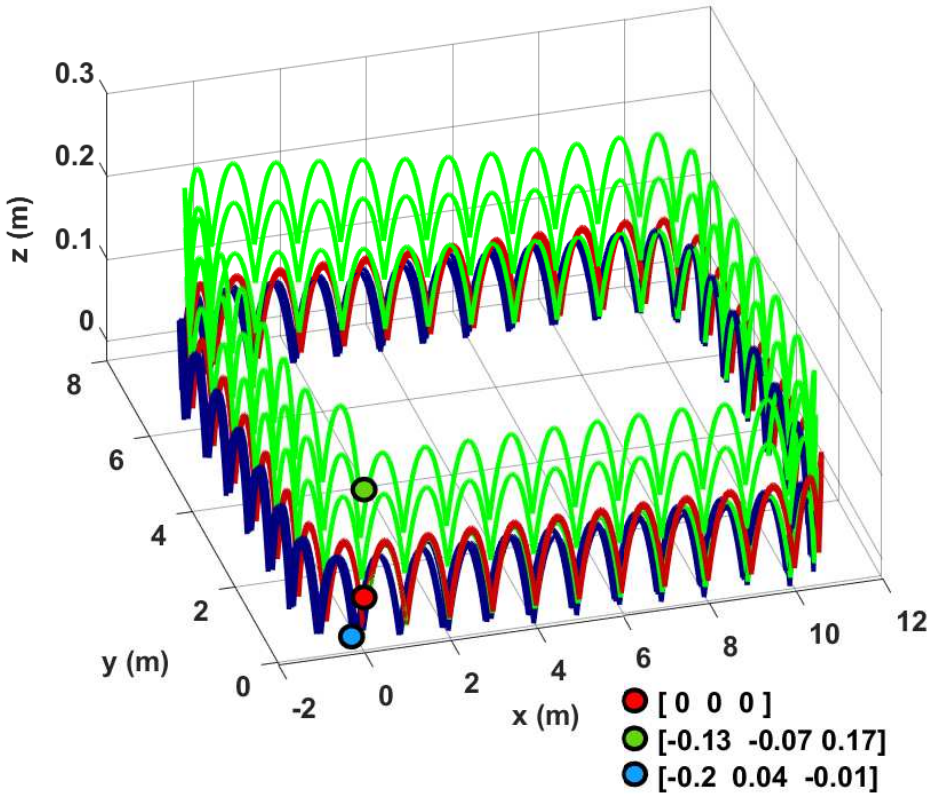

Figure 3.14: 3D trajectory reconstruction aided by ZUPT and corresponding arrival points. In red is the ground truth trajectory, in green is the main EKF-ZUPT estimation, and in blue is the proposed EKF-ZUPT one

In Table 3.7, a comparison between the traveled distance errors is displayed when ZUPT is added. First, it is underlined that the distance error is remarkably reduced from the case of not using the

Table 3.7: Estimation results of M^n with the proposed EKF and the main EKF

Metric	***Main EKF-ZUPT***	***Proposed EKF-ZUPT***
Traveled distance error (%)	0.59	0.2

ZUPT to the proposed EKF-ZUPT solution (distance error percentage that decreases from 21.86% to 0.2%). This justifies again, the advantage that ZUPT can bring to the trajectory estimation process, in the case of foot-mounted navigation applications. Second, similarly to the conclusions made through Figs. 3.13- 3.14, even after adding ZUPT, there is a clear advantage in estimating ∇B^b with the proposed magnetic field gradient-based EKF. This is why, in the continuity of this thesis, the proposed EKF solution is maintained.

What about ZUPT versus EKF-ZUPT ?

To reconstruct the velocity, one may wonder about the advantage of the proposed EKF-ZUPT solution, over simply applying ZUPT with a regular integration process of Eqs. 2.33-2.34.
While the ZUPT is considered as one of the most effective solutions in pedestrian velocity correction, it does not satisfy the generality aspect of a proposed approach, as it is very dependent on the sensor board location (i.e. the foot) to be able to detect the subject's walking dynamics. However, the aim of this work is to provide a rather global solution, that can be adopted by any other application, and that does not rely on any specific sensor board placement or movement dynamics. More on the limitations of the ZUPT method is presented in the next chapter.
Furthermore, even though the ZUPT can continuously reset the errors generated by Eq. 2.34 to zero, this does not guarantee the accurate estimation of the velocity. In fact, the velocity reconstruction is also dependent on the attitude which itself, suffers from drifts after integrating Eq. 2.33, as shown in Section 1.1.2. In Fig. 3.15, the velocity estimate $\widehat{v_x^b}$, obtained from the integration of Eqs. 2.33-2.34 and applying ZUPT, is plotted. As expected, despite that $\widehat{v_x^b}$ does not suffer from the drifting phenomena (i.e. accumulation of errors), it is far from the ground truth velocity v_x^b. This is mostly due to the quaternion estimation that is flawed because of the noise contained in the angular velocity measurements. As discussed in Section 1.1.2, several attitude estimation methods that rely on data fusion techniques, can be used to treat this issue. However, it is believed that, in a magnetically disturbed environment, with the sensor board attached to the subject's foot, the proposed EKF-ZUPT approach is a very adequate solution that easily succeeds to provide promising results.

3.4 Conclusion

Foot-mounted inertial navigation One possible application that can be considered when studying indoor navigation, is the one related to pedestrian trajectory reconstruction, and more particularly to the foot-mounted sensor framework. The advantage of such setup is that it provides rich information on the subject's walking dynamics (i.e. the phases of the gait cycle), enabling therefore, the design of adapted methods that rely on the detection of these phases.
Zero-velocity update technique The most used method in the literature when dealing with foot-

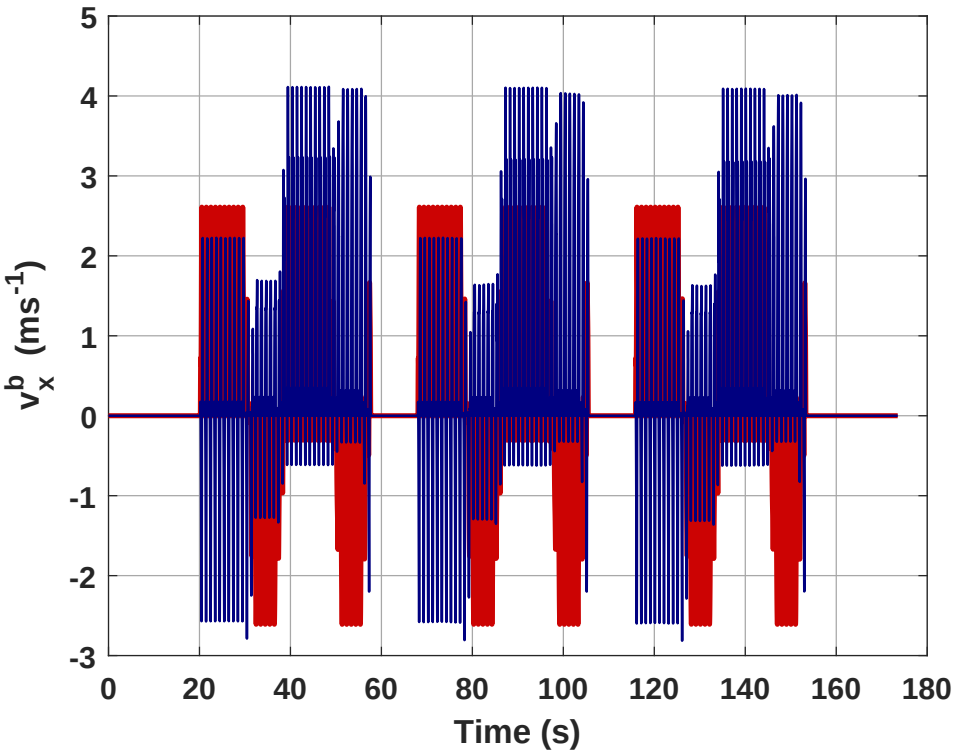

Figure 3.15: Estimation results of v_x^b through ZUPT. In red is the ground truth, and in blue is the ZUPT estimate $\widehat{v_x^b}$

mounted navigation is the ZUPT. It relies basically on the detection of static instants during one's gait cycle, using IMU measurements, and updating the velocity estimate to zero, each time these phases are identified.

Proposed EKF-ZUPT approach The magnetic field gradient-based EKF generates velocity estimation errors, especially during static instants (constant attitude and zero velocity) or very low/or equal to zero magnetic field gradient moments. This encourages combining it with the ZUPT, that not only stops the accumulation of velocity estimation errors but also enables a better trajectory reconstruction.

Better configuration of the magnetic field gradient-based EKF Instead of using the primary and the main EKF configuration, presented in Chapter 2, a single EKF architecture is proposed, to not only reduce the computation time needed for the algorithm to be executed, but also to provide better estimation accuracy results, while having a compact solution.

Evaluation of the proposed EKF-ZUPT approach with a foot-mounted sensor dataset A realistic simulation of a human walk pattern is used to assess the performance of the proposed approach. Different comparisons are conducted between the use of only the magnetic field gradient-based EKF, or the main EKF, and when considering the ZUPT. Different evaluation metrics are considered that demonstrate the efficiency of the EKF-ZUPT method in a foot-mounted framework.

On the limitations of the ZUPT The ZUPT is known to be very efficient when dealing with foot-mounted navigation. However, the latter usually requires the presence of the sensor board on the moving body's foot to detect specific walking dynamics. This is not always feasible, especially in non-pedestrian applications (e.g. vehicles, robotics, etc.). In the next chapter, an alternative solution is proposed that enables the correction of the magnetic field gradient-based EKF estimation errors, while representing a rather general approach that can be applied at any context.

Part II

Artificial Intelligence for Indoor Navigation

4

AI-based Kalman Filtering

This chapter starts by discussing in Section 4.1, the difficulties of the proposed magnetic field gradient-based EKF in providing an accurate estimation of the states, especially during low magnetic field gradient instants. Then, the inadequacy of the ZUPT to deal with such problem is demonstrated, when considering trajectory scenarios that are outside of the foot-mounted sensor framework. One way to tackle these limitations, is to consider an Artificial Intelligence (AI) based solution as widely conducted in the related literature. Nevertheless, relying entirely on Deep Neural Networks (DNNs) introduces several inconveniences that are discussed in Section 4.1. An innovative solution that takes advantage of both the EKF and a Bidirectional Long Short-Term Memory Network (BiLSTM) is then proposed in Section 4.3. The performance of the proposed approach is evaluated through the Openshoe dataset in Section 4.4, where an improvement on velocity and position accuracies is shown, in comparison with the only EKF or BiLSTM-based solutions.

Contents

4.1 Limitations of the magnetic field gradient-based EKF for velocity estimation

The magnetic field gradient-based EKF represents a very interesting solution for the magneto-inertial estimation problem thanks to its strong theoretical background and practical implementation. However, as discussed in Chapter 3, the accuracy of the EKF estimation can degrade under certain conditions. In such circumstances, the proposed EKF, with the equation describing the dynamics of the magnetic field gradient, outperforms the main MINAV EKF, as demonstrated in Section 3.3.3. Nevertheless, despite this improvement, several errors are still contained in the velocity estimate $\widehat{v^b}$, that should be corrected. From these errors, one can differentiate two main categories: the errors generated from the measurements and the EKF numerical implementation, and those induced by the surrounding environment characteristics and the nature of the performed trajectory. In the following, both these categories are discussed, to better understand the limitations that they introduce to the estimation problem.

4.1.1 Errors related to the EKF implementation

The EKF errors can be generated from multiple sources during the estimation process. For instance, the different noises contained in the inputs and the measurements of the EKF, that are assumed to be zero-mean, white and Gaussian (which is not necessarily true, especially using real experimental data), highly influence the estimation accuracy of the states. Their impact is mostly seen when tuning the process and measurement covariance matrices, that, if improperly configured, can lead not only to inaccurate estimation results, but even to the divergence of the EKF. Other than that, the linearization process of the transition and measurement functions of the dynamic model, around the current estimate $\widehat{X}$, also implies the addition of more error. This is due to the computation of Jacobians that require the use of numerical approximations. Finally, the discretization step of the proposed continuous-time model (using the Runge-Kutta $4th$ order method) is also considered as a potential source of error. By providing an approximated value of a function using a weighted average of four increments, the method cannot preserve the model's actual dynamics. Thus, important information on the temporal variation of the states can be lost in the process, leading consequently to estimation errors.
All of the above sources of errors suggest that the EKF performance is most likely to degrade even while having an appropriate modeling of observable states. However, such errors can always be bounded to an extent by choosing adequate numerical methods and a proper configuration of the EKF noise parameters. It is believed that further investigations can provide a better insight on the EKF estimation uncertainty with respect to the different possible errors. In the meantime, an innovative method is proposed, that enables reducing the impact of these errors, and provide good estimation accuracy results.

4.1.2 Errors related to the trajectory characteristics

The second category of EKF errors is related to those generated by the surrounding environment characteristics, and the nature of the performed trajectory. In fact, one should know by now, that the most important criterion that has to be satisfied to fully reconstruct the velocity, is the presence of sufficient magnetic disturbances around the moving body under study. This is in order to avoid having directions in ∇B^b that are close or equal to zero, affecting this way, the non-singularity requirement of the latter.
A magnetically disturbed environment generates a magnetic field gradient which eigenvalues, denoted by $\lambda_{1,\cdots,3}$, are around 0.05 Gm^{-1}. In case these values are really lower, the performance of the EKF may decrease depending on the trajectory's dynamics. In Ref. [Chesneau2018], it was demonstrated that, under low magnetic field gradient conditions, the noise contained in its

measurements increases the EKF estimation uncertainity even higher, leading to a some sort of a *damping effect*, which causes either under or over estimating the velocity. This is one more reason for modeling ∇B^b, as performed by the proposed magnetic field gradient-based EKF, in the purpose of reducing this measurement noise, and minimizing the inaccuracy of $\widehat{v^b}$ during the low magnetic field gradient case. In the same reference, it was also discussed that, any approximated calibration parameter (i.e. scale-factor, effective position) can cause unbounded velocity estimation errors close to singular magnetic field gradient conditions. Thus, the issue of velocity estimation during low magnetic field gradient conditions can also be considered as an issue of robustness to calibration uncertainty.
To visualize the effect of low magnetic field perturbations on the states' estimation when using the proposed EKF, an experiment is conducted. A real sensor board, containing a $3-axis$ accelerometer, a $3-axis$ gyroscope, and a magnetometer array, having the same architecture as the one in Fig. 2.1, is placed on the back pocket of a subject. The latter performs a circular trajectory in two different locations: first inside an office where there are sufficient magnetic disturbances, due to the presence of laptops, heaters, electric currents, etc. Second, along the building entrance/hallway, that is not equipped with any major sources of magnetic perturbations. In Fig. 4.1, the three eigenvalues of ∇B^b are plotted for the two tested locations, as they represent a direct evaluation on the presence of magnetic field disturbances (by looking at their amplitudes) and the maintaining of the non-singularity condition (i.e. they need to be non-zero). First, it is observed that the eigenvalues

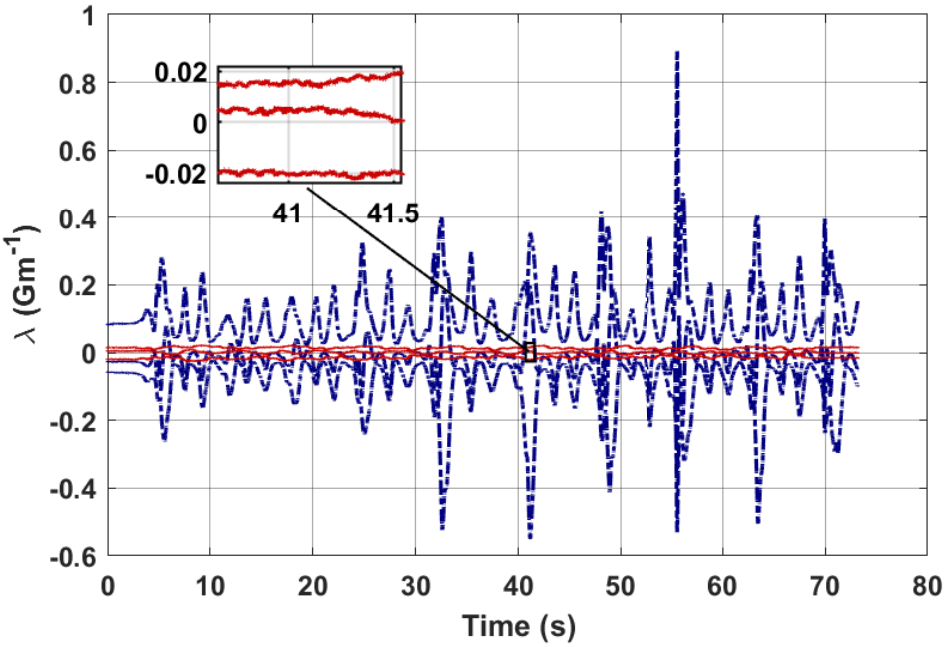

Figure 4.1: Eigenvalues of the magnetic field gradient for the two locations. In blue for the office, and in red for the hallway

of ∇B^b in the hallway are significantly lower than the ones in the office. This is expected as the magnetic disturbances are remarkably higher with the presence of office equipment. Through the zoomed area in Fig. 4.1, one can see that the three values of λ corresponding to the hallway are notably lower than the values usually observed indoor ($\lambda_{1,\cdots,3} \ll 0.05\ Gm^{-1}$). In addition one of the eigenvalues is almost equal to zero, which implies a possible loss of observability of at least one direction of the velocity estimate $\widehat{v^b}$, as the magnetic field gradient ∇B^b may become singular. Contrarily, the eigenvalues corresponding to ∇B^b in the office are around $\approx 0.1\ Gm^{-1}$, which is considered sufficient to recover $\widehat{v^b}$. Note also that these eigenvalues are different from zero, so no

singularity problem of ∇B^b occurs in this case.
To evaluate the impact of these magnetic field gradient eigenvalues on the performance of the magnetic field gradient-based EKF, the reconstructed position $\widehat{M^n}$ is presented in Figs. 4.2-4.3 for both the studied locations. Knowing that the performed trajectory is a circle, it is evident to con-

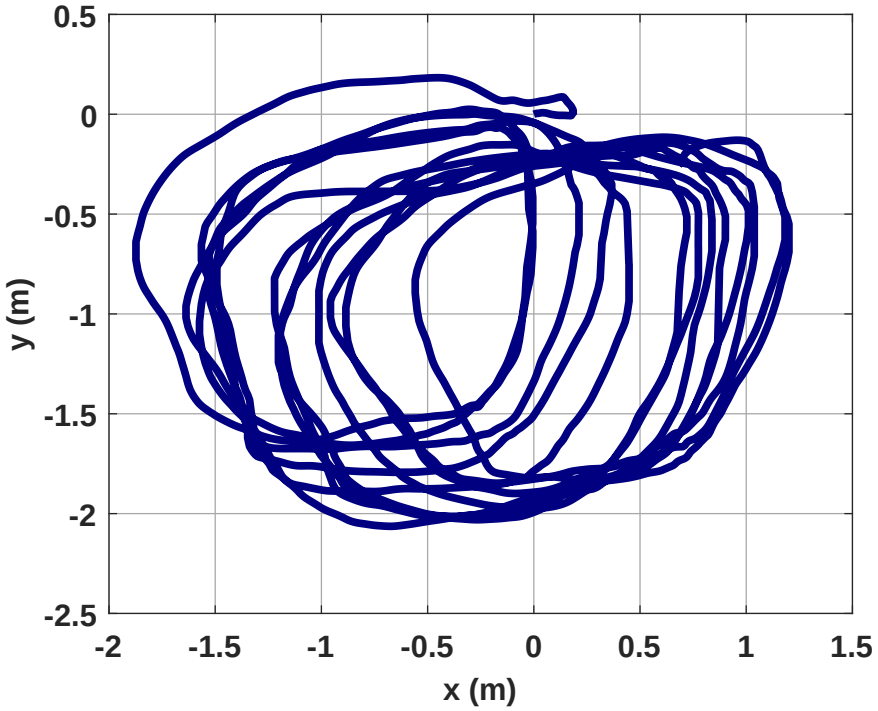

Figure 4.2: Magnetic field gradient-based EKF position estimation in the office

clude that the EKF performance is completely corrupted in the case of low magnetic disturbances (i.e. in the hallway), generating consequently a drifting trajectory in Fig. 4.3, that does not have any similar shape to a circle. On the opposite side, in Fig. 4.2, the magnetic field gradient-based EKF succeeds to reconstruct a trajectory that has the desired form, and that does not suffer from any noticeable drift. Nevertheless, as no ground truth data is available for this experiment, no further investigations on the accuracy of the estimation are conducted.
Finally, it is underlined that, even with the presence of magnetic field perturbations, there is a set of *indistinguishable trajectories* that may introduce observability issues to the studied model. From this set, one can recall the static trajectories case (i.e. constant attitude, zero velocity), mentioned in Remark 16, and discussed in detail in Ref. [Chesneau2018]. A further studying of the different possible characteristics that a trajectory may have, can help detect the times where the proposed model looses observability. However, no matter the case, a solution is needed to compensate for all the above limitations of the magnetic field gradient-based EKF and provide a rather global approach, that generates an accurate estimation of the states.

4.1.3 Limitations of the ZUPT for velocity correction in the EKF

In Chapter 3, a method called ZUPT was introduced in the context of foot-mounted navigation, as it is known to be very efficient in continuously correcting the EKF's velocity estimate $\widehat{v^b}$ and providing accurate trajectory reconstruction. However, as briefly discussed before, the ZUPT approach has several drawbacks, that make of it an inadequate solution to attenuate the errors generated by only using the EKF.
The first obvious limitation when applying ZUPT comes from the sensor board placement. For

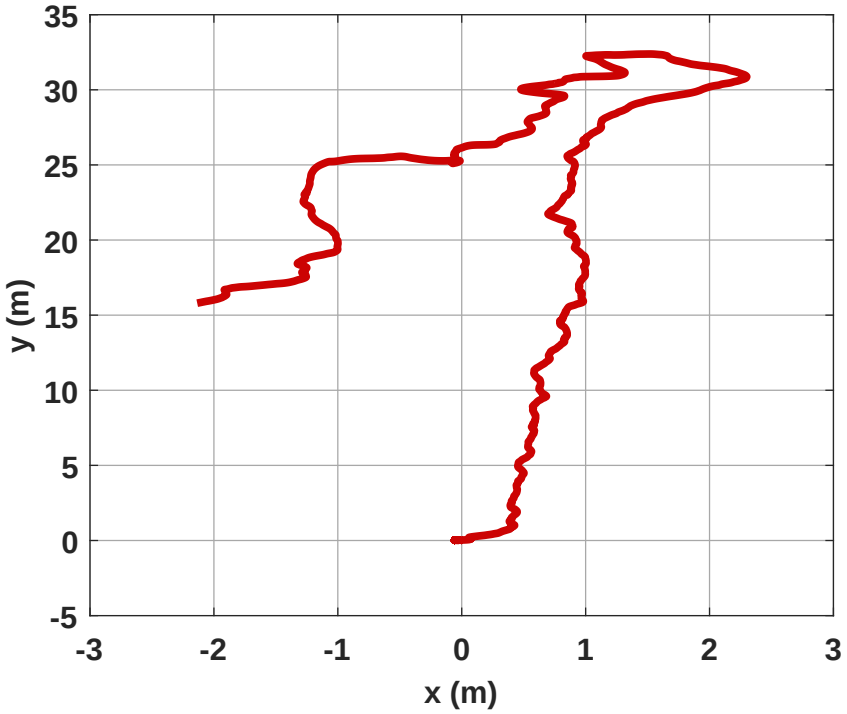

Figure 4.3: Magnetic field gradient-based EKF position estimation in the hallway

instance, if the moving body under study is a pedestrian, the sensor has to be attached to the foot, in order for this approach to work. This requirement is considered user-unfriendly as such sensor placement is uncomfortable and exposed.

In case the used sensor board is placed on any other body location beside the feet, the ZUPT can either suffer from false detections, or not detect any zero-velocity instances. To illustrate these issues, an experiment is conducted where the EKF-ZUPT from Chapter 3 is applied. Three databases are used, each one corresponding to a pedestrian trajectory with a triangular shape and a normal walking pace. One with the sensor board placed on the waist, another with the sensor placed on the ankle, and finally for comparisons, the sensor is attached to the foot. These placements, being on three different parts of the human body, enable the sensor board to observe different movement dynamics. Such comparison demonstrates to what extent the ZUPT can accurately detect zero-velocity instants, when having the sensor board placed on different body parts.

The Stance Hypothesis Optimal Detector (SHOE) is again used to identify zero-velocity moments, with a window size W_s set to be equal to 3 and a detection threshold δ_d of $0.03 * 10^5$. These values are inspired by the proposed algorithm in Ref. [Nilsson2012], and they have been proven efficient in determining stance phases during a normal walking pace scenario with the sensor board placed on the foot, as demonstrated in Fig. 4.4. First, instances where the SHOE detector indicates a zero-velocity are presented with the red dots. Simultaneously, the norm of v^b is plotted to better visualize the accuracy of these detections, i.e. if at time instant t, the velocity norm $||v^b(t)|| \approx 0$, it is highly likely that a zero-velocity detection should occur at the moment. As expected, when dealing with a foot-mounted framework, the SHOE detector can easily indicate when the foot touches the ground, enabling therefore, a periodic correction of the velocity estimate in the EKF, and an accurate trajectory reconstruction, as shown in Chapter 3.

Contrarily to the positive results above, in Figs. 4.5-4.6, the SHOE detection results are plotted for the rest of the studied sensor board placements (i.e. waist and ankle).

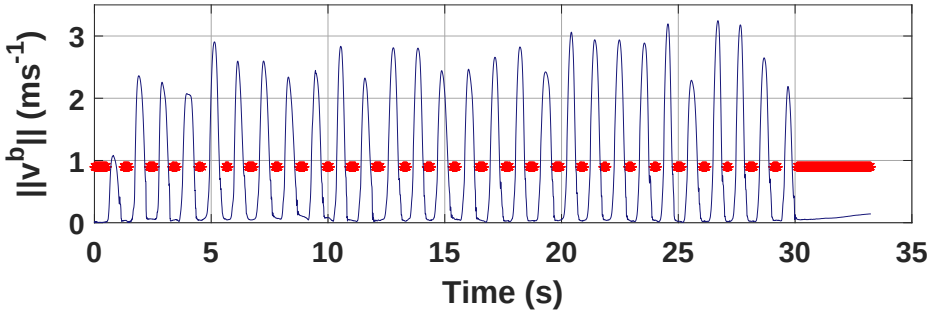

Figure 4.4: The velocity norm when the sensor is on the foot (blue line) and the instances where the ZUPT detector indicates a zero-velocity (red dots)

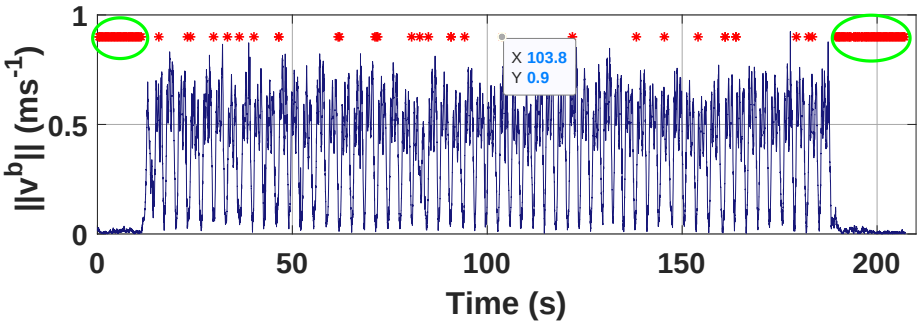

Figure 4.5: The velocity norm when the sensor is on the waist (blue line) and the instances where the ZUPT detector indicates a zero-velocity (red dots)

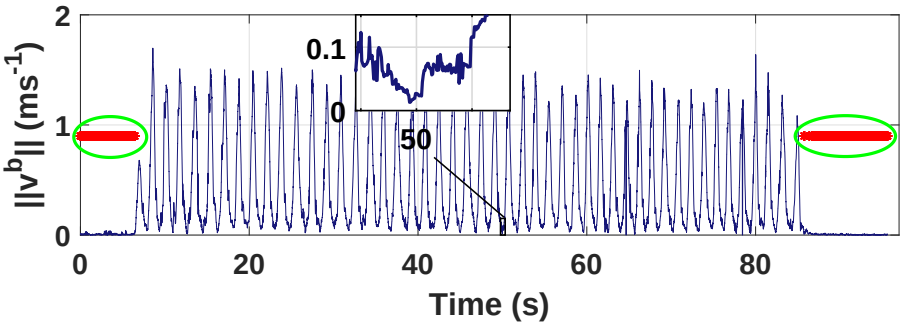

Figure 4.6: The velocity norm when the sensor is on the ankle (blue line) and the instances where the ZUPT detector indicates a zero-velocity (red dots)

In Fig. 4.5, when the sensor board is placed on the waist, the SHOE detector succeeds to accurately recognize the zero-velocities instants at the beginning and the end of the trajectory scenario (circled in green). However, it also detects other zero-velocity moments during the trajectory despite that the velocity norm is not necessarily equal to zero. For instance, a zero-velocity moment is detected at $t_1 = 103.8\ s$, corresponding to, $||v^b(t_1)|| = 0.9\ ms^{-1}$, which implies that this detection is rather false.

On the other side, it is expected that much more zero-velocity moments are detected when the sensor board is located on the ankle as this placement is very close to the one on the foot. So, the dynamics of v^b are somewhat similar to the ones observed from the foot. Nevertheless, in Fig. 4.6, it is observed that the SHOE only detects the static phases at the beginning and the end of the walking scenario (circled in green), without being able to recognize any other zero-velocity mo-

ments. For example, by looking at the zoomed area of Fig. 4.6, it is almost evident that at $t_2 = 50\ s$, a zero-velocity moment occurs as the velocity norm is very low, i.e. $||v^b(t_2)|| < 0.05\ ms^{-1}$, however, the SHOE fails at identifying not only this instance, but many other ones.
These false and/or undetected zero-velocity instances caused by the use of SHOE in a non foot-mounted framework affect the accuracy of the EKF-ZUPT approach, making of it an unsuitable solution for any other application that requires placing the sensor board somewhere other than the foot. Consequently, it becomes evident that such method (ZUPT) cannot be extended to applications outside of the pedestrian/humanoid scope, such as vehicles, aircrafts, etc.

Remark 17 *These detection results can vary to some extent with a different tuning of the ZUPT window and detection threshold parameters, but the same conclusions are made. The ZUPT cannot correct the velocity errors generated by the magnetic field gradient-based EKF, especially those caused by the low magnetic disturbances case, and when the sensor board is placed somewhere other than the foot of a pedestrian.*

From the remark above, one can notice that, in addition to limiting the location of the sensor board, and the nature of the motion to be studied (i.e. human-like), employing ZUPT introduces one more constraint that is related to the tuning of its detector's parameters (i.e. window size W_s and detection threshold δ_d). It is underlined here, that the statistical detector is selected from various choices that can be found in the related literature Ref. [Skog2010b], which represents itself an unstraightforward task.
The choice of these parameters is conducted taking into account the pedestrian's walking pace, the nature of the walk that varies from one subject to another, etc. This means that in order for ZUPT to work during multiple experiments, these parameters should be continuously tuned, to not only adapt to the different walking paces that may appear during one trajectory, but to be also applied on different targeted individuals.
This constraint gave rise to several works in the literature that aim to develop innovative methods, either to properly select these parameters such as in Ref. [Wang2015] or to adaptively tune them like in Refs. [Wahlström2019, Wang2019c, Wagstaff2017, Liu2014, Wang2018, Wagstaff2019]. In contrast, many other works are rather proposing approaches to achieve the zero-velocity detection without relying on any threshold-based methodology such as in Refs. [Cho2019, Sun2018]. From these works, a large variety are focusing on one powerful tool, known as Artificial Intelligence (AI) Ref. [Nilsson2014b], from which two concepts can be exploited: Machine Learning (ML) Ref. [Mitchell2013], and its subset, Deep Learning (DL) Ref. [LeCun2015]. Both these channels can perform the same task: deriving a model that enables the detection of zero-velocity moments through learning their relationship with sensors data features, as conducted in Refs. [Kone2020, Wagstaff2018] for example. Nevertheless, as efficient these approaches can be in terms of prediction accuracy, the use of AI raises many questions about the need to use large training datasets, the heavy computational cost that they require, and so on. These inconveniences are discussed further in detail in the next section.
For the time being, what needs to be recalled is that relying on the detection of zero-velocity instants, does not represent a general solution that can be applicable to any navigation scenario (i.e. with a non foot-mounted sensor, on vehicles, etc.) and introduces a lot of constraints (detector choice, parameters tuning, large training datasets, etc.). In the next sections, an alternative solution is proposed, that not only helps avoid the different disadvantages introduced by the ZUPT, but also provides very promising results, with minimal resources and under any navigation scenario.

4.2 Neural networks in indoor navigation

During the last decades, AI-based research has witnessed an exponential growth and a major interest in various applications (e.g. computer vision, robotics, natural language programming, etc.), from which indoor navigation takes part. More recently, one subset that emerged from the AI framework and proved its efficiency in performing prediction tasks is called *Deep Learning (DL)*, that is conducted using what are known as *Deep Neural Networks (DNNs)*. This fast development is the outcome of designing more powerful hardware through the years, that can perform complex and heavy computations, and the availability of more public data, that can be employed in the learning process.
The next sections discuss the use of deep learning in magneto-inertial indoor navigation and how it can be used to enhance a more "traditional" state estimation approach such as the Kalman filter.

4.2.1 Artificial neural networks overview

Before examining the role that Artificial Neural Networks (ANNs) occupy in the magneto-inertial navigation scheme, one should first understand how such approach works, and why its gaining an enormous interest from the research field.

Artificial neural network architecture

An Artificial neural network is a system whose structure is schematically inspired by the behavior of the human brain, mimicking the way that biological neurons communicate with one another. Neural networks are typically formed with layers: an input layer, one or more hidden layers and an output layer. An ANN with more than one hidden layer is considered a "deep" neural network. The layers are constituted of a number of interconnected *nodes*, or *artificial neurons*. An example of a DNN with two inputs, two hidden layers, and one output, is presented in Fig. 4.7.

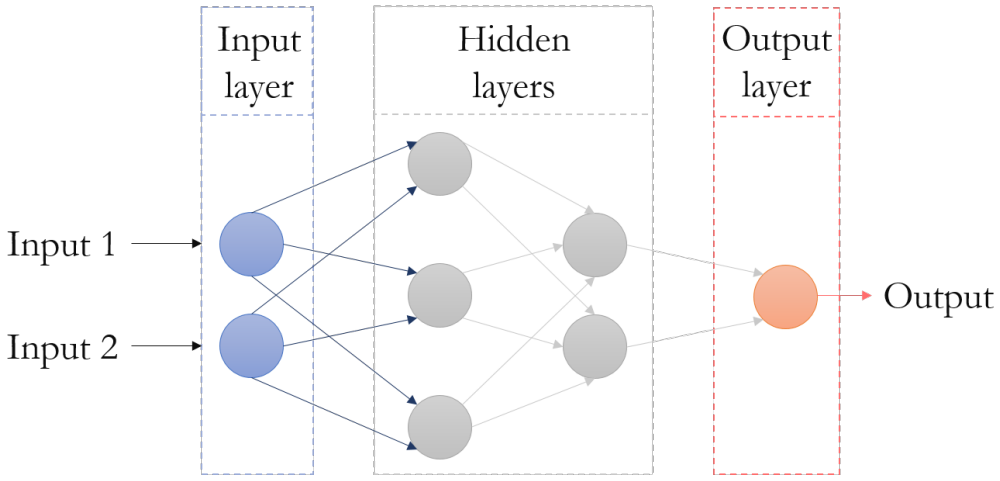

Figure 4.7: Example of a deep neural network architecture

Learning process of an artificial neural network

The training of a basic ANN architecture represents a *supervised learning* process Ref. [Reed1999] where a descriptive model is determined through learning the relationship between inputs and outputs from a particular training set.
In a neural network, each node in each layer (excluding input nodes) computes the weighted sum of its inputs, that is added to a scalar *bias* value, as illustrated in Fig. 4.8. The obtained vector is passed to an *activation function* (e.g. linear, tanh, sigmoid, etc.) that computes the output of that

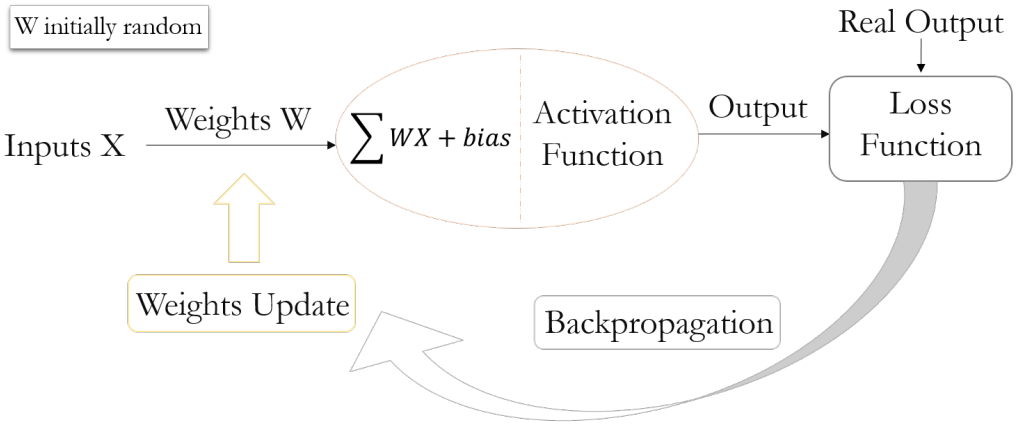

Figure 4.8: Output node example of the learning process

node Ref. [Sharma2017].
When the last output is generated from the output layer of the neural network, a *loss function* is calculated (e.g. MSE, MAE, etc), to compare the prediction of the network to the ground truth output (contained in the training set). Then, a reversed step is performed, known as *backpropagation* where the weights and the bias are adjusted, using a *gradient descent* scheme, to minimize the loss Ref. [Amari1993].
This process is repeated several times inside a loop, until the best prediction accuracy is reached (i.e. the loss function is at its minimum). In other words, determining the optimal values of weights and bias is the main objective of the training process, as these variables define the learned model that is used later to predict the outputs of the testing set from the corresponding inputs.
Designing any deep neural network, requires making multiple choices such as the number of layers, the number of nodes in each layer, the activation functions between the layers, the loss function, and many other parameters that play an important role in ensuring the best performance from the network. This variety in the configuration raises one question: to what extent using DNNs for magneto-inertial indoor navigation can be straightforward ? A discussion on the efficiency of the existing works in the related literature is conducted next.

4.2.2 State-of-the-art related works

The estimation of the trajectory using only a learned model from magneto-inertial measurements and a deep neural network is a methodology that is adopted by many works in the related literature. Nevertheless, most of these works are focusing on pedestrian-related applications and on particular human motion characteristics to recover the trajectory Refs. [Edel2015, Xing2017]. For instance, in Ref. [Wang2019b], authors propose a stride length estimation method, based on a Long Short-Term Memory Network (LSTM) Ref. [Hochreiter1997] and a Denoising Autoencoder (DAE) Ref. [Vincent2010]. While the proposed approach achieves encouraging results, to estimate an accurate position, the user must have not only a ground truth IMU attached to the foot but also hold the phone IMU in front of his/her chest, as the proposed solution is rotation-variant. This does not represent the general applicability condition, targeted by this thesis.
To address these challenges, in Refs. [Chen2018a, Chen2019b, Chen2020a], traditional PDR equations are reformulated as a polar vector based model, containing both the traveled distance of a moving body and its corresponding change of heading. These two variables are learned using raw IMU data, and different possible types of Recurrent Neural Networks (RNNs) Ref. [Medsker1999], to provide at the end, a trajectory estimation. The approach provides promising results, yet, it is assumed that the displacement with respect to the $z-axis$ is zero (i.e. navigation is conducted only on an horizontal plane). To extend the solution to the 3 dimensional

case, additional sensor modalities should be considered (e.g. barometer). This is against one of the requirements of this thesis, to use only magneto-inertial measurements and no other additional sensor.
In a different manner, in Ref. [Feigl2019], authors consider velocity estimation as a regression problem that is solved using a hybrid solution combining a Convolutional Neural Network (CNN) Ref. [Albawi2017], to extract features of human motion, and a Bidirectional LSTM network (BiLSTM) Ref. [Schuster1997], to track this motion over time. This is done by learning how to map IMU measurements to different human movement velocities such as walking, jogging, running, and a random combination of all. While the proposed approach provides interesting results in terms of velocity estimation accuracy (instantaneous velocity error ≤ 0.1 ms^{-1}), the training process of such solution requires 9 *hours* (h) of training for each considered set of parameters (i.e. sample rate, network window length, etc.), for a total of 800 *min* of data recordings. Similar observations are found in Ref. [Feigl2020], where the proposed CNN-BiLSTM solution of Ref. [Feigl2019] is further enhanced. In that work, several comparisons are conducted one the computational effort of the proposed approach with respect to other methods in the literature. It was shown that the proposed solution requires 15.6 h to train for a 1203 *min* training dataset (with 112500 windows), compared to the one in Ref. [Feigl2019], as it has a rather more complex network design. The approach is also compared to Ref. [Herath2020] that uses an LSTM for heading estimation and a Residual Neural Network (ResNet Ref. [He2016]), that is known to be computationally heavy due to its many parameters, generating then a training time of 11.2 h.
From the discussion above, one can draw two main conclusions:

- it seems that the most used types of Neural Networks (NNs) in the related state-of-the-art belong to the family of recurrent architectures. This is actually justifiable for time-series data and is explained in detail in the next section;
- using only a DL-based approach introduces several drawbacks, from which, the computational cost is the most remarkable, as well as the need to acquire large and diverse training datasets, which is not always accessible.

For the reasons above, a BiLSTM-aided approach is proposed later, that does not require any heavy training process and provides in the same time, an estimation accuracy that competes with top-ranked methods in the literature.

Remark 18 *It is underlined that, in this thesis, velocity estimation using DL, is handled as a regression problem, i.e. the predicted velocity is a continuous output variable, represented with a numerical value, and is not described as a label or a category, as the case for classification problems.*

4.3 Velocity estimation using BiLSTM

The different surveys and comparisons presented in related state-of-the-art Refs. [Alom2019, Nessa2020, Kang2018a, Feigl2020], suggest that estimating the velocity of a moving body using a BiLSTM architecture can provide promising results. Nevertheless, one should verify to what extent these results are useful, in the case of a light training process with a limited training dataset.

4.3.1 Introduction to the BiLSTM network

The BiLSTM architecture is an improved version of unidirectional LSTM, which itself, is an extension of the RNN architecture. To understand the benefit of employing a BiLSTM, one should

first explain the advantage of RNNs, compared to conventional feed-forward ANNs Ref. [Bebis1994].

Feed-forward neural network In a feed-forward ANN Ref. [Bebis1994], information is only transmitted in one direction: from the input layer, through the hidden layers, to the output layer. Such architecture only considers the current input to predict the next output, ignoring that way, all information about the past.

Recurrent neural network Contrarily to a feed-forward NN, a RNN Ref. [Medsker1999] performs a decision, by considering not only the current input, but also what it has learned from the inputs of the "recent" past (i.e. RNN has a short-term memory). An illustration of the information flow in an RNN is presented in Fig. 4.9.

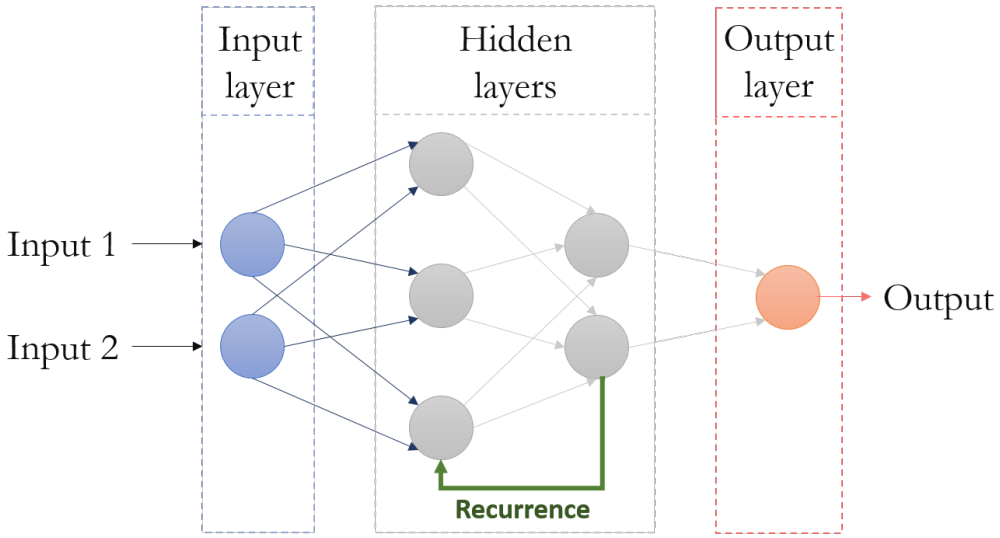

Figure 4.9: Illustration of a recurrent neural network

An RNN architecture is then very useful when dealing with sequential or time-series data, as it assumes that each sample in the data is dependent on previous ones, which is the case when analyzing inertial and magnetic measurements corresponding to a trajectory. In other words, the velocity of a moving body at a specific time-step, is indeed dependent on its previous values, which makes RNN an adequate solution to conduct its prediction.

Nevertheless, there is a major drawback when using a simple RNN architecture: vanishing and exploding gradients, i.e. during backpropagation, the network assigns too low or too high values to the weights, causing the model to either completely stop learning without reaching the optimal accuracy, or becoming unstable which results in predicted "NaN" values. This implies that RNNs cannot efficiently process long data sequences which calls for a better architecture to solve these issues, known as the LSTM network.

Unidirectional long short-term memory neural network Unidirectional LSTMs Ref. [Hochreiter1997] are an enhanced version of RNNs, that include a *memory cell*, enabling the network to memorize inputs over a longer period of time and solve especially the vanishing gradient problem. The particularity of an LSTM is its ability to control over time, using a set of *gates*, when an information enters the memory, when it outputs and when it is forgotten, based on a decided importance determined by learned weights. This sorting process keeps the training relatively short and the prediction accuracy rather high.

Bidirectional LSTM neural network To improve even further the performance of the network, two LSTM layers are combined to form what is known as the bidirectional LSTM Ref. [Schuster1997]. At every time step, the first LSTM takes the input sequence (time-series data in this case) as it is, i.e. in its forward direction, and the second LSTM receives a reversed copy of this sequence, i.e. in its backward direction. This enables the BiLSTM network during training to

preserve information from both the past and the future, contrarily to the LSTM that only takes into account previous information. By incorporating anterior and posterior knowledge, the BiLSTM is better at understanding context, which results in a faster learning process of long-term dependencies and thus consequently, higher prediction accuracy results, as shown in Ref. [Siami-Namini2019], for example.
For the reasons above, in the continuity of this thesis, the BiLSTM architecture is used to represent the DL part of the proposed approach.

4.3.2 Preliminary results and discussion

As discussed earlier, the BiLSTM network cannot provide accurate velocity estimation results if the network training process is not complex enough to account for the different dynamics that may occur during a specific trajectory scenario. To investigate further this idea, some tests are undertaken using real magneto-inertial measurements, acquired from a commonly used dataset in the related literature, called *Openshoe* Ref. [Nilsson2012].

Dataset and implementation details

Openshoe dataset The used Openshoe dataset in this chapter, contains real experimental (noisy and biased) foot-mounted inertial and magnetic measurements (a $3-axis$ accelerometer, a $3-axis$ gyroscope and a $3-axis$ magnetometer), sampled at a frequency of 250 Hz, representing some sort of a "figure-of-eight" trajectory. In addition to that dataset, a ZUPT-based algorithm is provided Ref. [Nilsson2012], that enables an accurate estimation of the velocity of the moving body, and consequently an accurate reconstruction of the performed trajectory. For the BiLSTM training process and for any comparisons, the ZUPT estimation is considered as the ground truth data (as it can be trusted during a foot-mounted framework), because no motion capture system information is provided with the dataset. In the rest of this chapter, "ground truth" refers then to "ZUPT estimate".
It is underlined that no magnetometer array measurements are provided with this dataset, thus, four magnetic fields are simulated in the same manner as in Chapter 3. These measurements are necessary to run the magnetic field gradient-based EKF, however, they are not used in the BiLSTM network.
BiLSTM training Before proceeding with any performance analysis, one should first choose a specific architecture for the BiLSTM-based network to enable the training process, and eventually the outputs' prediction. Several hyperparameters (e.g. number of hidden layers, number of nodes, etc.) have to be pre-identified, which represents itself a research problem that requires the implementation of optimization-based algorithms Ref. [Kaselimi2019], in order to provide the best prediction accuracy results.
Nevertheless, it is reminded that, the goal here is to provide a solution, that is simple, and computationally light, while also generating a useful prediction (i.e. not necessarily optimal) which somehow improves the velocity estimation accuracy of the magnetic field gradient-based EKF. A basic architecture design can actually satisfy these criteria and is proposed in Fig. 4.10. The network starts with a sequence input layer receiving 9 features, representing available sensor measurements, i.e. raw data of the $3-axis$ accelerometer, $3-axis$ gyroscope, and $3-axis$ magnetometer. Then, there is the first BiLSTM layer, containing 100 hidden units (i.e. nodes). This value is hand-tuned on the basis of two constraints: maintaining a fast training, and generating a good accuracy. Note that a *tanh* activation function is used for updating the cell and hidden states, and a *sigmoid* activation function is applied to the gates. These functions are the literature basic ones used in a BiLSTM layer.
Next, a *dropout* Ref. [Baldi2013] layer is considered. Briefly, dropout is a regularization technique that ignores (zeros out) a chosen percentage of neurons, randomly from each hidden layer, for every training sample, to obtain at the end different prediction models, that are averaged later

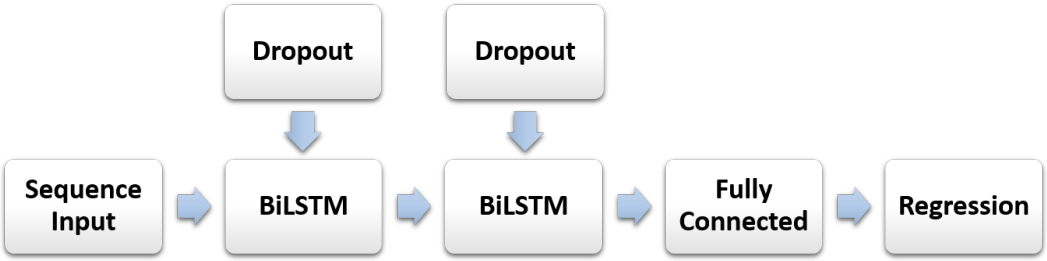

Figure 4.10: Diagram of the used BiLSTM network

on to form the final model. This is in order to prevent *overfitting*, i.e. when the learned model of the network is too representative of the training data to the extent that it cannot perform well on new testing data. A dropout of 25 % is chosen after few trial and error testings. Yet, this hyperparameter should be more carefully tuned if optimal results are targeted.
These two layers (BiLSTM and dropout) are added only twice to the network, in order to have the "deep" aspect of the proposed architecture, while preserving the desired simplicity.
The output of the last BiLSTM layer is fed to a fully connected layer Ref. [Sainath2015], which simply transforms that output into the form of the targeted $3-axis$ velocity to be predicted $v^b_{BiLSTM} = [v^b_{x,BiLSTM} \;\; v^b_{y,BiLSTM} \;\; v^b_{z,BiLSTM}] \in \mathbb{R}^{3\times 1}$. It is followed by a regression layer that computes the loss function (MSE in this case) between the ground truth velocity and the predicted one v^b_{BiLSTM}.
The objective of the proposed network is then to learn a model, that computes, for each time step k

$$v^b_{BiLSTM,k} = BiLSTM(\omega^b_k, a^b_k, B^b_k) \tag{4.1}$$

During training, Adam optimizer is applied Ref. [Kingma2015], to update the network's weights, thanks to its numerous advantages, compared to the basic stochastic gradient descent algorithm. The weights are adjusted using a learning rate, which initial value is chosen equal to 0.0015, and is dynamically reduced during training according to a pre-defined schedule (piecewise, with a drop period of 125 epochs) and a drop factor of 0.2. A detailed explanation on the learning rate configuration can be found in Ref. [Senior2013].
The training is set to run for a maximum of 500 epochs. Before proceeding, a standardization Ref. [Anysz2016] is applied on the training dataset, which consists basically in subtracting its arithmetic mean and dividing the result by its standard deviation. The same calculated mean and standard deviation are then used to standardize the testing set. The reason behind this step is to avoid using features at different scales, (as measurements have different units), as it may lead some features to outweigh others and thus do not contribute equally to the training process.
In the following analysis, the training set represents 50% of the Openshoe dataset, that is also used for validation, while the other 50% are kept for testing. The *validation patience* is set to 5 epochs, i.e. if the loss on the validation set does not decrease from the previous smallest loss for 5 consecutive epochs, an "early stopping" of the training occurs, to prevent overfitting and optimize computation time. The 50% training portion is equivalent to 7038 samples, which is considered very small for a training process. Yet, one needs to investigate the network performance in such condition, to see if it can be useful despite the light training process.
The implementation, training and prediction steps of the BiLSTM network are done under Matlab and its deep learning toolbox, on a CPU Intel Core $i7@1.9\ GHz$. The training of the BiLSTM-based network takes around 40 *min* to run the 500 epochs, which is considered very fast compared to related state-of-the-art works. This value decreases significantly (to ≈ 15 *min*) under a Graphics Processing Unit (GPU) environment (using python in Google Colab).

Velocity estimation using the BiLSTM-based network

In Fig. 4.11, the result of the velocity prediction using the proposed BiLSTM network, applied on the testing set, is displayed. From this figure, and by comparing to the ground truth, it seems

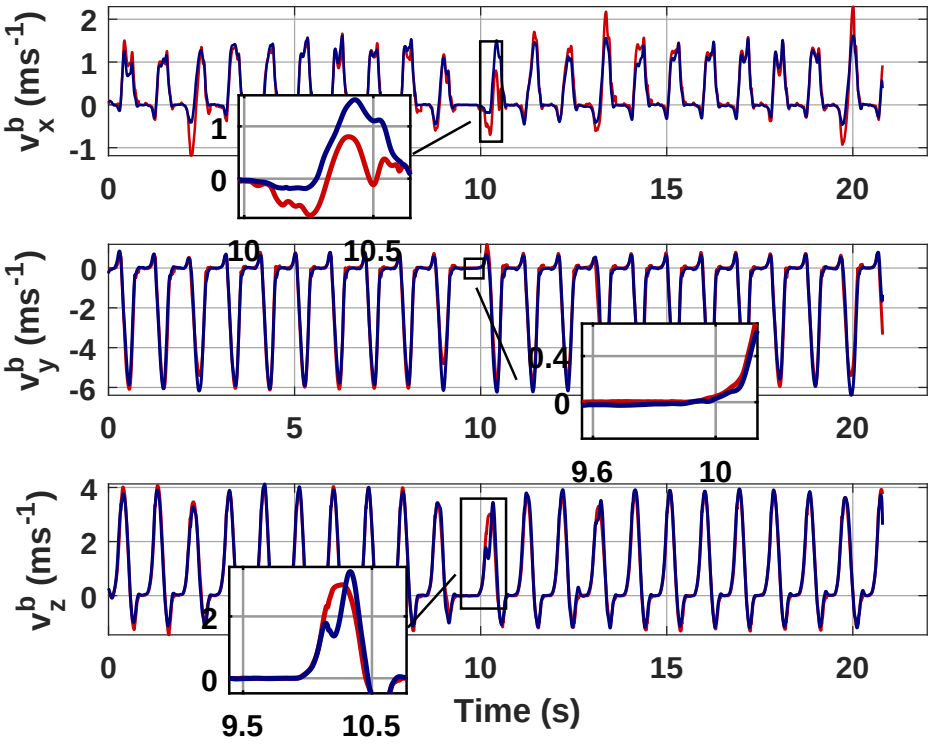

Figure 4.11: Prediction of v^b using only the BiLSTM network for the testing set. In red is the ground truth velocity and in blue is the BiLSTM estimate v^b_{BiLSTM}

that the BiLSTM prediction is quite accurate during instants where the velocity values are equal or close to zero (quasi-static phases) as indicated in the zoomed area of $v^b_{y,BiLSTM}$, for example. However, when the velocity amplitudes are rather large (dynamic phases), the BiLSTM prediction is most of the times unreliable, as clearly shown for instance in the subplot of $v^b_{x,BiLSTM}$.
Such behavior is the outcome of two main reasons: first, it is almost evident for the BiLSTM to detect quasi-static phases, as the corresponding sensor measurements at those times are quite representative and proportional to the targeted output, i.e. a low acceleration and angular rate, for example, will most likely correspond to a low amplitude velocity. Such conditions make it easier for the regression algorithm to fit the input data to the output, without requiring any complex modeling. On the contrary, when dealing with a dynamic behavior of data, the BiLSTM prediction task becomes less straightforward, as the multiple combinations of measurements' values generate different velocities, leading to some sort of a non-linear model that does not necessarily perform well under all possible scenarios. Second, it is believed that the limited training dataset (only 7038 samples), plays a huge role in the BiLSTM prediction inaccuracy during dynamic phases, as it lacks diversity of data that correspond to a varying velocity behavior, and cannot be used to derive an all-time working model. To back up this assumption, an analysis is conducted. First, to avoid being biased by the network's performance during quasi-static phases, any data corresponding to a velocity with an amplitude lower than 0.2 ms^{-1} (chosen value to represent a quasi-static velocity, see Section 4.5.1) is removed. This provides a solely dynamic phases-based dataset, with only 5541 samples, from which 70% (equivalent to 3878 samples) are for the training, and 30% (equivalent to 1663 samples) are for the testing. Then, the impact of the training

data percentage of this dynamic dataset on the prediction accuracy of v^b_{BiLSTM} is analyzed using the boxplot Ref. [Williamson1989] in Fig. 4.12. To do so, the RMSE between the ground truth and

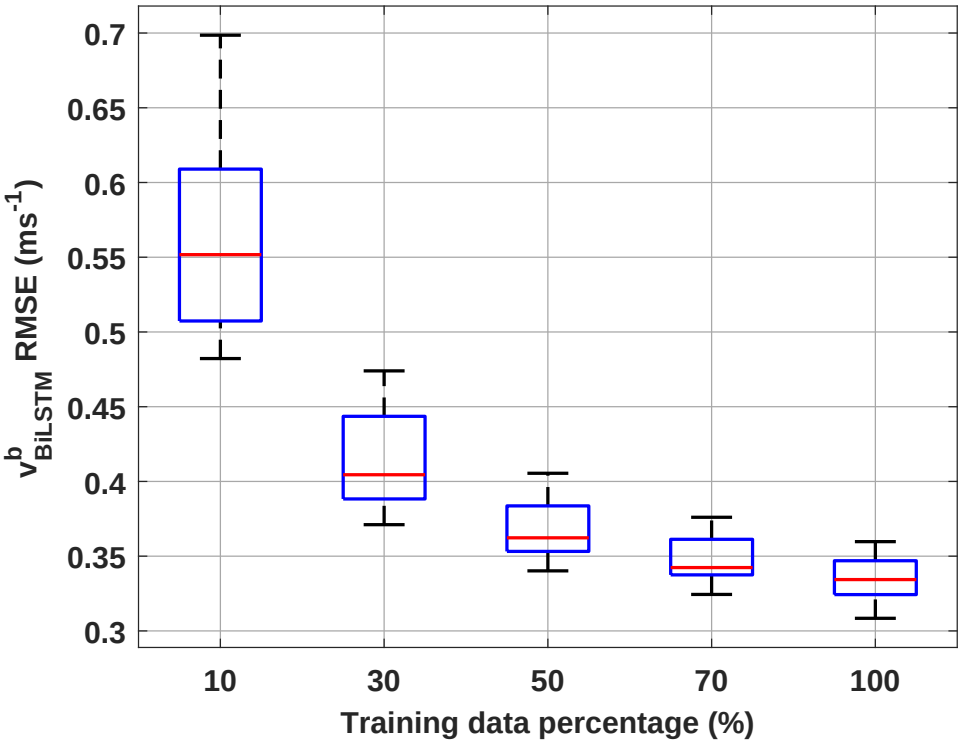

Figure 4.12: Effect of dynamic training data percentage on the RMSE of v^b_{BiLSTM}. Larger the percentage of the training data, the smaller velocity RMSE of the testing data becomes

the BiLSTM predicted velocity (of the testing set) is measured for different used percentages of the training dataset. The learning process is repeated 20 times for each training data percentage, as it is based on various randomnesses that affect the prediction accuracy during each run, and thus analyzing average results is more rigorous. Note that the 30% of data corresponding to the testing set are always fixed.
As the training data percentage increases, the RMSE of the predicted velocity of the testing set gradually decreases, for instance, by looking at the median values represented by the red horizontal lines in Fig. 4.12.
The results indicate that as more data of dynamic phases is provided to the BiLSTM during training, the prediction of v^b_{BiLSTM} at these times is more accurate. Nevertheless, optimal BiLSTM accuracy results for high amplitudes velocities is not of priority, especially if it requires having a large training dataset. The obtained accuracy for quasi-static instants is enough to proceed with the proposed approach and improve the estimation of the magnetic field gradient-based EKF, as presented in the following section.

4.4 Proposed EKF-BiLSTM estimation approach

So far, from the different conducted analyses, one can draw the following conclusion: the magnetic field gradient-based EKF may suffer from errors, mainly during low magnetic field gra-

dient instants as well as static or quasi-static trajectories. Meanwhile, a BiLSTM based approach, can provide a good velocity estimation during these instants, without the need to employ any large training dataset. An obvious idea that enables to take advantage of both the EKF and the BiLSTM estimations is then to combine both these approaches into one general solution that performs well, no matter the trajectory's nature.

4.4.1 Kalman filter and neural networks: related state-of-the-art

Difference between both methods

Combining Kalman filtering and deep learning methods is a methodology that has already been considered in many works in the related literature. While both these techniques can perform state estimation using a set of measurements, their mechanisms are completely different. The Kalman filter requires modeling the states' dynamics using pre-derived differential equations, but does not always succeed to mimic the reality. In contrast, neural networks learn the system's model from available training data that also does not necessarily cover all of its dynamics. This is what makes the Kalman filter and neural networks rather complementary and encourages coupling them in one efficient solution.

Related state-of-the-art

Incorporating deep learning into Kalman filtering can be performed in two different manners. A first methodology resides on using neural networks to learn the model of the Kalman filter from the available data. This can be done by acting directly on its state transition and measurement functions (f and h) as performed in Refs. [Chen2019a, Shen2020, Coskun2017, Li2020, Hosseinyalamdary2018], or/and by intervening in the tuning of its unknown parameters, such as the process and measurement noise covariance matrices (Q and N), as done in Refs. [Jamil2020, Ullah2019, Coskun2017].
The other concept is to use the neural network for an auxiliary and independent task, that generates a certain output to be fed to the Kalman filter once the training process is over Refs. [Ashraf2019, Brossard2020a]. In Ref. [Liu2020], authors propose an innovative ResNet-aided EKF architecture, that jointly enables the estimation of position, orientation, velocity, and IMU biases using only IMU data. In that work, the neural network outputs an estimate of a pedestrian $3D$ displacement and its corresponding uncertainty, that are then employed as a measurement update in the EKF. In a similar manner, but for intelligent vehicles applications, in Ref. [Brossard2020b], it is proposed to use a CNN to dynamically tune the noise parameters of an Invariant EKF (IEKF). This is done by assuming that, in a car frame, the lateral and vertical velocities are "roughly null". This knowledge on the dynamics of two velocity axes enables considering them as pseudo-measurements that are fed to the IEKF, and controlled using their corresponding noise parameters.

Chapter contribution

Following a similar principle to the one in Ref. [Brossard2020b], a novel method is proposed, that improves the performance of the magnetic field gradient-based EKF, especially when the latter fails at providing an accurate states estimation, such as during low magnetic field gradient instants, or static/quasi-static phases, as discussed in Section 4.1. This is achieved by taking advantage of the velocity information provided by the BiLSTM, and considering it as a pseudo-measurement in the EKF. Such process is conducted while simultaneously controlling the level of confidence given to this measurement through the adaptation of its corresponding noise covariance matrix in the EKF. More details on the proposed approach are given in the next section.

4.4.2 General overview of the EKF-BiLSTM approach

Main idea of the proposed approach

The proposed EKF-BiLSTM approach consists of three main blocks and is represented in Fig. 4.13.

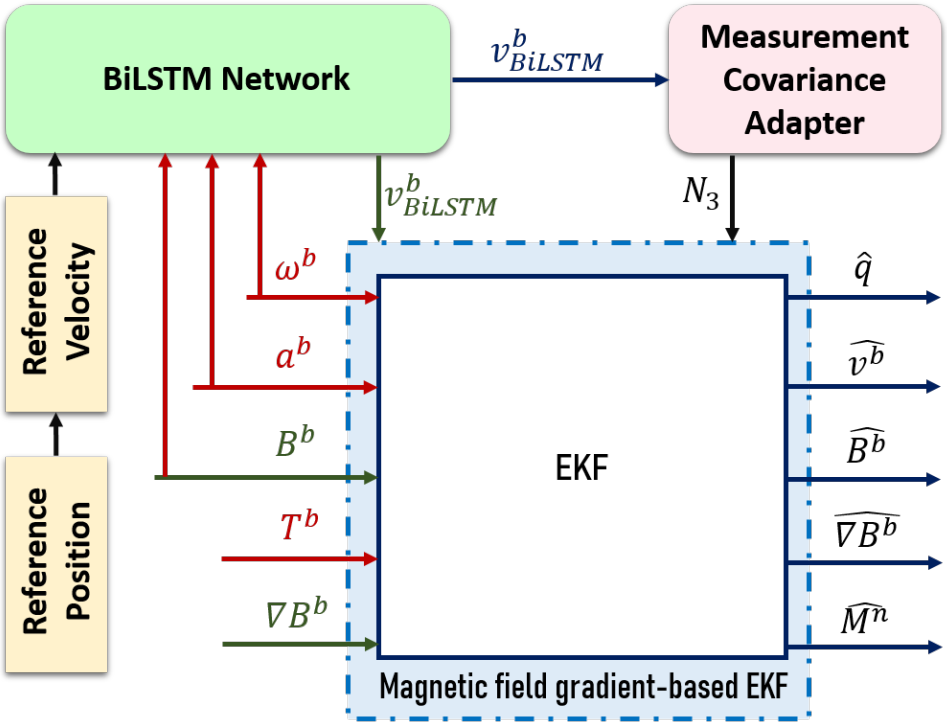

Figure 4.13: Diagram of the proposed EKF-BiLSTM estimation approach

The proposed estimation scheme can be summarized with the following steps:

- a training dataset is generated. The inputs are a set of raw sensor measurements (9 features, representing the angular rate, acceleration and magnetic field), while the output is a $3-axis$ reference velocity, usually computed from a reference position (orange blocs), acquired from a motion capture system;
- the training dataset is fed to the BiLSTM (green block), that uses it to learn a model, representing the relationship between the considered inputs and outputs;
- on the testing dataset, the BiLSTM is then able to predict the velocity v^b_{BiLSTM}, from the inputs of that particular data;
- the predicted velocity v^b_{BiLSTM} is considered as a pseudo-measurement, that is added to the output vector of the magnetic field gradient-based EKF (blue block), represented by the continuous-time dynamic model of Eqs. (2.33)-(2.37), such that $y(t) = [B^b \ \nabla B^b \ v^b_{BiLSTM}] \in \mathbb{R}^{11\times 1}$;
- a measurement covariance matrix adapter (red block) dynamically tunes the noise parameters corresponding to v^b_{BiLSTM}, to control in a way, the level of confidence given to this pseudo-measurement, by the EKF. In fact, after augmenting the output vector of the EKF with v^b_{BiLSTM}, the measurement noise covariance matrix becomes $N = diag(N_1,\ N_2,\ N_3) \in \mathbb{R}^{11\times 11}$, where $N_1 \in \mathbb{R}^{3\times 3}$, $N_2 \in \mathbb{R}^{5\times 5}$ and $N_3 \in \mathbb{R}^{3\times 3}$, are the noise covariance matrices, corresponding to B^b, ∇B^b and v^b_{BiLSTM}, respectively. This means that the dynamic tuning in this

proposed approach, concerns only N_3. Regarding N_1 and N_2, their values are fixed taking into account the sensor board's noise characteristics, which are usually provided in its corresponding datasheet. It is underlined here that no dynamic adaptation is performed for the process noise covariance matrix Q. As the previous chapters, the process noise parameters are fixed through a hand-tuning step under a trial and error scheme;

- the magnetic field gradient-based EKF uses the continuous-time dynamic model of Eqs. (2.33)-(2.37), inertial and magnetic measurements, v^b_{BiLSTM} and N_3 to better estimate the different states, especially under challenging instants (low magnetic field gradient, static phases, etc.).

Measurement covariance adapter

The basic idea of the measurement covariance adapter is to dynamically set the noise parameters of N_3, in order to implicitly decide which of the EKF or the BiLSTM velocity estimations is more likely to be accurate during a specific instant, and thus should be more trusted. Such process is based on Algorithm 1 and it works as follows

EKF initialization;
for $k = 1 : length\ (testdata)$ **do**
  $N_{3,k} = \alpha \mathbb{I}_3$;
  EKF prediction;
  if $v^b_{BiLSTM,k} \leq \varepsilon$ **then**
    $N_{3,k} = \mathbb{I}_3$;
  end
  EKF update;
end

Algorithm 1: Algorithm of the measurement covariance adapter

After initializing the magnetic field gradient-based EKF, and for the first time step k inside the EKF loop, high values are assigned to N_3 using a large multiplication factor $\alpha \in \mathbb{R}_{>0}$ that is multiplied with the identity matrix $\mathbb{I}_3$. This is in order to give more confidence to the EKF velocity estimation than the one of the BiLSTM, that cannot provide accurate results in the case of high amplitude velocities (dynamic instants), especially under a light training process with a small training dataset. On the contrary, during such a dynamic behavior, the EKF has proven to be efficient in determining a velocity estimate with minimal errors, as the magnetic field gradient is sufficiently strong at these times.
Next, the EKF prediction is performed to obtain a first velocity estimate. At this point, the algorithm checks if v^b_{BiLSTM} is below a certain threshold $\varepsilon \in \mathbb{R}_{>0}$, to indicate whether a static or quasi-static phase of the velocity is occurring (i.e. velocity is null or close to zero). If this condition is satisfied, the adapter attributes only $\mathbb{I}_3$ to N_3 (i.e. a small value) in order to trust more the BiLSTM prediction. In fact, when the velocity has low amplitudes, the BiLSTM is more accurate at determining its values because the regression task is much simpler under such condition, as discussed in Section 4.3.2. The EKF however, suffers from errors at those instants, as shown in Section 4.1, therefore, its estimation should be less taken into account.
Once the tuning is performed, the EKF update step is undertaken to take into account the chosen value of N_3, and provide a final velocity estimate on the basis of this adaptation.

What about observability?

Considering the BiLSTM predicted velocity v^b_{BiLSTM} as a pseudo-measurement in the EKF implies a change in the measurement matrix H, previously defined in Eq. (2.39). In the proposed EKF-

BiLSTM approach, not only does the velocity represent a state to be estimated, but it is also contained in the output vector of the EKF, which implies

$$H' = \begin{bmatrix} 0_{11\times4} & I_{11} & 0_{11\times3} \end{bmatrix} \tag{4.2}$$

where $H' \in \mathbb{R}^{11\times18}$ is the measurement matrix corresponding to the proposed EKF-BiLSTM approach.
As no modification is conducted to the model governed by Eqs. (2.33)-(2.37), the state matrix F, defined in Eq. (2.38), remains unchanged.
The observability matrix $\mathscr{O}''$ of the proposed EKF-BiLSTM approach is then defined such that

$$\mathscr{O}'' = \begin{bmatrix} 0_{3\times4} & I_3 & 0_{3\times3} & 0_{3\times5} & 0_{3\times3} \\ 0_{3\times4} & 0_{3\times3} & I_3 & 0_{3\times5} & 0_{3\times3} \\ 0_{5\times4} & 0_{5\times3} & 0_{5\times3} & I_5 & 0_{5\times3} \\ A_1 & -[\omega^b\times] & 0_{3\times3} & 0_{3\times5} & 0_{3\times3} \\ 0_{3\times4} & \nabla B^b & -[\omega^b\times] & A_4 & 0_{3\times3} \\ 0_{5\times4} & A_5 & 0_{5\times3} & A_6 & 0_{5\times3} \\ W_6 & [\omega^b\times]^2 & 0_{3\times3} & 0_{3\times5} & 0_{3\times3} \\ \nabla B^b A_1 & W_2 & [\omega^b\times]^2 & W_3 & 0_{3\times3} \\ A_5 A_1 & W_4 & 0_{5\times3} & A_6^2 & 0_{5\times3} \\ \frac{1}{2}W_6\Omega^b + [\omega^b\times]^2 A_1 & -[\omega^b\times]^3 & 0_{3\times3} & 0_{3\times5} & 0_{3\times3} \\ \frac{1}{2}\nabla B^b A_1\Omega^b + W_2 A_1 & W_5 & -[\omega^b\times]^3 & [\omega^b\times]^2 A_4 + W_3 A_6 & 0_{3\times3} \\ \frac{1}{2}A_5 A_1\Omega^b + W_4 A_1 & -W_4[\omega^b\times] + A_6^2 A_5 & 0_{5\times3} & A_6^3 & 0_{5\times3} \\ \vdots & \vdots & \vdots & \vdots & \vdots \end{bmatrix} \tag{4.3}$$

with $W_6 = \frac{1}{2}A_1\Omega^b - [\omega^b\times]A_1$.
In Section 2.2.2, after analyzing the observability matrix $\mathscr{O}'$ corresponding to the magnetic field gradient-based EKF, some conditions were imposed on the magnetic field gradient and hessian in order to ensure the observability of the states. In contrast, the proposed EKF-BiLSTM approach does not set any constraints on the magnetic field dynamics in order to observe the velocity. This can be easily detected by looking at the new observability matrix. In fact, an identity matrix appears on the second column of $\mathscr{O}''$, which implies that v^b is always observable, no matter the values of ∇B^b. Nevertheless, such flexibility in the velocity observability conditions does not guarantee the observability of quaternion that remains dependent firstly on the rank of A_1 (rank equal to 3 at max), and then, on the ranks of the following blocks (in the first column of $\mathscr{O}''$).

4.5 Experimental scenario and results

The proposed EKF-BiLSTM approach is applied on the Openshoe dataset, presented earlier in Section 4.3.2. To demonstrate the benefit of aiding the magnetic field gradient-based EKF with the BiLSTM-based network, the velocity estimation results of the EKF and the EKF-BiLSTM are

compared. The proposed solution exhibits a better performance in terms of estimation accuracy, and promising results when it comes to trajectory reconstruction.

4.5.1 Additional implementation details

Before implementing the EKF-BiLSTM solution, the measurement covariance adapter parameters have to be chosen, i.e. the multiplication factor α and the threshold ε.
The tuning of α is actually very straightforward. Its value should be set really high, so when it is assigned to N_3 (after being multiplied with the identity matrix I_3), the BiLSTM prediction (i.e v^b_{BiLSTM}), representing a pseudo-measurement in the EKF, is almost completely rejected by the EKF during the update step, because of this assigned large value, thus, it is chosen to be equal to $\alpha = 10^6$.
The threshold's tuning is less evident, but also remains very simple. In general, if a pedestrian navigation application is considered, the average value of the walking velocity of the latter can vary from 1 ms^{-1}, in the case of a low pace walk, until above 8 ms^{-1} during running. This means that in order to consider a velocity very low or quasi-static, it should have a value that is below approximately 0.5 ms^{-1}. This would apply on any kind of application and is not limited to human movement. Therefore, ε in the measurement covariance adapter is chosen in a way that represents a very small velocity value, nearly equal to zero, implying that the subject under study (or any moving body, such as a vehicle, for example) is almost immobile at that time instant. This is without being too close to zero as the main idea is to capture quasi-static instants and not zero-velocity moments. The choice of $\varepsilon = 0.2\ ms^{-1}$ is then done considering the above reasoning.
What makes the proposed approach stands out, is that such choice of parameters does not represent a critical problem that needs to be profoundly investigated (as the case for ZUPT parameters, for example). While the above tuning process remains important, it is believed that these two parameters do not necessarily have to be tuned every time the proposed approach is applied, as they are very general and not related to a particular movement nature, trajectory characteristics or sensor attachment. This supports the generality and applicability aspects of the proposed EKF-BiLSTM approach and indicates that it can be extended to any other application, whether its on pedestrians, vehicles, or robots.

4.5.2 Results of the magnetic field gradient-based EKF

One cannot asses the advantage of the proposed EKF-BiLSTM approach, without comparing its estimation accuracy results to when only the magnetic field gradient-based EKF is applied. To do so, the same implementation scenario of Section 4.3.2 is maintained, where 50% of the Openshoe dataset is used for testing.
As demonstrated in Section 4.1, the EKF encounters several limitations that highly influence its estimation accuracy results, from which, the low magnetic field gradient case is the most significant. To highlight this issue, the simulated magnetic field gradient from the magnetometer array measurements is set to have small eigenvalues (lower than 0.05 Gm^{-1}), as represented in Fig. 4.14.

Next, in Fig. 4.15, the velocity estimation results using only the magnetic field gradient-based EKF, for the considered scenario, are presented.

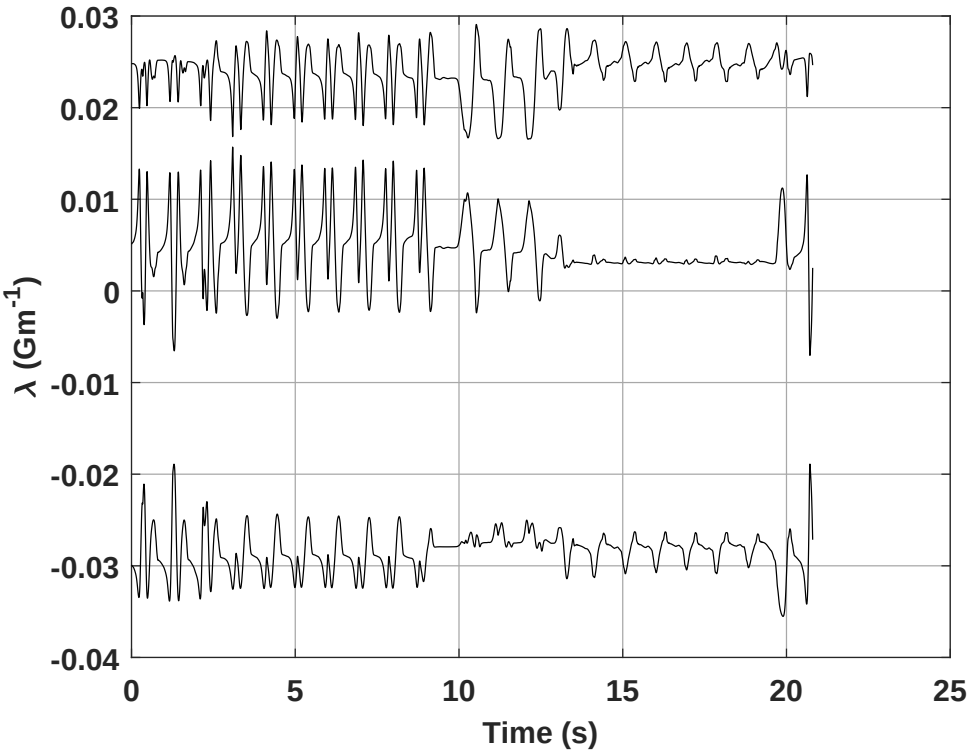

Figure 4.14: Eigenvalues of the magnetic field gradient

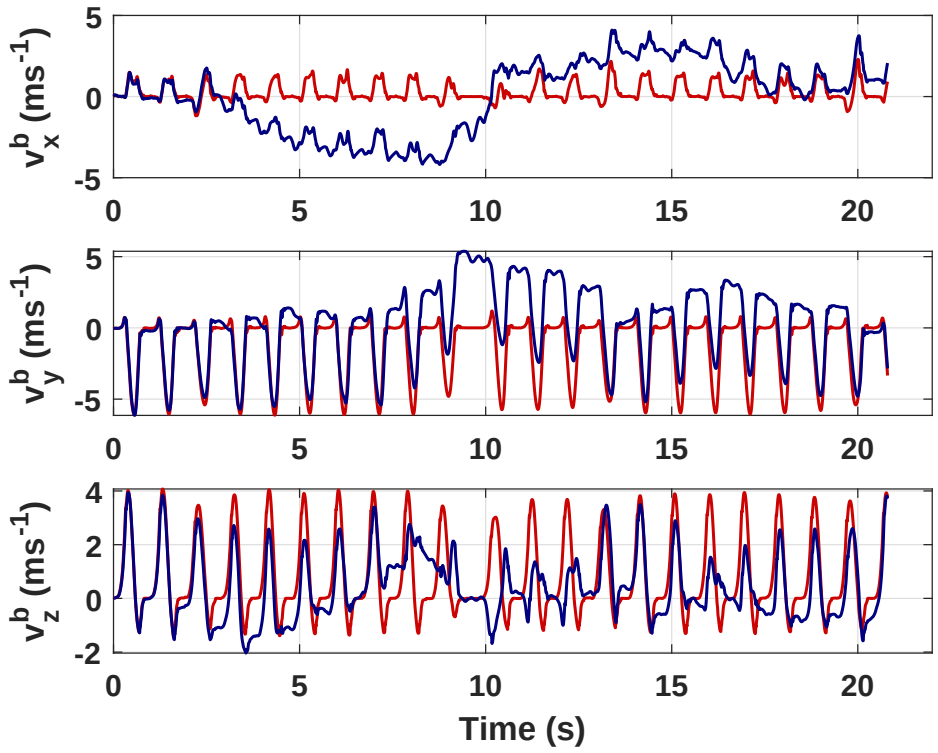

Figure 4.15: Estimation of v^b using only the magnetic field gradient-based EKF. In red is the ground truth velocity, and in blue is the estimated one

In the presence of low magnetic field gradient, the EKF generates inevitable errors, as observed in Fig. 4.15. However, the EKF does not completely diverge, in the sense that there is no drifting phenomena of the velocity estimate $\widehat{v^b}$ (i.e. does not go very far from the ground truth), and is rather continuously recovered during the trajectory scenario, thanks to the variation of ∇B^b that at times, can provide sufficient information in order for the velocity to be observable.
It is underlined that velocity estimation results using only the BiLSTM-based network have already been presented and discussed in Section 4.3.2, where it was demonstrated that relying only on a neural network, under a light training procedure, does not provide accurate predictions.

4.5.3 Results of the proposed EKF-BiLSTM approach

The performance of the proposed EKF-BiLSTM estimation approach is evaluated on the testing set, by comparing the obtained results to the ground truth ones. In Fig. 4.16, the $3-axis$ components of v^b are plotted. Unlike the results of the EKF in Fig. 4.15 and the BiLSTM in Fig. 4.11, the

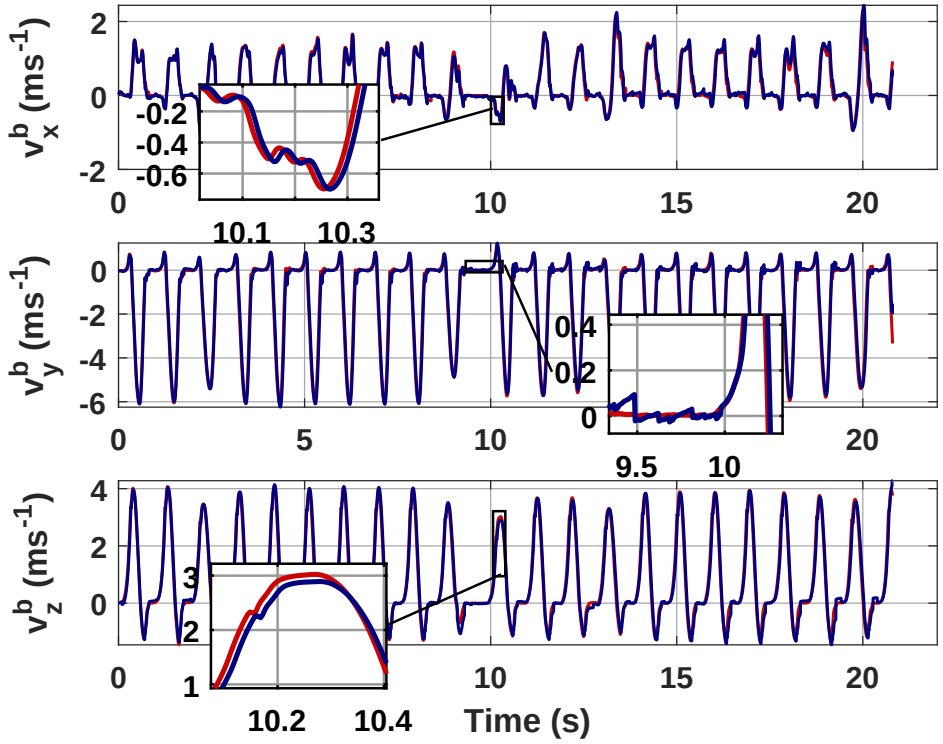

Figure 4.16: Estimation of v^b with the EKF-BiLSTM approach. In red is the ground truth velocity, and in blue is the estimated one

velocity estimate $\widehat{v^b}$ given by the proposed approach is now very close to the ground truth one, with an RMSE that is around 0.21 ms^{-1}, which is very promising considering that the proposed method does not rely on any trajectory assumptions nor sensor attachment (as the case for pedestrian foot-mounted applications), does not demand any heavy training procedure, and is tuning-free.
To analyze the effect of the velocity estimation on the trajectory reconstruction, the estimated position $\widehat{M^n}$ from the EKF-BiLSTM approach is plotted in its $2D$ form and represented in Fig. 4.17.
It is observed that the estimated trajectory is close to the ground truth one and the same squared shape is maintained. This level of accuracy is unreachable when integrating the velocity from Fig. 4.15 that actually generates a senseless trajectory as the case in Fig. 4.3.
Table 4.1 presents the traveled distance, as well as the coordinates of the arrival points for the estimated and ground truth trajectories. The arrival point of the ground truth trajectory is different

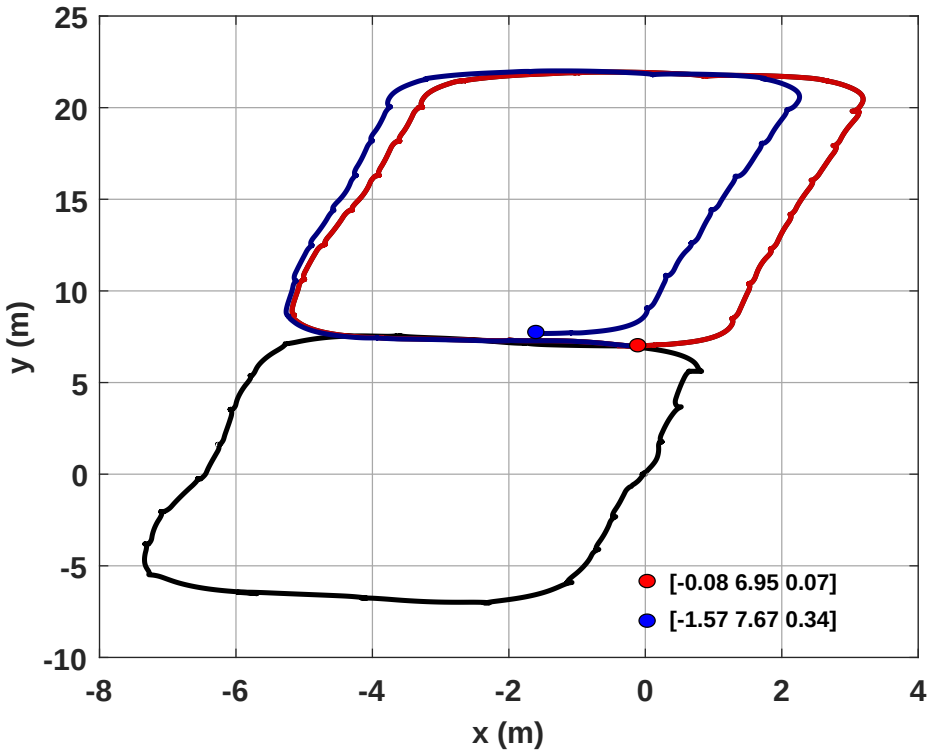

Figure 4.17: Estimation of M^n with the EKF-BiLSTM approach. In black is the training trajectory, in red is the ground truth of the tested trajectory, and in blue is the estimated one. Bullets stand for the coordinates of the arrival points

Table 4.1: Velocity error mean results

Metrics	***Ground truth***	***EKF-BiLSTM***
Traveled distance (m)	45.01	44
Arrival point coordinates (m)	[-0.41 7 0.06]	[-1.57 7.67 0.34]

from its starting point, that is the same for both the compared trajectories. The error of the final arrival point between the two trajectories is around 1.37 m which competes with top ranked methods in the literature, that require either heavy computations (only DL-based methods) or a very specific sensor location (as the case for ZUPT).
It is also important to recall that in these experiments, the Openshoe ZUPT estimation results are considered as the ground truth. However, no conclusions can be made on their accuracy, as no actual ground truth is provided. This means that results given by the proposed approach, can be closer to reality than the ones computed from the Openshoe ZUPT approach.

4.6 Conclusion

Weaknesses of the magnetic field gradient-based EKF The magnetic field gradient-based EKF represents a promising solution to the indoor navigation problem, for its strong theoretical foundation and easy applicability. Nevertheless, the latter encounters several limitations that are either related to its technical implementation, or to the surrounding environment characteristics, such as the presence of low magnetic field gradient, quasi-static or static trajectory phases, etc.
ZUPT is not adequate to compensate the EKF errors When the sensor board is attached to body placements other than the foot, the zero-velocities detection is completely inaccurate. In addition to that, such technique requires a continuous tuning of its parameters to account for the different trajectory scenarios, which sometimes demands heavy resources. This makes the ZUPT solution unfit to correct the errors generated by the EKF in more general cases.
BiLSTM for inertial navigation The many advantages of the BiLSTM over other ANN architectures encouraged its massive use in the related state-of-the-art works. Nevertheless, despite its promising accuracy results, employing an only DL-based solution remains debatable as it usually requires a large training dataset, intensive hyperparameters tuning, and heavy overall computations, that are not always so feasible.
Proposed EKF-BiLSTM approach The proposed approach enables correcting the magnetic field gradient-based EKF estimation and taking advantage in the same time of the prediction accuracy of a BiLSTM-based network. This is achieved while using a very small training dataset for the BiLSTM, and without requiring any sophisticated tuning of its parameters. The EKF-BiLSTM can be applied to any trajectory scenario, no matter the sensor board attachment and for any studied application, which makes of it, a very suitable solution to the indoor navigation problem.
Openshoe dataset for experimental validation While the Openshoe dataset represents a good starting point to evaluate the performance of the proposed approach, it does not form an optimal choice for experimental validation because of few reasons. First, this dataset corresponds to pedestrian foot-mounted IMU measurements and one single trajectory. This is considered very limited and does not demonstrate the generality of the proposed approach, that can be applied on any type of trajectory and for whatever sensor board placement, under various applications. Second, the dataset lacks measurements of the magnetometer array because only one magnetometer in an IMU is used, which leads to the simulation of imprecise data through approximations from a theoretical array. Finally, the used dataset is missing ground truth measurements. Thus, results from the ZUPT-based approach proposed by Ref. [Skog2010b] are assumed to be the ground truth, which is not entirely accurate.
In the next chapter, a real case study is conducted with a complete sensor board generating not only inertial but also magnetometer array measurements. Ground truth data is acquired from a motion capture system, and many trajectory scenarios and sensor board attachments are tested, to better demonstrate the efficiency of the proposed EKF-BiLSTM approach.

5

Real Case Study: The Magneto-Inertial Tachymeter

In this chapter, the proposed EKF-BiLSTM approach is evaluated on a real case study with a complete experimental benchmark and several testings. In Section 5.1, a fully-designed sensor board containing an IMU and a magnetometer array, called the Magneto-Inertial Tachymeter (MIT) is presented. With this sensor board, a motion capture system framework is also introduced, from which ground truth data is acquired and synchronized with the inertial and magnetic measurements. Then, in Section 5.2, the performance of the EKF-BiLSTM approach compared to other studied methods in this thesis is validated through multiple trajectory scenarios and sensor placements. The results demonstrate how the EKF-BiLSTM outperforms the other methods in terms of velocity estimation accuracy, and trajectory reconstruction.

Contents

5.1 Measurements and ground truth data

In the previous chapters, the discussed estimation approaches were evaluated using either simulated trajectory scenarios or real publicly available datasets. While both these strategies provide a prior knowledge on the methods' performances, they represent some inconveniences, from which the most important are first, the lack of actual magnetometer array measurements, and second, the absence of ground truth data. In the following, a complete experimental benchmark is presented that accounts for all these requirements.

5.1.1 Magneto-Inertial Tachymeter

The Magneto-Inertial Tachymeter (MIT) is a prototype system, provided by SYSNAV company Ref. [Sysnav2020], that has been designed for pedestrian navigation applications, to demonstrate indoor navigation capabilities. The SYSNAV tachymeter consists of two main components: a sensor module and a fusion module.

MIT sensor module

The sensor module of the MIT is shown in Fig. 5.1. It contains the different sensors ($3-axis$ accelerometer, $3-axis$ gyroscope and a $3-axis$ magnetometer array), the associated circuitry (A/D, power converters), a Serial Peripheral Interface (SPI), and a cable to connect it to the fusion module.

Figure 5.1: Sensor module of the used MIT

The sensor module is delivered in a bubble-wrap to protect it from any possible damages. This packaging plays also a role in the temperature regulation of the case during the calibration process. Note that, any mishandling of the sensor module can impact this calibration which results in the performance of the system being significantly deteriorated.

MIT fusion module

The fusion module of the MIT is presented in Fig. 5.2. It contains a Secure Digital (SD) card to save the measurements recorded by the sensor module, a battery, a SPI and Bluetooth interfaces. When the fusion module internal battery needs recharging, an external charger is plugged in through the CHG connector. The tri-state power switch, located on the side of the module, is placed on the "E/C" position, as represented in Fig. 5.2.

Figure 5.2: Fusion module of the used MIT

Operating instructions

The sensor module is first connected to the fusion module, then powered on by flipping the tri-state switch to the "BAT" position. The magnetometers and accelerometers are sensitive to temperature change. So, in order to ensure optimal performance, the system should reach a steady temperature state before starting any recordings, which occurs within 20 *min* of switching on the MIT.
It is also recommended to keep a safety distance between the sensor module and any magnetic elements to avoid any decalibration of the MIT.

Data extraction

Each time the MIT is powered up, a new session file is created on the SD card which contains the recorded inertial and magnetic measurements.
To extract these recordings, a USB cable is plugged to the computer and to the SD output of the fusion module (has to be powered on), and a program provided by SYSNAV is launched. The program automatically detects the SD card and indicates the different recorded session files contained in it. To extract a particular session data, the latter is simply selected and the corresponding data is extracted using the read button "Lire", as indicated in Fig. 5.3. The obtained files contain the

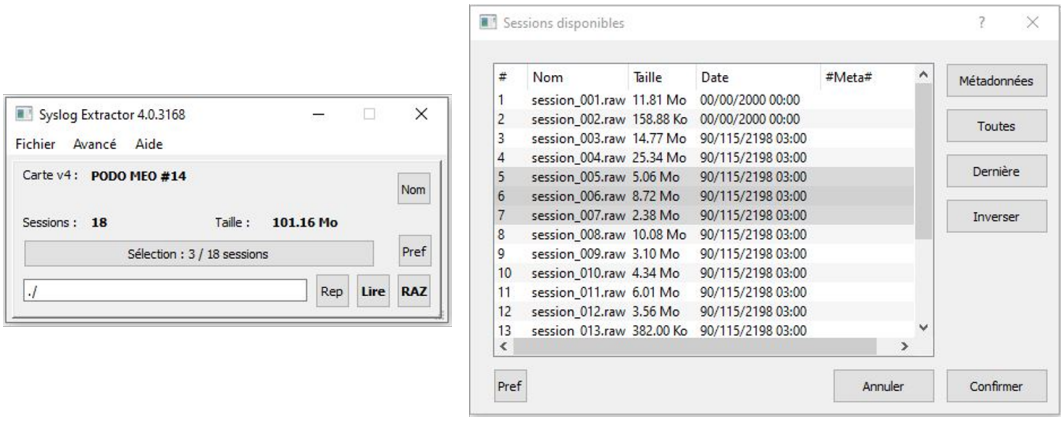

Figure 5.3: Data extraction using SYSNAV software

angular velocity, acceleration, as well as the five magnetometers' measurements.
The SD card can provide 15 *h* of recordings. Once full, the latter has to be freed by selecting the sessions to be deleted and clicking on the erase button "RAZ".

5.1.2 Reference system and data preparation

The evaluation of the states estimation accuracies using the different discussed methods in this thesis requires the presence of ground-truth data to be compared to. Furthermore, the training of the BiLSTM-based network of the EKF-BiLSTM approach demands a velocity ground truth data. For these reasons, all experiments conducted in this chapter are elaborated in the "Biomeca" room in GIPSA-Lab Ref. [Gipsa-lab0 19], equipped with a motion capture system from Qualisys brand Ref. [Qualisys2021]. The room has 9 cameras, as shown in Fig. 5.4, that provide a high accuracy of ground truth position (1 *mm*) as well as ground truth attitude (Euler angles and rotation matrix).

Figure 5.4: Qualisys cameras in the Biomeca room

Calibration of the cameras

The Qualysis Track Manager (QTM) software, used to conduct all camera's processings, needs to have information about the orientation and position of each of the 9 cameras in order to efficiently scale and locate the $3D$ coordinate system of the moving body in the measurement zone. Therefore, before conducting any experiments, the used cameras have to go through a calibration process. This can be done using a calibration kit that consists of two parts: a mirrored L-shaped reference structure and a calibration wand, as presented in Fig. 5.5. To perform the calibration, the L-shaped reference structure is placed on the ground, to obtain its corresponding coordinate system. Then, the calibration wand is moved inside the chosen measurement zone in all three directions, as illustrated in Fig. 5.5, in a way that allows all cameras to see the wand in as many orientations as possible. This is done to assure that all directions are properly scaled. It is underlined that the 9 cameras must be able to detect all markers of the calibration kit, and no sources of extra reflections (other than the markers) should be present, in order to avoid jeopardizing the calibration process. The QTM software estimates each camera's position and orientation by evaluating the camera's view of the wand during the calibration, and calculates the average residual error of this estimation, as indicated in Table. 5.1. It is observed that, in the performed calibration, the 9 cameras residual errors are around 1 *mm*, which is considered satisfactory for the targeted application, for comparisons as well as training.
It is underlined that, during the recordings, the moving body must move inside the covered zone by the calibration (around 9 m^2 of surface), as shown in Fig. 5.6.

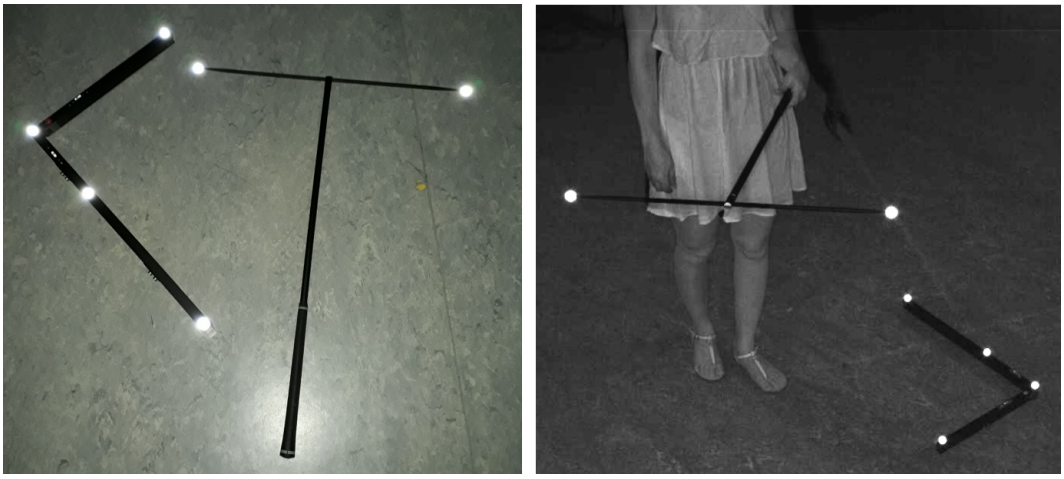

Figure 5.5: A subject sweeping the zone that needs to be covered by the Qualisys cameras using the calibration kit: the L-shaped reference structure and the calibration wand

Table 5.1: Average residual errors of estimated position by the nine cameras after calibration

Cameras	01	02	03	04	05	06	07	08	09
Average residual (mm)	1.14	1.10	0.83	0.87	1.16	0.92	0.79	1.10	1.06

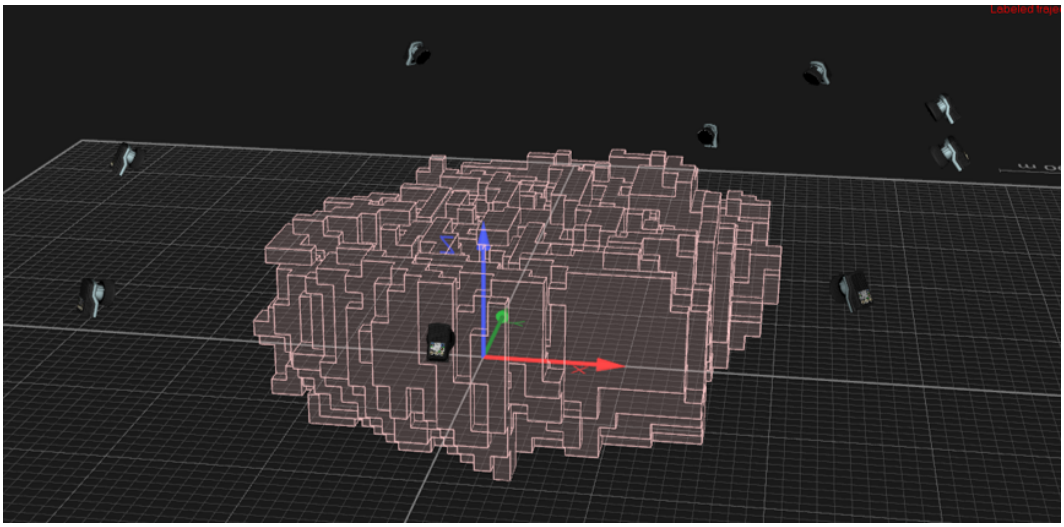

Figure 5.6: Covered zone from the cameras after calibration

Measurements and trajectories

Before acquiring any measurements from the MIT, the latter has to be equipped with a markers-based frame such that its motion can be captured by the cameras during the recordings. The frame is specially designed to be placed on the MIT using OpenSCAD, a free software of parametric modeling that enables creating Computer-Aided Design (CAD) solid objects for $3D$ printing, as illustrated in Fig. 5.7.
Once all discussed steps are conducted, data collection is performed. Five trajectories, achieved by a subject, are examined: square, circle, diagonal rectangle, triangle and heart. Trajectories are carried out under normal walking, and they last 3.5 *min* on average each. Evaluations are

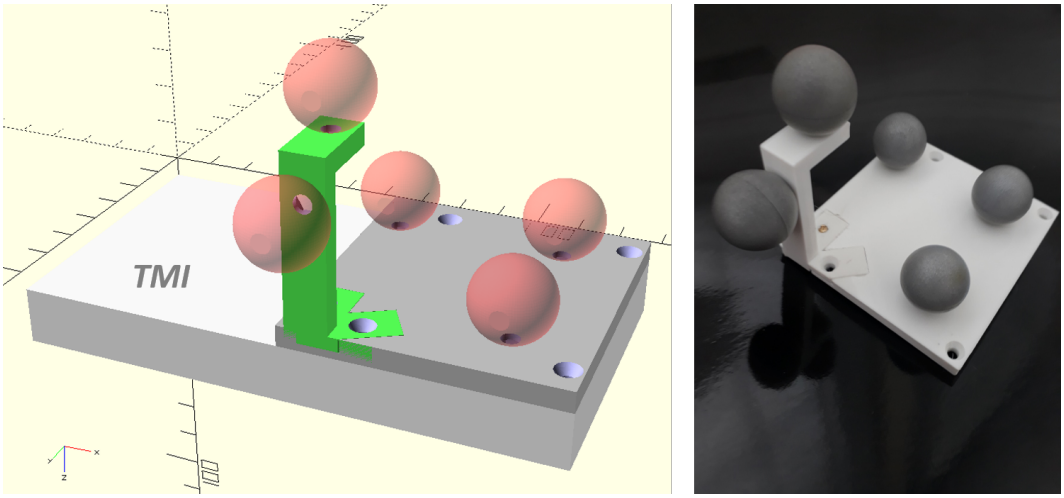

Figure 5.7: Markers-based frame designed to be place on the MIT

performed with three sensor attachments: right tibia, right front pocket, and waist. In Fig. 5.8, an illustration of the tibia and pocket placements is presented.

Figure 5.8: Examples of MIT attachments during the conducted experiments

Data synchronization

After recording the different trajectories, ground truth and MIT data are extracted and a synchronization procedure is conducted. In fact, the MIT is sampled at the frequency $fs_{MIT} = \frac{4*10^6}{12*1024} \approx 325.52\,Hz$, while the Qualysis system's frequency is chosen as $fs_{Qualisys} = 326\,Hz$. Thus, a *down-sampling* step is applied in order to obtain synchronized and ready-to-use databases.
In fact, from the example in Fig. 5.9, one can see that the Qualisys data is *oversampled* (6 samples for the TMI versus 7 for the Qualisys). The difference between the MIT and the Qualisys sample

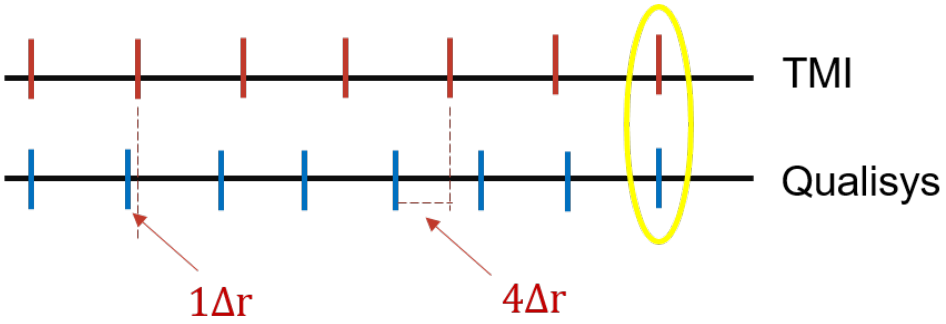

Figure 5.9: Illustration of the MIT and the qualisys motion capture system sampling. Every 7 steps, the qualisys system has one extra sample with respect to the MIT, as highlighted with the yellow circle

rates is denoted Δr such that

$$\Delta r = \frac{12 * 1024}{4 * 10^6} - \frac{1}{326} = 4.51 * 10^{-6} \tag{5.1}$$

One should look for $n \in \mathbb{N}_{>0}$ such that $n\Delta r = \frac{12 * 1024}{4 * 10^6}$, i.e. the needed number of Δr in order for the Qualisys system to have one extra sample with respect to the MIT. It yields that $n = 680$, which means that, for every $680th$ steps, a sample from the Qualisys data is removed.
While such methodology is efficient at ensuring data synchronization, one should notice that for all samples before the 680 step, the delay between the TMI and Qualisys measurements is not handled. For such reason, one can rather use traditional *interpolation* methods Ref. [Maeland1988] to account for this issue. Nevertheless, to avoid any change in signals' information, the downsampling technique is maintained as it has no major effect on the considered application. i.e. pedestrian walk at normal speed, which step frequency is known to vary between 1.6 Hz to 2.4 Hz.
Note also that before undergoing the synchronization step, the TMI and Qualisys datasets need to be modified to start at the same time. The ground truth dataset has to be cleaned from any "NAN" values, caused by the inability of the motion capture system, at some instants, to detect the TMI markers (when blocked by the subject, for example, during a certain movement).
It is finally underlined that, the choice of a pedestrian to represent the moving body in this study case, is taken for flexibility and comparison reasons. Nevertheless, it is believed that the proposed approach (EKF-BiLSTM) can be extended to other applications of indoor navigation.

5.2 Experimental results and comparisons

In this section, the performance of the proposed EKF-BiLSTM approach is evaluated under the presented experimental benchmark. Comparisons are conducted where it is demonstrated how the latter provides the best estimation accuracy results among other studied methods, which is mainly seen during trajectory reconstruction.

5.2.1 Implementation details of the EKF-BiLSTM

The implementation of the EKF-BiLSTM approach is done under the same network architecture previously introduced in Section 4.3.2. The only difference resides on the used datasets for the training, testing and validation processes. For each sensor placement, four trajectories are used to

construct the training set, and the remaining one is for the testing. Around 1% of the training set is left for validation. The training takes around 1 h on the CPU. This procedure is repeated 5 times so each trajectory can form the testing set one time. It is underlined that the training set remains very small ($\approx$ 14 *min*, 9 features and $\approx$ 200000 samples) compared to the state-of-the-art works Refs. [Feigl2019, Kang2018b] that use very large training databases.

5.2.2 Effect of the measurement covariance adapter

One comparison that must be conducted before preceding with the EKF-BiLSTM evaluation, is the one related to the measurement covariance adapter. One may wonder to what extent such algorithm can improve the estimation results of the proposed EKF-BiLSTM approach, and how far this approach can be accurate in case such adaptation is not considered, i.e. the pseudo-measurement v^b_{BiLSTM} is all the time trusted by the EKF by setting its corresponding noise covariance matrix to the identity matrix the entire time. To perform this evaluation, a walking rectangular trajectory is considered as the testing set, with the MIT placed on the right tibia of a subject. The training is done using a dataset containing four other forms of trajectories. Then, the proposed EKF-BiLSTM approach is applied with and without the measurement covariance adapter. In Fig. 5.10, the results of the velocity estimation corresponding to this experiment are plotted. To ease the reading, only

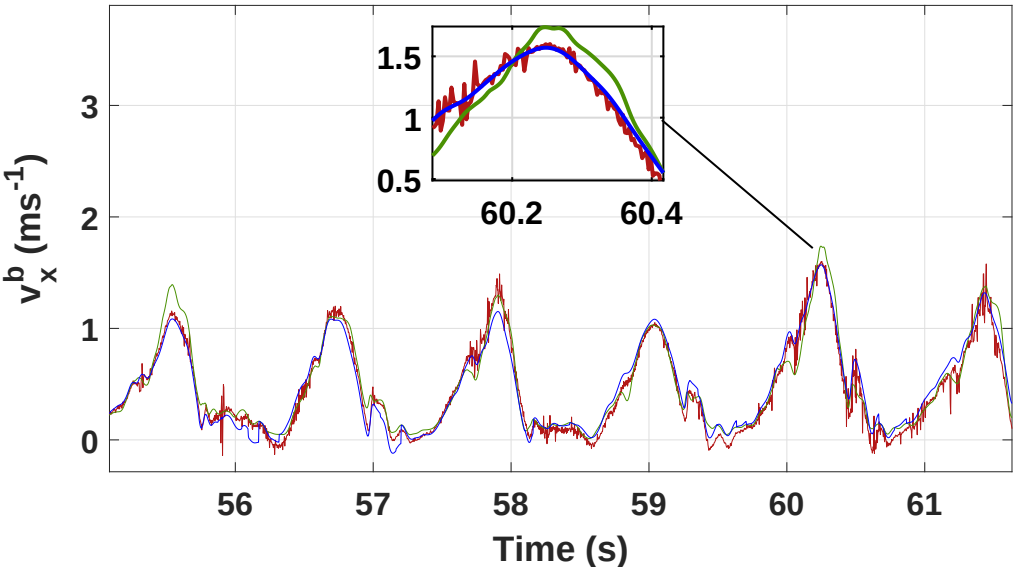

Figure 5.10: Estimation of v^b with the EKF-BiLSTM approach. In red is the ground truth velocity, in blue is the EKF-BiLSTM estimation with the measurement covariance adapter, and in green without it

the first axis v^b_x is plotted for about 7 s from the total time of the trajectory. The green line signal corresponds to when the pseudo-measurement v^b_{BiLSTM} is trusted the entire time by the EKF. This means that no dynamic adaptation of N_3 is taken into account and its values are rather fixed to the identity matrix. In this case, the inaccurate prediction of v^b_{BiLSTM} during moments when the velocity is higher than the threshold ε affects negatively the EKF velocity estimation. On the contrary, the blue line signal is found when Algorithm 1 is applied. A better velocity estimation accuracy is then observed after controlling the level of confidence given to v^b_{BiLSTM} by the EKF using the measurement covariance adapter.
In Fig. 5.11, the position reconstruction results are displayed in $2D$ and the same conclusions are made. Note here that, all numerical results (such as in Table 5.2, for example) take into account the 3 axes of the position vector M^n. Table 5.2 represents the distance error d_e between the proposed

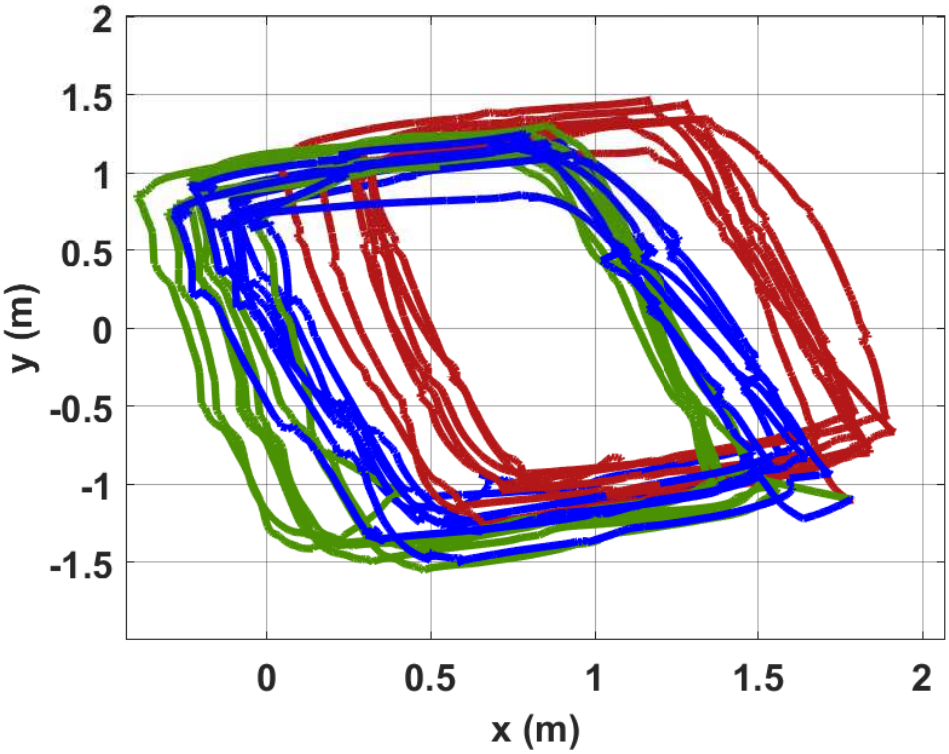

Figure 5.11: Estimation of M^n with the EKF-BiLSTM approach. In red is the ground truth position, in blue is the EKF-BiLSTM estimation with the measurement covariance adapter, and in green without it

EKF-BiLSTM position estimate $\widehat{M^n}$ and the ground truth one for both cases, with and without the measurement covariance adapter. This evaluation metric is borrowed from Ref. [Needham2003] and is defined such that

$$d_e = \|\widehat{M^n} - M^n\| \tag{5.2}$$

It is observed that a better estimation accuracy is obtained when the measurement covariance adapter is used, which proves the importance in including it in the EKF-BiLSTM solution.

Table 5.2: Distance error using the EKF-BiLSTM with and without the measurement covariance adapter

d_e (m)	Mean	Median	Max	Standard deviation
Without the adapter	1.93	1.87	3.88	1.20
With the adapter	0.43	0.45	0.71	0.15

It is stressed here that ε is maintained the same for all the next experiments (trajectories and sensor placements), which recalls one advantage of the proposed EKF-BiLSTM approach, that is tuning-free.

5.2.3 Main results and performance of the EKF-BiLSTM

This section starts by discussing the performance of the magnetic field gradient-based EKF (Chapter 2) under different magnetic field gradient conditions. Then, the estimation results from the proposed EKF-BiLSTM approach (Chapter 4) are presented, and compared to ground truth data

as well as the EKF and the EKF-ZUPT (Chapter 3) approaches. Evaluations demonstrate how the EKF-BiLSTM solution gives the best states' estimation results providing consequently an accurate trajectory reconstruction.

Magnetic field gradient and sensor placements

The design of the EKF-BiLSTM approach is independent from any particular sensor location or trajectory scenario. Therefore, one expects that the latter provides the same estimation accuracy results, no matter the attachment of the sensor board. Nevertheless, it turns out that there is a direct relationship between the sensor placement and the magnetic field variations, that somehow, still affect the performance of the EKF-BiLSTM approach. In other words, even though the BiLSTM attenuates the errors generated by the EKF in a low magnetic field gradient environment, it does not entirely eliminate them, which means that in all cases, the best estimation accuracy results are obtained when the magnetic field gradient is the strongest.
To back up such assumptions, a triangular trajectory is conducted for each sensor placement. Then, the magnetic field gradient is calculated using the magnetometer array from the MIT and the steps previously presented in Section 2.1.5. In Fig. 5.12, the three eigenvalues of ∇B^b for the different MIT placements are plotted.

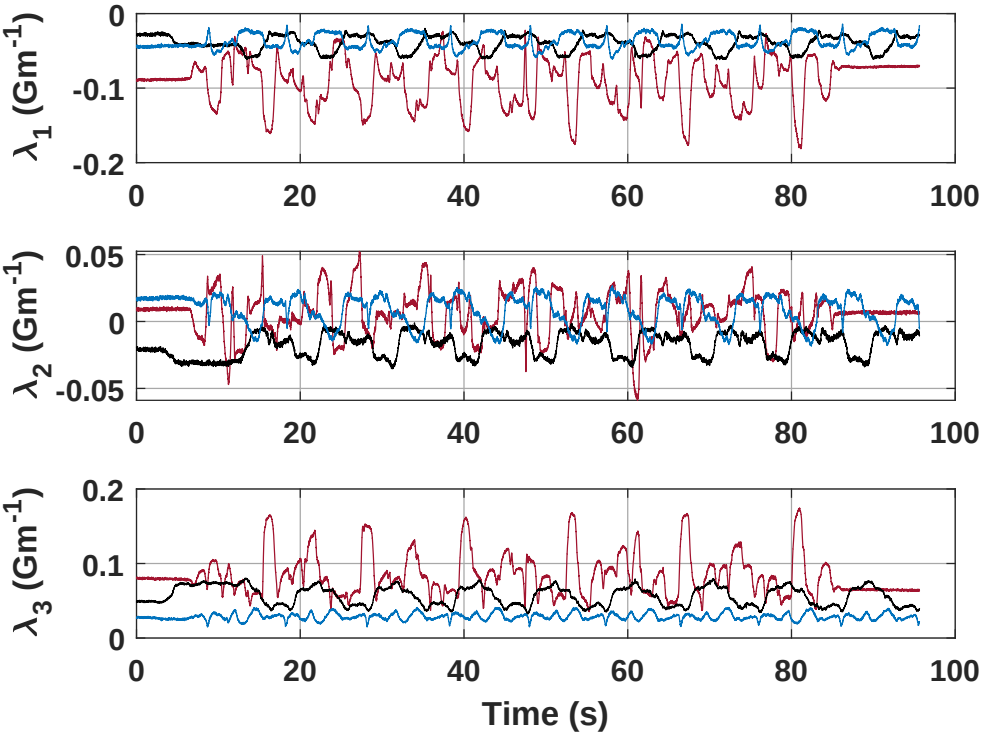

Figure 5.12: Eigenvalues of the magnetic field gradient for different sensor placements. In red for the tibia, in black for the waist and in blue for the pocket

What is demonstrated through Fig. 5.12, is that the magnetic field variations are more significant when the MIT module is placed on the tibia (red line). This can be explained by the metal structure of the floor in the motion capture room, that generates noticeable magnetic disturbances, making the corresponding eigenvalues of the magnetic field gradient superior to 0.05 Gm^{-1}. The room also contains office equipment (laptop, metallic table, etc.), as shown in Fig. 5.4, that produces significant magnetic disturbances. Yet, in order for these variations to be captured, the subject wearing the MIT (in the pocket or waist placements) has to move close to this equipment. Other-

wise, the recorded magnetic field gradient will not be as large as the one of the tibia placement. However, during all experiments, the subject was moving in the middle of the room and not very close to this equipment. For this reason, the pocket and waist sensor placements do not capture such high magnetic variations, which can be illustrated by the corresponding magnetic field gradient eigenvalues, that are inferior to 0.05 Gm^{-1}. It follows that the estimation results of the different compared algorithms (EKF, EKF-ZUPT and EKF-BiLSTM) are most accurate for the tibia sensor placement, as it has the largest magnetic disturbances. This will be detailed further in the next sections.

EKF performance under different sensor placements

To confirm that, for different sensor placements, the EKF estimation accuracy varies (because of the magnetic field gradient variation), the following experiment is undertaken. Two sensor placements are chosen for comparison: tibia (with high magnetic disturbances) and waist (with low magnetic disturbances). The same triangular trajectory of the previous section is considered. Figs. 5.13- 5.14 display a comparison between the estimated trajectory from the EKF and ground truth, for the two sensor placements.

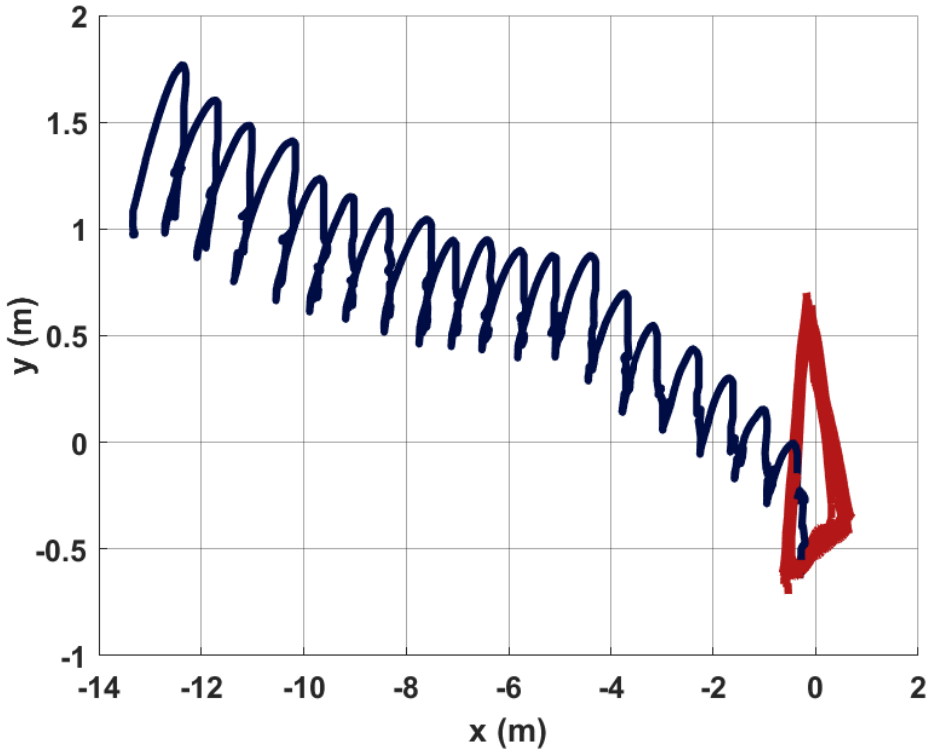

Figure 5.13: Position estimation from the EKF when the MIT is on the waist. In red is the ground truth trajectory from the motion capture system, and in blue is the EKF estimated one

From these figures, it is clear that the EKF provides better accuracy when the MIT is subject to enough magnetic field disturbances (MIT on the tibia), than the case of a low magnetic field gradient (MIT on the waist). This is expected as the EKF is highly sensitive to the magnetic field gradient as demonstrated in Section 4.1. Then, in the next Section, the results show how the proposed EKF-BiLSTM improves the estimation process when magnetic disturbances are low, for example when the MIT is on the waist. It is underlined here that adding the BiLSTM to the EKF in the case of high magnetic disturbances (MIT on the tibia) does not drastically improve the results from the case where only the EKF is used. This is because the latter can already provide good

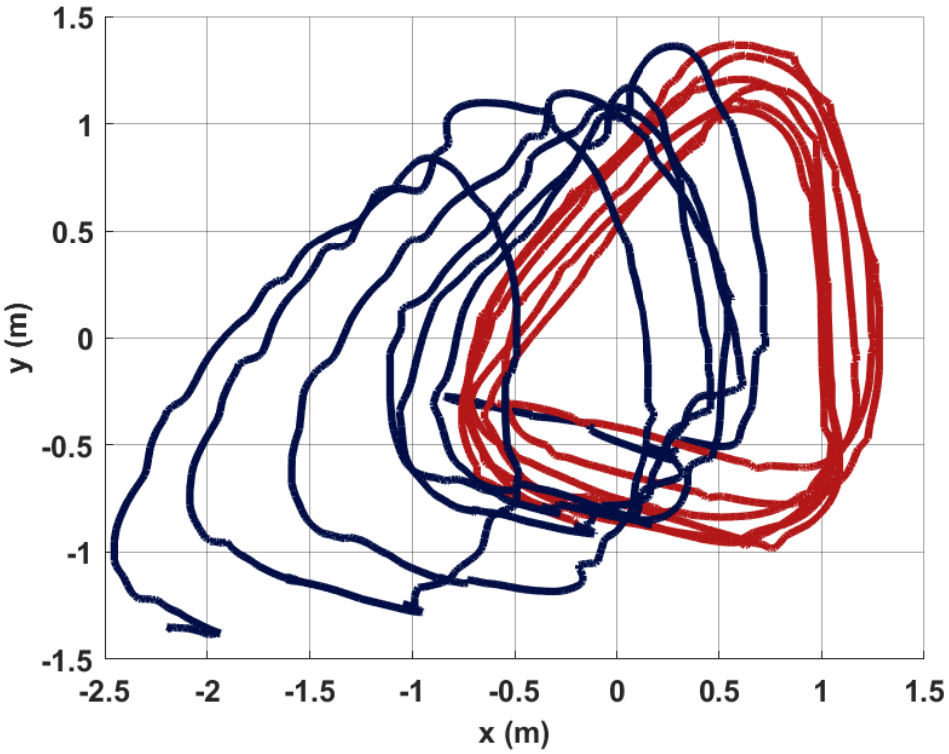

Figure 5.14: Position estimation from the EKF when the MIT is on the tibia. In red is the ground truth trajectory from the motion capture system, and in blue is the EKF estimated one

accuracy results as long as the magnetic field gradient is sufficiently large. In other words, the biggest impact of the BiLSTM algorithm on the magnetic field gradient-based EKF takes place when the EKF cannot perform well, under a low magnetic field gradient.

EKF-BiLSTM results

In this section, the performance of the EKF-BiLSTM approach is studied. First, in Figs. 5.15-5.16, the velocity estimation results are plotted for both the MIT placements (waist and tibia, respectively). To ease the reading, only about 10 s of each signal is plotted. Also, the axis v_x^b is chosen to be plotted. The other two axes have the same behavior. A comparison between using the magnetic field gradient-based EKF and the EKF-BiLSTM is undertaken. It is clear that the proposed approach outperforms the use of only the EKF, in both cases of lower and higher magnetic disturbances (waist and tibia placements). The difference in the estimation accuracy between the EKF and EKF-BiLSTM is clearer in Fig. 5.15, which proves the efficiency of the proposed approach, especially in low magnetic field gradient situations. Such improvement on the velocity estimation by the EKF-BiLSTM impacts the position reconstruction for the studied triangular trajectory.
In Fig. 5.17, it is seen that for the case where there are enough magnetic disturbances (tibia attachment), the EKF-BiLSTM succeeds to accurately estimate the trajectory with a small error. It also improves greatly the results when the MIT is on the waist (in Fig. 5.18), by reducing the drift previously seen in Fig. 5.13.

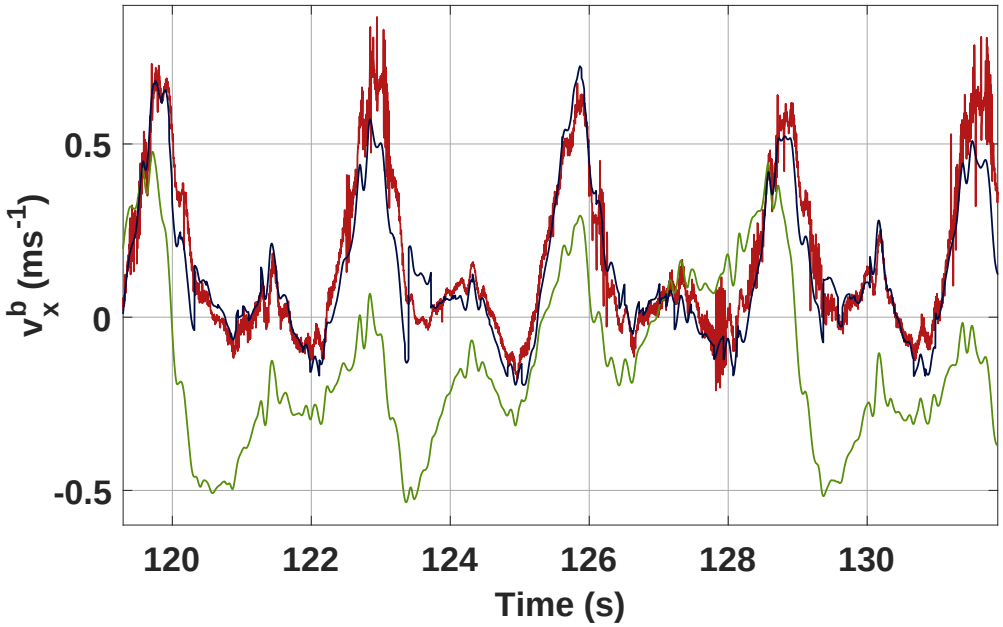

Figure 5.15: Velocity estimation from the EKF-BiLSTM when the MIT is on the waist. In red is the ground truth velocity deduced from the motion capture system, in green is its estimate when using the EKF and in blue is when using the proposed EKF-BiLSTM

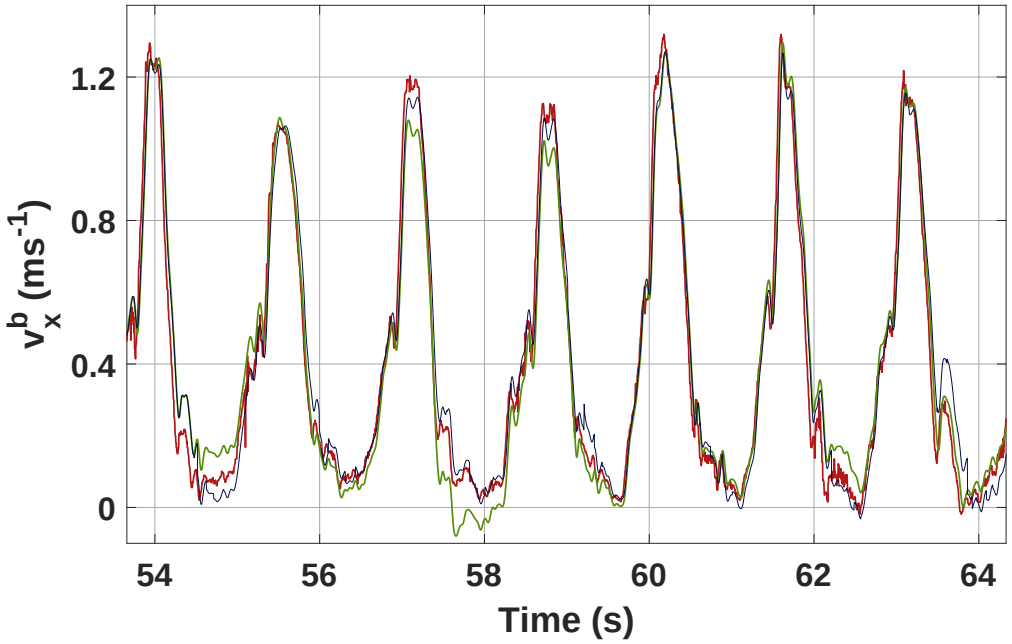

Figure 5.16: Velocity estimation from the EKF-BiLSTM when the MIT is on the tibia. In red is the ground truth velocity deduced from the motion capture system, in green is its estimate when using the EKF and in blue is when using the proposed EKF-BiLSTM

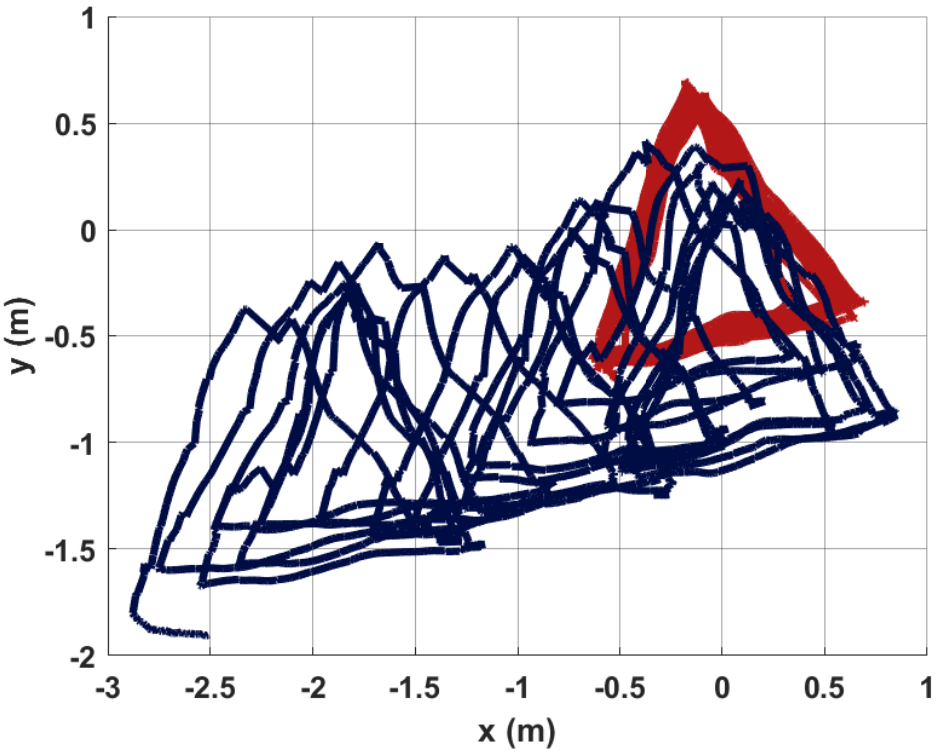

Figure 5.17: Position estimation from the EKF-BiLSTM when the MIT is on the waist. In red is the ground truth trajectory from the motion capture system, and in blue is the EKF-BiLSTM estimated one

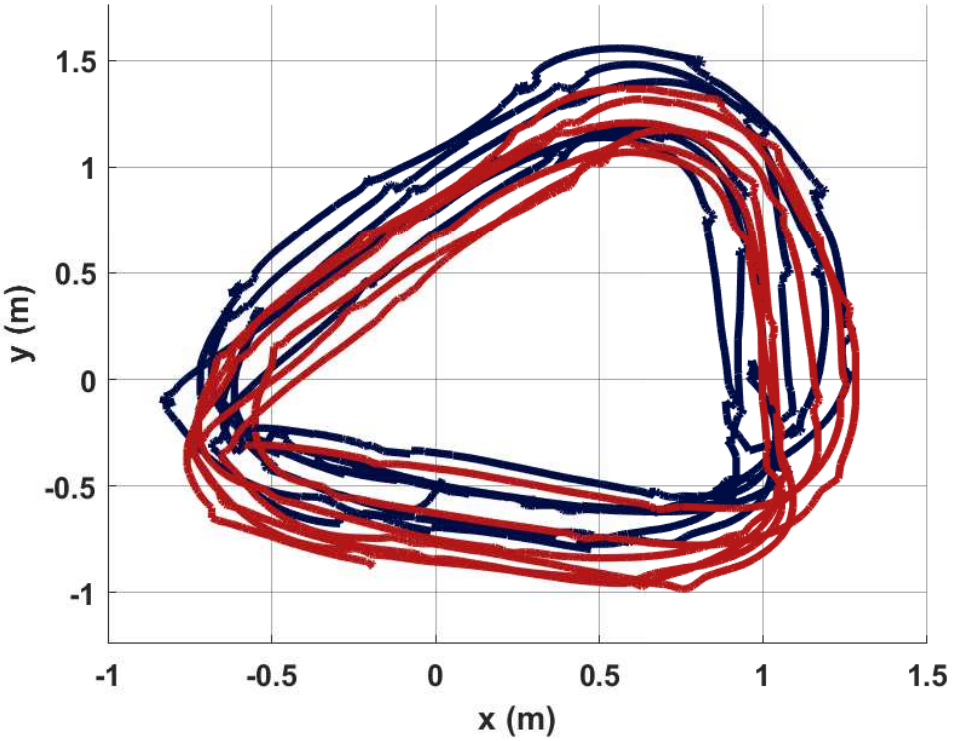

Figure 5.18: Position estimation from the EKF-BiLSTM when the MIT is on the tibia. In red is the ground truth trajectory from the motion capture system, and in blue is the EKF-BiLSTM estimated one

Comparisons and discussion

In Tables 5.3-5.4, the results from all discussed methods are presented (EKF, EKF-ZUPT and EKF-BiLSTM). For each sensor placement, the five trajectories mentioned in Section 5.1.2 are tested and the mean of their accuracy results is presented (as evaluations are conducted for each of the tested trajectories). Table 5.3 displays the RMSE and the MAE of the estimated velocity with respect to the ground truth one. Table 5.4 contains the mean, median, maximum and standard deviation of the distance error between the true and the estimated position. By looking at Tables 5.3-5.4, the proposed EKF-BiLSTM approach gives the best velocity and position estimation results compared to the other methods (EKF and EKF-ZUPT). In fact, for the velocity estimation, it succeeds to decrease the EKF's error with more than a factor of 2 for all the studied sensor placements. While for the position estimation, it is shown that the BiLSTM's impact is mostly seen under the pocket and waist attachments, which correspond to the low magnetic field gradient case. For instance, the velocity MAE of the waist attachment goes down from 0.21 ms^{-1} using only the EKF to 0.07 ms^{-1} with the EKF-BiLSTM approach, while the mean of the distance error of the position for the pocket placement is reduced from 11.35 m using the EKF to 3.72 m with the EKF-BiLSTM solution. This illustrates the benefit of the proposed EKF-BiLSTM approach in improving estimation accuracy results, especially under low magnetic field disturbances.

Table 5.3: Velocity error mean of the different sensor placements

Velocity (ms^{-1})		RMSE	MAE
Waist	EKF	0.282	0.214
	EKF-ZUPT	0.29	0.212
	EKF-BiLSTM	0.114	0.074
Pocket	EKF	0.206	0.166
	EKF-ZUPT	0.21	0.164
	EKF-BiLSTM	0.106	0.078
Tibia	EKF	0.164	0.116
	EKF-ZUPT	0.152	0.102
	EKF-BiLSTM	0.088	0.05

Table 5.4: Distance error mean of the different sensor placements

d_e (m)		Mean	Median	Max	STD
Waist	EKF	5.982	5.874	11.95	3.668
	EKF-ZUPT	5.79	5.624	11.61	3.528
	EKF-BiLSTM	3.65	3.516	7.254	2.176
Pocket	EKF	11.35	11.15	23.28	7.154
	EKF-ZUPT	11.29	11.17	23.15	7.094
	EKF-BiLSTM	3.726	3.662	7.312	2.204
Tibia	EKF	2.402	2.288	5.216	1.456
	EKF-ZUPT	2.072	1.966	4.53	1.42
	EKF-BiLSTM	1.356	1.356	2.286	0.542

It is also important to highlight that the difference in accuracy between the tested algorithms in terms of position estimation is less remarkable for the tibia case. For instance, the mean of the distance error of the position estimate is reduced from 2.4 m using the EKF to only 1.35 m with the proposed EKF-BiLSTM approach. This is because the EKF can already perform well alone, without considering the BiLSTM prediction, due to the presence of a strong magnetic field gradient like explained in Section 4.1. Note here that results between the EKF and the EKF-ZUPT are very similar, for all sensor placements, which proves again as demonstrated in Section 4.1.3 that the ZUPT is inefficient outside of the foot-mounted framework. This makes the proposed EKF-BiLSTM stand out, compared to state-of-the-art works, as it first, provides a very promising position reconstruction accuracy (≈ 1 m of error), under enough magnetic field disturbances, second, it can be applied on any sensor placement, and finally, can perform relatively well under the low magnetic field gradient condition (≈ 3 m of error).

5.3 Conclusion

Magneto-inertial tachymeter (MIT) The magneto-inertial tachymeter is a sensor board provided by SYSNAV company that generates real inertial and magnetic measurements. Unlike the publicly available datasets that are used in this entire thesis, the MIT consists of a magnetometer array, that enables the determination of the magnetic field gradient and hessian without having to conduct any simulations.

Motion capture system A motion capture system composed of 9 Qualisys cameras is used to provide ground truth data of the position, attitude, and consequently velocity of a moving body. This reference data is used for evaluating the different discussed approaches in this thesis and training the BiLSTM-based network. Before conducting any recordings, such system has to be carefully calibrated to provide accurate ground truth. After performing the experiments, the measurements from the MIT and the motion capture system are cleaned from any "NAN" values and then synchronized, to finally obtain appropriate and ready-to-use databases.

Importance of the measurement covariance adapter The BiLSTM velocity prediction is inaccurate during dynamic phases due to the use of a limited training dataset. In contrast, the EKF provides a better velocity estimation accuracy during these phases. It follows that trusting the BiLSTM estimate by the EKF the entire time is less efficient than controlling the level of confidence given to this pseudo-measurement, by adapting its corresponding noise covariance matrix.

EKF-BiLSTM provides the best estimation accuracy Evaluations on a real experimental benchmark demonstrate that the proposed EKF-BiLSTM approach outperforms the EKF and EKF-ZUPT under all studied sensor placements (tibia, pocket and waist), that are proportional to the presence of magnetic disturbances in the case of the conducted experiments. For the velocity estimation, the EKF-BiLSTM reduces the EKF's error with more than a factor of 2 for all the studied sensor placements. While for the position estimation, its impact is mostly seen under the low magnetic field gradient case (pocket and waist attachments). In the case of sufficient magnetic disturbances (tibia attachment), it provides the best results in terms of velocity as well as position accuracy (≈ 1 m of position error), which competes with state-of-the-art related works.

General Conclusion

Summary of main contributions

This thesis investigates the problem of GPS-free indoor navigation using only strapdown low-cost magneto-inertial sensors. The contributions in this work are the results of different improvements that are conducted on previously published solutions on the subject. These solutions rely basically on one efficient scheme, referred to as MINAV. This approach consists in combining classical inertial navigation equations with Eq. (1.33), to build a state-space model, that is representative of a moving body's motion. The particularity of this technique resides on the use of a magnetometer array to determine the spatial variations of the magnetic field, that are essential to the estimation process. More precisely, to ensure the observability of the estimated states, the magnetic field gradient must meet some conditions from which, the non-singularity is the most decisive. This highlights its crucial role in the MINAV approach.

In this sense, the study of the different published works that follow the MINAV technique has given rise to the following important issues:

- Being determined through approximation schemes from the magnetometer array measurements, such as finite differences or least squares, the magnetic field gradient suffers from uncertainties and noise. It follows that considering it as a known input in the state-space model introduces errors.
- In case the eigenvalues of the magnetic field gradient are really low ($<< 0.05\ Gm^{-1}$), the latter becomes close to the singularity condition. This implies the loss of observability of one or more velocity and/or attitude states, and consequently, generating inaccurate estimation results.

Both of these points encourage the modeling of the magnetic field gradient, to not only have a better estimation of its actual values, but to also gain extra degrees of freedom when it comes to the state-space model observability conditions.
Using the magnetometer array and the different properties of the magnetic field, higher order spatial derivatives are explored. Consequently, the magnetic field hessian is determined and used to model the dynamics of the magnetic field gradient, alongside with velocity and attitude, as represented by Eq. (2.8).
The presence of the magnetic field hessian in the proposed state-space model adds more flexibility to the conditions of observability, in a way that it can be maintained even if the magnetic field gradient is singular.

To evaluate the performance of the proposed model, a two EKFs-based approach is proposed and assessed on a simulated dataset. The benefit of adopting this specific setting comes mainly from the difficult tuning of the EKF noise covariance matrices, especially when comparisons of different models for a particular state are conducted. In fact, the proposed model given by Eq. (2.8) describing the dynamics of the magnetic field gradient is compared to state-of-the-art ones, and proved to outperform them in terms of noise compensation and velocity estimation accuracy. It comes without saying that such modeling enables reaching higher estimation accuracy than the case of not considering the magnetic field gradient in the state vector.

While the first architecture of two EKFs is of high benefit especially when tuning noise parameters, a compact design has also its advantages. Therefore, a second architecture of a single magnetic field gradient-based EKF is introduced, which performance is evaluated on the special case of pedestrian foot-mounted navigation. Comparisons of computation time and velocity estimation accuracy between the two proposed architectures have shown the better performance of the single EKF case, which justifies its use in the continuity of the thesis.

The performance of the single magnetic field gradient-based EKF is enhanced using the most common technique in foot-mounted applications, which is the ZUPT. As expected, this combination enables reaching high accuracy results not only for velocity estimation but also trajectory reconstruction. However, relying on ZUPT comes with few restrictions, that make it rather unsuitable in many cases. Not only it demands having the sensor board attached to the foot, which is not always feasible, but it also requires continuous tuning of its parameters in order to adapt to various walking speeds and subjects. For other applications that go beyond human motion, such as vehicles or robots, the ZUPT is practically useless.

Independently from the limitations of ZUPT, when the velocity is equal to zero and attitude is constant (i.e. static trajectory), the estimation suffers from inevitable drifts. These drifts are also increased by the different sources of errors related to the EKF numerical implementation, such as the discretization of the continuous-time model, the linearization process, etc. It is seen then, that in addition to errors generated by the low magnetic field gradient case, the single EKF solution has some weaknesses that must be compensated.

One way to tackle these limitations is to consider an AI-based solution as widely conducted in the related literature. Nevertheless, relying entirely on neural networks introduces several inconveniences from which the heavy training process and the hyperparameters tuning are the most influential. An innovative solution that combines the magnetic field gradient-based EKF with a BiLSTM network is then proposed. The main idea behind this approach is to obtain a velocity estimate from the BiLSTM, that is fed to the EKF as a pseudo-measurement. The level of confidence given to it by the EKF is controlled using a measurement covariance adapter. This is achieved while using a very small training dataset for the BiLSTM, and without requiring any sophisticated tuning of its hyperparameters. The EKF-BiLSTM can be applied to any trajectory scenario, no matter the sensor board attachment and for any studied application, which makes it a very suitable solution to the indoor navigation problem.

The performance evaluation of the EKF-BiLSTM is first conducted using an open-source dataset with real foot-mounted inertial and magnetic measurements, corresponding to one trajectory. This limited experimental scenario does not demonstrate the generality of the proposed approach, that can be applied on any type of trajectory and for whatever sensor board placement, under various applications. The used dataset also lacks measurements of a magnetometer array (only one magnetometer is considered) and is missing ground truth data. Therefore, acquiring a complete dataset is necessary to rigorously evaluate the proposed EKF-BiLSTM approach.

A real case study is then conducted with a complete sensor board provided by SYSNAV company (MIT), generating not only inertial but also magnetometer array measurements. In addition, ground truth data is acquired from a motion capture system composed of 9 cameras from Qualisys brand. Measurements of five trajectory scenarios (square, circle, diagonal rectangle, triangle and heart) and three sensor board attachments (right tibia, right front pocket, and waist) are recorded. The generation of datasets is conducted after going through calibration and synchronization steps.

Comparisons are performed between the different studied approaches in this thesis: EKF, EKF-ZUPT, and EKF-BiLSTM, where it is demonstrated that the proposed EKF-BiLSTM approach outperforms the EKF and EKF-ZUPT under all the studied sensor placements. For the velocity estimation, the EKF-BiLSTM succeeds to decrease the EKF's error with more than a factor of 2 for all studied sensor placements. While for the position estimation, it is shown that the BiLSTM's impact is mostly seen under the pocket and waist attachments, which correspond to the low magnetic field gradient case. The proposed EKF-BiLSTM approach provides the best accuracy results in the case of the tibia attachment, when there is sufficient magnetic disturbances, and generates a position error of approximately 1 m, which competes with state-of-the-art related works.

Challenges and perspectives

Indoor navigation using low-cost inertial and magnetic sensors under an EKF-based framework that is aided by AI, introduces different challenges such as

- Attitude observability conditions of the proposed navigation model are still dependent on the presence of magnetic field disturbances, the ranks of the magnetic field gradient and hessian matrices, as well as the nature of the trajectory (non-static). Having favorable conditions to ensure an all-time observability is not guaranteed even in an indoor environment, as the magnetic field perturbations can get really low at certain scenarios, or when the studied body remains immobile for a long period of time. The drift in attitude in these cases is the result of the presence of noise and bias in angular rate measurements that is not modeled in this thesis;

- Relying on an EKF-based framework generates several numerical errors, from which those induced by the non optimal tuning of noise covariance matrices are the most significant. The hand-tuning of the process Q and measurement N noise covariance matrices represents one of the main difficulties encountered in this thesis as the smallest change in their values can induce the divergence of the EKF;

- The choice of the neural network architecture and the values of its corresponding hyperparameters is conducted using a trial and error scheme. However, it is believed that further investigations can result in a better design in terms of prediction accuracy and computation time, especially if an online solution is considered;

- To the author's knowledge, there are no publicly available datasets of a magnetometer array with the needed architecture to apply the proposed solutions of this thesis. Until acquiring the sensor board (MIT) from SYSNAV company, the different discussed solutions were evaluated under datasets that contained only one magnetic field measurements, and thus the rest of the magnetometer array had to be simulated. While the theoretical array has enabled conducting the different performance validations, it does not entirely reflect the complexity of the magnetic field disturbances observed indoor, therefore it may introduce additional errors in the estimation process.

The different challenges discussed above encourage the following future work

- Further investigations on the observability conditions of the proposed navigation model may reveal the exact cases where the observability matrix becomes deficient. This can be done with a more precise understanding on the relationship between the ranks of the magnetic field gradient and the hessian matrices as well as their correlations with attitude and velocity.

It is reminded that, in challenging conditions such as the low magnetic field gradient case or static and quasi-static periods, attitude observability is the most influenced because of angular rate's noise and bias. A preliminary consideration in this case recalls the QSF approach that is discussed in the beginning of this thesis. Such technique enables not only the detection of this quasi-static periods where the magnetic field's magnitude and direction are constant, but it also uses them as measurements in an EKF filter, to mitigate gyroscope errors and consequently, better estimate the attitude. It is believed then, that the proposed solutions in this thesis that rely on the magnetic field's spatial gradient, and the QSF technique that rather considers the temporal one, are very complementary. Whether the trajectory is highly dynamic or almost static, the combination of both approaches can cover all possible scenarios, and may guarantee, an all-time observability on the states and remarkable estimation results;

- Sensors' biases and especially that of the gyroscope has to be modeled and subtracted from the angular rate measurements in order to lower its effect on attitude estimation, mainly when observability issues are encountered. A preliminary work has been done in this sense, inspired by Ref. [Brossard2020c], where authors propose a learning method for denoising gyroscopes using ground truth data, a neural network based on dilated convolutions, and a proper loss function. In a similar manner, and as an initial work, a BiLSTM-based network has been designed to receive noisy and biased gyroscope measurements as an input, and true angular measurements deduced from ground truth attitude as an output. Consequently, the BiLSTM learns a model that enables the prediction of true angular rate values whenever it is given noisy and biased measurements from the gyroscope. The main challenge encountered in such solution is obtaining true angular rates from ground truth attitude, as the latter is usually acquired from a motion capture system which itself, suffers from noise and occasional "bugs". Any pre-processing of this ground truth data may filter-out valuable information, that cause a change in the actual orientation and consequently a different trajectory is obtained. Further work is then expected in this sense to figure out how to handle such constraints;

- A sophisticated tuning of the EKF's process and measurement noise covariance matrices is mandatory to ensure its optimal performance. A profound review of state-of-the-art works have shown numerous solutions to treat this problem, such as adaptive Kalman filtering Refs. [Hashlamon2020, Akhlaghi2017, Yang2006], optimization techniques Refs. [Chen2018b, Kaur2016b, Kaur2016a, Karasalo2011], machine learning Ref. [Abbeel2005] and reinforcement learning through the *Q-learning* method Ref. [Xiong2020]. An attempt to apply such technique on a simplified navigation model, focusing only on quaternion and gyroscope bias estimation, has been conducted. Nevertheless, no significant improvement compared to the hand-tuning case is obtained. Further investigations must be performed to better understand the reasons for such initial results;

- If no sensor board containing the desired magnetometer array is available, one would have to simulate different magnetic fields from one magnetometer's measurements in a rigorous way, in order to have a complete benchmark for evaluations when performing magneto-inertial navigation. To do so, the spherical harmonic expansion of the Earth's magnetic field can be explored as conducted in Refs. [Tóth2011, Roithmayr2004, Tikhonov2002, Granzow1983], which may greatly serve in providing adequate and close to reality measurements from a theoretical magnetometer array.

Bibliography

[Abbeel2005] P. Abbeel, A. Coates, M. Montemerlo, A.-Y. Ng and S. Thrun. *Discriminative Training of Kalman Filters.* In Robotics: Science and systems, volume 2, page 1, Cambridge, Massachusetts, USA, 2005.

[Afraimovich2002] E.-L. Afraimovich, O.-S. Lesyuta and I.-I Ushakov. *Geomagnetic disturbances and operation of the GPS navigation system*. Geomagnetism and Aeronomy C/C of Geomagnetizm I Aeronomiia, vol. 42, no. 2, pages 208–215, 2002.

[Afzal2011a] M.-H. Afzal. Use of earth's magnetic field for pedestrian navigation. 2011.

[Afzal2011b] M.-H. Afzal, V. Renaudin and G. Lachapelle. *Magnetic field based heading estimation for pedestrian navigation environments*. In International Conference on Indoor Positioning and Indoor Navigation (IPIN), pages 1–10, Guimaraes, Portugal, 2011. IEEE.

[Afzal2011c] M.-H. Afzal, V. Renaudin and G. Lachapelle. *Use of earth's magnetic field for mitigating gyroscope errors regardless of magnetic perturbation*. Sensors, vol. 11, no. 12, pages 11390–11414, 2011.

[Akhlaghi2017] S. Akhlaghi, N. Zhou and Z. Huang. *Adaptive adjustment of noise covariance in Kalman filter for dynamic state estimation*. In Power & energy society general meeting, pages 1–5, Chicago, Illinois, USA, 2017. IEEE.

[Albawi2017] S. Albawi, T.-A. Mohammed and S. Al-Zawi. *Understanding of a convolutional neural network*. In International Conference on Engineering and Technology (ICET), pages 1–6, Antalya, Turkey, 2017. IEEE.

[Alom2019] M.-Z. Alom, T.-M Taha, C. Yakopcic, S. Westberg, P. Sidike, M.-S. Nasrin, M. Hasan, B.-C. Van Essen, A.-A. Awwal and V.-K. Asari. *A state-of-the-art survey on deep learning theory and architectures*. Electronics, vol. 8, no. 3, page 292, 2019.

[Amari1993] S.-i. Amari. *Backpropagation and stochastic gradient descent method*. Neurocomputing, vol. 5, no. 4-5, pages 185–196, 1993.

[Amirsadri2012] A. Amirsadri, J. Kim, L. Petersson and J. Trumpf. *Practical considerations in precise calibration of a low-cost MEMS IMU for road-mapping applications*. In American Control Conference (ACC), pages 881–888, Montréal, Canada, 2012. IEEE.

[Anysz2016] H. Anysz, A. Zbiciak and N. Ibadov. *The Influence of Input Data Standardization Method on Prediction Accuracy of Artificial Neural Networks*. Procedia Engineering, vol. 153, pages 66–70, 2016.

[Ashraf2019] I. Ashraf, S. Hur and Y. Park. *Application of deep convolutional neural networks and smartphone sensors for indoor localization*. Applied Sciences, vol. 9, no. 11, page 2337, 2019.

[Ashraf2021] I. Ashraf, Y.B. Zikria, S. Hur, A.K. Bashir, T. Alhussain and Y. Park. *Localizing pedestrians in indoor environments using magnetic field data with term frequency paradigm and deep neural networks*. International Journal of Machine Learning and Cybernetics, 2021.

[Atkinson1988] K-.A. Atkinson. *An Introduction to Numerical Analysis (2nd ed.)*. 1988.

[Bachmann2004] E.-R. Bachmann, X. Yun and C.-W. Peterson. *An investigation of the effects of magnetic variations on inertial/magnetic orientation sensors*. In International Conference on Robotics and Automation, pages 1115–1122, New Orleans, LA, USA, 2004. IEEE.

[Baldi2013] P. Baldi and P.-J. Sadowski. *Understanding dropout*. Advances in neural information processing systems, vol. 26, pages 2814–2822, 2013.

[Bancroft2012] Jared B Bancroft and Gérard Lachapelle. *Use of magnetic quasi static field (QSF) updates for pedestrian navigation*. In Position Location and Navigation Symposium (PLANS), pages 605–612, Myrtle Beach, SC, USA, 2012.

[Barrau2015] A. Barrau. *Non-linear state error based extended Kalman filters with applications to navigation*. PhD Thesis, Mines ParisTech, France, 2015.

[Batista2013] P. Batista, N. Petit, C. Silvestre and P. Oliveira. *Further results on the observability in magneto-inertial navigation*. In American Control Conference, pages 2503–2508, Washington, DC, USA, 2013. IEEE.

[Bebis1994] G. Bebis and M. Georgiopoulos. *Feed-forward neural networks*. IEEE Potentials, vol. 13, no. 4, pages 27–31, 1994.

[Benzerrouk2014] H. Benzerrouk, A. Nebylov, H. Salhi and P. Closas. *MEMS IMU/ZUPT based cubature kalman filter applied to pedestrian navigation system*. In International Electronic Conference on Sensors and Applications, pages 1–7, online, 2014.

[Besançon2007] G. Besançon. Nonlinear observers and applications. Springer Verlag, 2007.

[Black1964] H.-D. Black. *A passive system for determining the attitude of a satellite*. AIAA journal, vol. 2, no. 7, pages 1350–1351, 1964.

[Boyd2018] S. Boyd and L. Vandenberghe. Introduction to applied linear algebra: Vectors, matrices, and least squares. Cambridge University Press, 2018.

[Brossard2020a] M. Brossard. *Deep learning, Inertial Measurements Units, and Odometry: Some Modern Prototyping Techniques for Navigation Based on Multi-Sensor Fusion*. PhD Thesis, Mines ParisTech, France, 2020.

[Brossard2020b] M. Brossard, A. Barrau and S. Bonnabel. *AI-IMU Dead-Reckoning*. IEEE Transactions on Intelligent Vehicles, vol. 5, no. 4, pages 585–595, 2020.

[Brossard2020c] M. Brossard, S. Bonnabel and A. Barrau. *Denoising IMU Gyroscopes with Deep Learning for Open-Loop Attitude Estimation*. IEEE Robotics and Automation Letters, vol. 5, no. 3, pages 4796–4803, 2020.

[Caruso2016] D. Caruso, M. Sanfourche, G. Le Besnerais and D. Vissière. *Infrastructureless indoor navigation with an hybrid magneto-inertial and depth sensor system*. In International Conference on Indoor Positioning and Indoor Navigation (IPIN), pages 1–8, Madrid, Spain, 2016. IEEE.

[Caruso2017a] D. Caruso, A. Eudes, M. Sanfourche, D. Vissiere and G. le Besnerais. *An inverse square root filter for robust indoor/outdoor magneto-visual-inertial odometry*. In International Conference on Indoor Positioning and Indoor Navigation (IPIN), pages 1–8, Sapporo, Japan, 2017.

[Caruso2017b] D. Caruso, A. Eudes, M. Sanfourche, D. Vissière and G. le Besnerais. *Robust indoor/outdoor navigation through magneto-visual-inertial optimization-based estimation*. In IEEE/RSJ International Conference on Intelligent Robots and Systems (IROS), pages 4402–4409, Vancouver, Canada, 2017.

[Caruso2017c] D. Caruso, A. Eudes, M. Sanfourche, D. Vissière and G. A Le Besnerais. *Robust Indoor/Outdoor Navigation Filter Fusing Data from Vision and Magneto-Inertial Measurement Unit*. Sensors, vol. 17, page 2795, 2017.

[Caruso2018] David Caruso. *Improving Visual-Inertial Navigation Using Stationary Environmental Magnetic Disturbances*. PhD Thesis, Université Paris Saclay (COmUE), 2018.

[Caruso2019] D. Caruso, A. Eudes, M. Sanfourche, D. Vissière and G. le Besnerais. *Magneto-visual-inertial Dead-reckoning: Improving Estimation Consistency by Invariance*. In Conference on Decision and Control (CDC), pages 7923–7930, Nice, France, 2019.

[Chen2018a] C. Chen, X. Lu, A. Markham and N. Trigoni. *Ionet: Learning to cure the curse of drift in inertial odometry*. In Proceedings of the AAAI Conference on Artificial Intelligence, volume 32, 2018.

[Chen2018b] Z. Chen, C. Heckman, S. Julier and N. Ahmed. *Weak in the NEES?: Auto-tuning Kalman filters with Bayesian optimization*. In International Conference on Information Fusion (FUSION), pages 1072–1079, Cambridge, United Kingdom, 2018. IEEE.

[Chen2019a] C. Chen, C.-X. Lu, B. Wang, N. Trigoni and A. Markham. *DynaNet: Neural Kalman Dynamical Model for Motion Estimation and Prediction*. arXiv preprint arXiv:1908.03918, 2019.

[Chen2019b] C. Chen, X. Lu, J. Wahlstrom, A. Markham and N. Trigoni. *Deep neural network based inertial odometry using low-cost inertial measurement units*. IEEE Transactions on Mobile Computing, 2019.

[Chen2020a] C. Chen, P. Zhao, C.-X. Lu, W. Wang, A. Markham and N. Trigoni. *Deep-Learning-Based Pedestrian Inertial Navigation: Methods, Data Set, and On-Device Inference*. IEEE Internet of Things Journal, vol. 7, no. 5, pages 4431–4441, 2020.

[Chen2020b] L. Chen, J. Wu and C. Yang. *MeshMap: A Magnetic Field-Based Indoor Navigation System With Crowdsourcing Support*. IEEE Access, vol. 8, pages 39959–39970, 2020.

[Cheng2005] Y. Cheng and M.-D. Shuster. *Quest and the anti-quest: good and evil attitude estimation*. The Journal of the Astronautical Sciences, vol. 53, no. 3, pages 337–351, 2005.

[Chesneau2016] C.-I. Chesneau, M. Hillion and C. Prieur. *Motion estimation of a rigid body with an EKF using magneto-inertial measurements*. In International Conference on Indoor Positioning and Indoor Navigation (IPIN), pages 1–6, Alcalá de Henares, Madrid, Spain, 2016. IEEE.

[Chesneau2017] C.-I. Chesneau, M. Hillion, J. Hullo, G. Thibault and C. Prieur. *Improving magneto-inertial attitude and position estimation by means of a magnetic heading observer*. In International Conference on Indoor Positioning and Indoor Navigation (IPIN), pages 1–8, Sapporo, Japan, 2017. IEEE.

[Chesneau2018] C.-I. Chesneau. *Magneto-Inertial Dead Reckoning in inhomogeneous field and indoor applications*. PhD Thesis, Université Grenoble Alpes, 2018.

[Chesneau2019] C.-I. Chesneau, R. Robin, H. Meier, M. Hillion and C. Prieur. *Calibration of a magnetometer array using motion capture equipment*. Asian Journal of Control, vol. 21, no. 4, pages 1459–1469, 2019.

[Cho2019] S.-Y. Cho and C.-G. Park. *Threshold-less zero-velocity detection algorithm for pedestrian dead reckoning*. In European Navigation Conference (ENC), pages 1–5, Warsaw, Poland, 2019. IEEE.

[Choukroun2006] D. Choukroun, I.Y Bar-Itzhack and Y. Oshman. *Novel quaternion Kalman filter*. IEEE Transactions on Aerospace and Electronic Systems, vol. 42, no. 1, pages 174–190, 2006.

[Coskun2017] H. Coskun, F. Achilles, R. DiPietro, N. Navab and F. Tombari. *Long short-term memory kalman filters: Recurrent neural estimators for pose regularization*. In International Conference on Computer Vision, pages 5524–5532, Venice, Italy, 2017.

[Crassidis2007] J. Crassidis, L. Markley and Y. Cheng. *Survey of Nonlinear Attitude Estimation Methods*. Journal of Guidance Control and Dynamics, vol. 30, pages 12–28, 2007.

[Daum2015] F.-E. Daum. Extended kalman filters, pages 411–413. Springer London, 2015.

[De Celis2018] R. De Celis and L. Cadarso. *Attitude Determination Algorithms through Accelerometers, GNSS Sensors, and Gravity Vector Estimator*. International Journal of Aerospace Engineering, 2018.

[De Vries2009] W. De Vries, D. Veeger, C. Baten and F. van der Helm. *Magnetic distortion in motion labs, implications for validating inertial magnetic sensors*. Gait & posture, vol. 29, pages 535–541, 2009.

[Diaz2015] E.-M. Diaz, F. de Ponte Müller, A.-R. Jiménez and F. Zampella. *Evaluation of AHRS algorithms for inertial personal localization in industrial environments*. In International Conference on Industrial Technology (ICIT), pages 3412–3417, Seville, Spain, 2015. IEEE.

[Diebel2006] J. Diebel. *Representing Attitude : Euler Angles , Unit Quaternions , and Rotation Vectors*. In Stanford University, Stanford, California, 2006.

[Dorveaux2009] E. Dorveaux, D. Vissière, A.-P. Martin and N. Petit. *Iterative calibration method for inertial and magnetic sensors*. In Conference on Decision and Control (CDC) held jointly with Chinese Control Conference (CCC), pages 8296–8303, Shanghai, China, 2009. IEEE.

[Dorveaux2011a] E. Dorveaux. *Magneto-inertial navigation: principles and application to an indoor pedometer*. PhD Thesis, École Nationale Supérieure des Mines de Paris, 2011.

[Dorveaux2011b] E. Dorveaux, T. Boudot, M. Hillion and N. Petit. *Combining inertial measurements and distributed magnetometry for motion estimation*. In American Control Conference, pages 4249–4256, San Francisco, CA, USA, 2011. IEEE.

[Dorveaux2011c] E. Dorveaux and N. Petit. *Presentation of a magneto-inertial positioning system: navigating through magnetic disturbances*. In International Conference on Indoor Positioning and Indoor Navigation (IPIN), Guimarães, Portugal, 2011.

[Edel2015] M. Edel and E. Köppe. *An advanced method for pedestrian dead reckoning using BLSTM-RNNs*. In International Conference on Indoor Positioning and Indoor Navigation (IPIN), pages 1–6, Calgary, Canada, 2015. IEEE.

[Fallah2013] N. Fallah, I. Apostolopoulos, K. Bekris and E. Folmer. *Indoor human navigation systems: A survey*. Interacting with Computers, vol. 25, no. 1, pages 21–33, 2013.

[Feigl2019] T. Feigl, S. Kram, P. Woller, R. H. Siddiqui, M. Philippsen and C. Mutschler. *A Bidirectional LSTM for Estimating Dynamic Human Velocities from a Single IMU*. In International Conference on Indoor Positioning and Indoor Navigation (IPIN), pages 1–8, Pisa, Italy, 2019. IEEE.

[Feigl2020] T. Feigl, S. Kram, P. Woller, R. H. Siddiqui, M. Philippsen and C. Mutschler. *RNN-aided human velocity estimation from a single IMU*. Sensors, vol. 20, no. 13, page 3656, 2020.

[Forbes2011] C. Forbes, M. Evans, N. Hastings and B. Peacock. Statistical distributions. John Wiley & Sons, 2011.

[Foster2008] C.-C. Foster and G.-H. Elkaim. *Extension of a two-step calibration methodology to include nonorthogonal sensor axes*. IEEE Transactions on Aerospace and Electronic Systems, vol. 44, no. 3, pages 1070–1078, 2008.

[Fourati2015] H. Fourati. *Heterogeneous data fusion algorithm for pedestrian navigation via foot-mounted inertial measurement unit and complementary filter*. IEEE Transactions on Instrumentation and Measurement, vol. 64, no. 1, pages 221–229, 2015.

[Frix1994] W.-M. Frix, G.-G. Karady and B.-A. Venetz. *Comparison of calibration systems for magnetic field measurement equipment*. IEEE Transactions on Power Delivery, vol. 9, no. 1, pages 100–108, 1994.

[Galván-Tejada2020] C.E. Galván-Tejada, L.A. Zanella-Calzada, A. García-Domínguez, R. Magallanes-Quintanar, H. Luna-García, J.M. Celaya-Padilla, J.I. Galván-Tejada, A. Vélez-Rodríguez and H. Gamboa-Rosales. *Estimation of Indoor Location Through Magnetic Field Data: An Approach Based On Convolutional Neural Networks*. ISPRS International Journal of Geo-Information, vol. 9, page 226, 2020.

[Gipsa-lab0 19] Gipsa-lab. *Biomeca room presentation*. http://www.gipsa-lab.fr/recherche/poles-de-plates-formes/plates-formes.php?id_plateforme=71, Accessed: 2020-10-19.

[Granzow1983] K.-D. Granzow. *Spherical harmonic representation of the magnetic field in the presence of a current density*. Geophysical Journal International, vol. 74, no. 2, pages 489–505, 1983.

[Grewal2020] M. S. Grewal, A. P. Andrews and C. G. Bartone. Kalman filtering, pages 355–417. 2020.

[Grossmann2007] C. Grossmann, H.-G. Roos and M. Stynes. Numerical Treatment of Partial Differential Equations. Springer Science & Business Media, 2007.

[Hairer1996] E. Hairer and G. Wanner. Analysis by its history. Springer, 1996.

[Hanley2018] D. Hanley, X. Zhang, A. S. Dantas de Oliveira, D. Steinberg and T. Bretl. *Experimental Evaluation of the Planar Assumption in Magnetic Positioning*. In International Conference on Indoor Positioning and Indoor Navigation (IPIN), pages 1–8, Nantes, France, 2018.

[Hasan2009] A.-M. Hasan, K. Samsudin, A.-R. Ramli, R.-S. Azmir and S.-A. Ismaeel. *A review of navigation systems (integration and algorithms)*. Australian journal of basic and applied sciences, vol. 3, no. 2, pages 943–959, 2009.

[Hashlamon2020] I. Hashlamon. *A new adaptive extended Kalman filter for a class of nonlinear systems*. 2020.

[He2016] K. He, X. Zhang, S. Ren and J. Sun. *Deep residual learning for image recognition*. In IEEE conference on computer vision and pattern recognition, pages 770–778, Las Vegas, Nevada, USA, 2016.

[Herath2020] S. Herath, Hang Yan and Yasutaka Furukawa. *RoNIN: Robust Neural Inertial Navigation in the Wild: Benchmark, Evaluations, & New Methods*. In International Conference on Robotics and Automation (ICRA), pages 3146–3152, Online, 2020. IEEE.

[Hirano1974] K. Hirano, S. Nishimura and S. Mitra. *Design of digital notch filters*. IEEE Transactions on Communications, vol. 22, no. 7, pages 964–970, 1974.

[Hochreiter1997] S. Hochreiter and J. Schmidhuber. *Long short-term memory*. Neural Computation, vol. 9, no. 8, pages 1735–1780, 1997.

[Hosseinyalamdary2018] S. Hosseinyalamdary. *Deep Kalman filter: Simultaneous multi-sensor integration and modelling; A GNSS/IMU case study*. Sensors, vol. 18, no. 5, page 1316, 2018.

[Hou2020] X. Hou and J. Bergmann. *Pedestrian Dead Reckoning with Wearable Sensors: A Systematic Review*. IEEE Sensors Journal, vol. 21, no. 1, pages 143–152, 2020.

[Jackson1998] J.D. Jackson. Classical electrodynamics. Third Edition. John Wiley & Sons, Inc., 1998.

[Jamil2020] F. Jamil, N. Iqbal, S. Ahmad and D.-H. Kim. *Toward Accurate Position Estimation Using Learning to Prediction Algorithm in Indoor Navigation*. Sensors, vol. 20, no. 16, page 4410, 2020.

[Jang2020] J.-T. Jang, A. Santamaria-Navarro, B.-T. Lopez and A.-A. Aghamohammadi. *Analysis of State Estimation Drift on a MAV Using PX4 Autopilot and MEMS IMU During Dead-reckoning*. In IEEE Aerospace Conference, pages 1–11, Big Sky, Montana, USA, 2020. IEEE.

[Javed2020] M. A. Javed, M. Tahir and K. Ali. *Cascaded Kalman Filtering-Based Attitude and Gyro Bias Estimation With Efficient Compensation of External Accelerations*. IEEE Access, vol. 8, pages 50022–50035, 2020.

[Jiménez2009] A.-R. Jiménez, F. Seco, J.-C. Prieto and J. Guevara. *A comparison of pedestrian dead-reckoning algorithms using a low-cost MEMS IMU*. In International Symposium on Intelligent Signal Processing, pages 37–42, Budapest, Hungary, 2009. IEEE.

[Jiménez2010] A.-R. Jiménez, F. Seco, J.-C. Prieto and J. Guevara. *Indoor pedestrian navigation using an INS/EKF framework for yaw drift reduction and a foot-mounted IMU*. In Workshop on Positioning, Navigation and Communication, pages 135–143, Dresden, Germany, 2010. IEEE.

[Ju2018] H. Ju and C.-G. Park. *A pedestrian dead reckoning system using a foot kinematic constraint and shoe modeling for various motions*. Sensors and Actuators A: Physical, vol. 284, pages 135–144, 2018.

[Kaewpinjai2020] R. Kaewpinjai, T. Chuaubon and A. Apavatjrut. *On Improving Indoor Navigation Accuracy Using Bluetooth Beacons*. In International Conference on Electrical Engineering/Electronics, Computer, Telecommunications and Information Technology (ECTI-CON), pages 727–730, Phuket, Thailand, 2020. IEEE.

[Kalman1960a] R. E. Kalman. *A New Approach to Linear Filtering and Prediction Problems*. Transactions of the ASME - Journal of Basic Engineering, vol. 82, pages 35–45, 1960.

[Kalman1960b] R.-E. Kalman. *On the general theory of control systems*. In International Conference on Automatic Control, pages 481–492, Moscow, USSR, 1960.

[Kang2018a] J. Kang, J. Lee and D.-S. Eom. *Smartphone-based traveled distance estimation using individual walking patterns for indoor localization*. Sensors, vol. 18, no. 9, page 3149, 2018.

[Kang2018b] J. Kang, J. Lee and D.-S. Eom. *Smartphone-Based Traveled Distance Estimation Using Individual Walking Patterns for Indoor Localization*. Sensors, vol. 18, no. 9, page 3149, 2018.

[Karasalo2011] M. Karasalo and X. Hu. *An optimization approach to adaptive Kalman filtering*. Automatica, vol. 47, no. 8, pages 1785–1793, 2011.

[Kaselimi2019] M. Kaselimi, N. Doulamis, A. Doulamis, A. Voulodimos and E. Protopapadakis. *Bayesian-optimized bidirectional LSTM regression model for non-intrusive load monitoring*. In International Conference on Acoustics, Speech and Signal Processing (ICASSP), pages 2747–2751, Brighton, United Kingdom, 2019. IEEE.

[Kaur2016a] N. Kaur and A. Kaur. *A review on tuning of extended kalman filter using optimization techniques for state estimation*. International Journal of Computer Applications, vol. 145, no. 15, pages 1–5, 2016.

[Kaur2016b] N. Kaur and A. Kaur. *Tuning of extended kalman filter for nonlinear state estimation*. IOSR Journal of Computer Engineering, vol. 18, no. 05, pages 14–19, 2016.

[Kingma2015] D.-P. Kingma and J. Ba. *ADAM: A Method for Stochastic Optimization*. In International Conference on Learning Representations, San Diego, USA, 2015.

[Kok2018] M. Kok and A. Solin. *Scalable Magnetic Field SLAM in 3D Using Gaussian Process Maps*. In International Conference on Information Fusion (FUSION), pages 1353–1360, Cambridge, United Kingdom, 2018.

[Kone2020] Y. Kone, N. Zhu, V. Renaudin and M. Ortiz. *Machine learning-based zero-velocity detection for inertial pedestrian navigation*. IEEE Sensors Journal, vol. 20, no. 20, pages 12343–12353, 2020.

[Krauss1992] J. D. Krauss. Electromagnetics. McGraw-Hill, 1992.

[Kroese2014] D.-P. Kroese, T. Brereton, T. Taimre and Z. Botev. *Why the Monte Carlo method is so important today*. Wiley Interdisciplinary Reviews: Computational Statistics, vol. 6, pages 386–392, 2014.

[Kuang2018] J. Kuang, X. Niu, P. Zhang and X. Chen. *Indoor Positioning Based on Pedestrian Dead Reckoning and Magnetic Field Matching for Smartphones*. Sensors, vol. 18, page 4142, 2018.

[Kuipers1999] J.B. Kuipers. Quaternions and rotation sequences: a primer with applications to orbits, aerospace, and virtual reality. Princeton university press, 1999.

[LeCun2015] Y. LeCun, Y. Bengio and G. Hinton. *Deep learning*. nature, vol. 521, no. 7553, pages 436–444, 2015.

[Lee2008] J. Lee, Y. Zhu and A. Seshia. *Room temperature electrometry with SUB-10 electron charge resolution*. Journal of Micromechanics and Microengineering, vol. 18, no. 2, 2008.

[Li2001] X.-R. Li and Z. Zhao. *Measures of performance for evaluation of estimators and filters*. In International Symposium on Optical Science and Technology, San Diego, CA, United States, 2001.

[Li2016] J. Li, L. Deng, R. Haeb-Umbach and Y. Gong. *Chapter 6 - Explicit distortion modeling*. In Robust Automatic Speech Recognition, pages 137–170. Academic Press, 2016.

[Li2020] D. Li, X. Jia and J. Zhao. *A novel hybrid fusion algorithm for low-cost GPS/INS integrated navigation system during GPS outages*. IEEE Access, vol. 8, pages 53984–53996, 2020.

[Ligorio2013] G. Ligorio and A. Sabatini. *Extended Kalman Filter-Based Methods for Pose Estimation Using Visual, Inertial and Magnetic Sensors: Comparative Analysis and Performance Evaluation*. Sensors, vol. 13, no. 2, pages 1919–1941, 2013.

[Liu2014] H.-f. Liu, W. Ren, T. Zhang, J. Gong, J.-m. Liang, B. Liu, J.-w. Shi and Z. Huang. *An adaptive selection algorithm of threshold value in zero velocity updating for personal navigation system*. In Chinese Control Conference, pages 1035–1038, Nanjing, China, 2014. IEEE.

[Liu2019] X. Liu, S. Wang, X. Guo, W. Yang and G. Xu. *A Method for Gravitational Apparent Acceleration Identification and Accelerometer Bias Estimation*. IEEE Access, vol. 7, pages 38115–38122, 2019.

[Liu2020] W. Liu, D. Caruso, E. Ilg, J. Dong, A.-I. Mourikis, K. Daniilidis, V. Kumar and J. Engel. *TLIO: Tight Learned Inertial Odometry*. IEEE Robotics and Automation Letters, vol. 5, no. 4, pages 5653–5660, 2020.

[Liu2021] G. Liu, B. Yu, L. Huang, L. Shi, X. Gao and L. He. *Human-Interactive Mapping Method for Indoor Magnetic Based on Low-Cost MARG Sensors*. IEEE Transactions on Instrumentation and Measurement, vol. 70, pages 1–10, 2021.

[Lo2011] C.-C. Lo, C.-P. Chiu, Y.-C. Tseng, S.-A Chang and L.-C. Kuo. *A walking velocity update technique for pedestrian dead-reckoning applications*. In International Symposium on Personal, Indoor and Mobile Radio Communications (PIMRC), pages 1249–1253, Toronto, Canada, 2011. IEEE.

[LOPSI2021] LOPSI. *Downloads*. https://lopsi.weebly.com/downloads.html, 2021. 2021-12-04.

[Ma2018] M. Ma, Q. Song, Y. Gu, Y. Li and Z. Zhou. *An adaptive zero velocity detection algorithm based on multi-sensor fusion for a pedestrian navigation system*. Sensors, vol. 18, no. 10, page 3261, 2018.

[Madgwick2011] S.-O Madgwick, A.-J. Harrison and R. Vaidyanathan. *Estimation of IMU and MARG orientation using a gradient descent algorithm*. In International conference on rehabilitation robotics, pages 1–7, Zurich, Switzerland, 2011. IEEE.

[Madgwick2020] S.-O. Madgwick, S. Wilson, R. Turk, J. Burridge, C. Kapatos and R. Vaidyanathan. *An extended complementary filter for full-body MARG orientation estimation*. IEEE/ASME Transactions on Mechatronics, vol. 25, no. 4, pages 2054–2064, 2020.

[Maeland1988] E. Maeland. *On the comparison of interpolation methods*. IEEE transactions on medical imaging, vol. 7, no. 3, pages 213–217, 1988.

[Mahony2008] R. Mahony, T. Hamel and J.-M. Pflimlin. *Nonlinear complementary filters on the special orthogonal group*. IEEE Transactions on automatic control, vol. 53, no. 5, pages 1203–1218, 2008.

[Makni2014] A. Makni, H. Fourati and A.-Y Kibangou. *Adaptive Kalman filter for MEMS-IMU based attitude estimation under external acceleration and parsimonious use of gyroscopes*. In European Control Conference (ECC), pages 1379–1384, Strasbourg, France, 2014. IEEE.

[Makni2019] A. Makni, A.-Y. Kibangou and H. Fourati. *Data fusion-based descriptor approach for attitude estimation under accelerated maneuvers*. Asian Journal of Control, vol. 21, no. 4, pages 1433–1442, 2019.

[Manos2018] A. Manos, I. Klein and T. Hazan. *Gravity Direction Estimation and Heading Determination for Pedestrian Navigation*. pages 206–212, Nantes, France, 2018.

[Manski1991] C.-F. Manski. *Regression*. Journal of Economic Literature, vol. 29, pages 34–50, 1991.

[Markley2000] F.-L. Markley and D. Mortari. *Quaternion attitude estimation using vector observations*. The Journal of the Astronautical Sciences, vol. 48, no. 2, pages 359–380, 2000.

[Martín-Gorostiza2019] E. Martín-Gorostiza, M.-A. García-Garrido, D. Pizarro, D. Salido-Monzú and P. Torres. *An Indoor Positioning Approach Based on Fusion of Cameras and Infrared Sensors*. Sensors, vol. 19, no. 11, page 2519, 2019.

[Medsker1999] L. Medsker and L.-C. Jain. Recurrent neural networks: design and applications. CRC press, 1999.

[Michel2017] T. Michel. *On mobile augmented reality applications based on geolocation*. PhD Thesis, Université Grenoble Alpes, 2017.

[Miller2004] S.-L. Miller and D. Childers. Chapter 10 - power spectral density. Academic Press, 2004.

[Mitchell2013] R. Mitchell, J. Michalski and T. Carbonell. An artificial intelligence approach. Springer, 2013.

[Mohamadabadi2014] K. Mohamadabadi and M. Hillion. *An automated indoor scalar calibration method for three-axis vector magnetometers*. IEEE Sensors Journal, vol. 14, no. 9, pages 3076–3083, 2014.

[Motroni2021] A. Motroni, A. Buffi and P. Nepa. *A survey on Indoor Vehicle Localization through RFID Technology*. IEEE Access, vol. 9, pages 17921–17942, 2021.

[MTi2021] Xsens MTi. *Products*. https://www.xsens.com/mti-products, 2021. 2021-19-04.

[Myung2003] I.-J. Myung. *Tutorial on maximum likelihood estimation*. Journal of mathematical Psychology, vol. 47, no. 1, pages 90–100, 2003.

[Nazemipour2020] A. Nazemipour, M. T. Manzuri, D. Kamran and M. Karimian. *MEMS Gyro Bias Estimation in Accelerated Motions Using Sensor Fusion of Camera and Angular-Rate Gyroscope*. IEEE Transactions on Vehicular Technology, vol. 69, no. 4, pages 3841–3851, 2020.

[Needham2003] C.-J. Needham and R.-D. Boyle. *Performance evaluation metrics and statistics for positional tracker evaluation*. In International Conference on Computer Vision Systems (ICVS), pages 278–289, Graz, Austria, 2003. Springer.

[Nessa2020] A. Nessa, B. Adhikari, F. Hussain and X.-N. Fernando. *A Survey of Machine Learning for Indoor Positioning*. IEEE Access, vol. 8, pages 214945–214965, 2020.

[Nilsson2010] J.-O Nilsson, I. Skog and P. Händel. *Performance characterisation of foot-mounted ZUPT-aided INSs and other related systems*. In International Conference on Indoor Positioning and Indoor Navigation (IPIN), pages 1–7, Zurich, Switzerland, 2010. IEEE.

[Nilsson2012] J.-O. Nilsson, I. Skog, P. Händel and K.-V.-S. Hari. *Foot-mounted INS for everybody-an open-source embedded implementation*. In Position Location and Navigation Symposium (PLANS), pages 140–145, Myrtle Beach, SC, USA, 2012.

[Nilsson2014a] J.-O. Nilsson, A.-K. Gupta and P. Händel. *Foot-mounted inertial navigation made easy*. In International Conference on Indoor Positioning and Indoor Navigation (IPIN), pages 24–29, Busan, South Korea, 2014. IEEE.

[Nilsson2014b] N.-J. Nilsson. Principles of artificial intelligence. Morgan Kaufmann, 2014.

[Nilsson2016] J. Nilsson and I. Skog. *Inertial sensor arrays — A literature review*. In European Navigation Conference (ENC), pages 1–10, Helsinki, Finland, 2016.

[NOAA2021] NOAA. *National Oceanic and Atmospheric Administration (NOAA)*, 2021.

[Oppenheim2015] A.-V. Oppenheim and G.-C. Verghese. Signals, systems and inference. Pearson, 2015.

[Oshman2006] Y. Oshman and A. Carmi. *Attitude estimation from vector observations using a genetic-algorithm-embedded quaternion particle filter*. Journal of Guidance, Control, and Dynamics, vol. 29, no. 4, pages 879–891, 2006.

[Parakkal2017] P.-G. Parakkal and V.-S. Variyar. *GPS based navigation system for autonomous car*. In International Conference on Advances in Computing, Communications and Informatics (ICACCI), pages 1888–1893, Manipal, India, 2017. IEEE.

[Praly2013] N. Praly, P.-J. Bristeau, J. Laurent-Varin and N. Petit. *Using distributed magnetometry in navigation of heavy launchers and space vehicles*. Progress in Flight Dynamics, Guidance, Navigation, Control, Fault Detection, and Avionics, vol. 6, pages 45–54, 2013.

[Qualisys2021] Qualisys. *Website*. https://www.qualisys.com/, 2021. Accessed: 2021-05-25.

[Raquet2013] J.-F. Raquet, J.-A. Shockley and K.-A. Fisher. *Determining Absolute Position Using 3-Axis Magnetometers and the Need for Self-Building World Models*. NATO panel STO-EN-SET-197, 2013.

[Reed1999] R. Reed and R.-J. MarksII. Neural smithing: supervised learning in feedforward artificial neural networks. Mit Press, 1999.

[Reginya2018] S. Reginya, V. Nikolaenko, R. Voronov, A. Soloviev, A. Sikora and A. Moschevikin. *MEMS Sensors Bias Thermal Profiles Classification Using Machine Learning*. volume 2278 of *International Workshop on Stochastic Modeling and Applied Research of Technology*, pages 17 – 28, Petrozavodsk, Russia, 2018. RWTH.

[Renaudin2010] V. Renaudin, M.-H. Afzal and G. Lachapelle. *Complete triaxis magnetometer calibration in the magnetic domain*. Journal of sensors, vol. 2010, 2010.

[Renaudin2012a] V. Renaudin, M.-H. Afzal and G. Lachapelle. *Magnetic perturbations detection and heading estimation using magnetometers*. Journal of Location Based Services, vol. 6, no. 3, pages 161–185, 2012.

[Renaudin2012b] V. Renaudin, M. Susi and G. Lachapelle. *Step length estimation using handheld inertial sensors*. Sensors, vol. 12, no. 7, pages 8507–8525, 2012.

[Renaudin2014] V. Renaudin and C. Combettes. *Magnetic, acceleration fields and gyroscope quaternion (MAGYQ)-based attitude estimation with smartphone sensors for indoor pedestrian navigation*. Sensors, vol. 14, no. 12, pages 22864–22890, 2014.

[Robertson2013] P. Robertson, M. Frassl, M. Angermann, M. Doniec, B.-J. Julian, M.-G. Puyol, M. Khider, M. Lichtenstern and L. Bruno. *Simultaneous localization and mapping for pedestrians using distortions of the local magnetic field intensity in large indoor environments*. In International conference on indoor positioning and indoor navigation (IPIN), pages 1–10, Montbeliard-Belfort, France, 2013. IEEE.

[Roetenberg2005] D. Roetenberg, H.-J. Luinge, C.-T. Baten and P.-H. Veltink. *Compensation of magnetic disturbances improves inertial and magnetic sensing of human body segment orientation*. IEEE Transactions on neural systems and rehabilitation engineering, vol. 13, no. 3, pages 395–405, 2005.

[Roithmayr2004] C.-M. Roithmayr. *Contributions of spherical harmonics to magnetic and gravitational fields*. 2004.

[Árvai2020] L. Árvai and S. Homolya. *Filtering Methods for Indoor Magnetic Compass*. In International Carpathian Control Conference (ICCC), pages 1–5, High Tatras, Slovakia, 2020.

[Sabatini2006] A.-M Sabatini. *Quaternion-based extended Kalman filter for determining orientation by inertial and magnetic sensing*. IEEE transactions on Biomedical Engineering, vol. 53, no. 7, pages 1346–1356, 2006.

[Sainath2015] T.-N. Sainath, O. Vinyals, A. Senior and H. Sak. *Convolutional, long short-term memory, fully connected deep neural networks*. In International conference on acoustics, speech and signal processing (ICASSP), pages 4580–4584, Brisbane, Australia, 2015. IEEE.

[Schuster1997] M. Schuster and K.-K. Paliwal. *Bidirectional recurrent neural networks*. IEEE Transactions on Signal Processing, vol. 45, no. 11, pages 2673–2681, 1997.

[Senior2013] A. Senior, G. Heigold, M. Ranzato and K. Yang. *An empirical study of learning rates in deep neural networks for speech recognition*. In International conference on acoustics, speech and signal processing (ICASSP), pages 6724–6728, Vancouver, Canada, 2013. IEEE.

[Sharma2017] S. Sharma and S. Sharma. *Activation functions in neural networks*. Towards Data Science, vol. 6, no. 12, pages 310–316, 2017.

[Shen2020] C. Shen, Y. Zhang, X. Guo, X. Chen, H. Cao, J. Tang, J. Li and J. Liu. *Seamless GPS/inertial navigation system based on self-learning square-root cubature Kalman filter*. IEEE Transactions on Industrial Electronics, vol. 68, no. 1, pages 499–508, 2020.

[Shuster1981] M.-D. Shuster and S.-D. Oh. *Three-axis attitude determination from vector observations*. Journal of guidance and Control, vol. 4, no. 1, pages 70–77, 1981.

[Shuster1993] M. Shuster. *A survey of attitude representation*. Journal of The Astronautical Sciences, vol. 41, pages 439–517, 1993.

[Siami-Namini2019] S. Siami-Namini, N. Tavakoli and A.-S. Namin. *The performance of LSTM and BiLSTM in forecasting time series*. In International Conference on Big Data (Big Data), pages 3285–3292, Los Angeles, CA, USA, 2019. IEEE.

[Skog2010a] I. Skog, P. Handel, J.-O. Nilsson and J. Rantakokko. *Zero-velocity detection—An algorithm evaluation*. IEEE Transactions on Biomedical Engineering, vol. 57, no. 11, pages 2657–2666, 2010.

[Skog2010b] I. Skog, J.-O. Nilsson and P. Händel. *Evaluation of zero-velocity detectors for foot-mounted inertial navigation systems*. In International Conference on Indoor Positioning and Indoor Navigation (IPIN), pages 1–6, Zurich, Switzerland, 2010. IEEE.

[Skog2014] I. Skog, J. Nilsson and P. Händel. *An open-source multi inertial measurement unit MIMU platform*. In International Symposium on Inertial Sensors and Systems (ISISS), pages 1–4, Laguna Beach, CA, USA, 2014.

[Skog2016] I. Skog, J. Nilsson, P. Händel and A. Nehorai. *Inertial Sensor Arrays, Maximum Likelihood, and Cramér–Rao Bound*. IEEE Transactions on Signal Processing, vol. 64, no. 16, pages 4218–4227, 2016.

[Skog2018a] I. Skog. *Inertial and Magnetic-Field Sensor Arrays - Capabilities and Challenges*. In IEEE Sensors, pages 1–4, New Delhi, India, 2018. IEEE.

[Skog2018b] I. Skog, G. Hendeby and F. Gustafsson. *Magnetic Odometry - A Model-Based Approach Using a Sensor Array*. In International Conference on Information Fusion (FUSION), pages 794–798, Cambridge, United Kingdom, 2018.

[Skog2018c] I. Skog, J. Jaldén, J. Nilsson and F. Gustafsson. *Position and orientation estimation of a permanent magnet using a small-scale sensor array*. In International Instrumentation and Measurement Technology Conference (I2MTC), pages 1–5, Houston, Texas, USA, 2018.

[Storms2010] W. Storms, J. Shockley and J. Raquet. *Magnetic field navigation in an indoor environment*. In Ubiquitous Positioning Indoor Navigation and Location Based Service, pages 1–10, Helsinki, Finland, 2010. IEEE.

[Sun2018] W. Sun, W. Ding, H. Yan and S. Duan. *Zero velocity interval detection based on a continuous hidden Markov model in micro inertial pedestrian navigation*. Measurement Science and Technology, vol. 29, no. 6, page 065103, 2018.

[Susi2013] M. Susi, V. Renaudin and G. Lachapelle. *Motion mode recognition and step detection algorithms for mobile phone users*. Sensors, vol. 13, no. 2, pages 1539–1562, 2013.

[Sysnav2020] Sysnav. *Website*. https://www.sysnav.fr/?lang=en, 2020. Accessed: 2020-11-02.

[Tanygin2007] S. Tanygin and M.-D. Shuster. *The many triad algorithms*. Advances in the Astronautical Sciences, vol. 127, pages 81–99, 2007.

[Tie2018] J. Tie, J. Cao, L. Chang, S. Cai, M. Wu and J. Lian. *A Model of Gravity Vector Measurement Noise for Estimating Accelerometer Bias in Gravity Disturbance Compensation*. Sensors, vol. 18, no. 3, page 883, 2018.

[Tikhonov2002] A.-A. Tikhonov and K.-G. Petrov. *Multipole models of the earth's magnetic field*. Cosmic Research, vol. 40, no. 3, pages 203–212, 2002.

[Tong2019] X. Tong, Y. Su, Z. Li, C. Si, G. Han, J. Ning and F. Yang. *A double-step unscented Kalman filter and HMM-based zero-velocity update for pedestrian dead reckoning using MEMS sensors*. IEEE Transactions on Industrial Electronics, vol. 67, no. 1, pages 581–591, 2019.

[Tóth2011] G. Tóth, B. Van der Holst and Z. Huang. *Obtaining potential field solutions with spherical harmonics and finite differences*. The Astrophysical Journal, vol. 732, no. 2, page 102, 2011.

[Ullah2019] I. Ullah, M. Fayaz and D. Kim. *Improving Accuracy of the Kalman Filter Algorithm in Dynamic Conditions Using ANN-Based Learning Module*. Symmetry, vol. 11, no. 1, page 94, 2019.

[Vasconcelos2011] J.-F. Vasconcelos, G. Elkaim, C. Silvestre, P. Oliveira and B. Cardeira. *Geometric approach to strapdown magnetometer calibration in sensor frame*. IEEE Transactions on Aerospace and Electronic systems, vol. 47, no. 2, pages 1293–1306, 2011.

[Vincent2010] P. Vincent, H. Larochelle, I. Lajoie, Y. Bengio, P.-A. Manzagol and L. Bottou. *Stacked denoising autoencoders: Learning useful representations in a deep network with a local denoising criterion.* Journal of machine learning research, vol. 11, no. 12, 2010.

[Vissière2007a] D. Vissière, A.P. Martin and N. Petit. *Using magnetic disturbances to improve IMU-based position estimation*. In European Control Conference, pages 2853–2858, Kos, Greece, 2007. IEEE.

[Vissière2007b] D. Vissière, A.P. Martin and N. Petit. *Using spatially distributed magnetometers to increase IMU-based velocity estimation in perturbed areas*. In Conference on Decision and Control, pages 4924–4931, New Orleans, Louisiana, USA, 2007. IEEE.

[Wagstaff2017] B. Wagstaff, V. Peretroukhin and J. Kelly. *Improving foot-mounted inertial navigation through real-time motion classification*. In International Conference on Indoor Positioning and Indoor Navigation (IPIN), pages 1–8, Zurich, Switzerland, 2017. IEEE.

[Wagstaff2018] B. Wagstaff and J. Kelly. *LSTM-Based Zero-Velocity Detection for Robust Inertial Navigation*. In International Conference on Indoor Positioning and Indoor Navigation (IPIN), pages 1–8, Nantes, France, 2018.

[Wagstaff2019] B. Wagstaff, Va. Peretroukhin and J. Kelly. *Robust data-driven zero-velocity detection for foot-mounted inertial navigation*. IEEE Sensors Journal, vol. 20, no. 2, pages 957–967, 2019.

[Wahba1965] G. Wahba. *A least squares estimate of satellite attitude*. SIAM review, vol. 7, no. 3, pages 409–409, 1965.

[Wahlström2019] J. Wahlström, I. Skog, F. Gustafsson, A. Markham and N. Trigoni. *Zero-velocity detection—A Bayesian approach to adaptive thresholding*. IEEE Sensors Letters, vol. 3, no. 6, pages 1–4, 2019.

[Wahlström2020] J. Wahlström and I. Skog. *Fifteen Years of Progress at Zero Velocity: A Review*. IEEE Sensors Journal, 2020.

[Wang2015] Z. Wang, H. Zhao, S. Qiu and Q. Gao. *Stance-phase detection for ZUPT-aided foot-mounted pedestrian navigation system*. IEEE/ASME Transactions On Mechatronics, vol. 20, no. 6, pages 3170–3181, 2015.

[Wang2018] Q. Wang, Z. Guo, Z. Sun, X. Cui and K. Liu. *Research on the forward and reverse calculation based on the adaptive zero-velocity interval adjustment for the foot-mounted inertial pedestrian-positioning system*. Sensors, vol. 18, no. 5, page 1642, 2018.

[Wang2019a] A. Wang, X. Ou and B. Wang. *Improved step detection and step length estimation based on pedestrian dead reckoning*. In International Symposium on Electromagnetic Compatibility (ISEMC), pages 1–4, New Orleans, Los Angeles, USA, 2019. IEEE.

[Wang2019b] Q. Wang, L. Ye, H. Luo, A. Men, F. Zhao and Y. Huang. *Pedestrian stride-length estimation based on LSTM and denoising autoencoders*. Sensors, vol. 19, no. 4, page 840, 2019.

[Wang2019c] Y. Wang and A.-M. Shkel. *Adaptive threshold for zero-velocity detector in ZUPT-aided pedestrian inertial navigation*. IEEE Sensors Letters, vol. 3, no. 11, pages 1–4, 2019.

[Williamson1989] D.-F. Williamson, R.-A. Parker and J.-S. Kendrick. *The box plot: a simple visual method to interpret data*. Annals of internal medicine, vol. 110, no. 11, pages 916–921, 1989.

[Wu2018] D. Wu, L. Xia and J. Geng. *Heading Estimation for Pedestrian Dead Reckoning Based on Robust Adaptive Kalman Filtering*. Sensors, vol. 18, page 1970, 2018.

[Wu2019a] J. Wu, Z. Zhou, H. Fourati, R. Li and M. Liu. *Generalized Linear Quaternion Complementary Filter for Attitude Estimation from Multi-Sensor Observations: An Optimization Approach*. IEEE Transactions on Automation Science and Engineering, vol. 16, no. 3, pages 1330–1343, 2019.

[Wu2019b] Y. Wu, H.-B. Zhu, Q.-X. Du and S.-M. Tang. *A survey of the research status of pedestrian dead reckoning systems based on inertial sensors*. International Journal of Automation and Computing, vol. 16, no. 1, pages 65–83, 2019.

[Xing2017] H. Xing, J. Li, B. Hou, Y. Zhang and M. Guo. *Pedestrian stride length estimation from IMU measurements and ANN based algorithm*. Journal of Sensors, vol. 2017, 2017.

[Xiong2020] K. Xiong, C. Wei and H. Zhang. *Q-learning for noise covariance adaptation in extended KALMAN filter*. Asian Journal of Control, 2020.

[Yadav2014] N. Yadav and C. Bleakley. *Accurate orientation estimation using AHRS under conditions of magnetic distortion*. Sensors, vol. 14, no. 11, pages 20008–20024, 2014.

[Yang2006] Y. Yang and W. Gao. *An optimal adaptive Kalman filter*. Journal of Geodesy, vol. 80, no. 4, pages 177–183, 2006.

[Yao2020] Y. Yao, L. Pan, W. Fen, X. Xu, X. Liang and X. Xu. *A Robust Step Detection and Stride Length Estimation for Pedestrian Dead Reckoning Using a Smartphone*. IEEE Sensors Journal, vol. 20, no. 17, pages 9685–9697, 2020.

[Ye2020] F. Ye, F. Shi, Y. Lai, X. Zhou and K. Li. *Heading angle estimation using rotating magnetometer for mobile robots under environmental magnetic disturbances*. Intelligent Service Robotics, vol. 13, pages 459–477, 2020.

[Zampella2011] F.-J. Zampella, A.-R. Jiménez, F. Seco, J.-C. Prieto and J.-I. Guevara. *Simulation of foot-mounted IMU signals for the evaluation of PDR algorithms*. In International Conference on Indoor Positioning and Indoor Navigation (IPIN), pages 1–7. IEEE, 2011.

[Zhang2016] C. Zhang, A. Taghvaei and P.-G. Mehta. *Attitude estimation with feedback particle filter*. In Conference on Decision and Control (CDC), pages 5440–5445, Las Vegas, NV, USA, 2016. IEEE.

[Zhao2021] T. Zhao and M.-J. Ahamed. *Pseudo-zero velocity re-detection double threshold zero-velocity update (ZUPT) for inertial sensor-based pedestrian navigation (to appear)*. IEEE Sensors Journal, 2021.

[Zhou2021] Z. Zhou, C. Zeng, X. Tian, Q. Zeng and X. Lu. *A quaternion-based indirect Gaussian particle filter for nonlinear attitude estimation*. Review of Scientific Instruments, vol. 92, no. 5, page 055007, 2021.

List of Figures

List of Tables

Magnetometer Array-Based Indoor Navigation Using Kalman Filter

Résumé

Cette thèse porte sur la navigation intérieure sans GPS, en se basant uniquement sur des capteurs magnéto-inertiels à bas coût, et sans l'utilisation d'une cartographie préalable du champ magnétique, ou une infrastructure dédiée. L'idée principale est d'utiliser les perturbations du champ magnétique présentes à l'intérieur des bâtiments pour générer non seulement une estimation de la vitesse, mais aussi de l'attitude et de la position de l'objet mobile étudié, permettant ainsi de reconstruire toute trajectoire effectuée. Pour ce faire, les dérivées spatiales du champ magnétique sont explorées à travers un réseau de magnétomètres spécifique. À partir de ce réseau, le gradient du champ magnétique est déterminé à travers des approximations. Ainsi, il présente des incertitudes et du bruit. Pour cette raison, un modèle de navigation magnéto-inertielle standard (MINAV) a été amélioré en introduisant une nouvelle équation qui décrit la dynamique du gradient du champ magnétique. Le nouveau modèle proposé se démarque des modèles habituels utilisés dans la littérature correspondante, car il capture pleinement la richesse des variations du gradient du champ magnétique, et permet de réduire ses incertitudes et son bruit.
Ensuite, différents algorithmes basés sur le filtre de Kalman étendu (EKF) sont implémentés, pour mettre en œuvre le modèle proposé. Néanmoins, les performances de l'EKF se dégradent sous certaines conditions, principalement liées à la qualité des mesures. Par conséquent, il est nécessaire de le combiner avec la technique de la mise à jour de la vitesse nulle (ZUPT), dans le cas où le capteur est sur le pied, ou les réseaux de neurones profonds (DNNs) dans un cas plus général.
Les algorithmes proposés sont évalués non seulement sur des données simulées mais aussi sur un benchmark expérimental utilisant un réseau de capteurs réels en présence d'équipements de vérité-terrain. Les résultats obtenus illustrent l'apport de cette thèse sur l'estimation de la vitesse et par conséquent sur la reconstruction de trajectoires.

Mots-clés : Navigation intérieure, réseau de magnétomètres, capteurs inertiels, filtre de Kalman étendu, intelligence artificielle

Abstract

This thesis focuses on GPS-free indoor navigation using only strapdown low-cost magneto-inertial sensors and without relying on any prior-mapping of the magnetic field, nor on a dedicated infrastructure. The main idea is to take advantage of the magnetic field's disturbances present indoor to generate not only a velocity estimate, but also attitude, and position of the moving body under study, enabling therefore the reconstruction of any performed trajectory. To do so, the spatial derivatives of the magnetic field are explored throughout a specific set of a magnetometer array. From this array, the magnetic field gradient is determined using approximation methods. It follows that it suffers from uncertainties and noise. For this reason, a standard Magneto-Inertial Navigation (MINAV) model is enhanced by introducing a new equation that describes the magnetic field gradient dynamics. The new proposed model stands out from the usual ones used in the corresponding literature, as it fully captures the richness of the magnetic field gradient variations, and enables reducing its uncertainties and noise. Then, different algorithms based on Extended Kalman Filtering (EKF) are implemented, to make use of the proposed model. Nevertheless, the performance of the EKF is degraded under certain conditions, mostly related to measurements quality. Therefore, it becomes necessary to combine it with the Zero-velocity Update Technique (ZUPT), in the case of foot-mounted navigation or Deep Neural Networks (DNNs) in the more general case. The proposed algorithms are assessed not only on simulated data but also on a real experimental benchmark using a sensor array, in presence of ground truth equipment. The obtained results illustrate the contribution of this thesis on the velocity estimation and consequently on the trajectory reconstruction.

Keywords : Indoor navigation, magnetometer array, inertial sensors, extended Kalman filter, artificial intelligence